Quantum Magnetism in Coordination Polymers

by

Jamie Daniel Brambleby

Thesis

Submitted to the University of Warwick

for the degree of

Doctor of Philosophy

Department of Physics

April 2018

THE UNIVERSITY OF
WARWICK

Contents

List of Figures

N.B. All references appearing in the figure captions may be found on the respective page numbers listed here.

List of Tables

N.B. All references appearing in the table captions may be found on the respective page numbers listed here.

Acknowledgments

I would first of all like to thank my supervisor Paul A. Goddard for all of the support, encouragement and guidance that he has provided throughout this project and the writing of this thesis; and Martin R. Lees for generously offering his time and experimental expertise on countless occasions over the course of my graduate studies at the University of Warwick (UK). I would like to extend my thanks to all of those that I have collaborated with at Warwick, both in the laboratory and through the discussions of data, and in particular I am grateful to William J. A. Blackmore, Thomas J. Hicken, Benjamin A. Slater, Matthew M. Healey, Matthew J. Pearce, Laurence Ede, Robert C. Williams, David Walker, Guy Clarkson, and Steve Huband. I also thank Thomas E. Orton, Patrick Ruddy and Ali Julien for all of the support with experimental equipment that they provided.

I would especially like to thank John Singleton and Marcelo Jaime from the National High Magnetic Field Laboratory (NHMFL), Los Alamos (USA) for their insightful contributions to some of the papers resulting from this thesis, and also for all of the experimental assistance and advice they provided regarding the work performed at NHMFL. I would also like to thank all of the user support scientists that I met at NHMFL, Los Alamos, for making the trips both productive and enjoyable.

I am extremely grateful to Roger D. Johnson from the University of Oxford (UK); P. Manuel from the ISIS Neutron and Muon Source, Rutherford Appleton Laboratory (RAL) (UK); Matthew B. Stone from Oak Ridge National Laboratory (USA); Craig M. Brown from the National Institute of Standards and Technology (NIST) in Gaithersberg (USA); and all of the user support scientists I met at RAL

(UK) and NIST (USA), for all of their assistance regarding the neutron scattering measurements and analysis presented in this thesis, and also for being so welcoming on my visits to these facilities.

An extra special thanks are owed to Jamie L. Manson, Hope E. Tran, Peter K. Peterson, Peter M. Spurgeon, Jordan F. Corbey, Kimberley E. Carreiro, Jaqueline A. Villa, Sophie G. Schwalbe and Zachary E. Manson at Eastern Washington University (USA) for providing the all of the samples measured in this thesis; to Stephen J. Blundell (Univeristy of Oxford, UK) and Tom Lancaster (Durham University, UK) for each of the useful discussions we had, and for proof reading several of the publications resulting from the work in this thesis; to Craig V. Topping, Junjie Liu, Danielle Kaminski, Saman Ghannadzedah, and Francesca Foronda (University of Oxford, UK) for all of their assistance with the experiments and data analysis presented in this project; and to each and every other co-author of the publications (i)−(x) listed in the declarations below, which are referenced in this work.

I am grateful to the Engineering and Physical Sciences Research Council for funding this project, to NHMFL for the provision of magnet time, and to RAL (Science and Technologies Facilities Council) and NIST (U.S. Department of Commerce) for providing beam time. Work performed at NHMFL was supported by National Science Foundation Cooperative Agreement DMR-1157490, the State of Florida, U.S. Department of Energy, and through the Department of Energy Basic Energy Science Field Work Project "Science in 100 T". The samples produced at Eastern Washington University (USA) were prepared with the support of the National Science Foundation under Grant numbers DMR-1306158, DMR-1703003, and DMR-1157490, and with the NIST Cooperative Agreement 70NANB15H262.

I'd like to thank Hazel, Esther, Luke, Sarah, Violet, and all my family for all of their support and encouragement. Finally, this thesis would not have been possible were it not for extraordinary amount of support offered by Dariush Saeedi, Simon Kennedy, Annette Morgan, Anna Daniels, Tony Brownbridge, Victoria Brattan, Ganesh Sivaji, Mark Cavill, Meghana Devidas, Jade, and Nicola Scott. They are all owed a tremendous amount of thanks.

Declarations

The work in this thesis is my own, except in cases where explicitly stated in the acknowledgements (above) and the experimental details sections of Chapters 3−5. This thesis has not been submitted to any other institution for the award of a degree. The publications (i)−(x) resulting from this project are listed below. Chapter 3 of this thesis relates to Ref. (viii), Chapter 4 forms part of Ref. (x), Chapter 5 combines the work of Refs. (ii) and (ix), while some of the other publications are referenced, as appropriate, in Chapters 1−6.

(i) "A Single-Ion Magnet Based on a Heterometallic $Co^{III}_2Dy^{III}$ Complex", J. Goura, J. Brambleby, P. A. Goddard, and V. Chandrasekhar, Eur. J. Chem. **21**, 4926 (2015).

(ii) "Magnetic ground state of the two isostructual polymeric quantum magnets $[Cu(HF_2)(pyrazine)_2]SbF_6$ and $[Co(HF_2)(pyrazine)_2]SbF_6$ investigated with neutron powder diffraction", J. Brambleby, P. A. Goddard, R. D. Johnson, J. Liu, D. Kaminski, A. Ardavan, A. J. Steele, S. J. Blundell, T. Lancaster, P. Manuel, P. J. Baker, J. Singleton, S. G. Schwalbe, P. M. Spurgeon, H. E. Tran, P. K. Peterson, J. F. Corbey, and J. L. Manson, Phys. Rev. B **92**, 134406 (2015).

(iii) "Experimental and Theoretical Electron Density Analysis of Copper Pyrazine Nitrate Quasi-Low-Dimensional Quantum Magnets", L. H. R. Dos Santos, A. Lanza, A. M. Barton, J. Brambleby, W. J. A. Blackmore, P. A. Goddard, F. Xiao, R. C. Williams, T. Lancaster, F. L. Pratt, S. J. Blundell, J. Singleton, J. L. Manson, and P. Macchi, J. Am. Chem. Soc. **138**, 2280 (2016).

(iv) "Magnetism in a family of $S = 1$ square lattice antiferromagnets $NiX_2(pyz)_2$

(X = Cl, Br, I, NCS; pyz = pyrazine)", J. Liu, P. A. Goddard, J. Singleton, J. Brambleby, F. Foronda, J. S. Möller, Y. Kohama, S. Ghannadzadeh, A. Ardavan, S. J. Blundell, T. Lancaster, F. Xiao, R. C. Williams, F. L. Pratt, P. J. Baker, K. Wierschem, S. H. Lapidus, K. H. Stone, P. W. Stephens, J. Bendix, M. R. Lees, T. J. Woods, K. E. Carreiro, H. E. Tran, C. J. Villa, J. L. Manson, Inorg. Chem. **55**, 3515 (2016).

(v) "Control of the third dimension in copper-based square-lattice antiferromagnets", P. A. Goddard, J. Singleton, I. Franke, J. S. Möller, T. Lancaster, A. J. Steele, C. V. Topping, S. J. Blundell, F. L. Pratt, C. Baines, J. Bendix, R. D. McDonald, J. Brambleby, M. R. Lees, S. H. Lapidus, P. W. Stephens, B. W. Twamley, M. M. Conner, K. Funk, J. F. Corbey, H. E. Tran, J. A. Schlueter, and J. L. Manson, Phys. Rev. B **93**, 094430 (2016).

(vi) "Heterometallic Trinuclear $\{Co^{III}_2 Ln^{III}\}$ (Ln = Gd, Tb Ho and Er) Complexes in a Bent Geometry. Field-induced Single-Ion Magnet Behavior of the Er^{III} and Tb^{III} Analogues", V. Chandrasekhar, J. Goura, J. Brambleby, P. A. Goddard, C. V. Topping, R. S. Narayanan and A. K. Bar, Dalt. Trans. **45**, 9235 (2016).

(vii) "Octanuclear Heterobimetallic $\{Ni_4 Ln_4\}$ Assemblies Possessing Ln_4 Square Grid [2 × 2] Motifs: Synthesis, Structure, and Magnetism", S. Biswas, J. Goura, S. Das, C. V. Topping, J. Brambleby, P. A. Goddard, and V. Chandrasekhar, Inorg. Chem. **55** 8422 (2016).

(viii) "Adiabatic physics of an exchange-coupled spin-dimer system: Magnetocaloric effect, zero-point fluctuations, and possible two-dimensional universal behavior", J. Brambleby, P. A. Goddard, J. Singleton, M. Jaime, T. Lancaster, L. Huang, J. Wosnitza, C. V. Topping, K. E. Carreiro, H. E. Tran, Z. E. Manson, and J. L. Manson, Phys. Rev. B **95**, 024404 (2017).

(ix) "Combining microscopic and macroscopic probes to untangle the single-ion anisotropy and exchange energies in an $S = 1$ quantum antiferromagnet",
J. Brambleby, J. L. Manson, P. A. Goddard, M. B. Stone, R. D. Johnson, P. Manuel, J. A. Villa, C. M. Brown, H. Lu, S. Chikara, V. Zapf, S. H. Lapidus, R. Scatena, P.

Macchi, Y.-S. Chen, L.-C. Wu, and J. Singleton, Phys. Rev. B **95**, 13435 (2017).

(x) "Implications of bond disorder in a $S = 1$ kagome lattice", J. L. Manson, J. Brambleby, P. A. Goddard, P. M. Spurgeon, J. A. Villa, S. Ghannadzadeh, F. Foronda, J. Singleton, T. Lancaster, S. J. Clark, I. O. Thomas, F. Xiao, R. C. Williams, F. L. Pratt, S. J. Blundell, C. V. Topping, C. Baines, C. Campana, and B. Noll, Sci. Rep. **8**, 4745 (2018).

Part of this thesis was also presented at the following conferences:

(i) Contributed talk at Institute of Physics Magnetism, Leeds, UK (2015).

(ii) Poster presentation at the International Symposium of Crystalline Organic Materials, Bad Gögging, Germany (2015).

(iii) Poster presentation at Research in High Magnetic Fields, Grenoble, France (2015).

(iv) Contributed talk at the Theoretical and Experimental Magnetism Meeting, Rutherford Appleton Laboratory, UK (2016).

(v) Contributed talk and poster presentation at the Gordon Research Seminar, Conductivity and Magnetism in Molecular Materials, Mount Holyoke College, MA, USA (2016).

(vi) Poster presentation at the Gordon Research Conference, Conductivity and Magnetism in Molecular Materials, Mount Holyoke College, MA, USA (2016).

Abbreviations

2D = Two dimensional

3-Clpy = 3-Chloropyridine

3D = Three dimensional

3-Fpy = 3-Fluoropyridine

4-PhpyO = 4-Pheynyl-pyridine-*N*-oxide

Ac = Alternating current

AFM = Antiferromagnet

A.u. = Arbitrary units

BEC = Bose-Einstein condensate

BKT = Beresinski-Kosterlitz-Thouless

BSCCO = Bismuth strontium calcium copper oxide

CEF = Crystalline electric field

Dc = Direct current

DCS = Disc Chopper Spectrometer

DFT = Density-functional theory

DM = Dzyaloshinskii-Moriya

ESR = Electron spin-resonance

GE = General Electric™

Gly = Glycinate

GPS = Genneral Purpose Surface-Muon

INS = Inelastic neutron scattering

LP = Long-pulse

LRO = Long-range order

LTF = Low Temperature Facility

MCE = Magnetocaloric effect

MPMS = Magnetic Property Measurement System

NHMFL = National High Magnetic Field Laboratory

NKMFL = Nickolas Kurti Magnetic Field Laboratory

NIST = National Institute for Standards and Technology

NPD = Neutron powder diffraction

PCTFE = Polychlorotrifluoroethene

PDO = Proximity detector oscillation

PPMS = Physical Property Measurement System

PTFE = Polytetrafluoroethene

PyO = Pyridine-*N*-oxide

Pyz/pyz-d_4 = Pyrazine/deuterated pyrazine

QCP = Quantum critical point

QD = Quantum Design™

QMC = Quantum Monte-Carlo

QP = Quantum paramagnet

Q1D = Quasi-one-dimensional

Q2D = Quasi-two-dimensional

RAL = Rutherford Appleton Laboratory

R.l.u. = Reciprocal lattice units

SQUID = Superconducting quantum interference device

SP = Short-pulse

SμS = Swiss Muon Source

VSM = Vibrating sample magnetometer

YBCO = Yttrium barium copper oxide

ZPF = Zero-point fluctuations

μ^+SR = Muon spin-rotation

Abstract

This thesis presents an experimental and theoretical examination of five polymeric quantum magnets. The first of these is Cu(pyrazine)(glycinate)ClO_4, an exchange-coupled spin-dimer system that undergoes a powerful and continuous magnetocaloric effect (MCE) in a rapidly changing magnetic field H. The evolution of the sample temperature T with H must be accounted for in order to reconcile an apparent discrepancy between the results of magnetometry measurements performed in quasistatic and pulsed magnetic fields, and the MCE is likely to be an important consideration for pulsed-field experiments performed on similar insulating materials. Heat capacity measurements of Cu(pyrazine)(glycinate)ClO_4 are perturbed by zero-point fluctuations for $T > 400$ mK, and these data further suggest that this system exhibits possible two-dimensional universal behaviour.

The results of single crystal x-ray diffraction measurements of a second material $[H_2F]_2[NiF_2(3\text{-fluoropyridine})_4]_3[SbF_6]_2$ at 100 K indicate that the Ni^{2+} ions of this complex are arranged on the vertices of a two-dimensional kagome lattice, wherein the spin $S = 1$ ions are bridged via charge-assisted Ni-F$\cdots$H-F-H$\cdots$F-Ni linkages. However, a density-functional theory study indicates that a positional disorder of the H_2F^+ moieties within these bridges suppresses the intraplane spin-exchange interactions. Powder muon spin-rotation measurements imply that the system is paramagnetic for $T > 19$ mK, while polycrystalline electron spin-resonance (ESR), magnetization $M(H)$, and heat capacity experiments together indicate that the unixial and rhombohedral single-ion anisotropy of the Ni^{2+} ions are approximately $D/k_B = 8.3(4)$ K and $E/k_B = 1.2(3)$ K respectively.

Lastly, neutron powder diffraction measurements of three isotructural compounds $[M(HF_2)(\text{pyrazine})_2]SbF_6$ ($M = Cu^{2+}$, Ni^{2+} or Co^{2+}) reveal that each system is tetragonal ($P4/nmm$) and that the spin-exchange interactions facilitated by the pyrazine (J_{pyz}) and bifluoride (J_{FHF}) ligands are antiferromagnetic. The Cu^{2+} congener is a quasi-two-dimensional Heisenberg $S = 1/2$ antiferromagnet, which displays an ordered moment of $0.6(1)\mu_B$ per ion that is reduced from its paramagnetic value by quantum fluctuations. For the $S = 1$ Ni^{2+} complex, powder $M(H)$ measurements suggest that D has an easy-plane character while inelastic neutron scattering experiments determine $D/k_B = 13.3(3)$ K, $J_{FHF}/k_B = 10.4(3)$ K and $J_{pyz}/k_B = 1.4(2)$ K. The $S = 3/2$ Co^{2+} system adopts an Ising-like antiferromagnetic ground state below 7.1(1) K, and its magnetic properties are parameterized with an effective spin-1/2 Hamiltonian for $T < 50$ K.

Chapter 1

Introduction

1.1 Chapter overview

The aim of this chapter is to introduce some aspects of the current understanding of magnetism in condensed matter systems, which regards bulk magnetic properties as phenomena that emerge out of the short-range electronic interactions between individual spin quanta in a material. The next section provides an historical overview of the research into quantum spin systems and highlights that the concept of bulk magnetism as an emergent characteristic arose out of the collective effort of several individual physicists, culminating in an increased motivation to develop new magnetic materials that persists today. Section 1.3 presents coordination polymers (i.e. self-assembling crystalline compounds that consist of transition metal ions linked via molecular ligands) as designer materials for the exploration of quantum magnetism, and this section provides a brief survey of some of the key molecule-based magnets that have been developed to date before introducing the five polymeric systems that are investigated in this thesis. Following this, Section 1.4 provides definitions of the thermodynamic properties of magnetic complexes that are probed in the experimental investigations of this project and, finally, Section 1.5 elaborates upon the scope of this thesis, which is to research the quantum phenomena exhibited by molecular magnets; that is, the finite temperature observable characteristics of magnetic materials that cannot be explained semi-classically.

1.2 The historical interest in solid state magnetism

The modern day applications of magnetic materials as the functional components of technological devices such as power generators, hard-drives, loudspeakers, and

sensors are just some of the achievements of a sustained theoretical and experimental effort to obtain a microscopic understanding of magnetism. Early progress towards a quantitative model of magnetism took steps forward in the late 1800s when Pierre Curie firstly formulated the argument that the ferromagnetic properties of permanent magnets spontaneously develop below a critical temperature [1] before Zeeman went on to make a Nobel prize winning discovery that an externally applied magnetic field H modulated the wavelength of the spectral lines emitted by sodium vapour [2], which would later be understood in terms of the magnetic moment of individual Na ions coupling to the direction of H. In 1907 Weiss hypothesized that the individual moments of a large ensemble will each naturally orientate to the "mean field" produced by all of the other moments in the system [3], and thus introduced the idea that the bulk magnetic properties of a solid could be supported by the mutual interactions between moments on a microscopic level (e.g. Ref. [4]).

Further advancements in the understanding of the origins of solid state magnetism came about through the investigations led by Sommerfeld [5, 6], Stern-Gerlach [7] and Pauli [8] in the early 20^{th} century. Collectively, their work concluded that a stable transition metal or rare-earth ion has a magnetic moment that is parameterized by its total electronic spin and orbital angular momentum. In 1928, Heisenberg used this concept to explain the tendency for the orientations of individual spins in a material to adopt an ordered configuration with a short-range electronic interaction [9]. He posited that a direct spatial overlap of the wavefunctions of two electrons from neighbouring ions in a material results in a finite probability for the electrons to be exchanged, which causes the electrons' spin angular momentum to align collinearly. Anderson later formulated a description of a superexchange interaction [10], whereby the electronic exchange between two spin centres is mediated by an intervening ion and similarly causes neighbouring moments to orientate in a cooperative arrangement to lower the Coulomb energy of the system. Quantitatively, Anderson's electronic superexchange model considers two spins $\mathbf{S}_{1,2}$ interacting via a term in the magnetic Hamiltonian $\hat{\mathcal{H}}$ of the form

$$\hat{\mathcal{H}} = J\mathbf{S}_1 \cdot \mathbf{S}_2, \tag{1.1}$$

where J is the Heisenberg spin-exchange constant.

Néel extended the concept of ordered spin states to include antiferromagnets (AFMs) in 1932 [11]. These are magnetically ordered materials for which there is no net bulk magnetic moment since pairs of neighbouring spins preferentially adopt an antiparallel alignment. By 1949, such a spin configuration was observed with neutron diffraction experiments performed on the ionic compound MnO [12]. Here,

the Mn^{2+} spins order antiferromagnetically below 116 K and this was readily explained by a superexchange interaction (with $J > 0$) mediated by the O^{2-} ions. An interest surrounding AFMs that possess spin-exchange interactions in a low number of spatial dimensions grew with the realization that these materials often exhibited other exotic cooperative electronic phenomena, such as high temperature superconductivity in the cuprates (e.g. Refs. [13, 14]) and, more generally, materials that are predicted to exhibit zero-temperature phase transitions at a quantum critical point [15, 16]. Spin networks in low-dimensional spatial geometries captured the attention of Kosterlitz and Thouless [17,18], who collaborated to lead the investigation of two-dimensional systems with uniaxial symmetry, along with Haldane [19,20], who established a physical grounding for the magnetic properties of integer-spin chains, and the far-reaching implications of their work earned them the award of the 2016 Nobel Prize [21].

As the predictions for exotic magnetic phenomena grew, so too did the desire to find new materials to study these properties. However, the applicability of naturally occurring inorganic solid state systems to the investigation of magnetism is limited, largely, by the energy scale of their typical J values, which are characteristically much greater than the experimentally accessible temperature and applied magnetic field ranges within which it is possible to study these materials. One modern research trend, that aims to open up the range of systems that are suitable for experimental studies, is to investigate the extent to which bespoke spin-exchange interactions can be methodically engineered into a system. A particularly effective strategy in this endeavour is to synthesize organic coordination polymers [4, 22–24], which are designed to incorporate transition metal ions connected via molecular building blocks to mediate spin-exchange interactions. It is the application of these molecular materials to the study of quantum magnetism that is the focus of this thesis.

1.3 Coordination polymers: designer materials for the study of quantum magnetism

1.3.1 Introduction to coordination polymers

Utilizing organic coordination polymers as a route to develop new quantum magnets exploits the flexibility of carbon chemistry to produce networks of spin quanta in a wide range of crystalline architectures. This approach takes inspiration from the numerous examples of naturally occurring biological polymers that exhibit di-

verse functional properties despite containing relatively few ingredients [22]. Synthetic molecular materials have been developed to facilitate research in several condensed matter disciplines, which includes the use of organic materials as light emitting diodes that have a particularly low energy consumption [25]; organic systems that display ambient pressure superconductivity for critical temperatures as high as 38 K [26, 27]; and porous polymeric compounds that are employed as reusable gas separation devices [28], but it the application of coordination polymers to the study fundamental magnetism to which this section is dedicated.

The discussion of molecular magnets in the remainder of this section is organized into four parts: (i) a description of the single-ion physics of transition metals in octahedral coordination geometries; (ii) an introduction to spin-exchange interactions mediated by molecular ligands; (iii) a review of some of the key molecular magnets that have been used for the investigation of low-dimensional spin networks; and (iv) an overview of the five polymeric magnets studied in this thesis.

1.3.2 Transition metal ions in octahedral environments

(a) Section overview: Homometallic molecular magnets are a subset of coordination polymers designed around a single species of transition metal ion [24] and this section outlines two properties of transition metal ions in octahedral coordination environments that act as two degrees of freedom in the design of new magnets. Firstly, the choice of ion dictates its spin quantum number (S) via Hund's rules and secondly, individual ionic moments with $S \geq 1$ have anisotropic properties that are acquired from an electromagnetic interaction between their constituent electrons and a crystalline electric field (CEF) in addition to the spin-orbit coupling interaction. These two properties are discussed, in turn, below with reference to the specific examples of octahedrally coordinated Cu^{2+}, Ni^{2+} and Co^{2+} ions, which are relevant to the materials studied in this project.

(b) Spin quantum number and orbital quenching: Electrons have an intrinsic spin ($s = 1/2$), and an individual transition metal ion acquires its magnetic moment from the total spin (S) and orbital (L) angular momentum of unpaired electrons within its atomic orbitals. The z-component of the total spin m_s adopts half-integer values since S is derived from a fixed number of electrons. Each free-ion orbital furthermore consists of $2L + 1$ degenerate suborbitals labelled by m_L, the quantized z-component of L, where m_L takes integer values in the range $-L \leq m_L \leq L$ (e.g. Refs. [29–31]). To see why this is the case it is instructive to firstly consider the action of $\mathbf{L} = (\hat{L}^x, \hat{L}^y, \hat{L}^z)$ operators on a free-ion electronic wavefunction $|L, m_L, S, m_s\rangle$.

For instance, by writing $\hat{L}^x = \frac{1}{2}(\hat{L}^+ + \hat{L}^-)$, where $\hat{L}^{+/-}$ are the raising/lowering operators (e.g. Ref. [31]), the matrix element $\langle L, m'_L, S, m'_s|\hat{L}^x|L, m_L, S, m_s\rangle \neq 0$ providing $|m_L - m'_L| = 1$ and $m_s = m'_s$ and thus the operator is interpreted as transferring electrons between degenerate m_L-suborbitals without changing the electron's spin. In effect, **L** operators rotate the spatial probability distribution electrons giving rise to the analogy of "orbital" motion [31]. The condition that m_l takes integer values ensures that rotation operations such as $e^{2\pi i\hat{L}^z}|L, m_L\rangle = e^{2\pi i m_L}|L, m_L\rangle$ are equivalent to unitary transformations [31] and that the azimuthal part of the electronic wavefunction is single-valued [32].

Each m_L-suborbital has a maximum occupancy of two electrons, which must have opposite signs of s owing to Pauli's exclusion principle [33]. For a particular ion, electrons preferentially fill the orbitals with the lowest potential energy and Hund's rules for filling suborbitals apply if there is an insufficient number of electrons to fully occupy the highest energy level. These are summarized as [30]: (i) maximize S, which amounts to occupying separate m_L-suborbitals before electrons are paired up. This lowers spatial overlap of the electrons' wavefunctions, thereby lowering the extent to which electrons screen each other from the attractive nuclear charge; (ii) maximize L, which again lowers the total Coulomb energy of the system; and (iii) minimize the energy of the spin-orbit coupling interaction (that is, if the orbital is less than half full the total angular momentum is $|L - S|$, else it is $L + S$).

Stable transition metal ions commonly have unpaired electrons in d-orbitals ($L = 2$) for which there are five degenerate suborbitals [Fig. 1.1(a)] that each provide an electron with a unique spatial probability distribution. In coordination complexes, six molecular ligands individually donate a lone pair of electrons to a transition metal ion to form a coordination bond, usually, such that there is metal-ligand bond of this type along each of the Cartesian axes centred on the ion [Fig. 1.1(b)]. The negative charge density of the bonds around the ion generates a CEF that lifts the degeneracy of the ion's d-orbitals. In this coordination configuration, the Coulomb potentials of both the $d_{x^2-y^2}$ and d_{z^2} suborbitals [Fig. 1.1(a), red lobes] are raised, as electrons in these states are likely to be distributed along the Cartesian axes, towards the ligands. The d_{xy}, d_{yz} and d_{zx} suborbitals (blue lobes), meanwhile, become lower in energy as negatively charged electrons in these states have a relatively high probability to occupy the spaces between the Cartesian axes.

For Cu^{2+} ($3d^9$) [Fig. 1.1(c)], Hund's rules result in a single unpaired electron in the highest energy suborbital and therefore $S = 1/2$. The total energy of the ion is lowered by a spontaneous Jahn-Teller distortion, which results in an elongation of the z-axis of the octahedra around each ion. This, in turn, reduces the Coulomb

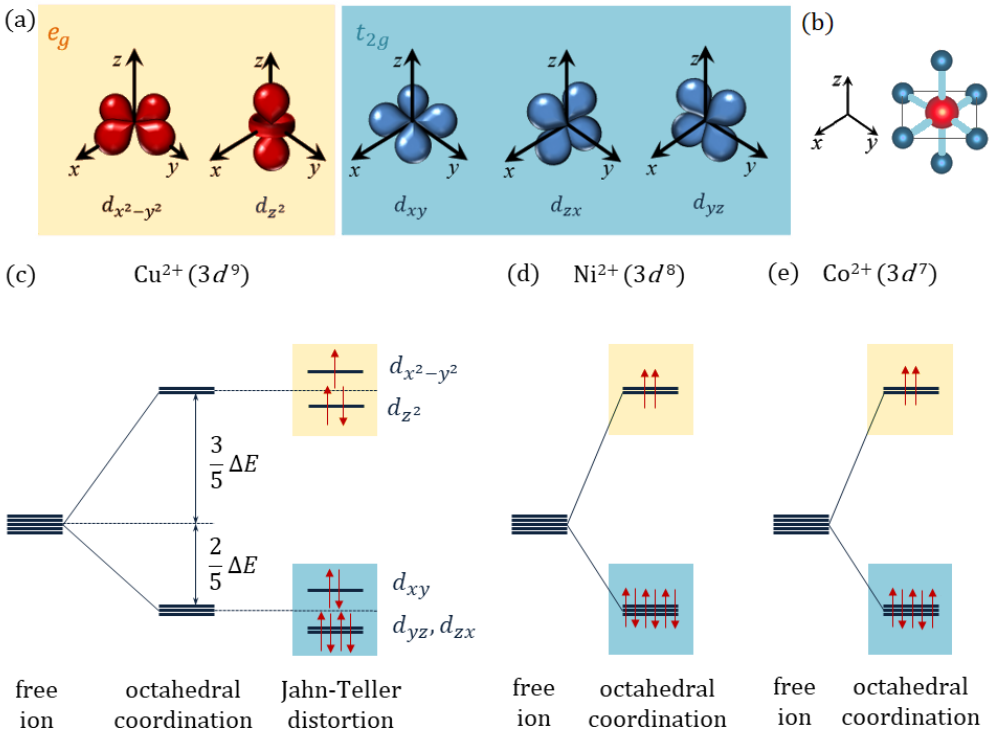

Figure 1.1: **(a)** Sketches of the spatial distributions of the five atomic d-suborbitals. **(b)** Transition metal ions (red sphere) ligated to six molecules (blue spheres) via coordination bonds (pale-blue lines) form octahedral environments. **(c)** Cu^{2+} $(3d^9)$ has one unpaired electron in the $d_{x^2-y^2}$ orbital owing to a spontaneous Jahn-Teller elongation of the surrounding octahedra (see text); **(d)** Ni^{2+} $(3d^8)$ has two unpaired electrons in each of the e_g orbitals; **(e)** High-spin Co^{2+} $(3d^7)$ has two unpaired electrons in each e_g orbital and one unpaired electron in the t_{2g} orbitals. Figures adapted from Refs. [22, 29]

potential of the doubly occupied d_{z^2} orbital at the expense of the singly occupied $d_{x^2-y^2}$ orbital. For Ni^{2+} $(3d^8)$ [Fig. 1.1(d)], Hund's rules dictate that there are two unpaired electrons with one in each of the $d_{x^2-y^2}$ and d_{z^2} orbitals. Consequently the spin $S = 1$ for this ion and the system is not Jahn-Teller active. For Co^{2+} $(3d^7)$, the first five electrons occupy individual d-orbitals and then one of two cases occurs: (i) if the Coulomb energy cost of pairing two electrons E_P exceeds the CEF splitting of the d-orbitals ΔE, the ion adopts a high-spin configuration with three unpaired electrons and $S = 3/2$ [Fig. 1.1(e)]; or (ii) if $\Delta E > E_P$ a low-spin $(S = 1/2)$ configuration is preferable.

The orbital contribution to the Cu^{2+}, Ni^{2+} and Co^{2+} ion's total magnetic moment is deduced by considering the effect of $\mathbf{L}$ operators acting on the spin states

depicted in Fig. 1.1. For octahedrally coordinated Cu^{2+} moments, the Jahn-Teller distortion means there are no degenerate d-orbitals that the unpaired electron can be transferred to by the action of an orbital angular momentum operator and therefore the orbital motion is quenched ($L = 0$ as a first order approximation). In Ni^{2+} the unpaired electrons occupy one of two degenerate orbitals, however $\mathbf{L}$ operators cannot transfer spins between them because this would pair electrons with parallel spins so, again, L is approximately zero. For $S = 3/2$ Co^{2+} in perfectly symmetric octahedra, electrons can be transferred between d-orbitals within the low lying triplet and, thus, the orbital motion is not necessarily quenched.

(c) Anisotropic terms in the single-ion spin Hamiltonian: As m_L dictates the spatial probability distribution of electrons [e.g. Fig. 1.1(a)] it indirectly determines the strength of the electromagnetic interaction between an electron in a particular suborbital and the CEF. Therefore, L adopts a preferential orientation so as to reduce the Coulomb energy of its constituent electrons in m_L suborbitals. This preferred direction is transferred to S so as to minimize the energy of the spin-orbital coupling interaction (e.g. Refs. [23, 29, 30]). For Co^{2+} ions, the potential for unquenched orbital degrees of freedom oftentimes leads to a strong local anisotropy for the preferred orientation of S [34]. For Cu^{2+} and Ni^{2+} this discussion is still relevant, as a lower than octahedral coordination symmetry around these ions in real materials may result in a partial quenching of the orbital momentum and, thus, residual spin-orbit coupling interactions. In this thesis, moments are considered as spin-only and orbital effects are incorporated into the spin Hamiltonian $\hat{\mathcal{H}}$ as anisotropic correction terms. Before spin-interactions are considered (see below), this has two effects on $\hat{\mathcal{H}}$ and these are described in the next two paragraphs.

Firstly, a spin $\mathbf{S} = (\hat{S}^x, \hat{S}^y, \hat{S}^z)^{\mathrm{T}}$, written here as a column vector of dimensionless spin operators, couples to an applied magnetic field $\mathbf{H}$ via a Zeeman term $\hat{\mathcal{H}}_{\mathrm{Z}}$ written as

$$\hat{\mathcal{H}}_{\mathrm{Z}} = \mu_{\mathrm{B}}\mu_0 \, \mathbf{H}^{\mathrm{T}} \boldsymbol{g} \, \mathbf{S}, \tag{1.2}$$

where $\boldsymbol{g} = \mathrm{diag}(g_x, g_y, g_z)$ is a tensor of g-factors and the diagonal components are not necessarily equal. For Cu^{2+} the component g-factors typically differ by $|g_z - g_{x,y}|/g_z \approx 0.1$ (see, for example, Ref. [23]). Moreover, in the cases of both Cu^{2+} and Ni^{2+} molecular compounds it is often the case that $g_{xy,z} > 2$, which further indicates the finite orbital contribution to the magnetic moment (e.g. Refs. [23, 35]).

Secondly, the preferred orientation of spins in zero-field is described by series of Steven's operators (e.g. Refs. [36, 37]), to which the largest contributors are

usually a uniaxial and rhombohedral anisotropy, D and E respectively. In this model, the zero-field single-ion Hamiltonian $\hat{\mathcal{H}}_{\rm SI}$ is[1]

$$\hat{\mathcal{H}}_{\rm SI} = D(\hat{S}^z)^2 + E[(\hat{S}^x)^2 - (\hat{S}^y)^2], \tag{1.3}$$

which only modulates the spin states for $S \geq 1$,[2] such that $S = 1/2$ Cu^{2+} moments approximate to isotropic (Heisenberg) spins. Meanwhile, an $S = 1$ Ni^{2+} ion with $E = 0$ may adopt a singlet ($m_s = 0$) or doublet ($m_s = \pm 1$) ground state, which correspond to easy-plane (XY) or easy-axis (Ising) anisotropy respectively. For $S = 3/2$ Co^{2+} ions, and in the case of axially compressed octahedral environments (which is relevant to the compound introduced later in this section), the moments evolve according Eq. 1.3 to produce a bistable Kramers doublet ground spin-state such that at low temperatures compared to $D/k_{\rm B}$ the Co^{2+} moments in these coordination environments approximate to two-level spin system [34]. More formally, a Schrieffer-Wolff transformation [38] of the spin Hamiltonian maps the two lowest lying spin energy levels onto an effective spin-1/2 ($\sigma = 1/2$) model, for which the size of the effective g-tensor absorbs the full paramagnetic length of the Co^{2+} moments and the spin-exchange interactions adopt an anisotropic (non-Heisenberg) nature [39, 40] (see Chapter 5).

1.3.3 Spin-exchange interactions via molecular linkages

(a) Section Overview: Spin-exchange interactions of the form of Eq. 1.1 result when an electronic exchange between two spin centres is mediated by an intermediary ion or molecule. In the development of magnetic coordination polymers, aromatic ligands containing carbon rings [Fig. 1.2(a)] and halogen-based inorganic ions with strong hydrogen bonds [Fig. 1.2(b)] are frequently used as effective mediators of spin-exchange interactions between metal ions (orange spheres). This necessarily requires a ligated ion to possess an unpaired electron in an orbital (pale blue lobes) that delocalizes spin-density towards the molecular linkage.

Pyrazine (pyz = $C_4H_4N_2$) molecules [Fig. 1.2(a)] are particularly versatile ligands that are often incorporated into polymeric magnets. A pyz molecule connects two metal ions via a donor pair of electrons on each N atom and while the ligand is known to mediate spin-exchange interactions (see below), the nature of the superexchange pathway across the molecule is a still an open point of discussion.

[1] Eq. 1.3 sometimes includes a constant term of the form $DS(S+1)/3$. However, this does not affect the separation of energy levels labelled by m_s and, consequently, this term is not included in the spin Hamiltonian for the calculations of the thermodynamic properties of spin systems in this thesis.

[2] Providing $L \neq 0$ as it is for ions with half-filled shells, e.g. Mn^{2+} ($3d^5$).

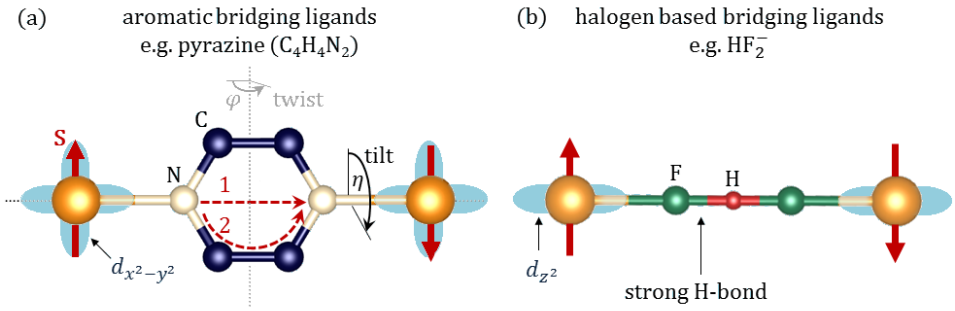

Figure 1.2: **(a)** Aromatic heterocyclic synthons (e.g. pyrazine = $C_4H_4N_2$, pictured here with H atoms removed) are molecular building blocks that are often used as mediators of magnetic exchange between two transition metal spins (red arrows), providing that the unpaired electrons in metal ion's d-orbitals (pale blue) have a spatial distribution that extends towards the ligand. For pyrazine, the delocalization of spin-density across the molecule (red dashed lines) could be: (1) a through-space delocalization across molecular π-orbitals; or (2) a through-bond pathway mediated by σ-orbitals. Two structural degrees of freedom for pyrazine linkages are a twist (φ) or tilt (η) of the molecule. **(b)** Halogen-based inorganic moieties with strong hydrogen bonds (e.g. HF_2^-, pictured) are also frequently used to construct rigid crystalline materials and to mediate spin-exchange interactions. This figure and all subsequent structural diagrams are plotted with VESTA [41].

Early investigations suggested that pyrazine's molecular π-orbitals mediated the spin-exchange [42], whereby spin-density is delocalized through space [Fig. 1.2(a), red dashed line 1], however more recent orbital overlap [43] and density-functional theory (DFT) [44] calculations imply that the molecular σ-orbitals provide the dominant spin-exchange pathway, such that there are a series of electronic exchange interactions across the bonds of the pyrazine ring (dashed line 2).

Experimentally, pyz is found to mediate antiferromagnetic spin-exchange interactions J_{pyz} between two d-block metal ions, where $J_{\mathrm{pyz}}/k_{\mathrm{B}}$ is typically ≈ 10 K for Cu^{2+} systems (e.g. Refs. [45,46]) and ≈ 1 K Ni^{2+} complexes (e.g. Refs. [47,48]). In the current understanding, the range of J_{pyz} values found in Nature is thought to be dictated, in part, by the precise length of the superexchange pathway, a twist (φ) or tilt (η) of the pyz molecule and, importantly, by changes in spin-density across the molecule that results from nearby ionic species in a crystalline lattice [45,46]. One advantage of pyz-based synthetic molecular magnets is that J_{pyz} is comparable to the accessible temperature and applied magnetic field ranges in a laboratory, which allows the magnetic properties of these systems to be investigated experimentally.

(b) Spatial-exchange anisotropy and non-Heisenberg interactions: This subsection describes two types of spin-exchange anisotropy that arises in crystalline materials. These are categorized as: (i) a spatial-exchange anisotropy; and (ii) a non-Heisenberg spin-exchange anisotropy. Spatial-exchange anisotropy occurs when metal ions are bridged via different molecules along separate crystallographic directions. For example, consider an array of Heisenberg coplanar spins ($\mathbf{S}$) positioned on the corners of a square-lattice spanning the xy-pane, with individual layers of this type stacked vertically on top of each other along z to form cubic structures. If the Heisenberg intralayer and interlayer spin-exchange constants are J and J' respectively, the zero-field spin Hamiltonian takes the form

$$\hat{\mathcal{H}} = J \sum_{\langle i,j \rangle} \mathbf{S}_i \cdot \mathbf{S}_j + J' \sum_{\langle i,j' \rangle} \mathbf{S}_i \cdot \mathbf{S}_{j'}, \tag{1.4}$$

where the first sum runs over unique pairs of nearest neighbour coplanar spins, while the second sum runs over unique pairs of spins in adjacent planes. In this context, the ratio J'/J dictates the spatial dimensionality of the spin-exchange network. Systems with $J'/J \gg 1$ produce quasi-one-dimensional (Q1D) chain-like spin networks that are strongly coupled along z, while $J'/J \ll 1$ yields quasi-two-dimensional (Q2D) planes of strongly coupled moments in the xy-plane. Multiple examples of real polymeric Q1D and Q2D AFMs are detailed in the section below.

Non-Heisenberg spin-exchange interactions occur in spin systems that exhibit a finite spin-orbit coupling. Anisotropic interactions of this type are most readily dealt with using exchange constants organized in a spin-exchange tensor $\mathbf{J}$ (see, for instance, Ref. [49]). In this notation, the spin-exchange terms are written as

$$\hat{\mathcal{H}} = \mathbf{S}_i^{\mathrm{T}} \, \mathbf{J} \, \mathbf{S}_j, \tag{1.5}$$

where $\mathbf{S}_{i,j} = (\hat{S}^x_{i,j}, \hat{S}^y_{i,j}, \hat{S}^z_{i,j})^{\mathrm{T}}$ are column vectors of spin-operators for two separate ions. For materials with axial symmetry $\mathbf{J}$ is diagonal and Eq. 1.5 simplifies to

$$\hat{\mathcal{H}} = J_{xy} \left(\hat{S}^x_i \hat{S}^x_j + \hat{S}^y_i \hat{S}^y_j \right) + J_z \hat{S}^z_i \hat{S}^z_j, \tag{1.6}$$

where, in general, $J_{xy} \neq J_z$. In a semi-classical interpretation of Eq. 1.6, $J_{xy} > J_z$ describes an XY-like interaction that encourages spins to have a larger portion of their moments constrained to the xy-plane; while $J_{xy} < J_z$ describes an Ising-like coupling, whereby the spins are largely projected onto the local z-axis. Spin-exchange interactions between moments in very low symmetry environments results in more complex spin-exchange tensors. For example, if there is no inversion centre between two spins Dzyaloshinskii-Moriya interactions develop (e.g. Ref. [50]) and these are incorporated into Eq. 1.5 with off-diagonal elements in the $\mathbf{J}$-tensor.

1.3.4 Coordination polymers applied to the study of magnetism

To summarize the last two sections, the principle of designing molecular magnets is to integrate transition metal ions into a crystalline lattice to act as spin centres that promote single-ion terms in the spin Hamiltonian (Eqs. 1.2 and 1.3), and to link them with molecular ligands to encourage spin-exchange interactions to develop (Eqs. 1.4 and 1.5). This section is intended to review the structures and bulk magnetic properties of just some of the low-dimensional coordination polymers that have been used to investigate quantum magnetism to date, focusing upon Q1D and Q2D $S = 1/2$ antiferromagnets (AFMs), a Haldane $S = 1$ chain and a family of magnets for which the spins are arranged on the corners of an approximately cubic lattice. It is important to stress from the outset that all of the real polymeric compounds referred to in this thesis form three-dimensional lattices and, here, low-dimensional refers to the nature of the dominant spin-exchange interactions in these complexes from the point of view of an ion within a chain or plane. Or, as E. A. Abbot puts it when writing from the perspective of an inhabitant of his two-dimensional fantasy world *Flatland*, "I call our world Flatland, not because we call it so, but to make its nature clearer to you, my happy readers, who are privileged to live in Space" [51].

A popular design motif for the study of condensed matter magnetism is to incorporate Heisenberg $S = 1/2$ Cu^{2+} ions ligated via pyz molecules [as in Fig. 1.2(a)] to form low-dimensional AFMs based on dimers, linear chains or square-lattice planes. These particular coordination geometries are favoured (in part) owing to the expectation for antiferromagnetic spin-dimers to adopt a nonmagnetic singlet ground-state at low temperatures (e.g. Ref [52]), and for ideal one-dimensional and two-dimensional Heisenberg $S = 1/2$ AFMs to exhibit strong quantum fluctuations (i.e. spin excitations that are predicted to persist down to zero temperature) [53], since these properties are anticipated to prevent the development of long-range magnetic order in these systems for $T > 0$.

Real examples of Q1D $S = 1/2$ AFMs include the polymeric systems of the form CuX_2(pyz) (where X is a monoanionic ligand), which contain octahedrally coordinated Cu^{2+} ions organized into linear Cu-pyz-Cu chains [Fig. 1.3(a)]. For $X = NO_3^-$ (a nitrate ion) [54] or HCO_2^- (a formate ion) [55], the Jahn-Teller axis of each Cu^{2+} spin-centre lies perpendicular to the pyz chain. The plane of the Cu^{2+} $d_{x^2-y^2}$ orbital contains the coordination bonds to the pyz ligands and a delocalization of spin density along this direction mediates an intrachain Cu-Cu Heisenberg spin-exchange interaction J_{pyz}. However the choice of X has a profound impact on the crystal structures and, hence, the magnetic properties of the two

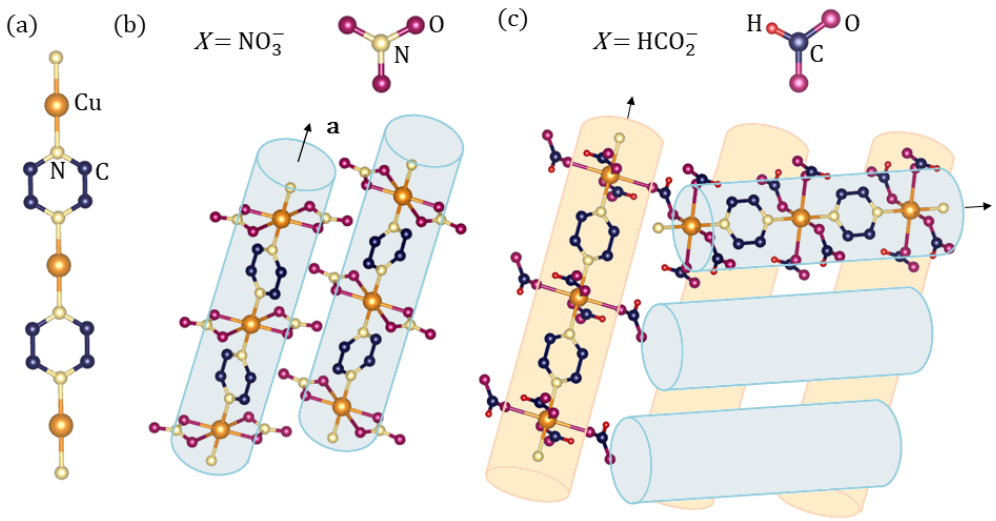

Figure 1.3: **(a)** Repeating Cu-pyz-Cu units form a chain of Heisenberg $S = 1/2$ moments. This design motif features in the 295 K published structures of $CuX_2(pyz)$, where **(b)** $X = NO_3^-$ [54] and **(c)** $X = HCO_2^-$ [55], as determined from single crystal x-ray diffraction. All pyrazine H atoms are omitted for clarity.

compounds. The nitrate ions act as non-bridging ligands and individual chains in this system are collinear as well as being isolated [Fig. 1.3(b)]. In the formate material parallel chains form layers, where alternate layers have chains running along differing crystallographic directions [Fig. 1.3(c)]. Moreover, each HCO_2^- anion ligates a Cu^{2+} ion from one chain to another Cu^{2+} spin from a chain in adjacent layer. While J_{pyz} is experimentally determined to be of the same order in each compound, $J_{pyz}/k_B = 10.4(1)$ K ($X = NO_3^-$) [56] and $J_{pyz}/k_B = 7.88(2)$ K ($X = HCO_2^-$) [55], the bulk magnetic properties are considerably different. The nitrate and formate compounds adopt ordered Néel phases below a temperature T_N of 0.107(1) K [57] and 1.97(8) K [58], respectively, which differ by an order of magnitude. Each finite T_N is driven by non-zero interchain spin-exchange interactions and it is the weak nature of these interactions between the isolated Cu-pyz chains of the NO_3^- system that supresses the onset of long-range magnetic order in this compound.

Heisenberg $S = 1/2$ square-lattice AFMs are investigated with polymeric systems based upon coordinately bonded $[Cu(pyz)_2]^{2+}$ sheets [Fig. 1.4(a)] and stable three-dimensional structures are formed by incorporating charge balancing anions into these systems. A prototypical $S = 1/2$ square-lattice AFM is $Cu(pyz)_2(ClO_4)_2$ [Fig. 1.4(b)] [60–63], wherein a Cu-O coordinate bond to two separate ClO_4^- (perchlorate) anions completes CuN_4O_2 octahedra. The plane of the Cu^{2+} $d_{x^2-y^2}$ orbital lies within the Cu-pyz layers, which promotes Q2D spatial-exchange interactions

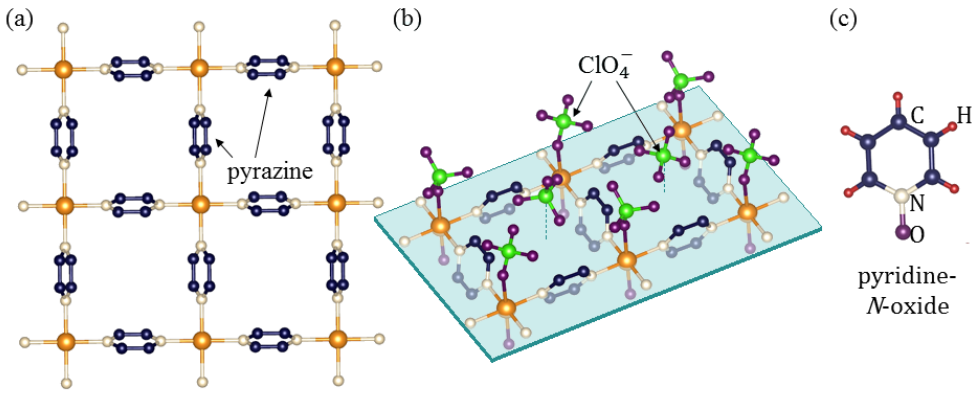

Figure 1.4: **(a)** Transition metal M ions (orange) (e.g. $M = Cu^{2+}$, Ni^{2+} or Co^{2+}), coordinate to four equatorial pyrazine ligands and form square-lattice $[M(pyz)_2]^{2+}$ plaquettes (motif displayed here is from published [59] 4 K powder neutron diffraction data). **(b)** Published [60, 61] single crystal x-ray diffraction measurements at 163 K indicate $Cu(pyz)_2(ClO_4)_2$ contains a weakly distorted $[Cu(pyz)_2]^{2+}$ square-lattice (blue) where two ClO_4^- ions above and below the sheets complete CuN_4Cl_2 octahedra. Separate non-coordinated ClO_4^- anions occupy the spaces above and below the approximate centres of the square plaquettes (along the dashed lines). **(c)** Pyridine-N-oxide ligands L (e.g. Ref. [65]), and its derivative 4-phenyl-pyridine-N-oxide, can replace the coordinated ClO_4^- ligands from panel (b) to push individual $[Cu(pyz)_2]^{2+}$ layers apart in a related series of magnets $[CuL_2(pyz)_2](ClO_4)_2$ [46].

mediated by the pyz ligands. Despite its characteristic low-dimensional spatial-exchange anisotropy, the system nevertheless adopts long-range antiferromagnetic order below a critical temperature $T_C \approx 4.2$ K, as observed in magnetometry [61] and muon spin-rotation (μ^+SR) [46] measurements. While finite interlayer interactions are predicted to be one driver of long-range order in Heisenberg $S = 1/2$ square-lattice AFMs [53] (see below), single crystal magnetometry measurements of $Cu(pyz)_2(ClO_4)_2$ [35] indicate the presence of weak XY-like non-Heisenberg intra-plane spin-exchange interactions, and this perturbation to the ideal Heisenberg $S = 1/2$ square-lattice model is primarily responsible for the finite T_C in this compound [35, 64]. X-ray diffraction measurements at 100 K [46] show that this material crystalizes in the monoclinic space group $C2/c$ and the weak spin-exchange anisotropy of this particular compound likely develops as a result of the low crystal symmetry at the Cu^{2+} sites.

Polymeric frameworks of the form $[CuL_2(pyz)_2](ClO_4)_2$ are a family of related XY-like Q2D AFMs that use a non-bridging aromatic ligand L, such as pyridine-N-oxide (C_5H_5NO) [Fig. 1.4(c)] or 4-phenylpyridine-N-oxide ($C_{11}H_9NO$),

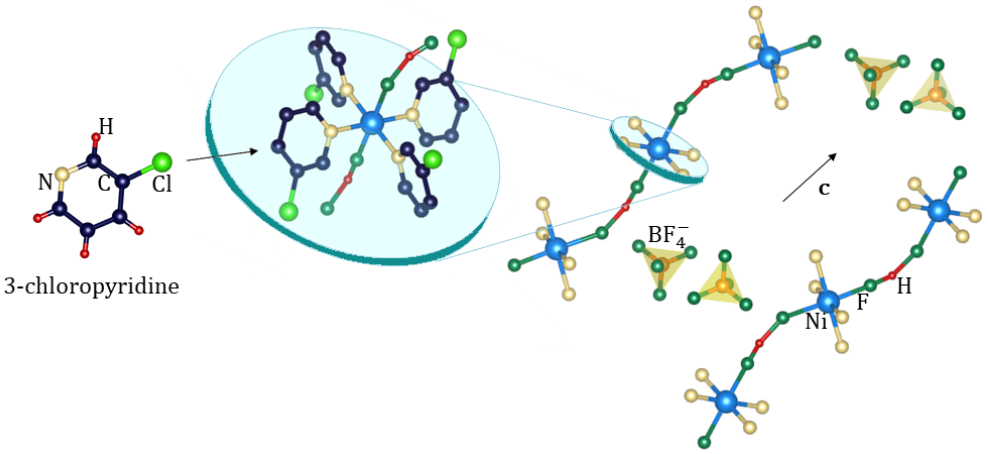

Figure 1.5: The 140 K published [66] structure of $[Ni(HF_2)(3\text{-Clpy})_4]BF_4$, deduced from single crystal x-ray diffraction, contains four 3-Clpy (C_5H_4NCl) molecules coordinated around the equator of a Ni^{2+} ion (blue spheres). 3-Clpy H atoms are removed for clarity. Distorted HF_2^- ions complete NiN_4F_2 octahedra and ligate individual $S = 1$ Ni^{2+} ions into a non-linear chain along the crystallographic **c**-axis (right hand image). Charge balancing tetrahedral BF_4^- counter ions (yellow shading) occupy sites between chains. 3-Clpy C and H atoms are removed for clarity.

to push individual $[Cu(pyz)_2]^{2+}$ layers apart. These materials provide another example of the flexibility of carbon chemistry being utilized to achieve control over the bulk magnetic properties of low-dimensional quantum spin systems. A magnetometry and x-ray diffraction study [46] of these compounds, along with $Cu(pyz)_2(ClO_4)_2$, demonstrated that the respective T_C values of these materials decreases as the ligand L increases the $[Cu(pyz)_2]^{2+}$ layer separation at a rate of ≈ 10 mKÅ^{-1}.

Incorporating metal ions with $S \geq 1$ into polymeric magnets produces a competition of single-ion and spin-exchange interactions in the spin Hamiltonian as, in the case of the Ni^{2+} coordination polymer $[Ni(HF_2)(3\text{-Clpy})_4]BF_4$, where 3-Clpy = 3-chloropyridine (C_5H_4NCl). At 140 K the system consists of four non-bridging 3-Clpy ligands around each Ni^{2+} centre (Fig. 1.5), while two separate HF_2^- ions complete NiN_4F_2 octahedra [66]. The HF_2^- anions form bridges between neighbouring Ni^{2+} ions along the **c**-axis to produce $S = 1$ chains and, despite a distortion of the Ni-FHF-Ni linkages, these moieties mediate an antiferromagnetic Heisenberg exchange interaction $J_{FHF}/k_B = 4.86$ K [66]. Each Ni^{2+} has an XY-like single-ion anisotropy, $D/k_B \approx 4.3$ K [66], and the small $D/J = 0.88$ ratio combined with the low-dimensional spatial-exchange anisotropy is sufficient promote a Haldane ground state with an energy gap to excitations of the system that is estimated from magnetometry measurements to be $< 0.05(1)$ K [67]. The suggested Haldane ground state

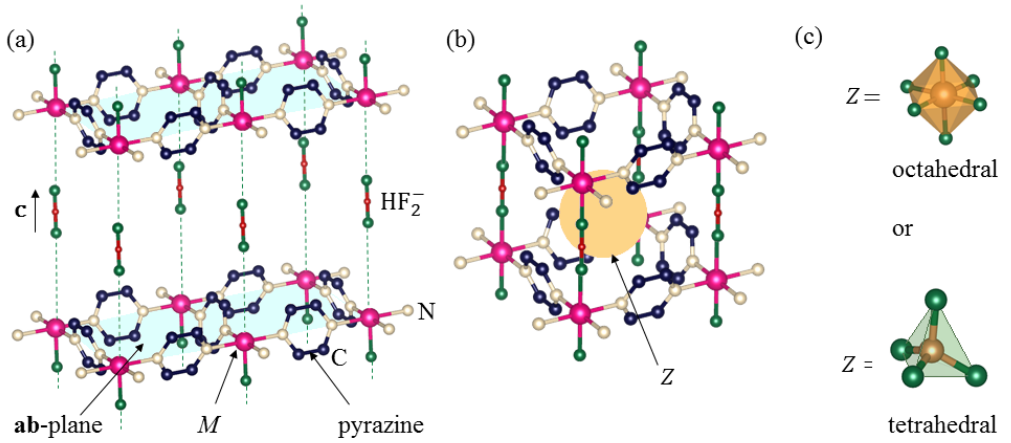

Figure 1.6: Polymeric magnets of the form $[M(\mathrm{HF_2})(\mathrm{pyz})_2]Z$, where $M = \mathrm{Cu}^{2+}$, Ni^{2+} or Co^{2+} (pink) and Z is monoanionic counterion, contain: **(a)** Square lattice $[M(\mathrm{pyz})_2]^{2+}$ layers, as in Fig. 1.4(a) (blue shading), linked via $\mathrm{HF_2^-}$ molecules along the **c**-axis (dashed lines). The layer separation here is exaggerated. **(b)** In the crystalline structure, M ions are arranged on the corners of an approximately cubic framework, while Z counter-ions occupy spaces enclosed by the cuboids (yellow shading). **(c)** Each Z species may be octahedral (upper panel) or tetrahedral (lower panel). Molecular components shown here are from published [59] powder neutron diffraction data at 4 K (and 163 K x-ray diffraction data for the tetrahedral counterion [60, 61]). All pyz H atoms are removed for clarity.

is in accord with the results of quantum Monte-Carlo (QMC) simulations of isolated $S = 1$ chains [68] that predict that a spin-gapped Haldane phase arises in the case of Heisenberg $S = 1$ chains, which gives way to a gapless state with increasing D once the single-ion anisotropy reaches a critical value of $D/J \approx 0.97$ (see Section 1.5).

Three dimensional frameworks of metal ions provide another class of material for the study of quantum magnetism. $[M(\mathrm{HF_2})(\mathrm{pyz})_2]Z$ is a family of polymeric compounds, wherein metal ions ($M = \mathrm{Cu}^{2+}$, Ni^{2+} or Co^{2+}) are organized into $[M(\mathrm{pyz})_2]^{2+}$ planes and linear $\mathrm{HF_2^-}$ pillars link adjacent layers [Fig. 1.6(a)] such that the M ions are positioned on the corners of approximate cuboids [Fig. 1.6(b)]. Non-coordinated counterions Z occupy the spaces within these cubes, where each Z species [Fig. 1.6(c)] may be tetrahedral (e.g. $\mathrm{ClO_4^-}$, $\mathrm{BF_4^-}$) or octahedral (e.g. $\mathrm{SbF_6^-}$, $\mathrm{PF_6^-}$). The structural and bulk magnetic properties of this family arise out of the complex electronic interactions between all of the constituent molecular building blocks. For instance, in the $M = \mathrm{Ni}^{2+}$ series the results of ambient pressure x-ray diffraction measurements at room temperature demonstrate that the crystal

structures vary from tetragonal (for $Z = SbF_6^-$) to monoclinic ($Z = PF_6^-$) [47]. In the $M = Cu^{2+}$ series, meanwhile, there are strong spin-exchange interactions between neighbouring Cu moments within $[Cu(pyz)_2]^{2+}$ layers for both octahedral and tetrahedral counterions, but octahedral Z ions tend to enhance the interplane spin-exchange interactions [45]. This variation of structural and magnetic properties across these families of polymeric magnetics likely derives from the size of the particular counterion Z, which in turn dictates the precise crystal structures and hence indirectly modifies the delocalization of spin-density between metal ions [45].

The popularity of exploiting molecular magnets in experimental investigations of magnetism has risen in recent decades in tandem with the advancement of the experimental techniques used to investigate them. Ever since the structures of Prussian Blue [69], the first synthetic molecular magnet, and $Cu(NO_3)_2(pyz)$ [54] were successfully solved with x-ray diffraction in the 1970s, this has paved the way for studies to be made into the relation between the crystallographic and magnetic properties of molecular systems. Additionally, it has become apparent that careful control of experimental parameters such as temperature, mechanical pressure or doping (see, for example, Refs. [70–72]), as well as applied magnetic fields may all modulate the magnet properties of molecular spin systems. Bulk magnetic property studies often rely upon the application of high magnetic fields, which has become possible in recent decades with the advent of pulsed field user facilities, while the local properties of spins are readily investigated with microscopic probes such as neutron diffraction and μ^+SR. Chapter 2 expands upon the modern crystallography and magnetometry techniques used and referenced in the experimental investigations of this project.

1.3.5 The coordination polymers studied in this thesis and the broad implications of these investigations

This section introduces the five coordination polymers that are the subjects of the experimental and theoretical investigations in this thesis. Firstly Chapter 3, which forms part of a recently published work (Ref. [73]), investigates $Cu(pyz)(gly)ClO_4$, where gly = glycinate ($NH_2CH_2CO_2^-$). At 298 K, this polymeric system consists of antiferromagnetic Cu-pyz-Cu dimers [Fig. 1.7(a)], which are ligated to four others by glycinate ions to form corrugated sheets [74]. Charge-balancing perchlorate (ClO_4^-) anions are positioned above and below each of the dimer layers [Fig. 1.7(b)]. These complete CuN_2O_4 octahedra and also connect two Cu^{2+} ions from separate dimers in adjacent sheets. However, there is a positional disorder of the perchlorate moieties such that each anion adopts one of three equally probable orientations

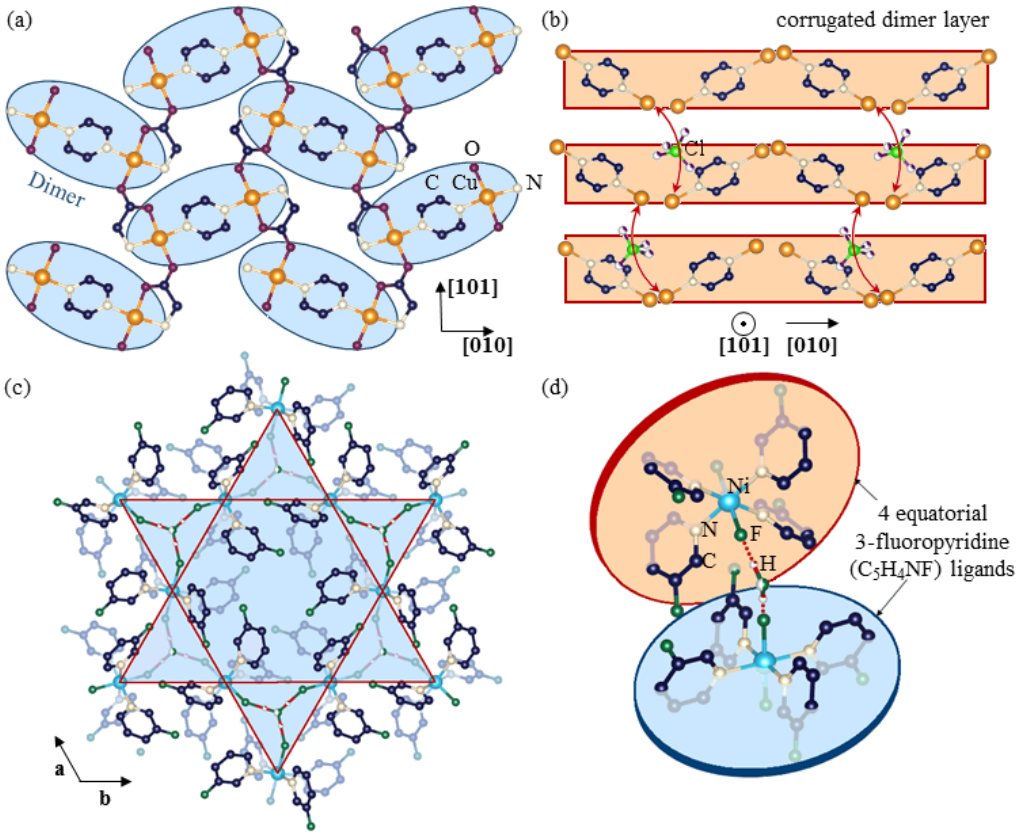

Figure 1.7: **(a)** At 298 K, $Cu(pyz)(gly)ClO_4$ contains Cu-pyz-Cu dimers (blue), each ligated to four others to form corrugated sheets via gly ions [74]. **(b)** ClO_4^- ions, above and below the sheets of dimers (orange shading), connect two Cu^{2+} ions from adjacent layers. **(c)** At 100 K, $[H_2F]_2[NiF_2(3\text{-}Fpy)_4]_3[SbF_6]_2$ crystalizes with coplanar Ni^{2+} ions arranged on the vertices of a kagome lattice (red lines) [75]. **(d)** Separate NiN_4F_2 octahdra are bridged by H_2F^+ linkages. All H atoms of organic molecules are removed in panels (a)-(d) for clarity.

[indicated by the fractionally filled spheres in panel (b)]. The system of antiferromagnetic spin-dimers exhibits a zero-field low-temperature quantum disordered phase, for which there is no long-range magnetic order as each pair of dimerized Cu^{2+} $S = 1/2$ moments forms a spin singlet at low temperatures compared to the intradimer spin-exchange interaction [74]. However, an applied magnetic field H couples to the Heisenberg moments to induce XY antiferromagnetic order for $2.5(1) \leq g\mu_B\mu_0 H/k_B \leq 9.0(2)$ K and temperatures below ≈ 1.4 K [74], and one of the aspects of the study of this material in Chapter 3 is to investigate the adiabatic physics of this compound that results from the strong coupling of the spin degrees of freedom to an applied magnetic field.

The main implications of study presented in Chapter 3 are: (i) the results of magnetometry measurements performed in quasistatic and pulsed magnetic fields are sensitive to the same phase of H induced magnetic order; (ii) $Cu(pyz)(gly)ClO_4$ undergoes a strong and continuous magnetocaloric effect (MCE) in pulsed magnetic field, i.e. the sample temperature evolves as a function of the applied magnetic field for all $H > 0$; (iii) the MCE in this material is accounted for with a general thermodynamic model, which suggests that the sample T is likely to be an important consideration for measurements performed on similar electrically-insulating samples in rapidly changing H; (iv) the planar arrangement of dimers in $Cu(pyz)(gly)ClO_4$ is likely to be related to the possible evidence for two-dimensional universal behaviour in the published [74] heat capacity measurements; and (v) the applied magnetic field dependence of the heat capacity suggests that the spin degrees of freedom of this $S = 1/2$ dimer complex are not only manipulated by H, but also by zero-point fluctuations (that is, spin fluctuations from the ground-state that are anticipated to persist at $T = 0$ K).

$[H_2F]_2[NiF_2(3\text{-Fpy})_4]_3[SbF_6]_2$ (3-Fpy = 3-fluoropyridine) is the second coordination complex studied in the work. The results of single-crystal x-ray diffraction experiments performed on this material (see below or Ref. [75]) demonstrate that the individual Ni^{2+} moments are arranged on the vertices of a two-dimensional kagome lattice [Fig. 1.7(c)]. The aromatic 3-Fpy ligands are non-bridging, forming a wheel of equatorially coordinated molecules around each metal ion [Fig. 1.7(d)], while F^- ions complete distorted NiN_4F_2 octahedra. Individual octahedra are bridged via H_2F^+ cations that provide charge-assisted Ni-F$\cdots$H-F-H$\cdots$F-Ni hydrogen bonded linkages. However, at 100 K there are two levels of positional disorder of the H_2F^+ moieties: (i) the central F atom of these ions occupies one of two equally probable sites; and (ii) for each of these cases the whole cation rotates about F to adopt one of three possible orientations. This generates a bond disorder between coplanar Ni^{2+} ions and the scope of the study of this system in Chapter 4, and the related publication [75], is to investigate the effects that the bond-disorder has on the bulk magnetic properties of this $S = 1$ kagome complex.

In broad terms, the results discussed in Chapter 4 imply: (i) one impact of the structural disorder of the H_2F^+ moieties in this material is weaken the strength of the nearest-neighbour Ni-Ni intraplane spin-exchange interactions to the extent that the system shows no evidence for long-range magnetic order at temperatures above 19 mK; and (ii) the thermodynamic properties at temperatures $T > 0.4$ K may be modelled by considering this polymeric complex as a system of independent spin $S = 1$ Ni^{2+} ions with an easy-plane uniaxial single-ion anisotropy. Further-

more, the models of the powder-average magnetization, heat capacity, and linear susceptibility that are developed in this chapter may be applicable to the analysis of future studies aimed at characterizing the energy scale of the single-ion anisotropy in similar powdered Ni^{2+} materials.

The final three compounds investigated in this work form a series of polymeric antiferromagnets of the form $[M(HF_2)(pyz)_2]SbF_6$ ($M = Cu^{2+}$, Ni^{2+} or Co^{2+}). In each isostructural compound the M ions reside on the corners of a square-lattice $[M(pyz)_2]^{2+}$ plaquettes spanning the **ab**-plane [Fig. 1.6(a)], linear HF_2^- bridges link individual sheets along the crystallographic **c**-axis, while octahedral SbF_6^- counterions occupy interstitial positions within the tetragonal frameworks [Fig. 1.6(b)]. The spin centres of the Cu^{2+} complex have an electronic configuration of $3d^9$ and, owing to a axial (Jahn-Teller) distortion of the CuN_4F_2 octahedra, the single unpaired electron resides within the $d_{x^2-y^2}$ suborbital. This leads to the efficient delocalization of spin density within individual $[Cu(pyz)_2]^{2+}$ sheets and this system approximates to a Q2D Heisenberg $S = 1/2$ square-lattice antiferromagnet (AFM) [45,76]. However, despite its low-dimensional magnetic character, the results of heat capacity and μ^+SR experiments determine that this material exhibits antiferromagnetic order below a finite critical temperature $T_C = 4.1$ K [76]. Contrasting, each octahedrally coordinated Ni^{2+} ($3d^8$) ion of $[Ni(HF_2)(pyz)_2]SbF_6$ has two unpaired electrons; that is, one in each of the $d_{x^2-y^2}$ and d_{z^2} suborbitals [47], and adopts antiferromagnetic long-range order below a critical temperature $T_C = 12.2$ K [47]. The results of published [47] ligand field theory calculations imply that the individual $S = 1$ Ni^{2+} ions have an intrinsic easy-plane character, while a density-function theory investigation suggests that there is a significant delocalization of spin-density along both of the pyz and HF_2^- ligands that is expected to result in a Q1D spin-exchange network. The magnetic properties of $[Co(HF_2(pyz)_2]SbF_6$ were unpublished prior to this project and this system is shown in Chapter 5 to adopt an antiferromagnetically ordered state for temperatures below $T_C = 7.1$ K wherein the individual Co^{2+} ($3d^7$) $S = 3/2$ moments have a strong Ising-like single-ion anisotropy. In summary, the main aspect of the study of these isostructural compounds in Chapter 5, and the related publications Refs. [59,77], is to examine how the magnetic ground state and some of the bulk thermodynamic properties and quantum phenomena exhibited by these systems evolve according to the choice of the transition metal spin-centre.

The main implications of the studies in Chapter 5 are: (i) the individual spin $S = 1/2$ quanta of $[Cu(HF_2)(pyz)_2]SbF_6$ have a Heisenberg character for temperatures $T > 1.5$ K, and this Q2D AFM exhibits a low-temperature ordered Cu^{2+} moment that is reduced from its paramagnetic value by quantum fluctuations; (ii) the

results of neutron diffraction, pulsed-field magnetometry, and inelastic neutron scattering investigations of a powdered sample of $[Ni(HF_2)(pyz)_2]SbF_6$ are used to classify this system as a Q1D XY-like $S = 1$ AFM in which the relative strengths of the uniaxial single-ion anisotropy and the nearest-neighbour Ni-Ni spin-exchange interactions along the pyz and HF_2^- ligands are responsible for stabilising a state of long-range antiferromagnetic order in zero-field for temperatures $T < 12.2$ K; and (iii) the Ising-like single-ion anisotropy of the individual Co^{2+} ions in $[Co(HF_2)(pyz)_2]SbF_6$ maps this system onto an effective spin $\sigma = 1/2$ model for temperatures $T < 50$ K. Finally, the semi-classical models of the magnetization of the Ni^{2+} and Co^{2+} spin systems outlined in Chapter 5 may also aid in the characterization of related materials when limited to powdered samples.

1.4 Thermodynamic properties of magnetic materials

1.4.1 Magnetization

The magnetization $\mathbf{M} = (M_x, M_y, M_z)^{\mathrm{T}}$ of an ensemble of spins $\mathbf{S}_i$ is a vector quantity defined as the total magnetic moment per unit volume V [29], such that

$$\mathbf{M} = -\frac{1}{V}\sum_i \mu_{\mathrm{B}} \boldsymbol{g}\, \mathbf{S}_i, \tag{1.7}$$

where $\mu_{\mathrm{B}} = 9.27{\times}10^{-24}$ Am^2 is the Bohr magneton and $\boldsymbol{g}$ is the g-tensor. The leading minus sign results from the fact individual moments in the ensemble are derived from the angular momentum of negatively charged atomic electrons. In this notation the orientation of magnetic moments, as distinct from spins, align to the direction of an applied magnetic field $\mathbf{H}$. In general, $\mathbf{M}$ is an anisotropic quantity and the powder average quantity M is derived directly from magnetometry measurements performed on polycrystalline samples.

1.4.2 Susceptibility

The susceptibility is a quantity that measures how strongly, and the manner in which, the magnetic moment of a material responds to an applied magnetic field [29]. All atoms and molecular bonds provide a small diamagnetic contribution to a sample's total susceptibility, owing to the magnetic response of electrons in filled atomic and molecular orbitals [78]. A quantity of interest in magnetometry experiments of coordination polymers is a component of the total susceptibility that derives from the degrees of freedom of spin quanta in a sample, which is generally investigated as a function of temperature T or an applied magnetic field H. For T-dependent

studies in static H, each component of the direct current (dc) linear susceptibility χ_i $(i = x, y, z)$ is defined as $\chi_i = M_i/H_i$. By analogy with the magnetization, χ_i components are generally anisotropic and the powder average quantity is χ. In H-dependent studies the related quantity of interest is the powder average differential susceptibility $\chi = \mathrm{d}M/\mathrm{d}H$.

Weiss' mean-field approximation (e.g. Ref. [29]) is often used to model the T dependence of the powder-average molar linear susceptibility (χ_{mol}) of a paramagnetic an ensemble of spins (S). In this model

$$\chi_{\mathrm{mol}} = \frac{\mu_0 N_{\mathrm{A}} \mu_{\mathrm{eff}}^2}{k_{\mathrm{B}}(T + \theta_{\mathrm{CW}})} + \chi_0, \tag{1.8}$$

where N_{A} is the Avogadro constant, $\mu_{\mathrm{eff}} = g\mu_{\mathrm{B}}\sqrt{S(S+1)}$ is the effective paramagnetic moment, g is the powder average g-factor, θ_{CW} is the Curie-Weiss temperature that reflects the approximate strength and nature of spin-exchange interactions, and χ_0 absorbs diamagnetic and temperature independent paramagnetic contributions to the measurement. At thermal energies $k_{\mathrm{B}}T$ comparable to the exchange interactions and zero-field splitting terms the spin Hamiltonian, however, Weiss' mean-field approach is insufficient to model χ_{mol}. Appropriate models for the linear susceptibility of independent $S = 1$ ions with single-ion anisotropy and Q2D Heisenberg $S = 1/2$ square-lattice AFMs are discussed in Chapters 4 and 5 respectively.

1.4.3 Heat capacity and magnetic entropy

The constant pressure heat capacity C_p measures a change in a system's internal energy U that results from a small variation in the material's temperature T (e.g. Ref. [79]) and is formally defined by

$$C_p = \left(\frac{\partial U}{\partial T}\right)_p. \tag{1.9}$$

When a system absorbs a small amount of thermal energy, this generates both lattice vibrations (phonons) and spin-excitations (such as single-ion excitations or spin-waves). The total sample heat capacity, $C_p = C_{\mathrm{latt}} + C_{\mathrm{mag}}$, is therefore a sum of lattice (C_{latt}) and magnetic (C_{mag}) terms.

For polymeric magnets, C_{latt} dominates C_p when $k_{\mathrm{B}}T$ exceeds the energy scale of magnetic terms in the Hamiltonian. Lattice vibrations are modelled with one Debye mode and a sum over Einstein modes with the expression [59, 73, 76]

$$C_{\mathrm{latt}} = \frac{3A_{\mathrm{D}}}{x_{\mathrm{D}}^3}\int_0^{x_{\mathrm{D}}} \frac{x^4 e^x}{(e^x - 1)^2}\mathrm{d}x + \sum_i A_{\mathrm{E}_i}\frac{e^{\theta_{\mathrm{E}_i}/T}}{(e^{\theta_{\mathrm{E}_i}/T} - 1)^2}, \tag{1.10}$$

where A_n, θ_n ($n = \mathrm{D}, \mathrm{E}_i$) are the amplitude ($A$) and temperature ($\theta$) of Debye (D)

and Einstein (E_i) modes respectively; and $x_D = \theta_D/T$.

A magnetic contribution to C_p arises when a small amount of heat δQ is introduced to a spin ensemble and individual moments re-orientate so as to absorb this energy. This alters the spin entropy S_{mag} by an amount $\delta S_{mag} = T^{-1}\delta Q$ and C_{mag} is given by

$$C_{mag} = T\left(\frac{\partial S_{mag}}{\partial T}\right)_p. \tag{1.11}$$

In a measurement of C_p, C_{latt} is modelled with Eq. 1.10 and subtracted from the total heat capacity to yield C_{mag}. This provides an indirect way to infer changes in spin entropy ΔS_{mag} via integration of Eq. 1.11, giving

$$\Delta S_{mag} = \int_{T_1}^{T_2} \frac{C_{mag}(T')}{T'} dT'. \tag{1.12}$$

For an ensemble of quantum spins (S), each moment has $(2S+1)$ degrees of freedom. For one mole of spins, the change in ΔS_{mag} as the system is cooled from a paramagnetic phase to a magnetically ordered state is $\Delta S_{mag} = R\ln(2S+1)$, where $R = 8.31$ JK^{-1}mol^{-1}. One source of error in calculations of ΔS_{mag} derives from the inherent uncertainty in the amplitude of C_{latt} that results from the fitted errors in the A terms of Eq. 1.10. When the phonon model is subtracted from the total heat capacity this therefore leads to a possible over or underestimation of the magnetic heat capacity. In this thesis, an error in ΔS_{mag} is calculated by subtracting upper and lower bounds of C_{latt} from measurements of C_p and then integrating these independent estimates of C_{mag} with Eq. 1.12 to yield a range of ΔS_{mag} values for a particular temperature window $[T_1, T_2]$.

1.4.4 Sample temperature and the magnetocaloric effect

In isothermal measurements the sample temperature T is a constant and controlled parameter, whereas in adiabatic experiments the entropy of a sample is constant and T becomes a quantity to be determined. The magnetocaloric effect (MCE) is a change in T induced by an adiabatic change of an applied magnetic field H [80,81].[3] In general, the spin entropy is a function of both T and H, such that the heat flow δQ between a spin system and its environment generalizes to [82]

$$\delta Q = T\left(\frac{\partial S_{mag}}{\partial T}\right)_H \delta T + T\left(\frac{\partial S_{mag}}{\partial H}\right)_T \delta H. \tag{1.13}$$

[3] H is reserved for the applied magnetic field, rather than the enthalpy, in the thermodynamic expressions in this thesis.

Dividing Eq. 1.13 by small time interval δt yields an equation for the power P of this flow of heat [82],

$$P = C_{\mathrm{mag}} \frac{\mathrm{d}T}{\mathrm{d}t} + T \left(\frac{\partial S_{\mathrm{mag}}}{\partial H} \right)_T \frac{\mathrm{d}H}{\mathrm{d}t}, \tag{1.14}$$

where $C_{\mathrm{mag}} = T \left(\partial S_{\mathrm{mag}} / \partial T \right)_H$ is the magnetic contribution to the heat capacity at constant H. The second term in Eq. 1.14 is the power generated as H is swept. It results from a coupling of the applied field to the spin-entropy of the system and it is responsible for the MCE [82]. A useful quantity to consider in a MCE experiment is $\Gamma = T^{-1} \left(\partial T / \partial H \right)$, which parameterizes the sign and strength of changes in a sample's temperature as an applied magnetic field is swept. For experiments performed in precisely adiabatic conditions then Γ is the magnetic Grüneisen parameter.

As an example of the MCE consider a collection of paramagnetic Heisenberg $S = 1/2$ ions, each with an isotropic g-factor, in an applied magnetic field H. The Zeeman energy levels of individual spins are $\pm(1/2) g \mu_{\mathrm{B}} \mu_0 H$ and the partition function $\mathcal{Z}$ (e.g. Ref. [79]) of the ensemble is

$$\mathcal{Z} = 2 \cosh \left(\frac{g \mu_{\mathrm{B}} \mu_0 H}{2 k_{\mathrm{B}} T} \right), \tag{1.15}$$

which is a function of the ratio H/T. The spin-entropy is related to Eq. 1.15 via

$$\frac{S_{\mathrm{mag}}}{k_{\mathrm{B}}} = -T \frac{\partial \ln \mathcal{Z}}{\partial T} + \ln \mathcal{Z}, \tag{1.16}$$

and this yields an analytical expression for S_{mag} for each ion

$$\frac{S_{\mathrm{mag}}}{k_{\mathrm{B}}} = -\frac{g \mu_{\mathrm{B}} \mu_0 H}{2 k_{\mathrm{B}} T} \tanh \left(\frac{g \mu_{\mathrm{B}} \mu_0 H}{2 k_{\mathrm{B}} T} \right) + \ln \left[2 \cosh \left(\frac{g \mu_{\mathrm{B}} \mu_0 H}{2 k_{\mathrm{B}} T} \right) \right], \tag{1.17}$$

that is also a function of the ratio H/T [79, 83]. In an adiabatic experiment, S_{mag} is constrained to be constant and so T evolves linearly with H. Therefore paramagnets undergo a cooling upon adiabatic demagnetization, a property which is exploited in the application of paramagnetic materials in solid state refrigeration devices [84–86].

1.5 Scope of this thesis: the investigation of quantum phenomena in low-dimensional AFMs

1.5.1 What are quantum phenomena?

Quantum phenomena are the emergent properties of spin systems that cannot be explained semi-classically. Ideal systems to explore quantum phenomena include: (i) materials with a quantum critical point (QCP), i.e. a zero temperature phase transition [15, 16]; or (ii) Heisenberg spin networks with spin-exchange interactions

in a low number of spatial dimensions. The tunability of magnetic interactions in coordination polymers offers a degree of control that can be exploited (through careful chemical synthesis or via mechanical/chemical pressure) to generate materials of types (i) and (ii) in the search for emergent properties. In this section, the quantum phenomena that arise in exchange-coupled spin-dimers; low-dimensional Heisenberg, XY and Ising $S = 1/2$ AFMs; and quasi-one-dimensional $S = 1$ chains with uniaxial single-ion anisotropy are discussed, with particular reference made to the five materials studied in this thesis.

1.5.2 Exchange-coupled spin-dimers

Pairs of spin-1/2 ions coupled via an antiferromagnetic Heisenberg spin-exchange constant J form a dimerized unit with a total spin S (e.g. Refs. [87, 88]) for which there is a singlet ground state ($S = 0$) that lies an energy J below triplet of $S = 1$ excited states [Fig. 1.8(a)]. In the Bleaney-Bowers model [23, 89], an ensemble of independent dimers is anticipated to exhibit paramagnetic properties for $T \gg J/k_{\mathrm{B}}$ while the the Boltzmann population of dimers in $S = 0$ state grows once $T < J/k_{\mathrm{B}}$. Even if there is a finite interdimer exchange interaction $J' < J$, there is no long-range magnetic order for $T < J'/k_{\mathrm{B}}$ since each dimer adopts a nonmagnetic singlet state. At these low temperatures, the spin system is described as a quantum paramagnet (QP), where the magnetic disorder on large length scales comes about as a result of the local antiparallel alignment of spins within each dimer.

An applied magnetic field H closes a dimer's spin-gap [Fig. 1.8(a)] and the system crosses over to a magnetic ground state. For dimers with a spin Hamiltonian possessing uniaxial symmetry, a Matsubara-Matsuda transformation maps the lowest lying energy levels onto a boson picture whereby each dimer is represented with an $S = 0$ or $|S^z| = 1$ (triplon) state [52, 90, 91]. A finite J' permits the hopping of triplons between dimers, giving these excitations a dispersion relation and a finite energy bandwidth Δ [90], hence each dimer's spin-gap is closed for a range of H bounded by two critical points, $H_{\mathrm{c1,2}}$ [Fig. 1.8(a)]. This model is akin to the field induced condensation of $S = 1$ bosons from a nonmagnetic vacuum, where a Bose-Einstein condensate (BEC) begins to form for $H > H_{\mathrm{c1}}$ and the number of triplons saturates at H_{c2} (e.g. Ref [52]). A comparable spin configuration is obtained for weakly coupled $S = 1$ chains with a strong XY-like uniaxial single-ion anisotropy D when a magnetic field is applied along z [Fig. 1.8(b)]. Here, it is the intrachain spin-exchange that gives rise to a band of single-ion bosonic excitations that are separated from the ground-state in zero-field by D.

In real organic and inorganic spin-gapped materials [Fig. 1.8(c)], the BEC

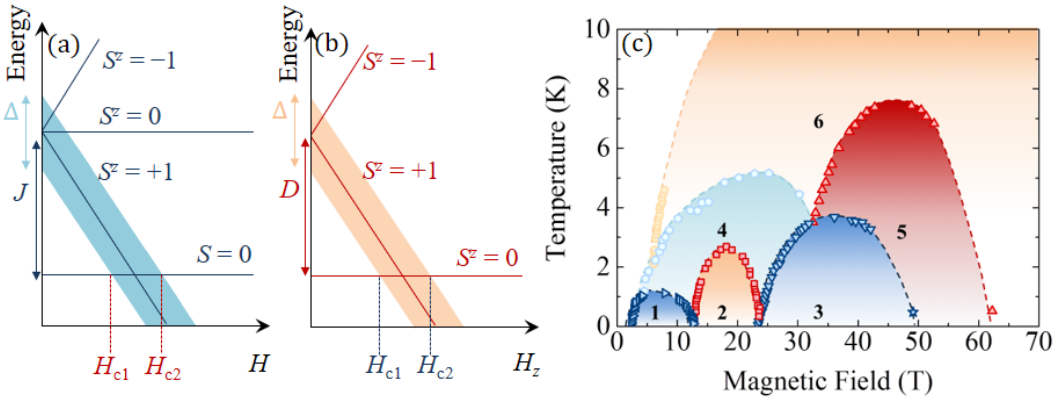

Figure 1.8: **(a)** Dimer spin energy levels vs. applied magnetic field (H) for an exchange-coupled dimer. Here, J is the Heisenberg antiferromagnetic intradimer spin-exchange constant and Δ is the bandwidth of excited states. **(b)** Field evolution of spin energy levels for individual ions of an XY-like $S = 1$ chain AFM for H parallel to z, where D is the uniaxial single-ion anisotropy and Δ is the bandwidth of excited states. **(c)** The $\mu_0 H - T$ phase diagram for molecular and inorganic materials that map onto the BEC of bosons from an nonmagnetic vacuum: (1) $NiCl_2$-4CS$(NH_2)_2$, (2) $Ba_3Cr_2O_8$, (3) $BaCuSi_2O_6$, (4) $Pb_2V_3O_9$, (5) $Sr_3Cr_2O_8$, and (6) $TlCuCl_3$. Figure adapted from Ref. [52].

phase forms within a dome in the $H - T$ plane that is bounded by the two QCPs ($H_{c1,2}$) and extends up to a finite T, which is often a small fraction of Δ/k_B. The coordination polymer $NiCl_2$-4SC$(NH_2)_2$ [92], No. 1 in Fig. 1.8(c), highlights one advantage of studying molecular magnets over inorganic materials to explore BEC systems. Molecular systems often exhibit weaker spin-exchange interactions than their inorganic counterparts, which consequently restricts the height and breadth of the BEC phase diagram to an accessible H and T range. Meanwhile, H_{c2} of some inorganic materials (notably $TlCuCl_3$, No. 6) is inaccessible with conventional (non-destructive) techniques to generate an applied H.

The experimental interests in BEC systems includes: (i) a strong MCE that is often studied in the vicinity of the QCPs [52,83,88]; (ii) a power law dependence of $C_p(T)$ for $H = H_{c1,2}$ with an exponent that depends on the spatial-dimensionality of the spin-exchange interactions [52,95]; and (iii) an asymmetry that is predicted, and observed, in the height of $C_p(H)$ anomalies at $H = H_{c1,2}$ [94]. Chapter 3 (and the related publication, Ref. [73]) utilizes the results of quasistatic and pulsed field magnetometry measurements along with MCE experiments to investigate the molecular spin-gapped exchange-coupled spin-dimer complex Cu(pyz)(gly)ClO_4 across its full $H-T$ phase diagram. The published [74] heat capacity is used to formulate a general

thermodynamic argument to show that a strong MCE in fact occurs for all $H > 0$ in this material, and therefore related systems, and that a failure to account for this phenomenon in pulsed field experiments can lead to an erroneous interpretation of the sample temperature. Furthermore, the structure of $Cu(pyz)(gly)ClO_4$ and the critical exponents of the heat capacity at H_{c2} are consistent with two-dimensional universal behaviour. Lastly, a small peak in $C_p(H)$ at H_{c1} relative to that at observed at H_{c2} is indicative of a role for zero-point fluctuations in manipulating the spin entropy of this material for $H \approx H_{c1}$ (i.e. there are excitations of the system that are attributed to the quantum nature of the spins).

1.5.3 Low-dimensional Heisenberg, XY and Ising $S = 1/2$ quantum magnets

(a) The interest in $S = 1/2$ AFMs: Heisenberg $S = 1/2$ materials are attractive for the investigation of magnetic quantum phenomena as they posses the lowest $S > 0$ quantum number and hence the ratio $\frac{\langle S^2 \rangle}{S^2} = \frac{S+1}{S}$ is furthest from the high-spin (semi-classical) limit of 1. One property of interest is that ideal Heisenberg $S = 1/2$ chains and square-lattice planes are not expected to order for $T > 0$. In 1931, Bethe deduced that an antiferromagnetic alignment of Heisenberg $S = 1/2$ moments was not an eigenstate of the spin Hamiltonian for one-dimensional chains [96] and, similarly, a comprehensive review of Heisenberg $S = 1/2$ square-lattice AFMs in 1991 [13] indicates that there is no proven theorem for these systems to adopt a Néel state at finite T either. The latter work does, however, anticipate that magnetic order still occurs in isolated square-lattice planes as $T \to 0$, albeit with a reduced ordered moment [see part (c)]. While ideal Heisenberg $S = 1/2$ chains (planes) do not order at finite T, it is nevertheless energetically favourable for the orientations of a small cluster of neighbouring moments to antiferromagnetically align once $k_B T < J$, where J is the intrachain (intraplane) Heisenberg spin-exchange interaction [22]. If each moment has z neighbouring ions the average number of spins that are instantaneously antiferromagnetically coupled at finite T is $\xi \approx zJS(S+1)(k_B T)^{-1}$ [22]. This estimates the spin correlation length and only diverges as $T \to 0$.

(b) Drivers of long range order in Q1D and Q2D systems: The finite extent of Heisenberg interchain (or interplane) exchange interactions J' in real polymeric materials is an important perturbation to the case of ideal one (or two) dimensional systems and, significantly, this is one mechanism to drive these systems to an ordered Néel phase a finite temperature T_N. The results of quantum Monte-Carlo (QMC) simulations for Heisenberg $S = 1/2$ moments on a cubic lattice [53] predict

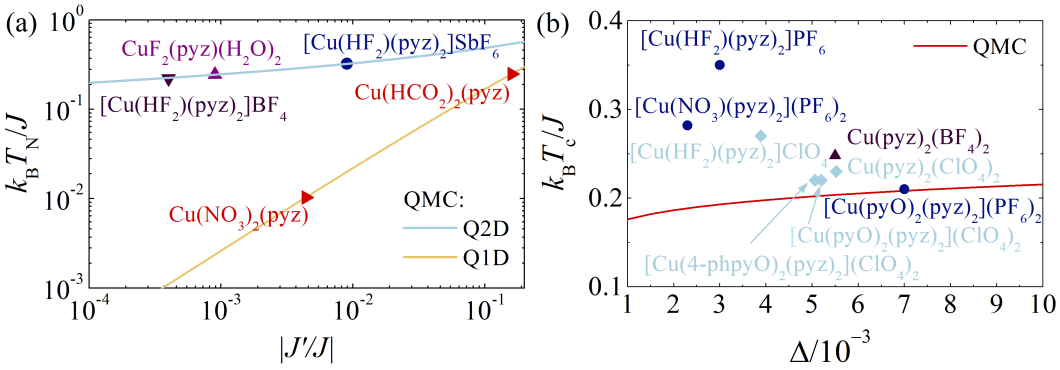

Figure 1.9: **(a)** The interchain/interplane interactions of real Heisenberg $S = 1/2$ Q1D/Q2D polymeric magnets (points) are estimated from a measurement of the finite ordering temperature, T_N, and the intrachain/intraplane Heisenberg spin-exchange constant, J, using Eq. 1.18/Eq. 1.19 (solid lines) [45, 57, 58]. **(b)** Experimentally determined [35, 46] values of k_BT_C/J vs. Δ for several Q2D $S = 1/2$ square-lattice AFMs (points), compared to a QMC simulation (Eq. 1.20) for ideal $S = 1/2$ square-lattice AFMs (solid line).

that in the case of quasi-one-dimensional systems, T_N measures the relative strength of the interchain Heisenberg exchange $|J'|$ via the expression

$$\frac{|J'|}{J} = \frac{1}{4}\left(0.233x\sqrt{\ln 2.6x + \frac{1}{2}\ln\ln 2.6x}\right)^{-1}, \tag{1.18}$$

where $x = J(k_BT_N)^{-1}$ and J is the intrachain Heisenberg exchange constant. In the case of quasi-two-dimensional Heisenberg $S = 1/2$ systems, the QMC simulations [53] relate T_N to a finite interplane interaction J' with

$$\frac{|J'|}{J} = \exp\left[2.43 - 4\pi\left(0.183x\right)\right], \tag{1.19}$$

where $x = J(k_BT_N)^{-1}$ and J is the intraplane Heisenberg exchange constant.

For polymeric magnets, if T_N is estimated from heat capacity or μ^+SR experiments and the dominant exchange interaction J is derived from bulk magnetometry measurements [see part (d)], then Eqs. 1.18 and 1.19 may be used to estimate $|J'|$ for both Q1D and Q2D systems [e.g. Fig. 1.9(a)]. Materials closer to the left hand side of the figure are better approximated to ideal systems and it is the ability to incorporate different molecular ligands into polymeric quantum spin-networks that has been utilized to develop this array of low-dimensional systems in which to study quantum magnetism.

Non-Heisenberg spin interactions are another perturbation that takes real materials away from the ideal Heisenberg $S = 1/2$ approximation and, for Cu^{2+}

systems in particular, the spin-orbit coupling interaction is one mechanism to give rise to this effect. For square-lattice $S = 1/2$ materials, the spin-exchange anisotropy is parameterized with Eq. 1.5 where $J_z/J_{xy} = (1-\Delta)$ and Δ is a small positive constant that yields an XY-like character for the spin-exchange interaction. The results of QMC simulations [64] predict that a finite Δ induces an XY-antiferromagnetic state for $T \leq T_{\rm C}$, where

$$\frac{k_{\rm B}T_{\rm C}}{J} = \frac{2.22}{\ln(360/\Delta)}. \tag{1.20}$$

In an experiment, Δ is measured by a change in slope of the magnetization that occurs for fields applied with the XY-plane once the Zeeman energy is sufficient to allow moments to rotate out of the easy-plane and cant towards the direction of H [35, 46]. The measured values of Δ and $T_{\rm C}$ for several Q2D Cu^{2+} polymeric magnets are compared to Eq. 1.20 in Fig. 1.9(b). The bulk magnetic properties of materials further from the theoretical line are influenced by other perturbations in the spin Hamiltonian besides Δ, such as finite interplane spin-exchange interactions [35]. In Chapter 5, the results of neutron powder diffraction (NPD) and single-crystal magnetometry measurements of the tetragonal system $[Cu(HF_2)(pyz)_2]SbF_6$ are discussed in terms of the extent to which this high symmetry compound's finite magnetic ordering temperature can be explained within a Heisenberg $S = 1/2$ model.

(c) Reduced ordered moment in Heisenberg square-lattice AFMs: Below the ordering temperature $T_{\rm N}$ of a spin system, the ordered moment size μ is an order parameter that follows a general T dependence of the form

$$\mu(T) = \mu(0)\left[1 - \left(\frac{T}{T_{\rm N}}\right)^{\alpha}\right]^{\beta}, \tag{1.21}$$

where α and β are constants. A prediction for Q2D Heisenberg $S = 1/2$ AFMs from renormalization group analysis in the nonlinear sigma model [97] is that each plane of spins adopts a Néel phase, but the low temperature moment per ion $\mu(0)$ is reduced from its classical value $\mu_{\rm C} = g\mu_{\rm B}S$ by quantum fluctuations at $T = 0$. The ordered phase occurs at thermal energies below

$$k_{\rm B}T_{\rm N} \approx J'\left[\frac{\mu(0)}{\mu_{\rm C}}\right]^2 \xi^2, \tag{1.22}$$

where ξ is the correlation length within the planes at $T = T_{\rm N}$ in units of the lattice constant.

Linear spin-wave calculations for ideal square-lattice Heisenberg AFMs suggest that $\mu(0) = 0.6\mu_{\rm C}$ for $S = 1/2$ and $0.87\mu_{\rm C}$ for $S = 3/2$ [13, 98], but in order to test the predictions of Eq. 1.22 and linear spin-wave theory it is important for

the sample T to be sufficiently low so that ordered moment is suppressed by quantum rather than thermal fluctuations (as in Eq. 1.21). To ensure $\mu \approx \mu(0)$, an independent estimate of the order parameter is provided by μ^+SR as these experiments are sensitive to the internal magnetic flux B of an AFM at interstitial lattice sites, which is generated by individual magnetic moments in the crystal (e.g. Refs. [99,100]). For a magnetically ordered system, B saturates towards a low temperature limit and neutron diffraction experiments to estimate $\mu(0)$ may be therefore be performed at a temperature for which B is measured to be close to its $T = 0$ limiting value. As an illustrative example, single crystal neutron diffraction measurements of $Cu(pyz)_2(ClO_4)_2$ at 2.3 K reveal the ordered Cu^{2+} moment is $0.47(5)\mu_B$ per ion [101], which approximately 50% of its classical value ($\approx 1\mu_B$ per ion), even though μ^+SR indicates the internal B has approached 95% of its low-T limit [46]. Quantum fluctuations are also modulated by an applied magnetic field, such that in square-lattice $S = 1/2$ AFMs they are initially enhanced but ultimately supressed by the field [101]. This renders zero-field probes of $\mu(0)$, such as NPD or μ^+SR, as the suitable techniques to investigate ordered moments of low-dimensional AFMs that have no bulk magnetization.

The results of NPD measurements of $[Cu(HF_2)(pyz)_2]SbF_6$ are discussed in Chapter 5, where it is the Q2D spatial-exchange anisotropy and low S quantum number of this compound that make this material an interesting candidate to search for a reduced ordered moment. These results are compared against those obtained from NPD of $[Co(HF_2)(pyz)_2]SbF_6$, which approximates to an Ising-like effective spin-1/2 system for temperatures comparable to its magnetic ordering temperature. The size of the ordered moment in this Co^{2+}, material, compared to its classical (paramagnetic) value, is considered in terms of how a strong easy-axis single-ion anisotropy influences the size of the ordered moment in quantum magnets.

(d) Thermodynamic properties of low-dimensional Heisenberg and Ising $S = 1/2$ materials: Other observable characteristics of low-dimensional $S = 1/2$ systems occur in bulk magnetization and heat capacity measurements. The results of QMC simulations for exchange-coupled Heisenberg $S = 1/2$ systems [Fig. 1.10(a)] show that the magnetization M for quasi-one-dimensional (triangles) and two-dimensional (2D) AFMs (diamonds) evolves as a concave trace with an increasing magnetic field H, such that M is reduced relative to a system with isotropic (3D) spatial-exchange interactions (circles). The published [76] pulsed-field powder magnetization of $[Cu(HF_2)(pyz)_2]SbF_6$ (solid line) falls between the 3D and 2D QMC simulations, which is indicative of a weak but finite interlayer spin-exchange

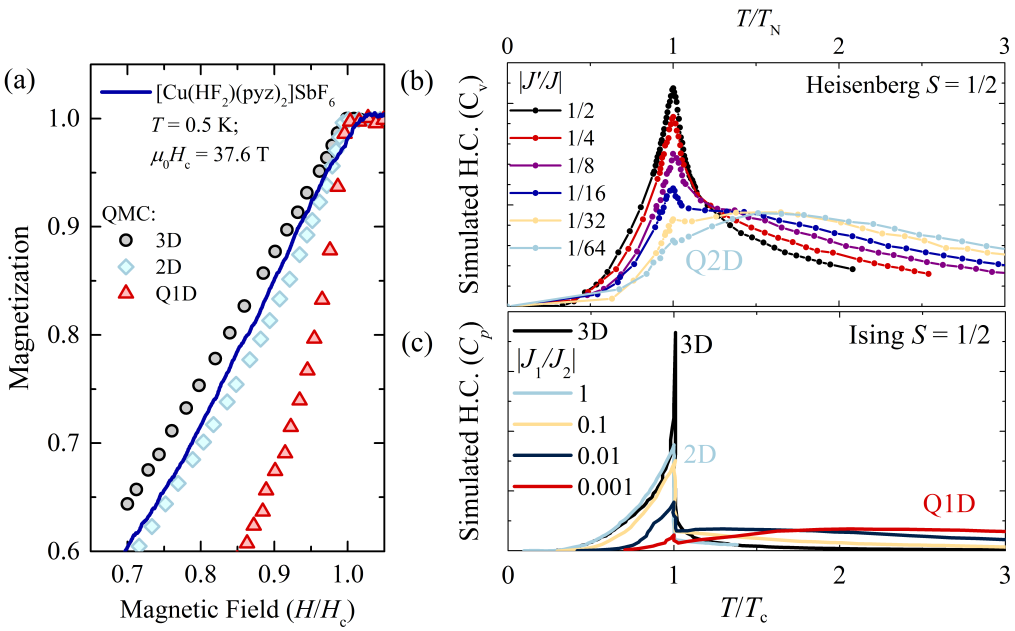

Figure 1.10: **(a)** QMC simulation of the magnetization (normalized to saturation) vs. applied magnetic field H (normalized to the saturation field H_c), for Heisenberg $S = 1/2$ ions with spin-exchange interactions in three (circles) and two (diamonds) [45] spatial dimensions, and for a Q1D spin chain [65] with an interchain-to-intrachain exchange ratio of 1/50 (triangles) [65]. The solid line is the published [76] powder magnetization of $[Cu(HF_2)(pyz)_2]SbF_6$. **(b)** QMC simulation [102] of the heat capacity (H.C.) vs. temperature T for square-lattice Heisenberg $S = 1/2$ AFMs for various ratios of $|J'/J|$, where J (J') is the Heisenberg intraplane (interplane) exchange constant. **(c)** Simulated H.C. vs. T for Ising $S = 1/2$ moments on a cubic (3D) lattice [103] and for square-lattice Ising ferromagnets [105] where J_1 and J_2 are the exchange constants along the x and y directions respectively.

interaction in this material. Obtaining an estimate of the saturation field $H_{\rm sat}$ of low-dimensional Heisenberg $S = 1/2$ AFMs from $M(H)$ measurements is an effective strategy to determine the Heisenberg spin-exchange interactions. QMC calculations [45] deduced that for Q1D and Q2D systems, $H_{\rm sat}$ is given by

$$g\mu_{\rm B}\mu_0 H_{\rm sat} = zJ + z'J', \tag{1.23}$$

where J is the intrachain (intraplane) Hesiernberg exchange to z nearest neighbours and J' is the interchain (interplane) Heisenberg exchange to z' neighbours.

QMC simulations of the heat capacity for Q2D square-lattice Heisenberg $S = 1/2$ AFMs predict that, for $T > T_{\rm N}$, there is a build up of short-range spin correlations on cooling the system that results in a broad maximum in the heat capacity at $T \approx J/k_{\rm B}$ [Fig. 1.10(b)] [102]. This feature becomes more prominent as

the relative strength of the interlayer coupling, $|J'/J|$, decreases. Furthermore, the release of spin-entropy at the ordering temperature becomes smaller with decreasing $|J'/J|$ and the size of peak at $T_{\rm N}$ is reduced.

The published [103] results of QMC simulations and series expansions of the heat capacity for Ising spins arranged on a cubic lattice [Fig. 1.10(c), black line], meanwhile, combine to suggest that these systems exhibit a sharp anomaly a critical temperature $T_{\rm C}$, which is concurrent with the transition from a paramagnetic to a magnetically ordered phase, and this predicted form of the heat capacity is consistent with the results of experiments performed on the real tetragonal Ising-like AFM Rb_3CoCl_5 [103, 104]. A representative example of the expected form of the heat capacity for low-dimensional Ising systems derives from the results of correlated-effective-field theory calculations of Ising $S = 1/2$ moments arranged on the vertices of an anisotropic square-lattice. In this particular model, each spin is coupled via nearest-neighbour ferromagnetic interactions of differing strengths along the two orthogonal intraplane directions [105]. For ideal square-lattice systems [Fig. 1.10(c), pale-blue line] a sharp heat capacity anomaly at $T_{\rm C}$ is anticipated to occur, while the size of the peak at the critical temperature is suppressed by the build-up of short-range spin-correlations in the case of close-to-ideal Ising $S = 1/2$ chains (red line) [105]. The prediction for a sharp peak in the heat capacity for the ideal square-lattice model is firstly in accord with Onsager's exact solution of the two dimensional Ising model, which suggests that the heat capacity diverges at $T = T_{\rm c}$ [106]; and secondly it is comparable to the form of the experimental heat capacity derived from measurements of the square-lattice Ising AFMs K_2CoF_4 and Rb_2CoF_4 [107]. Together these observations imply that a sharp peak at $T_{\rm C}$ is a common feature of square-lattice Ising systems. The expectation of a broad hump in the heat capacity for Ising spin-chains, meanwhile, is characteristic of the results analytical calculations of the heat capacity for ideal one-dimensional Ising systems, which predict that the heat capacity ought to exhibit a broad Schottky anomaly at $T \approx J/k_{\rm B}$ where J is the intrachain spin-exchange constant (e.g. Ref [108]). The relation between the overall shape of the magnetic heat capacity of Ising systems and the underlying spatial-dimensionality of the spin-exchange network is referred to in Chapter 5 in reference to the results of heat capacity measurements of the Ising-like complex $[Co(HF_2)(pyz)_2]SbF_6$.

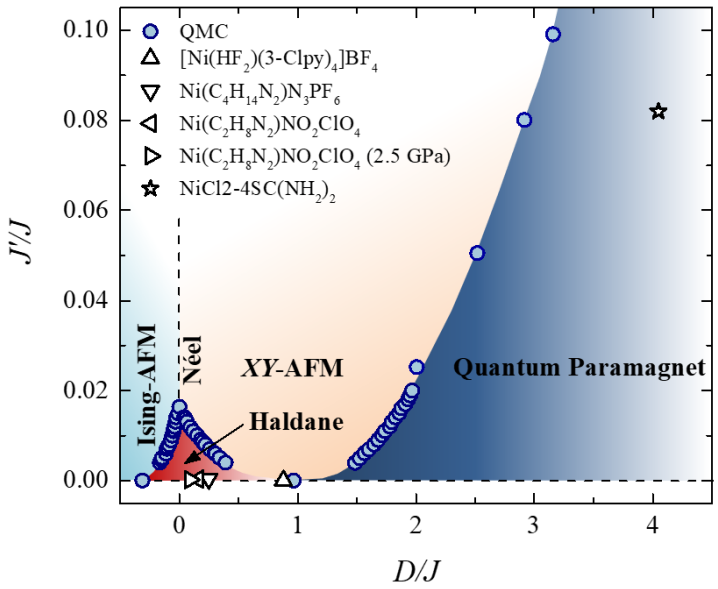

Figure 1.11: QMC simulation [68] (circles) for the $T = 0$ ground-state of $S = 1$ chain AFMs. Here, the Heisenberg intrachain and interchain exchange interactions are J and J' respectively, while the uniaxial single-ion anisotropy is D. The relative strengths of the ratios D/J and J'/J determine whether a system is an Ising-antiferromagnet (Ising-AFM); a conventional Néel AFM; a spin-gapped Haldane or quantum paramagnet (QP) material; or an XY-AFM. The Haldane, QP and XY-AFM phases meet at $J' = 0$ and $D/J \approx 0.97$. Several real molecular Haldane compounds [66,72,109] (triangles) and one QP system [92] (star) are displayed using published results.

1.5.4 Magnetism in Q1D $S = 1$ AFMs with uniaxial single-ion anisotropy

Coordination polymers are a proven means for generating antiferromagnetic $S = 1$ chains, for which the competition of the single-ion and spatial-exchange anisotropy gives rise to myriad of magnetic ground states. For instance, a low-temperature quantum paramagnet (QP) phase is adopted by $NiCl_2$-$4SC(NH_2)_2$ [68, 92]; a Haldane phase is exhibited by $Ni(C_4H_{14}N_2)N_3PF_6$ [109], $[Ni(C_2H_8N_2)_2NO_3]ClO_4$ [72] and $Ni(HF_2)(3\text{-}Clpy)_4]BF_4$ [66]; while the tetragonal polymer $[Ni(HF_2)(pyz)_2]SbF_6$, and the related monoclinic material $[Ni(HF_2)(pyz)_2]PF_6$, are suggested to be an XY-AFM and an Ising-AFM respectively [47]. Moreover, the spin-gap of $NiCl_2$-$4SC(NH_2)_2$ is found to be tunable when the Cl sites are doped with Br at the sample synthesis stage [71], while the magnetic properties of $[Ni(C_2H_8N_2)_2NO_3]ClO_4$ are perturbed with the application of a mechanical pressure of 2.5 GPa [72].

The results of QMC simulations [68] performed on Q1D $S = 1$ AFMs param-

eterize the diverse range of possible $T = 0$ ground states in these systems in terms of the ratios D/J and J'/J (Fig. 1.11), where D is the uniaxial anisotropy and J (J') labels the Heisenberg intrachain (interchain) spin-exchange constant. These simulations indicate that a zero temperature Haldane phase (red region in Fig. 1.11) occurs in the case of isolated ($J' = 0$) Heisenberg ($D = 0$) chains, but this yields to a QP phase (dark blue) once the uniaxial anisotropy exceeds a critical value of $D \approx 0.97J$. A finite interchain exchange interaction, meanwhile, acts to stabilize long-range magnetic order in form of an XY-AFM state if $D > 0$ (orange); a Néel phase if $D = 0$ (white); or an Ising-AFM state if $D < 0$ (pale blue).

For $[Ni(HF_2)(pyz)_2]SbF_6$, the previously published [47] bulk thermodynamic measurements, plus ligand field theory and DFT calculations, suggest $D \approx J$ and $J > |J'|$, thus positioning the material close to the $D/J \approx 0.97$ QCP. However, limited to a powdered sample, the investigations fell short of unambiguously characterising the ground-state and disentangling the energy scale of the three microscopic parameters D, J and J'. In order to position the material on the phase diagram of Fig. 1.11 it is essential to experimentally determine the precise nature of the magnetic ground state and to obtain unambiguous estimates of the ratios D/J and J'/J.

Chapter 4, and Ref. [75], demonstrate the experimental determination of an XY-like single-ion anisotropy from a polycrystalline sample of the kagome complex $[H_2F]_2[NiF_2(3\text{-}Fpy)_4]_3[SbF_6]_2$ using the results of high-frequency (GHz) electron spin-resonance, heat capacity and magnetization measurements. These methods are applicable providing the magnetometry measurements are performed for temperatures below $T \approx 0.18D/k_B$ and, importantly, that the spin-exchange interactions in the Hamiltonian are much less than D. It is the second point that means these techniques cannot be used to estimate D for $[Ni(HF_2)(pyz)_2]SbF_6$, where the energy scale of the single-ion anisotropy is of the same order as the intrachain Heisenberg exchange constant [47]. In Chapter 5, and in the related publication Ref. [77], a semi-classical model and the results of pulsed field magnetization measurements are used to infer the strengths of D and the average spin-exchange interactions of $[Ni(HF_2)(pyz)_2]SbF_6$ along the bifluoride and pyz linkages, while inelastic neutron scattering measurements of a powdered sample are necessary to extract unique estimates of D, J and J'

Chapter 2

Experimental Methods

2.1 Chapter overview

This chapter aims to outline some of the main principles of the experimental and computational methods utilized and referenced in this thesis. Firstly, Section 2.2 describes the various approaches used to generate quasistatic and pulsed magnetic fields for the investigation of condensed matter systems. Next, Section 2.3 offers an explanation of four magnetometry techniques. These are: (i) superconducting quantum interference device (SQUID) magnetometry; (ii) vibrating sample magnetometry; (iii) compensated coil extraction magnetometry; and (iv) proximity detector oscillation (PDO) magnetometry. Sections 2.4 and 2.5 review the experimental procedures for heat capacity and magnetocaloric effect measurements respectively, before Section 2.6 establishes a theoretical background to neutron scattering and introduces the two powder instruments that are used to collect data presented in this project. Lastly, Section 2.7 discusses the numerical simulations developed for the investigations of the Ni^{2+} compounds in Chapters 4 and 5. This includes an outline of model that determines the powder-average magnetization $M(H)$ and heat capacity of spin $S = 1$ materials with single-ion anisotropy, and an explanation of a semi-classical Monte-Carlo simulation that estimates $M(H)$ for a cluster of eight exchange coupled XY-like $S = 1$ ions arranged on a cubic lattice.

2.2 Generating quasistatic and pulsed magnetic fields

2.2.1 Obtaining static and quasistatic magnetic fields

Applying a homogeneous magnetic field H across a sample is an important experimental tool for examining the functional properties of magnetic materials and

synthetic rare-earth alloys provide one proven means to produce large permanent dipole magnetic fields in the laboratory. For instance, Nb-Fe-B and Sm-Co compounds exhibit an energy product $BH_{\max}$ [110] that is equivalent the energy density of a uniform H in free space with $\mu_0 H \approx 1$ T [Fig. 2.1(a), yellow bar]. However, the application of permanent magnets to the study of coordination polymers is limited since H cannot be swept, a uniform H is difficult to achieve over an extended volume and $|H|$ is small compared to the typical strengths of the spin-exchange interactions and single-ion anisotropies found in typical molecular materials. To make use of higher applied magnetic fields, it is necessary to use the quasistatic H produced in the bore of current carrying solenoids.

In 1820 Ørsted published [111] the experimental evidence demonstrating that a current carrying wire generates a magnetic field, while Ampère and Maxwell's formulation of this effect predicts that a long current-carrying solenoid generates a uniform magnetic flux through its centre (e.g. Ref. [112]). Modern day direct current (dc) solenoid magnets fall into three categories: (i) resistive; (ii) superconducting; and (iii) hybrid magnets. In general, the goal of magnet design is to maximize the current density in the solenoid, while providing sufficient mechanical support to contain the radial Lorentz force and axial clamping force that put stress on the magnet coil [113]. The radial force pushes out on the magnet coil and results from the coupling of the current flowing around the coil to the magnetic field generated by the solenoid itself. Meanwhile, the attractive axial clamping force arises since the current in each loop of a magnet coil flows in parallel with all of the others and is strongest near the central most windings.

High-field resistive Cu magnets at the National High Magnetic Field Laboratory (NHMFL), Tallahassee, employ Florida-Bitter coils to achieve $\mu_0 H \leq 35$ T [114] [Fig. 2.1(a), red bar]. These magnets are comprised of hundreds of high purity Cu discs stacked to form a solenoid. Holes and azimuthal slits in the discs create channels that run down the length of magnet, parallel to the bore, for up to 15×10^3 Ls^{-1} of deionized water to flow through and cool the system when in operation. The coolant both reduces the coil's resistance and improves the mechanical strength of the magnet. A 20 MW continuous dc power source supplies the necessary current to reach the peak field and this, in addition to the material costs and cooling equipment, renders the technique very expensive to run.

In superconducting magnets [Fig. 2.1(a), pale blue bars], a highly homogeneous H is generated by a persistent current that flows around a closed superconducting loop. Nb-based superconductors are commonly used for laboratory magnets, where NbTi coils produce $\mu_0 H \leq 12$ T at 2.2 K [115] and Nb_3Sn systems operate

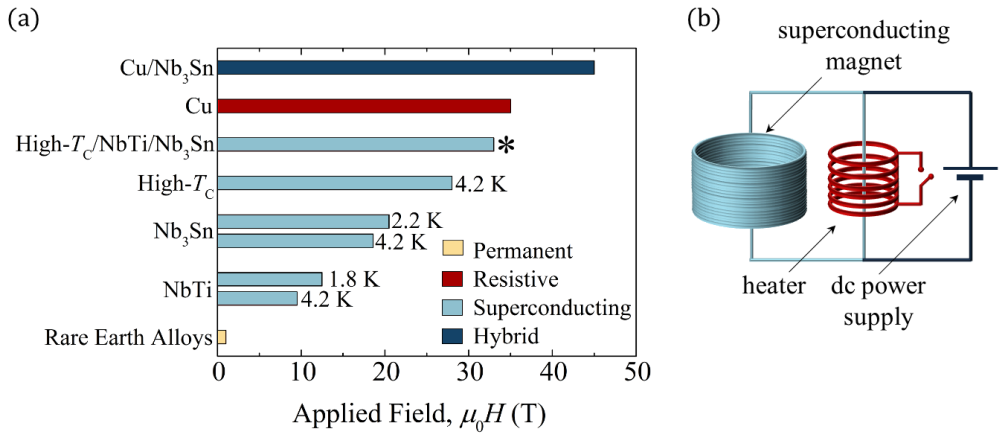

Figure 2.1: **(a)** Summary of the applied field capabilities of: (i) rare-earth alloy permanent magnets (yellow) [110]; (ii) resistive Florida-Bitter Cu solenoids at NHMFL, Tallahassee (red) [114]; (iii) NbTi, Nb_3Sn [115] and a high-T_c BSCCO [117] superconducting magnet (light-blue), where bars are labelled by the temperature of operation and the asterisk indicates a proposed magnet that incorporates high-T_c YBCO coils into a modular hybrid magnet at NHMFL, Tallahassee [118]; and (iv) a resistive-superconducting hybrid magnet at NHMFL, Tallahassee (dark-blue) [114]. **(b)** The circuitry for charging a superconducting solenoid magnet of the Quantum Design MPMS [120] employs a dc power supply and a heater that warms a superconducting wire to connect the power supply to the magnet coil.

for $\mu_0 H \leq 19$ T at 1.8 K [115]. These magnets are cheaper to run than their resistive counter parts since they do not necessarily require a continuous power supply to operate. The typical current density of superconductors (e.g. 10^9 Am^{-2} for Nb_3Sn [116]) is several orders of magnitude greater than in Cu, so superconducting magnets tend to be more compact. One disadvantage of superconducting systems is that they must be cryogenically cooled below their critical temperature (T_c) to operate and the critical current density of the materials places a fundamental limit on the maximum H that can be achieved in a particular coil. High-T_c superconductors [e.g. compounds of the form $YBa_2Cu_3O_{7-x}$ (YBCO) or $Bi_2Sr_2Ca_{n-1}Cu_nO_{2n+4+x}$ (BSCCO)] have a particularly high critical current density and an effort to incorporate YBCO tape into an all superconducting 32 T hybrid magnet at NHMFL, Tallahassee, is near completion [118]. By combining both resistive and superconducting magnet coils into a modular design, a Cu/Nb_3Sn hybrid magnet of this kind at NHMFL achieves quasistatic fields $\mu_0 H \leq 45$ T [114] [Fig. 2.1(a), dark-blue bar], which in 1999 set the world record for the highest continuous applied magnetic field.

2.2.2 Principles of operation of superconducting magnets

For data presented in this project, ^{4}He cooled superconducting magnets are used to generate quasistatic $\mu_0 H \leq 14$ T. The two ends of a solenoid magnet coil are connected with a superconducting wire to form a closed superconducting loop [Fig. 2.1(b)] such that a persistent current, which is generated in the coil by an external power supply, continues to flow around this loop once the power supply is disconnected. As an illustrative example, the method to charge the magnet of the Quantum Design™ (QD) Magnetic Property Measurement System (MPMS) is discussed in the remainder of this paragraph (following Ref. [120]). The circuitry for charging a magnet employs a heater [Fig. 2.1(b)] that surrounds the superconducting wire joining the two ends of the solenoid. With the magnet discharged and the heater on, the wire running through the heater is resistive and current may flow from the power supply to the magnet. Once the current in the magnet reaches the desired value the heater is turned off, the power supply is ramped down and a persistent current flows through the solenoid generating a magnetic field through its centre. To change an applied magnetic field, the current in the power supply is first matched to the current in the solenoid before the heater is turned on.

Two important features of superconducting magnets are: (i) the applied H is quasistatic, i.e. after a persistent current is first set the field within the magnet bore slowly relaxes with time; and (ii) once a magnet is discharged to zero current, a remnant flux can be trapped by the superconducting material. Property (i) results from flux lines in superconductor relaxing to their equilibrium positions once a persistent current is first established [121], where the relaxation timescale increases with the amplitude of H that is set [120]. For high precision magnetometry measurements of condensed matter systems in superconducting magnets, this slow change in flux at the sample position is one source of noise in an experiment. Property (ii), meanwhile, is important consideration when discharging a superconducting magnet. Oscillating the current from the power supply to zero is one method to minimize the trapped flux. For instance during the operation of the superconducting magnet of the QD MPMS, the automated oscillatory approach to setting zero field results in a remnant magnetic of $\mu_0|H| \approx 3 \times 10^{-4}$ T, whereas the instrument's no overshoot method of discharging the solenoid produces remnant fields up to $\mu_0|H| \approx 10^{-3}$ T [120]. If necessary, the trapped flux in a superconducting magnet is reduced further by warming the whole magnet above T_c to quench the system and a superconducting shield is sometimes placed around the magnet to reduce ambient flux from becoming trapped in the coil when the system is first cooled [121].

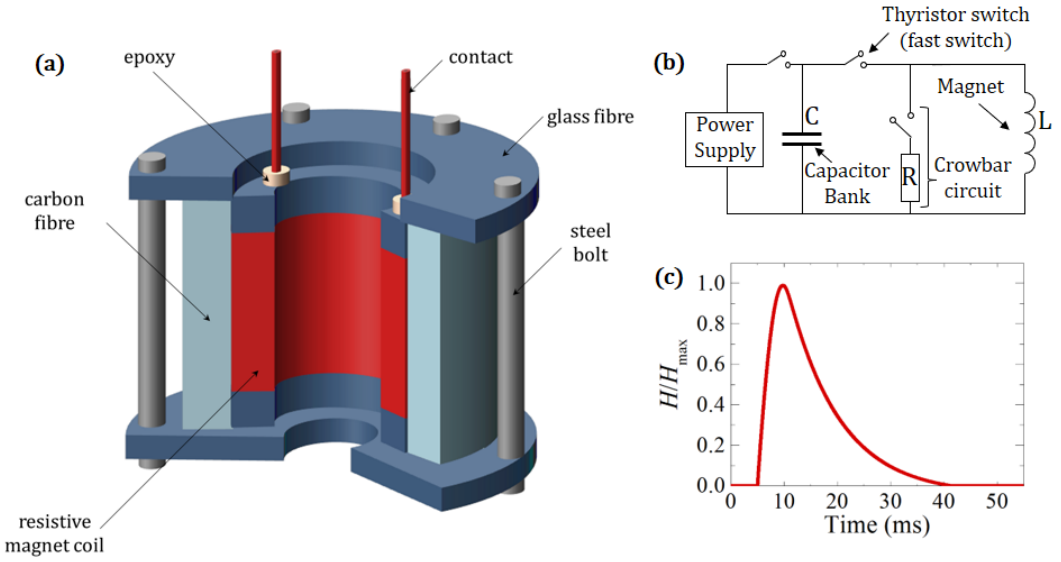

Figure 2.2: **(a)** Schematic cross-section diagram of the capacitor-driven short-pulse magnet at NHMFL, Los Alamos. The resistive magnet coil (red) is encased in carbon fibre (pale blue) and glass fibre discs (dark blue) that provide mechanical support to the magnet during its operation. **(b)** A dc power supply charges a capacitor bank and a thyristor switch allows the stored energy of the bank to be delivered to the magnet in a short pulse. **(c)** A typical profile of the applied field H as a function of time for a capacitor-driven magnet. Figure (a) is adapted from Ref. [113].

2.2.3 Capacitor-driven short-pulse magnets

Capacitor-driven short-pulse magnets are employed to produce applied magnetic fields with a higher flux density than that which can be sustained by superconducting materials. Two systems of this type are used to collect data presented in this thesis. The first is a magnet that provides $\mu_0 H \leq 65$ T at NHMFL, Los Alamos (USA), where the peak field is reached during an ≈ 10 ms pulse; the second is a magnet that generates $\mu_0 H \leq 60$ T in an ≈ 5 ms pulse at the University of Oxford (UK).

The NHMFL short-pulse magnet coil [113] demonstrates the key design features of these systems and is described in the remainder of this section. The magnet coil [Fig. 2.2(a)] is a resistive solenoid encased in carbon fibre for increased radial strength [113]. Glass fibre discs above and below the coil assist the magnetic clamping force to provide axial support and steel bolts that run the length of the magnet, outside the coil, provide extra reinforcement. A current is provided to the coil from a capacitor bank (see below) via two contacts that run through cavities in the glass fibre casing. Ultimately, the maximum field capability and lifetime of pulsed magnets is limited by the strength of the materials used in their construction. The coil

must contain the radial Lorentz force and resultant Maxwell stress that pushes out on the magnet coil during operation. The stress scales with H^2, reaching ≈ 1.7 GPa at $\mu_0 H = 65$ T [113]. In an experiment, the magnet sits in a liquid N_2 cryostat that cools the magnet coil prior to a field sweep. This acts to both strengthen the materials of the system and to lower the resistance of current carrying wires. During a field pulse, the heat capacity of the magnet adiabatically absorbs the heat produced by the resistive coil [113]. As a result, the magnet's temperature and resistance rise significantly during a field pulse and it must be cooled with liquid N_2 before it is safe to be used again.

Prior to a field pulse at NHMFL, Los Alamos, a 2.6 MJ capacitor bank is charged to a voltage V_c with a variable dc power supply [Fig. 2.2(b)]. Discharging the capacitors through the magnet coil provides the current necessary to reach the high applied magnetic fields. Since the capacitor and resistive solenoid form an LCR circuit, the initial rise in the magnetic field of the coil is closely modelled with a damped sine wave [Fig. 2.2(c)] [113] and, shortly after the peak field is reached, a crowbar diode extends the decay of H to an exponential relaxation with time. The pulse duration of a particular magnet is determined by the capacitance of the circuit, while the pulse height is dictated by V_c (i.e. the energy delivered to the magnet by the capacitor bank) [113].

2.2.4 The generator-driven long-pulse magnet at NHMFL

The long-pulse magnet at NHMFL, Los Alamos, consists of nine resistive magnet coils arranged in a modular coil design [Fig. 2.3(a)] and is capable of achieving $\mu_0 H \leq 60$ T with a pulse duration lasting several seconds. The modular design allows a current to be supplied separately to the inner, central and outer sections of the magnets via three busbar risers. By shaping the current supplied to each part of the system in this way, the pulse profile of the magnet can be adapted [Fig. 2.3(b)]. This is a significant advantage over capacitor-driven system for studies where the applied field sweep rate is important.

Current is delivered to the magnet from a 1.4 GW flywheel generator [119] that provides up to 750 MJ to the magnet from the energy stored in rotating drive-shaft that has a mass exceeding 260 tonnes. As the drive-shaft's rotation is slowed, a three-phase alternating voltage is produced and transformed down to 8 kV. The alternating current (ac) is rectified by five water cooled thyristors, which act as gated $p-n$ junctions. Regulating the gate voltage of the thyristors controls how much current passes through these devices and this offers a degree of control over the current that is delivered to each section of the modular magnet coil, therefore

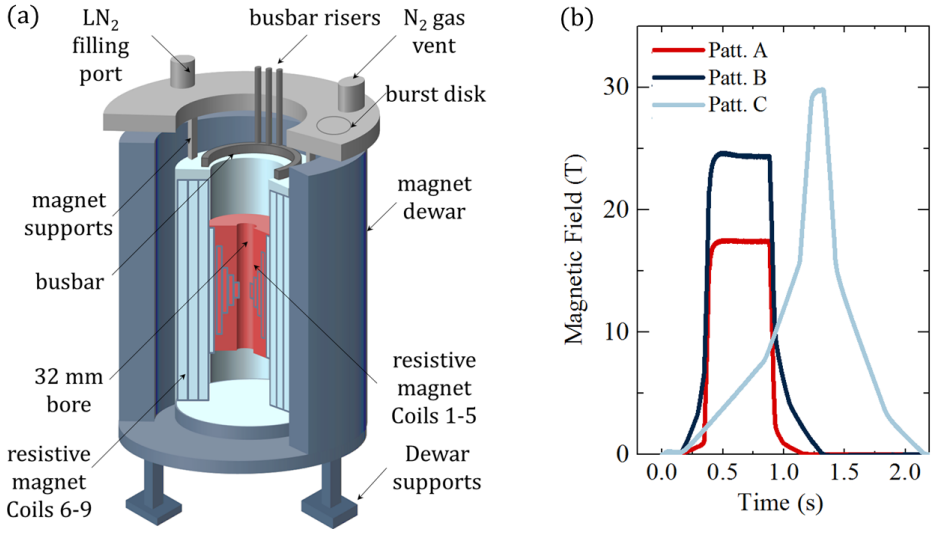

Figure 2.3: **(a)** Schematic cross-section diagram of the modular design of the resistive generator-driven long-pulse magnet at NHMFL, Los Alamos. Current is delivered separately to the inner, central and outer part of the magnet via three busbar risers. This allows various pulse profiles to be generated. Figure adapted from Ref. [113]. **(b)** Applied field pulse profiles as a function of time for the measurements performed with this system in Chapter 3.

allowing the pulse profile of the magnet to be designed. The shaping of a field pulse typically aims to raise H faster than it decays, which limits the amount of resistive heating in the magnet coil by the time peak field is reached and, in turn, lessens the increase of the resistance of the solenoid wires during this part of the pulse thereby maximizing the value of H that can be achieved.

As with capacitor-driven systems, the long-pulse magnet is encased in a liquid N_2 dewar and cooled prior to a field sweep. The dewar itself is supported from the ground, while the magnet hangs in the dewar from above [Fig. 2.3(a)]. This set up reduces the intensity of mechanical vibrations in the dewar that propagate to the magnet coil and thus reduces one source of noise in an experiment. Prior to a field pulse, once the magnet is cold, the liquid N_2 dewar is drained to a reservoir. This avoids N_2 from rapidly boiling off during a field pulse [113], which would otherwise act as a source of vibrations during an experiment.

2.3 Magnetometry techniques

2.3.1 SQUID magnetometry

(a) Overview of the magnetometer: Dc SQUID magnetometry measurements are performed with a QD MPMS [120]. The principle of the measurement is to determine the magnetic moment of a sample as it moves through a superconducting measurement coil. The sample space of the MPMS is a 9 mm diameter static ^{4}He chamber that provides temperatures in the range $1.8 \leq T \leq 400$ K [Fig. 2.4(a)] and the lower 30 cm of this space is lined with Cu to ensure a high thermal uniformity around the sample during an experiment. A sample is lowered into the MPMS on the end of long rod (see below) to position it within the bore of superconducting magnet, which provides $\mu_0|H| \leq 7$ T, and the top of the rod is attached to a stepper motor that allows the material to be translated though a superconducting measurement coil that is wound coaxial with, but outside, the sample chamber. This measurement coil is inductively coupled to a SQUID sensor that is positioned ≈ 11 cm below the sample position and surrounded by a superconducting shield.

SQUID magnetometry is sensitive to sample magnetic moments $\geq 10^{-11}$ Am^2 for $\mu_0 H \leq 2.5$ T, and those $\geq 10^{-9}$ Am^2 for $2.5 \leq \mu_0|H| \leq 7$ T [120]. Above these fields this technique loses its sensitivity advantage to vibrating sample magnetometry [120] (see below). The sensitivity of SQUID magnetometry relies on the superconducting shield surrounding the SQUID sensor and the geometry of the measurement coil. In part, the superconducting shield protects the SQUID and coupling transformers from changes in stray laboratory magnetic fields, but its primary purpose is to provide a stable flux across the SQUID by trapping any ambient fields across the sensor once the circuit is cooled to ^{4}He temperatures [120]. The superconducting measurement coil [Fig. 2.4(a)] is wound as a second order gradiometer [120, 122] and it consists of four turns. There is a single turn of the coil at the top and the bottom, in addition to a double counter-wound loop at the coil's centre. Ideally, this geometry means that a uniform change to the applied flux across the coils generates zero voltage and therefore an induced signal in an experiment comes from a magnetic sample moving though the coil's centre. Nevertheless, a small miss-match of the areas of each turn of the coil and non-uniform relaxation in H from the magnet are two sources of experimental noise in a SQUID magnetometer measurement [120].

(b) Extracting the magnetization: During a measurement a sample is moved along the applied field direction (z) a total of 4.0 cm in 24 discrete steps [120, 122].

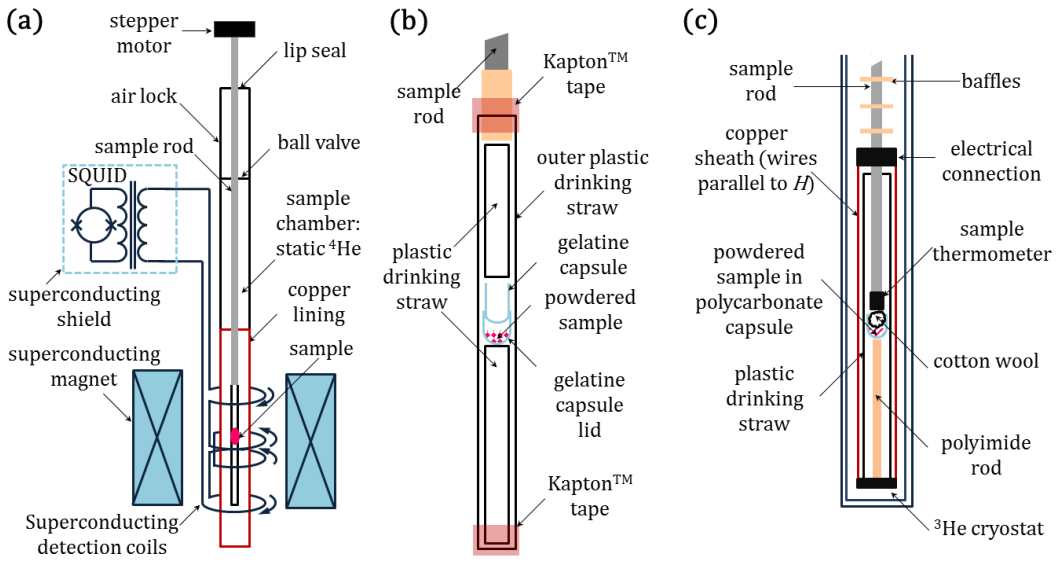

Figure 2.4: **(a)** Schematic experimental configuration of the Quantum Design MPMS SQUID magnetometer. **(b)** The sample holder for SQUID magnetometry measurements is a plastic drinking straw positioned at the end of a long rod, wherein a sample is secured in a gelatin capsule. **(c)** Diagrammatic representation of the sample holder for the iQuantum™ Helium-3 insert to the MPMS. The sample is secured in a polycarbonate capsule and a thermometer ≈ 1 cm from the sample records its temperature during an experiment.

The stepped motion of the magnetic material incrementally changes the persistent current in the measurement coil's superconducting wires so that a voltage is induced across the inductively coupled SQUID sensor. The current output of the SQUID is a monotonic function of the voltage across the device [123] and therefore it is directly related to the voltage V induced in the measurement coil [120]. In a measurement of $V(z)$, the sample is modelled as a point-like dipole with an automated linear regression fitting procedure [122], where the amplitude of V scales with the sample's dipole moment. This is used to infer the magnetization M of a material given a separate measurement of its mass. For small H the linear molar susceptibility χ_{mol} is related to M via $\chi_{\text{mol}} = M/(nH)$, where n is the number of moles of the sample.

(c) Preparing a measurement: For measurements below 300 K, it is appropriate to position sample at the centre of a plastic long drinking straw [122]. This ensures that the proportion of the sample holder within the pick-up coils is approximately constant as the sample is translated along z. Powdered samples are placed in the lid of a gelatin capsule and gently restrained with the narrower portion of the capsule

[Fig. 2.4(b)], while large single crystal samples are secured inside a closed capsule and supported with a small amount of cotton wool or Vaseline™. Samples less than ≈ 0.5 cm in length along the vertical direction tend to produce $V(z)$ traces that are accurately modelled by the MPMS's automated fitting procedure. Capsules are secured within the plastic straw from above and below using two pieces of a second drinking straw and the sample holder is then attached to the end of the sample rod with the application of Kapton™ tape. Prior to an experiment a sample is zero-field cooled to the desired T and centred within the measurement coils with a small quasistatic applied field before M is recorded at fixed T and H over their respective ranges of interest. In this project, the centering field is usually $\mu_0 H = 0.1$ T but, more generally, H needs to be sufficient to induce a clear peak in $V(z)$. A thermal expansion of the sample holder or rod may change a sample's centring position within the measurement coils during an experiment. The instrument's automated linear regression tracking measurement option [120, 122] is employed to re-centre a sample's position throughout H and T sweeps.

(d) ^{3}He measurements: The iQuantum™ Helium-3 insert provides sample temperatures above 0.45 K within a 7 mm diameter cryostat. Polycrystalline samples are loaded into the lid of a polycarbonate capsule and loosely restrained with cotton wool [Fig. 2.4(c)]. The capsule is placed in a plastic drinking straw and supported from below by a polyimide rod, while a calibrated thermometer is positioned ≈ 1 cm above the sample to monitor the sample's temperature. The plastic straw is wrapped in a Cu sheath that consists of thin wires aligned parallel to the applied field direction and encourages a high thermal uniformity in the sample holder during an experiment. An electrical connection is made between the sample holder to a probe that provides a heater and a charcoal pump close to the sample position. The length of the probe itself has a series of baffles that reduce the amount of infrared radiation that can reach the sample from the top of the instrument. The probe and sample holder are then lowered into the ^{3}He cryostat.

The cryostat is inserted into the ^{4}He chamber of the MPMS at 300 K and evacuated with a turbo molecular pump. The ^{4}He space is cooled to 5 K before ^{3}He gas is injected into the cryostat from a reservoir. At this stage the heater on the probe is set to 20 K, thus preventing the charcoal from becoming saturated with ^{3}He. As the ^{4}He chamber is cooled 1.6 K, ^{3}He liquid condenses in the cryostat once the temperature inside falls below ≈ 3 K. To reach 0.45 K, the turbo molecular pump is used again to lower the gas pressure in the ^{3}He cryostat and the heater is switched off to make use of the charcoal pump. The ^{3}He cryostat's base T hold time

is approximately 5.5 hours, which is sufficient time for approximately 170 measurements of the sample's magnetic moment.

(e) Ac susceptibility measurements: Ac susceptibility measurements are performed in quasistatic applied fields $\mu_0 H \leq 5$ T by following the time dependent magnetic moment of a sample $M(t)$ when the applied field is modulated by a sinusoidally oscillating ac field with an amplitude $H_{\rm ac}$ and frequency $\nu_{\rm ac}$ [124,125]. The oscillatory field is generated by a Cu coil, wound concentric with the axis of the sample chamber [124], and the sample moment evolves according to [125]

$$M(t) = \left(\frac{{\rm d}M}{{\rm d}H}\right) H_{\rm ac} \sin(2\pi\nu_{\rm ac} t + \phi), \tag{2.1}$$

where $\chi = {\rm d}M/{\rm d}H$ is the differential susceptibility, and ϕ is the phase of the oscillatory moment with respect to the drive signal.

The components of the susceptibility that vary in-phase ($\chi' = \chi\cos\phi$) and out-of-phase ($\chi'' = \chi\sin\phi$) with the ac modulation signal are recorded with two individual measurements. First, a stationary sample is positioned in the centre of a pick-up coil situated near the base of the MPMS chamber. A current is induced in this superconducting coil owing to the field modulation from the applied ac field, which produces a current in the inductively coupled SQUID sensor. The frequency of the SQUID device's voltage output is recorded and a local waveform is generated so as to nullify this signal [124]. Second, the sample is moved up into a separate measurement coil that has twice as many turns as the first and is also wound with an opposite polarity. The signal induced in this pick-up coil is recorded with the SQUID-based detection circuitry where it is further amplified by superimposing the measured voltage with the locally generated waveform derived from the first measurement. An analogue-to-digital converter measures the oscillatory sample moment from the amplitude of the total voltage output of detection circuitry [124].

2.3.2 Vibrating sample magnetometer

(a) Overview of the magnetometer: A vibrating sample magnetometer (VSM) measures the magnetic moment of a sinusoidally oscillating sample by synchronously measuring the induced voltage in a gradiometer pick-up coil positioned close to the sample (e.g. Ref. [126]). The VSM magnetization measurements presented in Chapter 5 make use of an Oxford Instruments™ superconducting magnet ($\mu_0|H| \leq$ 12 T) and ^{4}He flow cryostat ($1.4 \leq T \leq 300$ K), which regulates the sample T with a needle valve, a heater, one roughing pump, and one turbo pump (Fig. 2.5). An ac voltage, supplied to a linear motor by a Stanford Research Systems™ digital lock-in

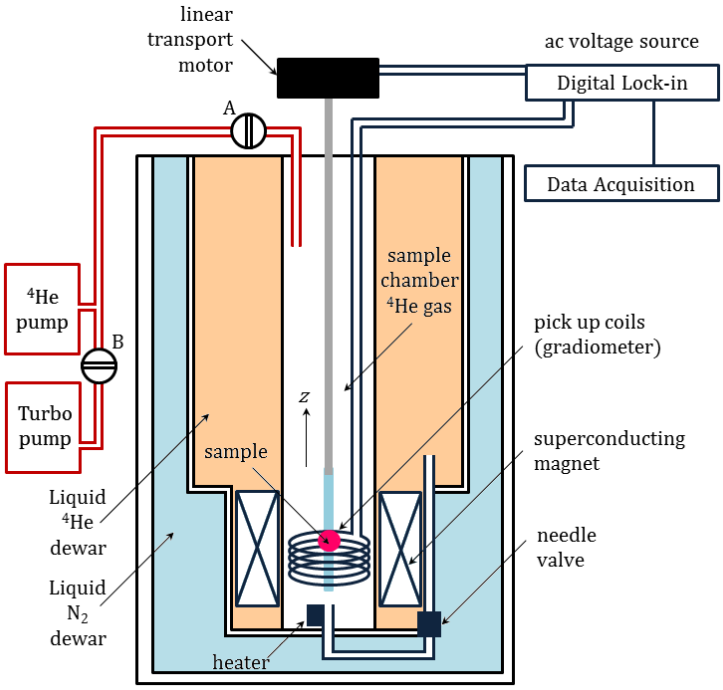

Figure 2.5: Diagrammatic representation of a vibrating sample magnetometer. An ac voltage applied to a linear motor oscillates a sample in the z direction and the voltage picked up in a gradiometer is synchronously recorded at the oscillation frequency. A ^{4}He flow cryostat regulates the sample temperature with a needle valve, a heater and two pumps: valve A connects the sample chamber to a roughing pump; while valve B connects the chamber to a turbo molecular pump to achieve $T \leq 1.7$ K.

amplifier, sinusoidally oscillates the sample to generate an ac voltage in the pick-up coil and the component of induced voltage that varies in-phase with the drive signal is extracted with the lock-in amplifier. An oscillation frequency of 55 Hz is employed to reduce interference in the measurement that may be generated by the mains powered detection circuitry. Two advantages of the VSM technique over SQUID magnetometry are firstly that the 55 Hz field modulation at the pick-up coil allows measurements to be recorded as H is swept slowly compared to the oscillation time period; and secondly that the applied magnetic field need only be homogenous over a small volume as a sample typically only moves 1-3 mm in a VSM measurement.

(b) Measuring the sample moment: For sample oscillations at frequency ν along the z-direction, a changing flux $\mathrm{d}\Phi/\mathrm{d}t$ is generated through the gradiometer.

This induces a voltage V, which is given by Faraday's law as [126]

$$V \propto \frac{\mathrm{d}\Phi}{\mathrm{d}t} = \left(\frac{\mathrm{d}\Phi}{\mathrm{d}z}\right)\left(\frac{\mathrm{d}z}{\mathrm{d}t}\right). \tag{2.2}$$

For sinusoidal oscillations, the amplitude of V is proportional to both ν and sample's bulk magnetic moment along the z direction [126]. In an experiment, a sample's magnetization is inferred from a measurement of the sample's mass and by measuring the amplitude of V once it has been independently calibrated against the voltage observed for a Ni sample whose absolute magnetic moment has been determined with SQUID magnetometry.

(c) Preparing a measurement: For sinusoidal oscillations with a frequency of 55 Hz and an amplitude of 1.5 mm, the ratio of the peak force on a sample to its own weight reaches a value of approximately 18 during a measurement. It is therefore necessary to securely mount a powdered material to its sample holder in an experiment. First, polycrystalline materials are pressed into a 5 mm diameter pellet with a hydraulic ram. During this procedure, the ram pushes a 5 mm diameter plunger to compact the sample between two die. No more than 0.05 tonnes is applied to the ram, which equates to 2 tonnes (25 MPa) on the plunger. The pellet is secured to a flat surface of polyether ether ketone (PEEK) sample holder with silicone vacuum grease so that the plane of the pellet is parallel with H. The pellet and rod are then wrapped in ≈ 5 turns of Teflon™ tape to prevent the material from coming loose. The sample holder is lowered into the instrument before the sample is zero-field cooled to 1.7 K and centred in the gradiometer pick-up coil in a small quasistatic applied magnetic field (typically $\mu_0 H = 0.1$ T). This is achieved by oscillating the sample and translating the whole linear motor along z until the output voltage in the pick-up coil is maximized. For M vs. H measurements, the field sweep-rate is regulated to prevent the wires connecting the magnet to its power supply from overheating. The sweep-rates $\mu_0|\mathrm{d}H/\mathrm{d}t|$ used are: (i) 0.5 Ts^{-1} for $\mu_0 H \leq 10$ T; (ii) 0.2 Ts^{-1} for $10 \leq \mu_0 H \leq 11$ T; and (iii) 0.1 Ts^{-1} for $11 \leq \mu_0 H \leq 12$ T.

2.3.3 Compensated coil extraction magnetometry

(a) Overview of the magnetometer: In the context of the insulating samples studied in this project, a compensated coil extraction magnetometer [45] measures the differential susceptibility ($\chi = \mathrm{d}M/\mathrm{d}H$) of a material in the applied magnetic field of a capacitor-driven short-pulse magnet. The large $\mathrm{d}H/\mathrm{d}t$ of the pulsed magnet provides a field modulation in a measurement coil that is wrapped around a static

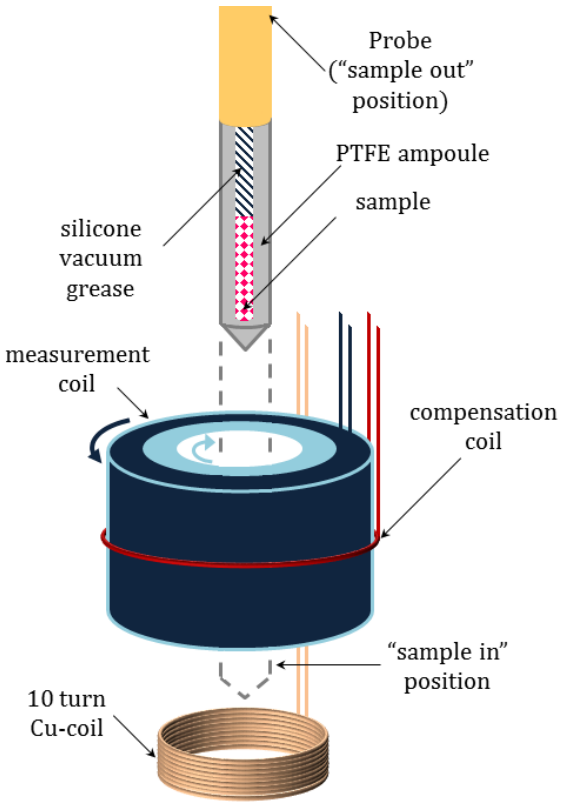

Figure 2.6: Diagram of the compensated coil extraction magnetometer probe. The measurement coil is made from 50 gauge Cu wire and consists of approximately 1000 turns (pale-blue) wound in one direction in addition to approximately 500 counter-wound turns (dark-blue). A single turn compensation coil (red) is coaxial with the measurement coil, while a 10 turn high-purity Cu-coil (close to the sample position) is used to determine H during an experiment (see text). The "sample out" position is depicted and the "sample in" position is indicated by the dashed lines.

sample. The measurement coil (Fig. 2.6) is made from 50 gauge Cu wire and two counter-wound sections. The inner part has a 1.5 mm bore and consists of ≈ 1000 turns, while the outer part of the coil comprises of ≈ 500 counter-wound turns. The exact number of windings is adjusted so that an alternating current applied the coil at room temperature generates a voltage in each counter-wound section that approximately cancels. An additional single turn compensation coil is wound around the measurement coil and, once the experimental set-up is cryogenically cooled, a $\mu_0 H = 10$ T amplitude magnetic field-pulse is applied to the system. A fraction of the voltage induced in the compensation coil is added to (or subtracted from) the voltage measured across the measurement coil to give a combined voltage output of zero and this is the compensated voltage V that is digitized in an experiment.

Finally, a separate fixed 10 turn Cu-coil is also mounted on the probe. This coil measures $\mathrm{d}H/\mathrm{d}t$, which is integrated to deduce the strength of the applied magnetic field, and it is calibrated using the de Haas-van Alphen oscillations in the signal coil arising from the belly orbits about the Cu Fermi surface [45].

(b) Extracting the magnetization: In an experiment a sample is mounted inside a polychlorotrifluoroethene (PCTFE) ampoule at the end of a long thin probe [see part (c)], which allows the sample to be translated vertically in and out of a measurement coil. A magnetization measurement requires two field sweeps to record V for both the "sample in" and "sample out" positions (Fig. 2.6). During a field pulse, V is given by [45]

$$V \propto \left(\frac{\mathrm{d}M}{\mathrm{d}t}\right) = \left(\frac{\mathrm{d}M}{\mathrm{d}H}\right)\left(\frac{\mathrm{d}H}{\mathrm{d}t}\right). \tag{2.3}$$

Since V and $\mathrm{d}H/\mathrm{d}t$ are both experimentally determined, a measurement of the integrated differential susceptibility of an empty coil subtracted from a measurement of the integrated susceptibility with the sample in the measurement coil is proportional to the material's magnetization.

(c) Preparing a measurement: A sample is loaded into the 1 mm diameter cavity of a PCTFE ampoule. The cavity is 4 mm long in the direction of H and is typically half-filled with compacted powder or a single crystal. The sample is restrained from moving by filling the rest of the ampoule with silicone vacuum grease and the ampoule is secured to a long thin rod with GE-varnish™. The rod and sample is inserted into a ^{3}He jacket, which is evacuated before the sample is positioned at the centre of a capacitor-driven short-pulse magnet. Finally, the sample is zero-field cooled to the desired T before an experiment.

2.3.4 Proximity detector oscillation magnetometer

(a) Overview of the magnetometer: A proximity detector oscillation (PDO) magnetometer is a contactless radio frequency method to determine the differential susceptibility, $\chi = \mathrm{d}M/\mathrm{d}H$, of insulators as a function of an applied magnetic field H. The detection circuitry uses a commercially available PDO sensor that is inductively coupled to a Cu measurement coil wrapped around the sample (Fig. 2.7). In essence, this forms the inductive part of an LCR circuit that resonates at a frequency ω [127]. When a MHz ac voltage is delivered to the measurement coil through a coaxial cable, the oscillating field within the coil's centre provides a field modulation at the sample position. The inductance of the coil depends upon the relative

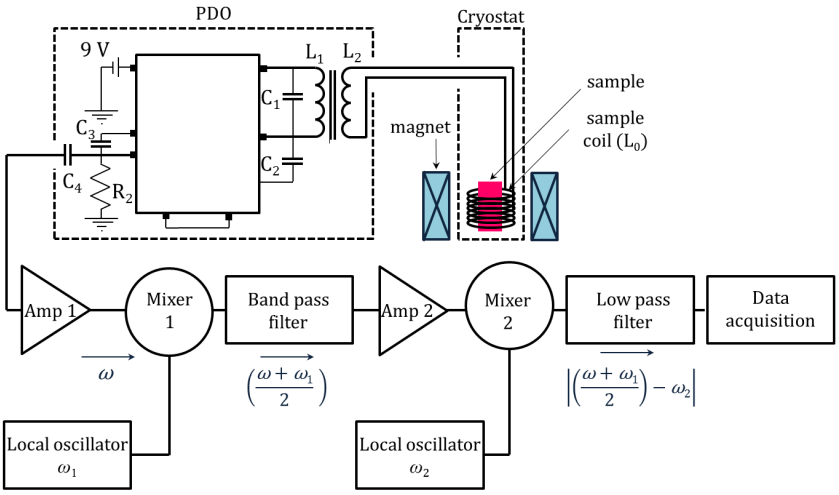

Figure 2.7: A schematic circuit flow diagram for the PDO magnetometry measurements. The circuit's MHz resonant frequency ω is mixed down in a two stage process to the kHz range before it is digitized (Figure adapted from Ref. [128]).

permeability of an electrically insulating sample and so this parameter, along with ω, evolves with χ [128].

(b) Extracting the magnetization: In order for the MHz resonant frequency of the PDO circuit to be digitized in an experiment, ω is first reduced to the kHz range before it is recorded. When two sinusoidal waves ($\sin \omega_{\mathrm{a,b}} t$) superimpose the resultant wave

$$\sin \omega_{\mathrm{a}} t + \sin \omega_{\mathrm{a}} t = 2 \sin \left(\frac{\omega_{\mathrm{a}} + \omega_{\mathrm{b}}}{2} \, t \right) \cos \left(\frac{|\omega_{\mathrm{a}} - \omega_{\mathrm{b}}|}{2} \, t \right) \tag{2.4}$$

has a fast oscillatory component, $(\omega_{\mathrm{a}} + \omega_{\mathrm{b}})/2$, while the amplitude of the summed waves is modulated at the slower angular frequency of $|\omega_{\mathrm{a}} - \omega_{\mathrm{b}}|/2$. The PDO measurement circuit (Fig. 2.7) employs a series of two radio-frequency mixers that combine the detection circuit's oscillatory signal with the MHz sine waves from two local oscillators. First the PDO circuit's signal (ω) is superimposed with an ac voltage (ω_1) and a MHz band-pass filter extracts the high-frequency component of the summed waves, $(\omega + \omega_1)/2$. Next, the band-pass filter's output is mixed with a second MHz wave (ω_2) and the low-frequency component of the second mixer's output, $\omega_{\mathrm{meas}} = |\omega_2 - (\omega + \omega_1)/2|$, is isolated with a kHz low-pass filter. This is the oscillatory signal V that is digitized in an experiment.

Providing the digitization rate satisfies the Nyquist limit (i.e. the sampling rate is $\geq 2\omega_{\mathrm{meas}}$, see for instance Ref. [128]) a Fourier transform of the measured

$V(H)$ curves extracts ω_{meas} as a function H and, since the frequencies of the two local signal generators are known, this is used to deduce $\omega(H)$. At constant T, the change in ω with H is given by [128]

$$\Delta\omega = -a\Delta\chi - b\Delta R_0 \tag{2.5}$$

where a and b are constants, while R_0 is the magnetoresistance of the sample measurement coil and connecting coaxial cables. When no sample is present, ω is measured with one field sweep to determine the background $\Delta\omega_{\text{bkgd}} = -bR_0$. When $\Delta\omega$ is re-measured in a second field sweep with the sample inside the measurement coil, $\Delta\omega_{\text{bkgd}}$ and Eq. 2.5 are used to produce a quantity proportional to χ [128].

(c) Preparing a measurement: Individual Cu measurement coils are wound to fit a particular sample and each turn of the coil is held together with the application of GE-varnish™. If a coil cannot be wrapped around a sample directly (for instance if the sample is sensitive to methanol and toluene solvents) coils are instead wound around a 1.3 mm diameter PCTFE ampoule. A single crystal or a powdered sample is fitted inside the ampoule, and the space at the top of the sample holder cavity is filled with silicone vacuum grease to restrain the material during an experiment.

2.4 Heat Capacity

2.4.1 Overview of the calorimeter

Constant pressure p heat capacity measurements of polycrystalline and single crystal samples are performed with a QD Physical Property Measurement System (PPMS) [129, 130]. The PPMS [Fig. 2.8(a)] consists of a high vacuum ^{4}He sample chamber that provides temperatures $1.6 \leq T \leq 400$ K close to the sample position. For investigations below 300 K, samples are secured to a 3×3 mm alumina platform with Apiezon™ N grease [Fig. 2.8(b)]. The platform is linked to a Cu puck via eight thin wires, which provide electrical connections to a thin-film heater evaporated onto the underside of the platform and a calibrated Cernox™ resistor that monitors the platform temperature ($T = T_1$). A second thermometer ($T = T_0$) is located below the puck, within the sample chamber. A superconducting magnet provides a quasistatic field $\mu_0|H| \leq 9$ T in persistent mode, where the direction of H is perpendicular to the sample platform.

2.4.2 Extraction of the heat capacity

For a sample with a heat capacity C_x at a temperature T_x [Fig. 2.8(b)], the Apiezon™ N grease provides a thermal conductance κ_2 to the alumina stage, while the total heat capacity of the stage plus grease is C_1. The wires connecting the alumina stage to the puck provide a thermal conductance κ_1, such that the puck acts as a heat sink in an experiment. In a heat capacity measurement, a power P is applied to the heater and the relaxation of the stage temperature T_1 with time is governed by the coupled differential equations [129, 130]

$$P = C_1 \frac{\mathrm{d}T_1}{\mathrm{d}t} + \kappa_2(T_1 - T_x) + \kappa_1(T_1 - T_0), \tag{2.6}$$

and

$$0 = C_x \frac{\mathrm{d}T_x}{\mathrm{d}t} + \kappa_2(T_x - T_1). \tag{2.7}$$

Following a heater pulse, T_1 relaxes with a general expression of the form [129, 130]

$$T_1(t) = T_0 + T_\alpha e^{-t/\tau_\alpha} + T_\beta e^{-t/\tau_\beta}, \tag{2.8}$$

where $T_{\alpha,\beta}$ and $\tau_{\alpha,\beta}$ are functions of $C_{1,x}$ and $\kappa_{1,2}$. Here, τ_α is a characteristically slow relaxation time accounting for heat flowing from the alumina platform to the puck, while τ_β is a faster relaxation dominated by heat flowing from the sample to the platform [129]. If $\kappa_2 \gg \kappa_1$ (i.e. there is strong thermal coupling to the sample), then $T_x \simeq T_1$ and Eqs. 2.6 and 2.7 imply a thermal relaxation of T_1 given by the expression [129, 130]

$$T_1(t) = T_0 + \Delta T_1 e^{-t/\tau}, \tag{2.9}$$

where $\tau = (C_x + C_1)/\kappa_1$. The determination of C_x from thermal relaxation experiments requires two separate measurements, which are discussed in the next two paragraphs.

Firstly, addenda experiments are performed with no sample in place. A heater pulse raises the alumina platform temperature by an amount $\Delta T_1 = P/\kappa_1$ and measurements of $T_1(t)$ are analysed with Eq. 2.9 (with $C_x = 0$), so that C_1 and κ_1 are known quantities over the T and H range of interest [129–131]. The field dependence of the addenda is only monitored for $T < 20$ K, where this consideration is most significant [Fig. 2.8(c)]. In an experiment, the amplitude of P is a controlled parameter so as to provide fractional temperature rises $\rho = \Delta T_1/T_1$ of approximately $0.01 - 0.03$. Prior to a heat capacity measurement, the ratio $|T_1 - T_0|/T_0$ is stabilized at a user defined value (usually 1-3% of ρ) so that thermal fluctuations of the system are much smaller than the controlled change in T_1 during an experiment.

Secondly, the sample is attached to the stage and measurements of the total

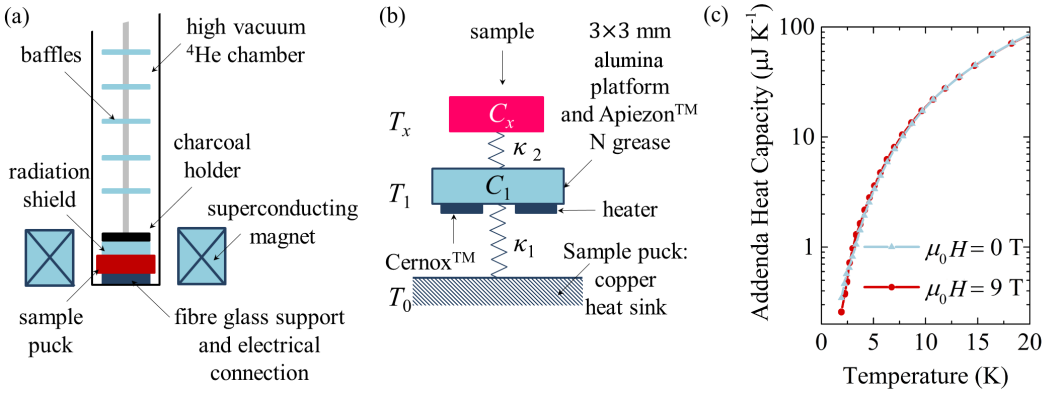

Figure 2.8: **(a)** Schematic set-up for Quantum Design PPMS heat capacity measurements. The sample is mounted on a puck positioned at the base of a high vacuum chamber within the bore of a 9 T superconducting magnet. A radiation shield protects the sample from warmer parts of the chamber. An assembly of baffles is used to absorb infrared radiation leaking in from the top of the chamber, while a charcoal holder positioned close to the sample helps to maintain a high vacuum below 10 K. **(b)** Heat flow diagram for the heat capacity measurements, adapted from Ref. [129]. **(c)** Typical addenda heat capacity as a function of temperature, for $\mu_0 H = 0$ and 9 T, demonstrating the weak field dependence of these background measurements.

heat capacity $C_1 + C_x$ are performed. In the first instance the measured $T_1(t)$ curves are modelled by numerically integrating Eq. 2.8 and fitting the unknown parameters to the data with a non-linear least squares fitting algorithm [129–131], where κ_1 and the addenda heat capacity (interpolated to the measurement temperature) are treated as constants. If no convergence between the fitted model and the data is obtained in this analysis, the quantity $C_1 + C_x$ is estimated from a least squares fitting of the $T_1(t)$ data to Eq. 2.9 and the addenda heat capacity is subtracted from this estimate of the total heat capacity to find C_x [130].

2.4.3 Preparing addenda and sample measurements

Addenda measurements proceed as follows: (i) the alumina stage is coated in a thin layer of Apiezon™ N grease and the puck is covered with a radiation shield [Fig. 2.8(a)]; (ii) the puck is lowered into the bore of the superconducting magnet before brass baffles are inserted along the length of the sample space to prevent infrared radiation reaching the base of the instrument. The baffle assembly has a small charcoal pump at its lower end, which aids in the removal of ^{4}He exchange gas around the sample below 10 K [129]. (iii) The chamber is flooded with ^{4}He gas and evacuated to 10-25 Pa with a roughing pump before a high vacuum ($p \leq 0.1$ mPa) is achieved with the use of an additional charcoal sorption pump; (iv) the puck is

zero-field cooled; and (v) addenda measurements of C_1 are collected at fixed T_0 and H across the ranges of interest.

Polycrystalline materials are prepared by pressing samples into a 5 mm diameter pellet with a hydraulic ram (see Section 2.3.2). While C_x scales with the mass m of a sample, and so a larger m increases the sample-to-addenda signal ratio, it is advantageous to use a relatively thin (≈ 0.5 mm) pellet to ensure the insulating sample is in good thermal contact with the alumina platform. The area of the pellet is cut to $< 3 \times 3$ mm, producing a sample with $m \approx 1$ mg that is attached to the platform with Apiezon™ N grease. Steps (ii)-(iv) from the passage above are repeated before the sample measurements proceed.

2.4.4 ^{3}He measurements

A Quantum Design ^{3}He insert provides sample temperatures from 0.4 to 20 K. The puck design for this probe is principally the same as for the standard measurements, although the sample platform is rotated by 90° such that H is applied within the plane of the sample platform. An additional feature of this puck is that the sample platform is stabilized by a small wire support that is in contact with the centre of the platform on the side opposite from the sample. This damps mechanical vibrations of the stage that would otherwise produce unwanted heating of the sample as a result of a current induced in the thermometer and heater circuitry during an applied field measurement. Prior to an experiment the sample puck is secured to the ^{3}He probe, covered with a radiation shield, and the assembly is inserted into the PPMS at 295 K. The cool down routine outlined in steps (ii)-(v) in part (c) is used again here, although a slow initial cool down rate for the sample chamber of 3 K per minute is employed to allow the large insert to thermalize as T is lowered and this aids in efficiently reaching 0.45 K.

2.5 Magnetocaloric Effect

2.5.1 Overview of the measurement

The principle of magnetocaloric effect measurements is to monitor a sample's temperature during an adiabatic applied magnetic field sweep. The large $\mathrm{d}H/\mathrm{d}t$ necessary for the MCE measurements (see Eq. 1.14) is achieved by utilizing the generator-driven long-pulse and the capacitor-driven short-pulse magnets at NHMFL, Los Alamos. The sample temperature is investigated by following the magnetoresistance R of a calibrated bare-chip Cernox™ resistor, which is directly attached to

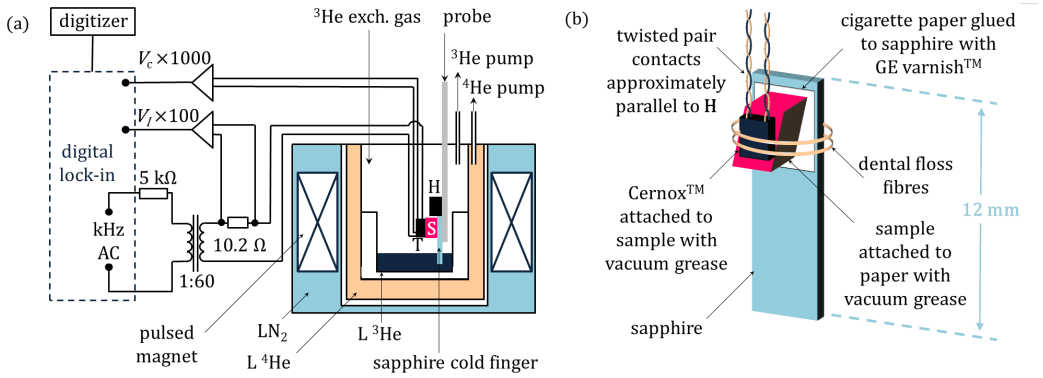

Figure 2.9: **(a)** A schematic circuit flow diagram for the four wire ac resistance measurement of a Cernox™ resistor (T) attached to a sample (S) in the magnetocaloric effect experiments (e.g. Ref. [82]). A heater (H) is positioned close to the sample and aids in regulating the temperature prior to a pulse. **(b)** The sample (pink) is mounted on a sapphire cold finger (pale blue), while the thermometer (dark blue) is directly attached to the sample with vacuum grease and further secured with dental floss fibres (yellow).

a sample with vacuum grease, with a four-wire ac resistance technique [82]. First, the sample and Cernox™ are inserted into the tail of a ^{3}He cryostat on the end of a thin probe such that the sample rests within the bore of the long-pulse (or short-pulse) magnet at the field centre position [Fig. 2.9(a)]. A digital lock-in provides a constant amplitude alternating current by feeding its 30 kHz (60 kHz), 1 V (2 V), ac voltage output through a 5 kΩ (1 kΩ) shunt resistor. The ac voltage is passed through a 1:60 turn step-up transformer and fed to the Cernox™ via a twisted pair of contacts that run along the probe, approximately parallel to the direction of H. The voltage drop V_I across a fixed resistor ($R_0 = 10.2\ \Omega$) that is positioned after the transformer [Fig. 2.9(a)] monitors the amplitude of the alternating current supplied to the Cernox™, which is typically $\approx 5\ \mu$A for the experimental set-ups described here. The voltage drop V_c across the Cernox™ is also extracted, this time with a second twisted pair of contacts that run back up the length of the probe. Both V_I and V_c are amplified (by factors of 100 and 1000 respectively) with Stanford Research Systems™ Low Noise Preamplifiers and are recorded as a function of time during a magnetic field pulse with the lock-in amplifier that provides the original ac voltage output.

The lock-in amplifier provides a measurement of both the in-phase (V') and out-of-phase (V'') components of the current-monitor and Cernox™ resistor voltages, where the overall phase of the oscillatory signals is chosen to minimize V_I''. The

Cernox™ magnetoresistance is then estimated from

$$R = R_0 \left(\frac{V_{\rm c}'}{1000} \right) \left(\frac{100}{V_I'} \right). \tag{2.10}$$

The (H, T) dependence of R is calibrated with no sample in place using the pulse-profiles from Fig. 2.2(b) and initial temperatures prior to the pulses are considered for He bath temperatures in the range $0.45 \leq T \leq 10$ K. The resistance R is modelled with the invertible empirical relation

$$R = \exp\left(a_1 + \frac{a_2}{T_{\rm Cer}^{a_3}} \right), \tag{2.11}$$

where $T_{\rm Cer}$ is the Cernox™ temperature during a field pulse and $a_i = \sum_{j=0}^{4} c_{ij} H^j$ are polynomials in the applied field H. In a magnetocaloric effect measurement of a sample, $T_{\rm Cer}$ is deduced from a measurement of R at a particular H via Eq. 2.11. The error in $T_{\rm Cer}$ extracted from this method is 1-3% for the He bath temperature and H ranges of interest for the MCE experiments reported in Chapter 4.

2.5.2 Sample mounting considerations

A number of probe design features are aimed at achieving adiabatic conditions during a field pulse. Firstly, the thermometer is attached directly to the sample with vacuum grease and the sample is in turn attached to thermally insulating cigarette paper with a further application of grease [Fig. 2.9(b)]. The paper is glued to a sapphire cold finger with GE-varnish™ positioning the sample approximately 10 mm above the bottom of the cryostat. In this configuration, the sapphire cold finger extends into liquid He that collects in the cryostat tail and this was the set-up used for the MCE measurements reported in Chapter 4.

2.6 Neutron powder diffraction

2.6.1 The differential cross-section

Neutrons are hadrons that have a spin angular momentum $S^z = \pm 1/2$ and, therefore, they scatter from atomic nuclei in a sample via the strong nuclear force as well as from individual atomic dipole moments in a crystal through electromagnetic interactions. In a neutron diffraction experiment [Fig. 2.10(a)] an incident neutron with a wave vector $\mathbf{k}_{\rm i}$, a spin-state $S_{\rm i}^z$ and kinetic energy $E_{\rm i}$, is scattered from a crystalline sample through an angle of 2θ into a new state characterized by $\mathbf{k}_{\rm f}$, $S_{\rm f}^z$ and $E_{\rm f}$. For scattering in the Born Approximation, which is an appropriate model for both the nuclear and magnetic scattering mechanisms owing to their weak nature,

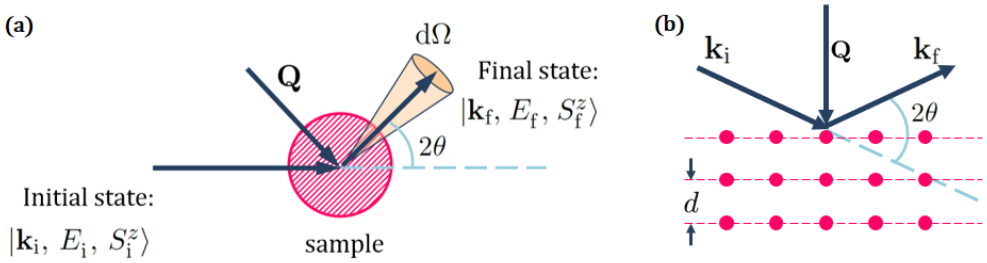

Figure 2.10: **(a)** Incident neutrons with wave vector $\mathbf{k}_\mathrm{i}$, kinetic energy = E_i and spin-state S_i^z are scattered from a sample (pink) through an angle 2θ into a new state determined by $\mathbf{k}_\mathrm{f}$, E_f and S_f^z. The scattered neutrons subtend a small solid angle $\mathrm{d}\Omega$ (yellow shading). **(b)** In the Laue scattering condition, neutrons diffract from planes of nuclei/moments (pink) with spacings of d when the momentum transfer $\mathbf{Q}$ is equal to a reciprocal lattice vector $\mathbf{G}$. Figure adapted from Ref. [132].

neutrons are transferred from an initial state $|\mathbf{k}_\mathrm{i}, E_\mathrm{i}, S_\mathrm{i}^z\rangle$ by a single scattering event via a crystalline sample's scattering potential $\mathbf{V}$ into a final state $|\mathbf{k}_\mathrm{f}, E_\mathrm{f}, S_\mathrm{f}^z\rangle$.

A quantity of interest in diffraction experiments is the neutron scattering cross-section σ. This is derived from the differential cross-section $\frac{\mathrm{d}^2\sigma}{\mathrm{d}E\mathrm{d}\Omega}$, which measures the probability that a neutron is scattered into a small solid angle $\mathrm{d}\Omega$ with a small change in energy $\mathrm{d}E$ and, more formally, it is defined as the scattered current density in phase-space normalized to the incident flux [133]. An expression for the differential cross-section for coherent neutron scattering is formulated with two assumptions: (i) the wave vector dependence of the wavefunctions of the incident and outgoing neutrons, at real-space coordinate $\mathbf{r}$, are modelled as a plane-waves of the form $\langle \mathbf{r}|\mathbf{k}\rangle = e^{i\mathbf{k}\cdot\mathbf{r}}$; and (ii) the rate at which neutrons are transferred to the final state by the potential $\mathbf{V}$ is determined with Fermi's golden rule. Defining $\mathbf{b} = -\frac{m_\mathrm{n}}{2\pi\hbar^2}\mathbf{V}$ as the neutron scattering length operator, where m_n is the neutron mass, the differential cross-section is given by an expression of the form [133]

$$\frac{\mathrm{d}^2\sigma}{\mathrm{d}E\mathrm{d}\Omega} = \frac{k_\mathrm{f}}{k_\mathrm{i}}|\langle E_\mathrm{f}^\mathrm{tot}, S_\mathrm{f}^z|\tilde{\mathbf{b}}|E_\mathrm{i}^\mathrm{tot}, S_\mathrm{i}^z\rangle|^2\delta(E_\mathrm{i} - E_\mathrm{f} - \hbar\omega). \tag{2.12}$$

Here the delta function preserves the conservation of energy, such that the energy transferred to the sample is $\hbar\omega = E_\mathrm{i} - E_\mathrm{f}$, while

$$\mathbf{Q} = \mathbf{k}_\mathrm{i} - \mathbf{k}_\mathrm{f} \tag{2.13}$$

is the momentum transferred to the material [134]. Finally,

$$\tilde{\mathbf{b}} = \int \mathrm{d}\mathbf{r}\, \mathbf{b}(\mathbf{r})e^{-i\mathbf{Q}\cdot\mathbf{r}} \tag{2.14}$$

is the Fourier transform of the scattering length (e.g. Ref. [133]).

Taking the dot product of Eq. 2.13 with itself and using $E_{\mathrm{i,f}} = \frac{\hbar^2 k_{\mathrm{i,f}}^2}{2m_{\mathrm{n}}}$, the $\hbar\omega$-dependence of the scattering vector $\mathbf{Q}$ is found to be [134]

$$\frac{\hbar^2|\mathbf{Q}|^2}{2m_{\mathrm{n}}} = 2E_{\mathrm{i}} - \hbar\omega - 2\sqrt{E_{\mathrm{i}}(E_{\mathrm{i}} - \hbar\omega)}\cos 2\theta. \tag{2.15}$$

This expression suggests that the experimentally accessible $|\mathbf{Q}|$-range is determined by the detector coverage of the scattering angle 2θ, the energy of the incident neutrons (i.e. the wavelength $\lambda = 2\pi/k$), and whether the neutrons scatter elastically ($\hbar\omega = 0$) or inelastically ($|\hbar\omega| > 0$) from the sample. In the next two sections the Fourier transformed scattering length (Eq. 2.14) is discussed further, as applied to both the nuclear and magnetic scattering mechanisms.

2.6.2 Nuclear scattering

(a) Bragg's Law: Neutrons at a real-space coordinate $\mathbf{r}$ scatter from atomic nuclei within a crystalline material via the strong nuclear force. As the range of this force ($\leq 10^{-14}$ m) is much smaller than the typical neutron wavelengths in an experiment ($\lambda \approx 1$ Å), each nucleus is treated as delta function at coordinate $\mathbf{R}_{\mathrm{N}}$. In this approximation, the nuclear scattering length for crystalline materials $\mathbf{b}_{\mathrm{N}}$ is given by the expression [133]

$$\mathbf{b}_{\mathrm{N}} = \sum_{\text{cells}} \sum_{\mathrm{N}_i} b_{\mathrm{N}_i} \delta(\mathbf{r} - \mathbf{R}_{\mathrm{N}_i}), \tag{2.16}$$

where the inner summation runs over all nuclei N_i within each crystallographic unit cell, the outer sum runs over all units cells, while b_{N_i} is the scattering length of each isotope and is, in general, a complex number [133,135]. Eqs. 2.14 and 2.16 are used to determine $\tilde{\mathbf{b}}_{\mathrm{N}}$ [132,133], where

$$\tilde{\mathbf{b}}_{\mathrm{N}} = \sum_{\mathrm{N}_i} b_{\mathrm{N}_i} e^{-i\mathbf{G}\cdot\mathbf{R}_{\mathrm{N}_i}}. \tag{2.17}$$

This defines the nuclear structure factor and, along with Eq. 2.12, it dictates that the probability for coherent nuclear scattering is only non-zero if $\mathbf{Q} = \mathbf{G}$; i.e. the momentum transfer is a reciprocal lattice vector for which $|\mathbf{G}| = 2\pi d^{-1}$ and d is the plane spacing of scatterers in a crystal [Fig. 2.10(b)]. This scattering geometry is referred to as the Laue scattering condition (e.g., Ref. [132]) and in the case of elastic scattering ($\hbar\omega = 0$), inserting $|\mathbf{Q}| = 2\pi d^{-1}$ into Eq. 2.13 yields the expression

$$\lambda = 2d\sin\theta, \tag{2.18}$$

which is precisely Bragg's law for first order neutron diffraction. A measurement of the nuclear Bragg peak positions in a diffraction experiment is used to infer the plane spacings of nuclei within a crystalline sample.

(b) Incoherent nuclear scattering: In addition to scattering events driven by the strong-nuclear force, a neutron may also scatter incoherently from a nucleus via an interaction of the neutron's dipole moment with the spin angular momentum of a nucleus. Thus, the b value for a particular isotope is separated into a coherent (b_{c}) and an incoherent (b_{i}) part [135]. A measurable quantity in an experiment is the total probability that neutrons scatter from a nucleus. This is expressed as the total scattering cross-section $\sigma_{\mathrm{s}} = 4\pi\langle|b|^2\rangle$, it has units of barns (bn = 10^{-23} m^2), and it considers a weighted average over all possible orientations of the neutron and nuclear spins [135]. The total scattering cross-section of nucleus is a sum of coherent ($\sigma_{\mathrm{c}} = 4\pi|b_{\mathrm{c}}|^2$) and incoherent ($\sigma_{\mathrm{i}} = 4\pi|b_{\mathrm{i}}|^2$) terms [135], which give rise to nuclear Bragg peaks and a background contribution to a diffraction pattern respectively.

Reducing the total $\sigma_{\mathrm{i}}/\sigma_{\mathrm{c}}$ ratio for a sample in a scattering experiment is one means to increase the signal-to-background ratio for the nuclear Bragg reflections. One important consideration for measurements performed on organic polymeric magnets is the relative size of σ_{i} for the hydrogen (^{1}H) and deuterium (^{2}D) isotopes, which are measured to be 80.27(6) bn and 2.05(3) bn respectively [135]. Given the relatively large σ_{i} value for ^{1}H, the neutron diffraction experiments presented in Chapter 5 are performed on materials for which pyrazine (pyz = $C_4H_4N_2$) is replaced with pyz-d_4 ($C_4D_4N_2$) at the sample synthesis stage.

(c) Absorption cross-section: The neutron absorption cross-section of a nucleus is $\sigma_{\mathrm{a}} = 4\pi k^{-1}\langle b_{\mathrm{c}}''\rangle$, where $|\mathbf{k}| = k$ is the incident neutron wavevector and b_{c}'' is the imaginary part of b_{c} [135]. Due to the finite probability of neutrons being absorbed during an experiments, sample holders (which must necessarily be placed in the neutron beam) are constructed from weakly absorbing materials such as V [$\sigma_{\mathrm{a}} = 5.08(4)$ bn] or Al [$\sigma_{\mathrm{a}} = 0.231(3)$ bn] [135]. Absorption may also be a useful property in a diffraction measurement; neutron detectors often use ^{3}He gas, which has a high neutron capture cross section, while Cd has $\sigma_{\mathrm{a}} = 2520(50)$ bn [135] and is frequently employed to mask experimental components from an incident neutron beam.

2.6.3 Magnetic scattering

Neutrons with a dipole moment $\boldsymbol{\mu}_{\mathrm{n}}$ scatter from the total electronic dipole moment $\boldsymbol{\mu}_i$ of a particular ion (i) within a crystalline lattice. Treating the neutron (at position $\mathbf{r}$) and the ion as point-like dipoles, the Fourier transformed magnetic scattering length is [133]

$$\tilde{\mathbf{b}}_{\mathrm{mag},i} = -\frac{m_{\mathrm{n}}}{2\pi\hbar^2}\frac{4\pi}{|\mathbf{Q}|^2}\,\boldsymbol{\mu}_{\mathrm{n}} \cdot \left[\mathbf{Q} \times \left(\mathbf{Q} \times e^{-i\mathbf{Q}\cdot\mathbf{r}}\boldsymbol{\mu}_i\right)\right]. \tag{2.19}$$

This expression dictates that neutrons only scatter from the proportion of an ion's dipole moment that is perpendicular to the momentum transfer $\mathbf{Q}$. The neutron diffraction data presented in Chapter 5 are measured from powdered samples and, consequently, Eq. 2.19 is averaged over all orientations of $\boldsymbol{\mu}_{\mathrm{n}}$ and $\boldsymbol{\mu}_i$. Together, Eqs. 2.12 and 2.19 indicate that the intensity of magnetic Bragg reflections is sensitive to the square of an ion's moment size.

For a magnetically ordered materials, the individual ionic moments are arranged in a periodic lattice and the magnetic scattering lengths for each ion are incorporated into a magnetic structure factor in an analogous way to Eq. 2.17. In a powder diffraction experiment, this yields magnetic Bragg peaks at $\mathbf{Q} = \mathbf{G}_{\mathrm{mag}}$, where $\mathbf{G}_{\mathrm{mag}}$ are reciprocal lattice vectors derived from the magnetic unit cell. For paramagnetic materials, the periodicity of the magnetic scattering potential is lost and there are no coherent Bragg reflections and, therefore, monitoring the intensity of Bragg reflections above and below a material's ordering temperature is one means to differentiate Bragg peaks that originate from nuclear or magnetic scattering. The finite distribution of spin-density around a transition metal ion centre in a real material weakens the point dipole approximation used in Eq. 2.19. This is corrected for with a magnetic form factor that modulates intensity of magnetic Bragg reflections and tends to diminish the peak intensities at large momentum transfers [133].

2.6.4 Wish: a time-of-flight powder diffractometer

(a) Overview of the Wish diffractometer: The Wish diffractometer [136] at the ISIS pulsed neutron and muon source, part of the Rutherford Appleton Laboratory (UK), utilizes a 10 Hz white neutron beam that is produced via spallation when synchrotron-accelerated 800 MeV protons collide with a tungsten target. The neutrons are thermalized to 50 K with solid methane moderator and enter an elliptical waveguide that begins 1.7 m from the source and ends 0.5 m from a sample (Fig. 2.11). A series of five choppers along the guide remove high energy particles from the beam and produce a single pulse of neutrons with accurate start and end

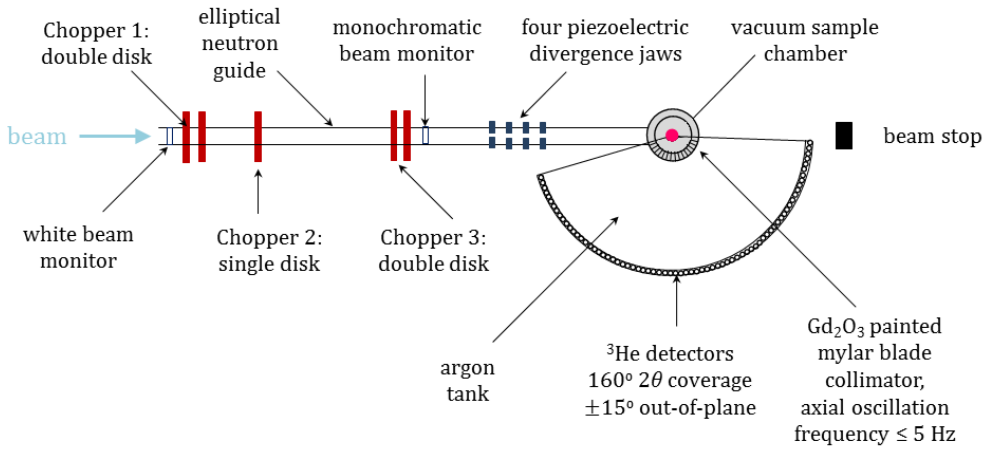

Figure 2.11: Schematic diagram of the Wish diffractometer. A 10 Hz pulsed white neutron beam enters a waveguide opening that is approximately 1.7 m from a 50 K solid methane moderator. Neutrons are guided though five choppers (red) and four piezoelectric divergence jaws (blue) to a 20×40 mm rectangular Al window that is 0.5 m from the sample (pink). The total source to sample distance is 40.0 m. The detector array is segregated into ten banks. The average 2θ angles of Banks 1 to 5 are 27.081°, 58.330°, 90.000°, 121.660° and 152.827° respectively. Banks 6 to 10 (not shown) are at negative 2θ angles and are directly opposite Banks 5-1; that is they are numbered in order of decreasing $|2\theta|$. Figure adapted from Ref. [136].

times. Four piezoelectric divergence jaws refocus the angular width of the neutron pulse and the beam enters an evacuated sample chamber through a 20×40 mm rectangular Al window. Neutrons scattered from a sample pass through a Gd_2O_3 collimator that consists of 20 mm blades extending radially away from the sample with angular separations of 0.75°. This directs neutrons through a 101 kPa Ar chamber to ten banks of gaseous ^{3}He detector tubes. Collectively, these detectors cover a continuous 2θ range of 160° and extend ±15° out of the plane of Fig. 2.11.

(b) Extracting a diffraction pattern: Neutrons are detected indirectly with low pressure gaseous ^{3}He detector tubes. A neutron striking a ^{3}He nucleus is readily absorbed in a process that releases ionizing radiation and, since a voltage is applied along the length of the tube, a current proportional to the neutron flux is generated once the ionizing radiation is produced. In an experiment, each detector records a histogram of the number of neutrons that arrive with flight-times between 5 and 99.9 ms timed from the start of the pulse. Data are collected in 4500 time channels that are logarithmically spaced in time and so evenly spaced in neutron energy [136]. A summed histogram of neutron intensity vs. flight-time (i.e. λ)

for each of the five detector banks is produced. The known average 2θ scattering angles of each detector bank is used together with Bragg's law (Eq. 2.18) to infer the scattered neutron intensity as a function of d.

One advantage of a pulsed source is the large intensity of the neutron beam [136] (compared to the continuous neutron source of the other instrument used in this thesis, see Section 2.6.5). This is important for the investigation of low dimensional $S = 1/2$ molecular systems where the reduced size of the ordered moment and the low density of magnetic moments in the crystal are both expected to contribute to relatively weak magnetic Bragg reflections. Furthermore, the low (10 Hz) pulse frequency at Wish allows slow neutrons to reach the sample and this is responsible for the relatively large wavelength bandwidth ($\Delta\lambda_{\mathrm{bw}} = 9.4$ Å) of the instrument. This extensive $\Delta\lambda_{\mathrm{bw}}$ range, in conjunction with Eq. 2.15, grants access to: (i) high resolution Bragg scattering at large $|\mathbf{Q}|$, which is sensitive to fine spatial details of molecular materials; and (ii) small $|\mathbf{Q}|$ scattering that allows the magnetic structure of transitional metal complexes to be probed, since the intensity of magnetic reflections for $3d$ ions is diminished at large $|\mathbf{Q}|$ by the magnetic form factor (e.g. Ref. [133]).

2.6.5 The Disc Chopper Spectrometer: a time-of-flight inelastic powder spectrometer

(a) Overview of DCS: The Disc Chopper Spectrometer (DCS) [134, 137–139] at the National Institute for Standards and Technology, Gaithersburg (USA), is an instrument used to perform time-of-flight inelastic neutron scattering experiments that provide a measurement of the scattered neutron intensity as a function of both the energy transferred to the sample $\hbar\omega$ and the change in neutron wavevector $|\mathbf{Q}|$. In an experiment the neutrons are sourced from a 20 MW reactor, thermalized to 20 K with a liquid H_2 cooled moderator, and passed through an optical filter [Fig. 2.12(a)]. The filter's primary purpose is to prevent fast neutrons or γ-rays from reaching the sample chamber. It consists of a 60 mm wide rectangular wave guide, which is 12.0 m long and feeds the neutrons through a concrete shielded section for 6.9 m. The guide width is restricted to a 30 mm and the neutron beam is deflected through an angle of 0.25° and, as there is no line of sight from the cold source to the instrument, this reduces the intensity of energetic particles incident on the sample and detectors.

After exiting the concrete shielding the neutrons pass through a liquid N_2 cooled pyrolytic graphite crystal filter, which removes epithermal neutrons from the beam, before the neutrons are fed through seven rotating disk choppers along a 9.0 m

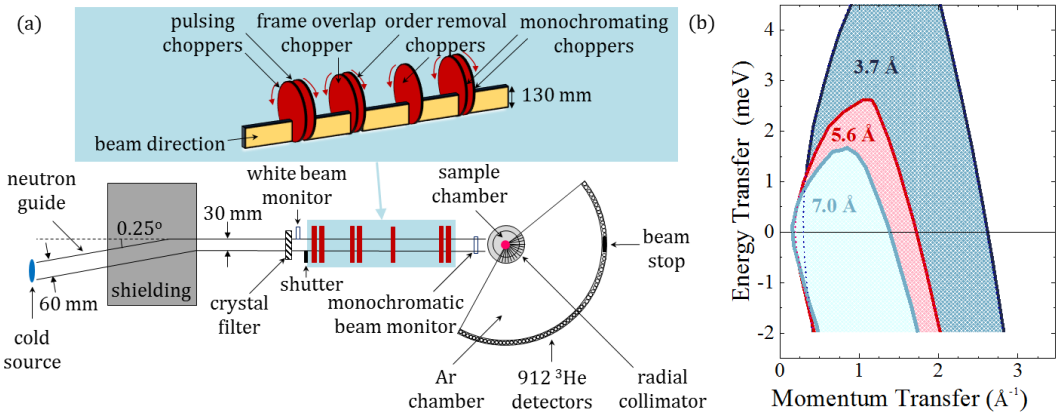

Figure 2.12: **(a)** Schematic diagram of the Disc Chopper Spectrometer (DCS). The optical filter (bent waveguide geometry) removes high energy particle from the beam. A series of seven choppers (inset) provides a pulsed monochromatic beam at the sample position. Neutrons are detected with gaseous ^{3}He tubes that are 400 mm long with a 31×12 mm cross-section. **(b)** The neutron energy and momentum transfer range for selected neutron wavelengths available at DCS. Figures (a) and (b) adapted from Refs. [134, 137–139]; inset adapted from Refs. [134, 137]

section of the guide [Fig. 2.12(a), inset]. There are two pulsing choppers that allow a burst of neutrons to pass through with pulse durations < 50 ms, one frame overlap chopper, two order removal choppers, and two time-of-flight monochromating choppers. A monochromatic beam with wavelength λ_i enters the sample chamber via a thin Al window and, following being scattered from a sample, the neutrons continue through a radial collimator into an Ar flight chamber before they are detected with an array of 913 ^{3}He tubes positioned 4.0 m from the sample. One bank of detectors records neutrons that are scattered within the plane of Fig. 2.12(a) and covers a non-continuous 2θ range of $-30 \leq 2\theta \leq -5°$ and $5 \leq 2\theta \leq 140°$. Two separate detector banks are located above and below the scattering plane and each of these has an angular coverage of $-30 \leq 2\theta \leq -10°$ and $10 \leq 2\theta \leq 140°$.

(b) Extracting a diffraction pattern: As λ_i is controlled by the phase and rotation frequency of the monochromatic choppers, the neutron time-of-flight from the choppers to the detectors allows the final neutron wavelength λ_f to be determined. Each ^{3}He detector tube records the scattered neutron intensity in 1024 time channels during a neutron pulse [138] and, from this, the energy transferred to the sample $\hbar\omega$ is determined from the conservation of energy. As the angular position of each detector is also known, the momentum transferred $|\mathbf{Q}|$ is inferred from Eq. 2.13. Arrays of the scattered neutron intensity as a function of $\hbar\omega$ and

$|\mathbf{Q}|$ from each detector are summed together to produce a histogram of the total scattered neutron intensity in the $\hbar\omega - |\mathbf{Q}|$ plane.

(c) Preparing a measurement: Selecting λ_i is an important experimental consideration. Firstly, it must avoid drops in the neutron intensity caused by the nuclear scattering and absorption from the graphite filter and Al in the beam [138]. Secondly, the $\hbar\omega - |\mathbf{Q}|$ coverage of a measurement is governed by λ_i (and the fixed detector coverages) via Eq. 2.15, such that neutrons with a shorter λ_i may transfer more energy and momentum to the sample [Fig. 2.12(b)]. The accessible range of $\hbar\omega$ must be sufficient to probe the energy scale terms in the spin Hamiltonian of a specific sample, while the $|\mathbf{Q}|$-range must exceed the d-spacings of ordered moments in a particular system.

2.7 Computational methods

2.7.1 Powder average simulations of $M(H)$ and $C_p(T)$ for $S = 1$ ions with single-ion anisotropy

A model Hamiltonian $\hat{\mathcal{H}}$ for spin $S = 1$ ions [Fig. 2.13(a)] in an applied magnetic field $\mathbf{H}$ is given by the expression

$$\hat{\mathcal{H}} = D(\hat{S}^z)^2 + E[(\hat{S}^x)^2 - (\hat{S}^y)^2] + \mu_\mathrm{B}\mu_0 \mathbf{H}^\mathrm{T} \boldsymbol{g}\, \mathbf{S}, \tag{2.20}$$

where D is the uniaxial single-ion anisotropy, E is the rhombohedral distortion anisotropy, $\boldsymbol{g} = \mathrm{diag}(g_{xy},\, g_{xy},\, g_z)$ is the anisotropic g-tensor and $\mathbf{S} = (\hat{S}^x,\, \hat{S}^y,\, \hat{S}^z)^\mathrm{T}$ is a column vector of the $S = 1$ spin operators. Defining $\mu_0\mathbf{H} = (B_x, B_y, B_z)^\mathrm{T}$ and writing the free ion's eigenstates as $|S, m_s\rangle$, where $\hat{S}_z|S, m_s\rangle = m_s|S, m_s\rangle$, then Eq. 2.20 in the $\{|S, m_S\rangle\}$ basis becomes [23]

$$\hat{\mathcal{H}} = \begin{pmatrix} D + g_z\mu_\mathrm{B}B_z & \frac{1}{\sqrt{2}}g_{xy}\mu_\mathrm{B}(B_x - iB_y) & E \\ \frac{1}{\sqrt{2}}g_{xy}\mu_\mathrm{B}(B_x + iB_y) & 0 & \frac{1}{\sqrt{2}}g_{xy}\mu_\mathrm{B}(B_x - iB_y) \\ E & \frac{1}{\sqrt{2}}g_{xy}\mu_\mathrm{B}(B_x + iB_y) & D - g_z\mu_\mathrm{B}B_z \end{pmatrix}. \tag{2.21}$$

For magnetic fields applied parallel to the x, y and z axes, the three exact eigenvalues $(\epsilon_n; n = 1, 2, 3)$ of Eq 2.21 are plotted in Fig. 2.13(b). This illustrative figure shows that the ϵ_n parameters are dependent on both the amplitude and orientation of the applied field.

A simulation of the powder average magnetization for an ensemble of $S = 1$ ions must consider the field evolution of the three ϵ_n values for all angles of the

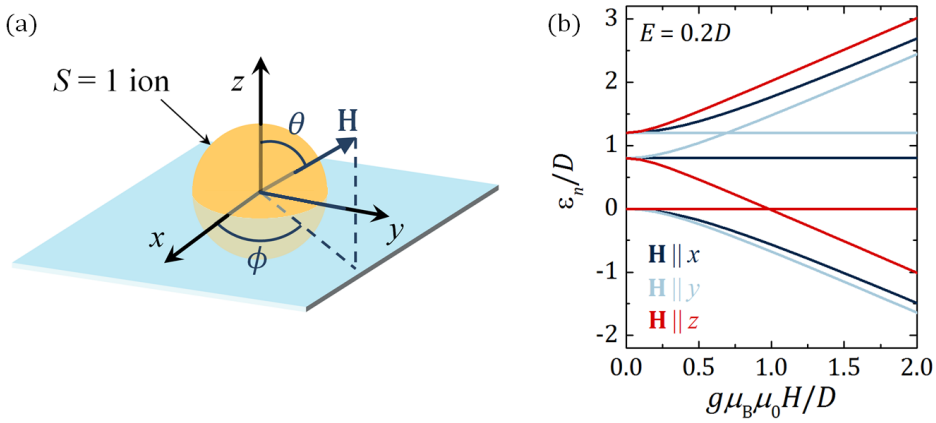

Figure 2.13: **(a)** For the powder average magnetization and powder average heat capacity simulations a magnetic field $\mathbf{H}$ is applied with polar angles (θ_i, ϕ_j) to $S = 1$ ions, where the local Cartesian axes are defined by the uniaxial (easy-plane) single-ion anisotropy. **(b)** The dimensionless spin eigenstates of Eq. 2.21 ($\epsilon_n/D; n = 1, 2, 3$) as a function of the applied Zeeman energy (normalized to D) for $\mathbf{H}$ parallel to x, y and z. For illustrative purposes g is taken to be isotropic and $E = 0.2D$.

applied field. The calculation begins by determining algebraic expressions for ϵ_n by applying the "EIG" function to the Hamiltonian in Eq. 2.21 in MATLAB [140], which returns the ϵ_n values in terms of $B_{x,y,z}$ using a matrix decomposition method. At a fixed temperature T, the partition function is

$$\mathcal{Z} = \sum_{n=1}^{3} e^{-\beta\epsilon_n}. \tag{2.22}$$

where $\beta = (k_{\mathrm{B}}T)^{-1}$. The magnetization $\mathbf{M} = (M_x, M_y, M_z)^{\mathrm{T}}$ follows from Eq. 2.22 (e.g. Ref [79]) by symbolically differentiating

$$M_\alpha = -k_{\mathrm{B}}T \frac{\partial}{\partial B_\alpha} \ln \mathcal{Z}, \tag{2.23}$$

in MATLAB, where $\alpha = (x, y, z)$.

For a particular applied field orientation (θ_i, ϕ_j) [Fig. 2.13(a)] and strength $(\mu_0 H)$, numerical values of (B_x, B_y, B_z) are substituted into each component of the magnetization. By considering each of the polar angles θ_i and ϕ_j in twenty evenly spaced increments of $\Delta\theta$ and $\Delta\phi$ across the respective inclusive ranges $[0,\ \pi]$ and $[0,\ 2\pi]$, the powder average magnetization $\langle M(H)\rangle$ is approximated by

$$\langle M(H)\rangle = \frac{\sum_{i,j} \mathbf{M}(H, \theta_i, \phi_j) \cdot \hat{\mathbf{H}} \sin\theta_i \, \Delta\theta \, \Delta\phi}{\sum_{i,j} \sin\theta_i \, \Delta\theta \, \Delta\phi}. \tag{2.24}$$

The T dependence of $\langle M(H)\rangle$ is inferred from calculations repeated at different fixed T values.

A simulation of the constant field heat capacity begins by defining numerical values for H and the field orientation (θ_i, ϕ_j). Numerical values for ϵ_n are obtained with the "EIG" function in MATLAB and inserted into Eq. 2.22. From this, the internal energy of the system U at a particular T and polar angle combination is

$$U(T, \theta_i, \phi_i) = \frac{\sum_{n=1}^{3} \epsilon_n e^{-\beta\epsilon_n}}{\mathcal{Z}}. \tag{2.25}$$

The magnetic contribution to the heat capacity $C_{\mathrm{mag}}(T, \theta_i, \phi_i)$ at fixed H follows by symbolically differentiating Eq. 2.25 in MATLAB via

$$C_{\mathrm{mag}}(T, \theta_i, \phi_i) = \frac{\partial}{\partial T} U(T, \theta_i, \phi_i). \tag{2.26}$$

Evaluating Eq. 2.26 at a particular T yields a numerical estimate of the heat capacity for a particular orientation of the applied field. By analogy with the calculation of the powder magnetization, 400 field orientations are considered and the powder average magnetic heat capacity at particular applied magnetic field strength $\langle C_{\mathrm{mag}}(T)\rangle$ is estimated with

$$\langle C_{\mathrm{mag}}(T)\rangle = \frac{\sum_{i,j} C_{\mathrm{mag}}(T, \theta_i, \phi_j)\ \sin\theta_i\ \Delta\theta\ \Delta\phi}{\sum_{i,j} \sin\theta_i\ \Delta\theta\ \Delta\phi}. \tag{2.27}$$

The field dependence of the heat capacity is examined by repeating the calculation at different fixed values of H.

2.7.2 Semi-classical Monte-Carlo simulation of the magnetization for a cluster of XY-like exchange-coupled $S = 1$ ions

Attempts to apply quantum-Monte-Carlo (QMC) methods to model the magnetic properties of low-dimensional $S = 1$ systems have thus far been limited [68], which is partly due to the reliance of these simulations on extracting the expectation value of the density-matrix $e^{-\beta\hat{\mathcal{H}}} = \sum_n (-\beta\hat{\mathcal{H}})^n/n!$, where $\hat{\mathcal{H}}$ is the spin Hamiltonian. Oftentimes, $S = 1$ chains are modelled as a string of moments connected by bond operators, i.e. each term in the series expansion of $e^{-\beta\hat{\mathcal{H}}}$ contains products of bond operators and has an overall sign that depends upon the number of bonds in the model (see for instance Ref. [68]). Stochastic sampling Markov chain Monte-Carlo methods [142] are often employed to model $S = 1$ systems [141] and this section is dedicated outlining a semi-classical Monte-Carlo energy minimization routine that

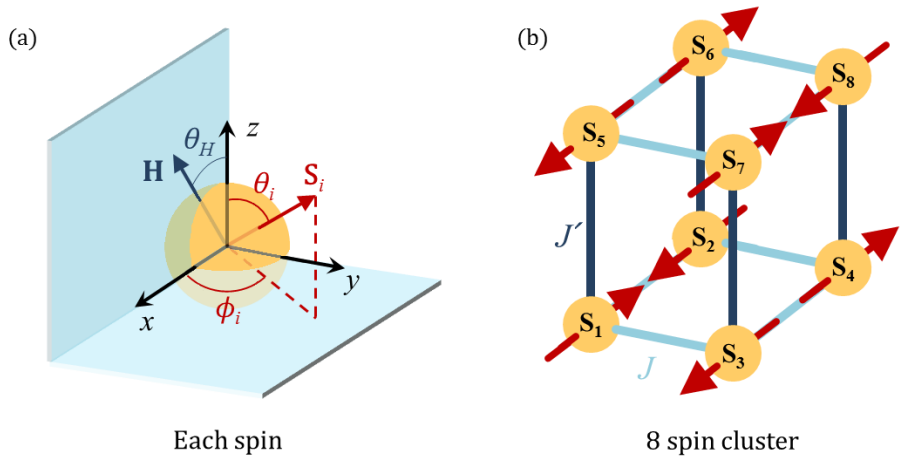

Figure 2.14: **(a)** The Cartesian and polar coordinate geometry of the applied field **H** (dark-blue) and the classical spin vector **S** (red) used to represent each $S = 1$ ion in the powder average Monte Carlo magnetization simulation. **(b)** The eight spins are arranged in a cubic cluster and coupled via Heisenberg interplane and intraplane spin-exchanges, J and J', respectively. The red arrows depict the zero-field spin configuration that was used as an input for the powder average $M(H)$ simulation.

has been developed in this project for estimating the powder-average magnetization M of a cluster of eight $S = 1$ ions in MATLAB.

The calculation is based on a model for which the spin $\mathbf{S}_i$ of each ion (i) is represented with a classical vector of fixed length, while the polar angles θ_i and ϕ_i [Fig. 2.14(a)] of this moment are each limited to 100 evenly-spaced discrete values in the ranges $[0,\ \pi]$ and $[0,\ 2\pi]$ respectively. The eight spin centres are arranged into a cluster comprised of two planes [Fig. 2.14(b)] for which the intraplane and interplane Heisenberg spin-exchange constants are, in turn, J and J'. Defining the uniaxial single ion anisotropy as D and assuming that the g-factor is isotropic, the spin Hamiltonian becomes

$$\hat{\mathcal{H}} \;=\; J\sum_{\langle i,j\rangle}\mathbf{S}_i\cdot\mathbf{S}_j \;+\; J'\sum_{\langle i,j'\rangle_\perp}\mathbf{S}_i\cdot\mathbf{S}_{j'} \;+\; \sum_i\left[D(\hat{S}_i^z)^2 + g\mu_{\mathrm{B}}\mu_0\mathbf{H}\cdot\mathbf{S}_i\right], \quad (2.28)$$

where the indices label each spin, the first sum extends over unique nearest-neighbour coplanar spins, the second sum runs over nearest-neighbours in adjacent planes, while the applied magnetic field **H** has a magnitude H and makes an angle θ_H with the z-axis. For a simulation of the magnetization of the tetragonal material $[Ni(HF_2)(pyz)_2]SbF_6$ in Chapter 5, periodic boundary conditions are used, which amounts to summing over each bond twice. For fixed J, J', D and g the expectation value of Eq. 2.28 is a function sixteen variables; i.e. the (θ_i, ϕ_i) values for

each spin. The goal of the $M(H)$ simulation is to find the bulk moment of the spin cluster for a given applied magnetic field once the energy of Eq. 2.28 is at a global minimum. This is performed with a Monte-Carlo routine that explores the energy landscape by incrementally randomizing the spin orientations to find low energy spin configurations, while seeking to avoid becoming attracted to local minima.

The powder-average $M(H)$ simulation for $[Ni(HF_2)(pyz)_2]SbF_6$ firstly assumes experimental estimates of D, J, J' and g (see Chapter 5) and the semi-classical Monte-Carlo algorithm proceeds as follows: (i) For $H = 0$ the results of NPD (Chapter 5) motivates the choice for the initial spin configuration [Fig. 2.14(b)], wherein neighbouring moments are collinear, antiparallel and perpendicular to z; (ii) for fixed θ_H the applied field strength is incremented to $H + \Delta H$ and the energy ϵ of the cluster is computed with Eq. 2.28; (iii) for a particular spin i, the angle θ_i is changed to a new random value in the range $0 \leq \theta_i \leq \pi$; (iv) the energy of the new spin configuration ϵ' is calculated from Eq. 2.28; (v) If $\epsilon' < \epsilon$ the new value for the polar angle is kept; (vi) If $\epsilon' - \epsilon = \Delta\epsilon$ is positive then the change in spin orientation is accepted with a probability $p = e^{-\beta\Delta\epsilon}$, otherwise the change is rejected. Here $\beta = (k_{\mathrm{B}}T)^{-1}$ is a user defined parameter, whereby if T is small compared to D, J and J' then changes in the spin orientation that raise the total energy are less probable. Allowing the energy to be raised with a finite p prevents the energy minimization routine from tending towards a local minimum in the energy landscape; (vii) The angle ϕ_i of the same spin is randomized in the range $0 \leq \phi_i \leq 2\pi$ and steps (iv)$-$(vi) are performed again. The index i is then incremented (via a cyclic permutation) until steps (iii)$-$(vii) have been performed on each spin. This process is then repeated 2000 times, with the aim of minimizing the energy of the cluster as a whole, before the magnetization at this particular combination of H and θ_H is determined by summing over the individual magnetic moments using

$$M(H, \theta_H) = -\sum_{i=1}^{8} g\mu_{\mathrm{B}}\, \mathbf{S}_i \cdot \hat{\mathbf{H}}, \tag{2.29}$$

where the leading minus sign results from the fact that the Ni^{2+} spin angular momentum derives from two negatively charged unpaired electrons.

The algorithm returns to step (ii) until the magnetic field reaches the maximum desired value. Thus, a full magnetization curve for a particular orientation of the applied field is obtained. Following this, θ_H is incremented in even steps for values in the range $0 \leq \theta_H \leq \frac{\pi}{2}$ and, by assuming $M(H, \theta_H) = M(H, \pi - \theta_H)$ from the symmetry of the uniaxial spin Hamiltonian (Eq. 2.28), the powder average

magnetization is approximated by

$$\langle M(H)\rangle = \frac{\sum_{\theta_H=0}^{\pi} M(H,\theta_H)\,\sin\theta_H\,\Delta\theta_H}{\sum_{\theta_H=0}^{\pi} \sin\theta_H\,\Delta\theta_H}, \tag{2.30}$$

where each sum runs over the complete set of θ_H values.

Chapter 3

Adiabatic physics of a spin-dimer network

$Cu(pyz)(gly)ClO_4$ (pyz = pyrazine; gly = glycinate) is an exchange-coupled spin-dimer system that undergoes a powerful and continuous magnetocaloric effect (MCE) under the application of a rapidly changing applied magnetic field H. The sample temperature T is reduced by up to 37% as H is increased and this adiabatic phenomenon must be accounted for in order to reconcile an apparent discrepancy between the results of magnetometry measurements performed in pulsed and quasistatic H without invoking separate physics. The isentropes of $Cu(pyz)(gly)ClO_4$ are derived across the $H-T$ plane from quasistatic heat capacity measurements and the form of these constant spin-entropy contours, which account for the nature of the MCE in adiabatic applied magnetic field sweeps, are consistent with the observations of direct MCE experiments as well as a thermodynamic model of the heat capacity. The T dependence of the experimental heat capacity is indicative of two-dimensional universal behaviour within this spin system, whilst the H dependence of the heat capacity and differential susceptibility suggest that zero-point fluctuations perturb the magnetic degrees of freedom for sample temperatures close to 400 mK. The results of this chapter, and the recent publication [73] derived from this work, suggest that the sample T of electrically-insulating systems (and not just conductors, see for instance Ref [113]) needs to be carefully considered when experiments are performed with pulsed magnetic fields.

3.1 Introduction

3.1.1 The arrangement of dimers in Cu(pyz)(gly)ClO_4

The results [74] of single-crystal x-ray diffraction measurements of Cu(pyz)(gly)ClO_4 (pyz = pyrazine; gly = glycinate) at 298(2) K reveal that this material crystallizes in the monoclinic $C2/c$ space-group wherein the individual Cu^{2+} ions are ligated with pyz molecules to form dimers [Fig. 3.1(a), blue shading]. A quasistatic magnetometry investigation of this complex [74] furthermore indicates that the pyz linkages facilitate an antiferromagnetic intradimer Heisenberg spin-exchange J (blue arrow) while the four separate gly ligands, which link the dimers into corrugated layers, mediate a weaker interdimer Heisenberg spin-exchange J' (pink arrow). Within this coordination geometry the dimer centres (blue circles) are coplanar and form a repeating rectangular motif (solid red lines).

Individual $[Cu(pyz)(gly)]^+$ sheets are stacked along the $[\mathbf{10\bar{1}}]$ crystallographic direction with a staggered arrangement [Fig. 3.1(b)], whereby each pyz-gly layer (orange shading) is displaced along the [**010**] lattice-vector with respect to the sheet directly below. Charge-balancing perchlorate (ClO_4^-) anions provide a bridge that links two Cu^{2+} ions from adjacent $[Cu(pyz)(gly)]^+$ layers along the green lines in Fig. 3.1(b). The nonlinear Cu$\cdots$O-Cl-O$\cdots$Cu superexchange pathways

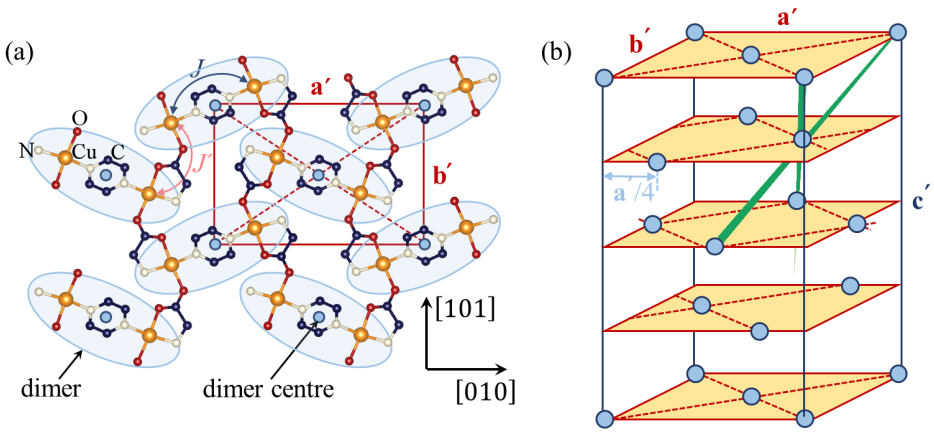

Figure 3.1: **(a)** At 298 K, Cu-pyz-Cu dimers (blue shading) are linked via gly ions to form corrugated sheets, where the dimer centres (blue dots) are coplanar. In a reduced structural scheme, nearest neighbour coplanar dimer centres are separated by the four real-space vectors: $\frac{1}{2}(\mathbf{a}' \pm \mathbf{b}')$, and $\frac{1}{2}(-\mathbf{a}' \pm \mathbf{b}')$. **(b)** Planes of dimers (orange shading) are stacked along $\mathbf{c}'$, where each sheet is displaced from the one below by $\frac{1}{4}\mathbf{a}'$. Separate perchlorate (ClO_4^-) anions link each dimer to four others along the real-space vectors: $\frac{1}{2}[\mathbf{b}' \pm \frac{1}{2}(\mathbf{a}' \mp \mathbf{c}')]$, and $\frac{1}{2}[-\mathbf{b}' \pm \frac{1}{2}(\mathbf{a}' \mp \mathbf{c}')]$ (green lines).

are ≈ 8.3 Å in length and provide an interlayer spin-exchange J''. However, there is a structural disorder in the room temperature structure; the individual O atoms of each ClO_4^- moiety occupy one of three equally likely positions and, consequently, the internal Cl-O bond lengths of the ClO_4^- anions vary from 1.395 to 1.448 Å.

The Cu^{2+} spin centres reside within CuN_2O_4 octahedra for which the Cu-O bonds between the Cu^{2+} ion and two separate ClO_4^- anions (positioned above and below the $[Cu(pyz)(gly)]^+$ layers) form the Jahn-Teller axis. This spontaneous distortion of the local coordination environment constrains the orientation of the plane of the Cu^{2+} $d_{x^2-y^2}$ orbital to lie predominantly within the pyz-gly sheets. Thus, there is an expectation for the spatial delocalization of the unpaired Cu^{2+} electron (and hence the spin-density) to be greatest within individual $[Cu(pyz)(gly)]^+$ layers and this observation, in conjunction with the structural disorder of the interlayer superexchange pathways, implies that the dominant spin-exchange interactions in this compound are likely to be mediated by the pyz and gly ligands.

3.1.2 Isothermal magnetic properties and a boson model for the magnetic excitations of Cu(pyz)(gly)ClO_4

Quasistatic magnetometry, heat capacity and muon-spin rotation (μ^+SR) measurements of $Cu(pyz)(gly)ClO_4$ combine to suggest that this system exhibits a zero-field disordered ground state and, for sample temperatures below ≈ 1.4 K, this nonmagnetic phase gives way to an H-induced phase that is confined to a dome in the $H-T$ plane [74]. The projection of the dome's phase boundary onto the $T = 0$ axis implies this system has two field-induced quantum critical points (QCPs) that are expected to occur at $g\mu_B\mu_0 H_{C1,2}/k_B = 2.5(1)$ and 9.02(2) K respectively [74]. The results of these isothermal measurements are characteristic of the properties exhibited by the extended family of inorganic and organic spin-gapped systems introduced in Section 1.5 [Fig. 1.8(c)], for which the magnetic properties in $H > 0$ are akin to a Bose-Einstein condensate (BEC) phase that forms from a nonmagnetic vacuum [52].

A bosonic model is pertinent to the discussion of the magnetic properties of $Cu(pyz)(gly)ClO_4$ providing: (i) the spin system is below the paramagnetic limit (i.e. $T \leq J/k_B$); and (ii) k_BT is furthermore in excess of the energy scale of any interactions in the spin Hamiltonian that might break the uniaxial symmetry [52]. Dzyaloshinskii-Moriya interactions are one example of symmetry breaking terms that cannot be ruled out from the structure of $Cu(pyz)(gly)ClO_4$ alone [74] and, if present, will act change the universality class of the spin quanta at low temperatures. However as no low-energy symmetry-breaking interactions have thus far been detected in $Cu(pyz)(gly)ClO_4$ for experimental investigations performed above

400 mK [74], the discussion of the magnetic properties of this system above this temperature proceeds with the hard-core boson model that, as it will be seen, provides a good description of the observed thermodynamic properties of the system.

Considering $Cu(pyz)(gly)ClO_4$ in a boson model the two lowest lying dimer spin-states for $H > 0$ [e.g. Fig. 1.8(a)] are represented by a nonmagnetic $S = 0$ or $|S^z| = 1$ (triplon) state localized at the dimer centre position, while the finite J' facilitates the hoping of triplons between dimers to neighbouring coplanar sites [52, 90, 91]. For $Cu(pyz)(gly)ClO_4$, the dimer centres are separated by the four real-space vectors $\frac{1}{2}(\mathbf{a}' \pm \mathbf{b}')$, and $\frac{1}{2}(-\mathbf{a}' \pm \mathbf{b}')$ [Fig. 3.1(a), dashed lines] and this geometry of the interdimer spin-exchange interactions gives the bosonic excitations a dispersion relation $\epsilon_{\rm t}(\mathbf{k})$ of the form

$$\epsilon_{\rm t}(\mathbf{k}) = J + 2J' \cos k_x \cos k_y - g\mu_{\rm B}\mu_0 H, \tag{3.1}$$

where $\mathbf{k} = (k_x, k_y)$ is the dimensionless triplon wave vector. Eq. 3.1 dictates that the triplons have a finite energy bandwidth of $\Delta = 4J'$, such that the dimer spin-gap is closed for a range of magnetic fields bounded by two quantum critical points (QCPs) whose positions are dictated by the relation $g\mu_{\rm B}\mu_0 H_{\rm C1,2} = J \mp 2|J'|$. This expression for $H_{\rm C1,2}$ combines with the experimentally determined [74] values for the two QCPs of $Cu(pyz)(gly)ClO_4$ to estimate $J/k_{\rm B} = 5.8(3)$ K and $|J'|/k_{\rm B} = 1.6(1)$ K.

3.2 Experimental details

3.2.1 Sample synthesis

Single-crystal samples are synthesized by J. L. Manson, Z. E. Manson, K. E. Carreiro, and H. E. Tran at Eastern Washington University (USA) following the procedure outlined in Ref. [74] and the supporting information therein.

3.2.2 Pulsed-field and quasistatic magnetometry

(a) Pulsed-field compensated coil extraction magnetometry: Pulsed-field magnetometry measurements of the differential susceptibility $\mathrm{d}M/\mathrm{d}H$ are performed by J. Singleton at the National High Magnetic Field Laboratory (NHMFL), Los Alamos (USA), using the capacitor-driven short-pulse (SP) magnet. The applied magnetic field rises to a peak value of $\mu_0 H = 10$ T in ≈ 10 ms [Fig. 2.2(c)]. The experiments utilize a single-crystal sample mounted inside a PCTFE ampoule and consider initial sample temperatures in the range $0.54 \leq T_0 \leq 3.60$ K.

(b) PDO magnetometry: In addition to the published [74] PDO magneomtery

measurements, which are shown and used in the analysis of this Chapter, further PDO magnetometry measurements are conducted in this work in collaboration with J. Singleton using the capacitor-driven SP magnet at NHMFL (Los Alamos). A single-crystal sample is positioned inside a 1.3 mm diameter PCTFE ampoule and secured with a small amount of vacuum grease. A 5-turn Cu coil is wrapped around the sample and ampoule to form the inductive part of the PDO circuit in the experiment, and $\mathrm{d}M/\mathrm{d}H$ vs. H is recorded for initial sample temperatures in the range $0.57 \leq T_0 \leq 3.01$ K.

(c) Ac susceptibility: As part of this work, isothermal measurements of the time-dependent magnetic moment of $Cu(pyz)(gly)ClO_4$ are recorded with a Quantum Design™ (QD) MPMS at the University of Warwick (UK). An 8.76 mg single-crystal sample is positioned inside a gelatin capsule, secured with Vaseline™ and, for sample temperatures $T \geq 1.8$ K, the magnetic moment M is recorded in response to a sinusoidally oscillating magnetic field that has an amplitude $\mu_0 H_{\mathrm{ac}} = 0.1$ mT and a frequency $\nu_{\mathrm{ac}} = 3$, 33, or 99 Hz. The component of the sample's magnetic moment that varies in-phase (M') and out of phase (M'') with respect to the ac field is followed for measurements performed in quasistatic applied dc fields $\mu_0 H \leq 5$ T. The in-phase and out-of-phase components of the molar ac differential susceptibility are estimated from $\chi^i = M^i/(nH_{\mathrm{ac}})$, where n is the number of moles of the sample and i is a primed or double-primed index.

3.2.3 Heat capacity

In addition to the published [74] heat capacity data collected by L. Huang and J. Wosnitza at the Hochfeld-Magnetlabor Dresden (Germany), which are presented and reanalyzed in this chapter, a separate measurement and analysis of the H dependence of the heat capacity of $Cu(pyz)(gly)ClO_4$ is performed as part of this work with a 1.03 mg single-crystal sample using the ^{3}He insert to a QD PPMS at the University of Warwick (UK). Sample temperatures are considered in the range $0.4 \leq T \leq 1.4$ K and each measurement is recorded in the quasistatic applied field of a superconducting magnet for $\mu_0 H \leq 7$ T.

3.2.4 Magnetocaloric effect

The magnetocaloric effect of $Cu(pyz)(gly)ClO_4$ is monitored in this work with measurements that utilize both the capacitor-driven short-pulse (SP) and generator-driven long-pulse (LP) magnets at NHMFL (Los Alamos) to generate rapidly chang-

ing magnetic fields. These measurements are performed with the assistance of M. Jaime and J. Singleton, both NHMFL (Los Alamos). The sample T is monitored by following the magnetoresistance of a calibrated bare-chip Cernox^{TM}, which is directly fixed to a single-crystal sample with vacuum grease, using a four-wire ac measurement. The pulse profiles for the SP and LP magnets are displayed in Fig. 2.2(c), with $\mu_0 H_{\rm max} = 10$ T, and Fig. 2.3(b) respectively.

3.3 Experimental results

3.3.1 Pulsed-field and quasistatic magnetometry

A published [74] PDO magnetometry investigation of $Cu(pyz)(gly)ClO_4$ records the differential susceptibility dM/dH as a function of a quasistatic applied magnetic field H [Fig. 3.2(a)]. For experiments performed at initial sample temperatures $T_0 < 1.31$ K, the dM/dH traces exhibit sharp kinks at each of the two field-induced BEC boundaries. However, PDO and compensated coil extraction magnetometer measurements of dM/dH, which are repeated in the rapidly changing

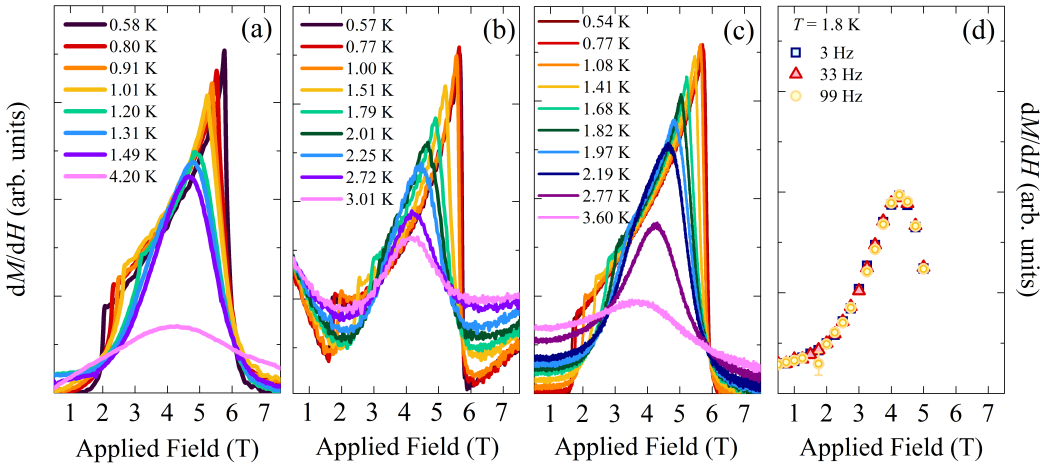

Figure 3.2: Differential susceptibility dM/dH vs. an applied magnetic field $\mu_0 H$ for: **(a)** the published [74] PDO magnetometry measurements performed in the quasistatic H of a superconducting magnet; **(b)** PDO magnetometry data collected in the rapidly changing H of a capacitor-driven SP magnet; and **(c)** compensated coil extraction magnetometry measured in a SP magnet. Data in panels (a)−(c) are labelled by the initial sample temperature T_0. **(d)** The in-phase differential susceptibility vs. quasistatic $\mu_0 H$ determined from ac SQUID magnetometry at 1.8 K. The sinusoidal modulation field has an amplitude of $\mu_0 H_{\rm ac} = 0.1$ T and an ac frequency of 3, 33 or 99 Hz (points). The out-of-phase susceptibility of these measurements (not shown) is negligible for dc fields $\mu_0 H \leq 5$ T.

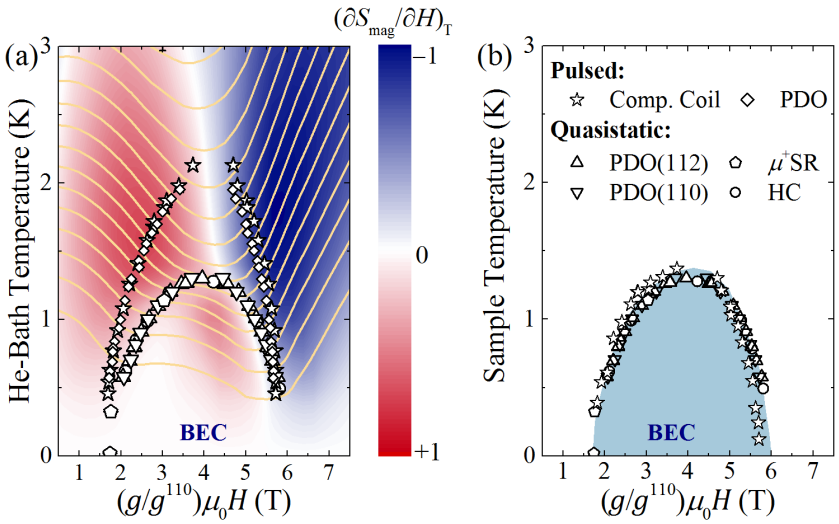

Figure 3.3: **(a)** BEC phase boundary of $Cu(pyz)(gly)ClO_4$ determined from the results of PDO magnetometry (triangles), heat capacity (circles) and μ^+SR (pentagons) measurements performed in quasistatic H [74] compared to the results of pulsed-field PDO (diamonds) and compensated coil extraction magnetometry (stars). The published [74] heat capacity is used to derive the isentropes (solid lines) and $(\partial S_{\rm mag}/\partial H)_T$ (colourmap in arbitrary units). **(b)** If the pulsed-field measurements from panel (a) are assumed to be adiabatic, the field-induced phase boundaries map onto the results of measurements in quasistatic fields.

H produced a capacitor-driven SP magnet [Fig. 3.2, panels (b) and (c)], display field-induced peaks that persist to be observable in $\mathrm{d}M/\mathrm{d}H$ for experiments with T_0 as high as 1.8 K. Further magnetometry experiments examine the ac susceptibility of $Cu(pyz)(gly)ClO_4$ and follow the time dependent magnetic moment in quasistatic applied dc magnetic fields $\mu_0 H \leq 5$ T [Fig. 3.2(d)]. The magnetization varies in phase with the sinusoidal oscillating applied modulation field for ac frequencies $\nu_{\rm ac} \leq 99$ Hz and the smooth evolution of $\mathrm{d}M/\mathrm{d}H$ across the investigated H range in these measurements is consistent with the results of the $\nu_{\rm ac} \approx 20$ MHz PDO magnetometry data collected in quasistatic H [Fig. 3.2(a)]. This demonstrates that it is the effect of the rapid field sweep rate, rather than the applied field modulation frequency, that is responsible for the apparent discrepancy in the results of magnetometry experiments performed in quasistatic and pulsed-fields [panels (a)−(c)].

If positions of the peaks in $\mathrm{d}M/\mathrm{d}H$ are extracted from the results of pulsed-field measurements and plotted as a function of the initial He bath temperature prior to a field sweep [Fig. 3.3(a)], these critical points appear to map out a dome that extends to higher temperatures in the $H-T$ plane compared to the BEC phase that is observed from the published [74] results of quasistatic magnetometry, heat capacity

and μ^+SR measurements. Taken at face value, the apparent extension of the phase diagram to higher T for measurements conducted in rapidly changing H strongly resembles the results of pulsed-field magnetometry and ultrasound measurements performed on a related three-dimensional exchange-coupled dimerized spin network $Sr_3Cr_2O_8$ [143,144]. In the study of the Cr^{2+} spin-system, the pulsed-field measurements are reported to map out a magnon liquid state that extends to temperatures above a low T magnetically ordered phase (akin to BEC) that was observed in isothermal measurements [143, 144]. However, the need to invoke a separate magnetic phase to explain the pulsed-field magnetometry data of $Cu(pyz)(gly)ClO_4$ is removed by appealing to the adiabatic nature of these experiments.

For $Cu(pyz)(gly)ClO_4$, lines of constant entropy (or isentropes) are derived from heat capacity measurements performed in quasistatic applied fields [Fig. 3.3(a), solid lines] (see below). These isentropes dictate the path across the $H - T$ plane that is taken by a sample during an adiabatic field sweep, as distinct from the horizontal isotherms that are traversed as H is swept slowly in a constant temperature experiment. If the pulsed-field magnetometry measurements of $Cu(pyz)(gly)ClO_4$ are assumed to be adiabatic, then the sample temperature at each of the two field induced phase boundaries is inferred by following an isentrope that begins at a similar initial temperature as the pulsed-field measurement. Under this assumption, the critical fields derived from the results of the magnetometry measurements performed in rapidly-changing applied magnetic fields map directly onto BEC phase boundary extracted from quasistatic field experiments [Fig. 3.3(b)]. Thus, the adiabatic and isothermal magnetometry measurement techniques are concluded to be sensitive to the same magnetic phases. This analysis indicates that the strong adiabaticity of the pulsed-field measurements induces a powerful and continuous MCE for all $H > 0$, such that the initial sample temperature is reduced by as much as 37% as H swept, and that this adiabatic phenomenon is likely to be an important consideration for measurements of related electrically-insulated materials; i.e. the sample T is not just a relevant factor in the measurements of conducting samples, which are known to undergo effects such as eddy current heating in rapidly changing H (e.g. Ref [113]).

3.3.2 Heat capacity and isentropes

(a) Heat capacity: The published [74] zero-field heat capacity of $Cu(pyz)(gly)ClO_4$ [Fig. 3.4(a) (points)] exhibits a broad maximum superimposed on a sloping background. In this work, the lattice contribution to measurement C_{latt} is modelled for $15 \leq T \leq 50$ K with Eq. 1.10 using one Debye (D) and one Einstein (E) mode (solid line). The fitted amplitude (A) and temperature (θ) of each mode are:

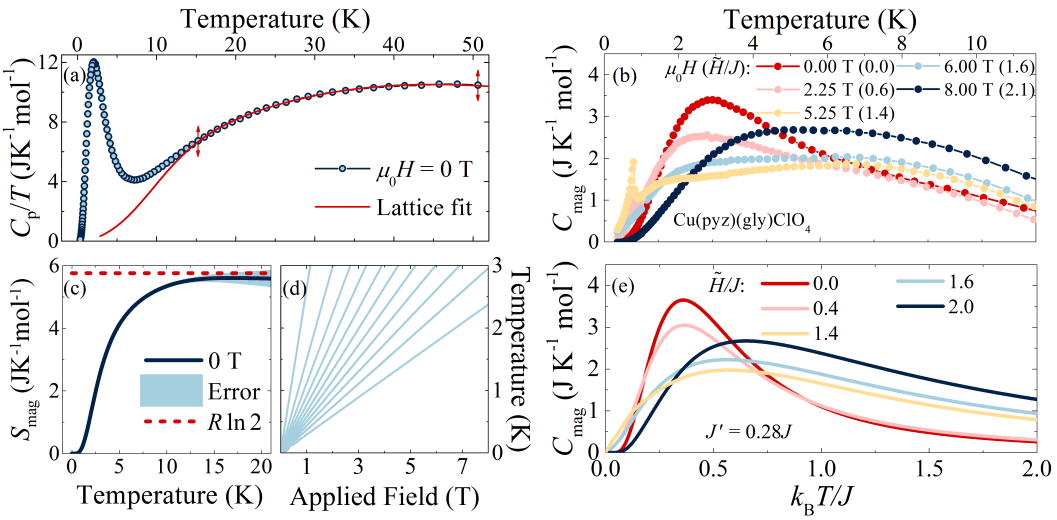

Figure 3.4: **(a)** The published [74] zero-field heat capacity $C_p(T)$ of Cu(pyz)(gly)ClO$_4$ (points). In the present work, C_p/T is fitted to Eq. 1.10 for $15 \leq T \leq 50$ K using one Debye (D) and one Einstein (E) mode (solid line). **(b)** Representative magnetic heat capacity $C_{\rm mag}(T)$ curves. Data are labelled by the quasistatic applied magnetic field $\mu_0 H$ and the ratio $\tilde{H}/J$ (in brackets), where $\tilde{H} = g\mu_{\rm B}\mu_0 H$. **(c)** For $\mu_0 H = 0$ T, the change in spin-entropy $S_{\rm mag}$ of Cu(pyz)(gly)ClO$_4$ (solid line) on cooling from $T > J/k_{\rm B}$ is consistent with a value of Rln2 per ion (dashed line). **(d)** The calculated isentropes of a $S = 1/2$ paramagnet (Eq. 1.17) are linear in the $H - T$ plane. **(e)** The simulated heat capacity (Eqs. 3.4 and 3.5) for an ensemble of dimers with a two-dimensional triplon dispersion relation, calculated at similar H values compared to the data in panel (b).

$A_{\rm D} = 41(1)$ JK^{-1}mol^{-1}, $\theta_{\rm D} = 86(1)$ K; and $A_{\rm E} = 67(1)$ JK^{-1}mol^{-1}, $\theta_{\rm E} = 171(3)$ K, which are characteristic of the energy scales of the lattice modes recorded in C_p studies of other homometallic-organic coordination polymers [59, 76, 77].

The magnetic heat capacity $C_{\rm mag} = C_p - C_{\rm latt}$ is estimated by interpolating the phonon model to each measurement of $C_p(T)$ collected in quasistatic $\mu_0 H \leq 9$ T. The $C_{\rm mag}(T)$ curves [Fig. 3.4(b)] exhibit two predominant features: (i) there is a sharp anomaly in $C_{\rm mag}(T)$ indicating the boundary of the BEC phase for measurements with $H_{\rm C1} \leq H \leq H_{\rm C2}$; and (ii) there is an H-dependent broad maximum that is present in each data set, which extends to temperatures above the BEC phase. This Schottky anomaly is indicative of the thermal depopulation of excited dimer spin states as the temperature is reduced below $\approx J/k_{\rm B}$ and the field evolution of this broad maximum is detailed in terms of a thermodynamic model in Section 3.4.

(b) Isentropes: Integrating the measured $C_{\rm mag}(T)/T$ curves with Eq. 1.12 de-

termines the temperature dependence of the spin-entropy $S_{\mathrm{mag}}(T)$ in quasistatic H. This calculation considers temperatures $T \leq 10$ K and assumes $C_{\mathrm{mag}} = 0$ at $T = 0$ K. In zero-field the change in spin-entropy of the system on cooling from 10 K [Fig. 3.4(c)] is consistent with a value of $R\ln 2$ per ion; i.e. $R\ln 4$ per dimer. This is the value of ΔS_{mag} expected for the cooling of an ensemble of antiferromagnetic spin-1/2 dimers from a paramagnetic phase, where there are four thermally accessible spin-states, to a temperature at which each dimer adopts a singlet state.

The isentropes of $Cu(pyz)(gly)ClO_4$ [Fig. 3.3(a), solid lines] are extracted from constant entropy cuts through the $S_{\mathrm{mag}}(T)$ curves calculated from the constant H heat capacity measurements. Two field-induced minima are evident in the isentropes that start from initial temperatures T_0 below ≈ 1.5 K. These features become more pronounced as T_0 is lowered further and, in the low T limit, these minima mark the approximate positions of the two quantum critical points (QCPs); that is, the locations of the phase boundaries as they are anticipated to occur at $T = 0$. The two dips in the isentropes owe their origin to the competition of magnetic phases, and thus the relatively high-spin entropy, that occurs at each boundary to the BEC phase; i.e. during an adiabatic field sweep (where S_{mag} must remain constant) the sample temperature is reduced as H approaches each phase boundary so as to prevent the material from entering a region of high spin-entropy.

For applied magnetic fields $H > H_{c2}$ the constant S_{mag} contours tend towards a linear dependence on H. This behaviour is analogous to the form of the isentropes calculated for a paramagnetic spin-ensemble, which are linear across the full $H-T$ plane [Fig. 3.4(d)] [83]. The paramagnetic model is a reasonable approximation to $Cu(pyz)(gly)ClO_4$ for $H \geq H_{c2}$ since the Zeeman energy at these vales of the applied field dominates all other terms in the spin Hamiltonian. Thus, the partition function and spin-entropy become closely modelled by a function of H/T.

The H dependence of spin-entropy is investigated by following S_{mag} along isotherms in the $H-T$ plane. These constant T cuts are linearly interpolated to evenly spaced $\mu_0 \Delta H = 0.25$ T intervals and smoothed with a low-pass digital filter in MATLAB, which averages the isothermal spin-entropy curves with a five-point moving-window function. These interpolated data are numerically differentiated as a function of H and smoothed again, as above, to determine $(\partial S_{\mathrm{mag}}/\partial H)_T$. The bright red and blue regions of Fig. 3.3(a) depict the regions of the $H-T$ plane where there is a strong field dependence to the spin-entropy (or where the isentropes have a steep gradient) and thus show where a sample is expected to undergo powerful MCE during an adiabatic H sweep (Eq. 1.14). The zones of large $|(\partial S_{\mathrm{mag}}/\partial H)_T|$ are in fact coincident with the $H-T$ range over which the MCE was inferred from

the pulsed-field magnetometry data.

3.3.3 Magnetocaloric effect measurements

Magnetocaloric effect (MCE) measurements monitor the temperature of a single-crystal sample of Cu(pyz)(gly)ClO_4 with a four-wire ac magnetoresistance measurement of a calibrated bare-chip Cernox™ thermometer that is directly attached to the sample. In these experiments, a rapidly changing magnetic field is provided by the capacitor-driven short-pulse (SP) or generator-driven long-pulse (LP) magnet at NHMFL (Los Alamos). While the measurements made with each pulsed-field system may have a different degree of adiabaticity to each other, and to the SP magnetometry measurements displayed in Fig. 3.3, the large $(\partial S_{\rm mag}/\partial H)_T$ of this material and Eq. 1.14 together imply that any experiment that departs from isothermal conditions ought to exhibit a finite MCE.

For measurements performed with the SP magnet, the field evolution of the Cernox™ temperature $T_{\rm Cer}$ is recorded on decreasing H [Fig. 3.5(a)] and these traces exhibits two features that resemble the form of the experimentally determined isentropes of Cu(pyz)(gly)ClO_4. Firstly, a kink (or minimum) is observed near $\mu_0 H \approx 2$ T (dark blue arrows). QMC simulations of networks of spin-dimers with interdimer spin-exchange interactions in two-spatial dimensions [88] predict that a rapid increase $\Gamma = T^{-1}(\partial T/\partial H)$ occurs at two stages during an adiabatic H sweep, once when the applied field is sufficient for triplons to first condense and again once the number of $S = 1$ bosons saturates. The low-field kink in the measured data is concurrent with a change in sign in the measured parameter $\Gamma = T_{\rm Cer}^{-1}(\partial T_{\rm Cer}/\partial H)$, as determined by a peak in $\mathrm{d}\Gamma/\mathrm{d}H$ [Fig. 3.5(b)], and this is therefore taken as the estimate for $H_{\rm c1}$. A second feature of $T_{\rm Cer}(H)$ measurements is that a linear response is recorded for applied magnetic fields in excess of $\mu_0 H \approx 5.5$ T. This is indicative of a field and temperature regime where $S_{\rm mag}$ is approximately governed by a function of H/T, as is determined to be the case for Cu(pyz)(gly)ClO_4 from an analysis of the isentropes in the spin-polarized phase (see above). While the measured change in behaviour of $T_{\rm Cer}$ around 5.5 T is too subtle to induce resolvable peaks in $\mathrm{d}\Gamma/\mathrm{d}H$, the position of the upper phase boundary is determined from the point at which a linear fit to the $T_{\rm Cer}(H)$ traces for $\mu_0 H \geq 7$ T departs the measured data [Fig. 3.5(a), blue lines]. The linear fit models the data to an accuracy of $\pm 0.3\%$ over the fitted temperature range and $H_{\rm c2}$ is estimated from the low-field point at which the linear fit and measured data diverge by more than 0.3% (light blue arrows).

For MCE measurements performed with the LP magnet, limiting the applied field sweep rate $\mu_0|\mathrm{d}H/\mathrm{d}t|$ to approximately 100 Ts^{-1} is found to increase the sensi-

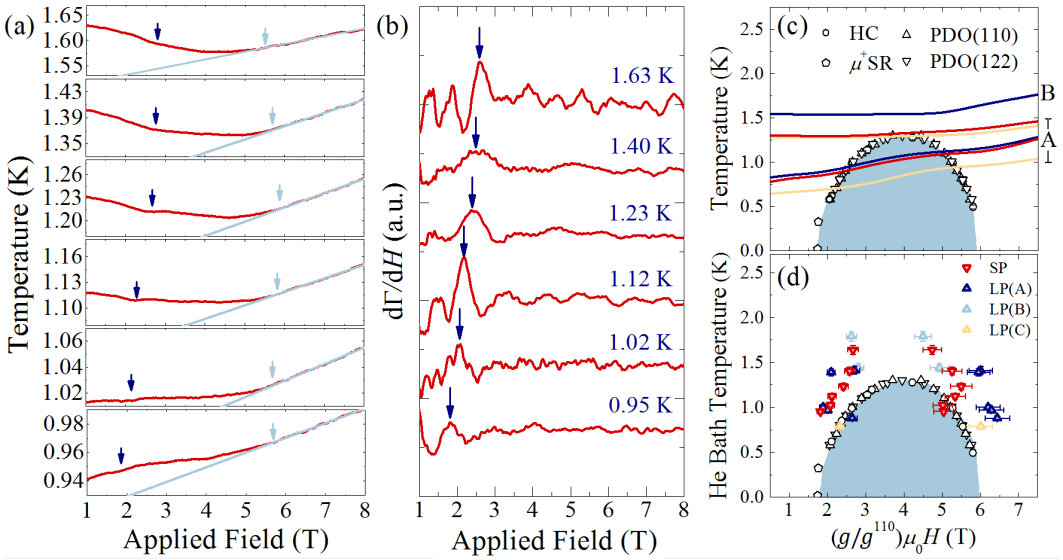

Figure 3.5: The field evolution of: **(a)** the Cernox™ temperature; and **(b)** dΓ/dH (red lines), for MCE measurements performed with the capacitor-driven SP magnet recorded on the field down sweeps. In panel (a), data for $\mu_0 H \geq 7$ T are fitted to straight line (pale blue). Arrows mark estimates of H_{c1} (dark blue) and H_{c2} (pale blue), respectively (see text). **(c)** Field evolution of the Cernox™ temperature (lines) for MCE measurements utilizing the generator-driven LP magnet. Data are labelled by the pulse profile from Fig. 2.3(b) and are superimposed on the published [74] quasistatic measurements of the BEC phase boundary. (**d**) Critical fields from the MCE measurements (triangles) plotted as a function of the initial He bath temperature; phase diagram from panel (c) repeated here.

tivity of the Cernox™ thermometer to changes in the sample T compared to the SP experiments. Minima develop at H_{c1} and H_{c2} in the LP $T_{Cer}(H)$ traces [Fig. 3.5(c)] and, furthermore, these features become more prominent as the initial sample temperature is lowered, which suggests that the features of the $T_{Cer}(H)$ derive from changes in the sample temperature. The critical fields determined from the SP and LP MCE experiments are plotted as a function of the initial He bath temperature T_0 in Fig. 3.5(d) (triangles), where both H_{c1} and H_{c2} in the LP experiments are extracted from peaks in dΓ/dH (Fig. 3.6). The phase boundaries extracted from the pulsed-field MCE measurements tend to follow the form of the extended dome as per the case of Fig. 3.2(a). This supports the conclusion that a MCE occurred during the pulsed-field magnetometry measurements, whereby the sample is cooled for $H > 0$ even when T_0 exceeds the maximum temperature of the BEC dome.

While the features observed in the $T_{Cer}(H)$ traces during the MCE experiments of Cu(pyz)(gly)ClO_4 are indicative of changes occurring in the sample T as H

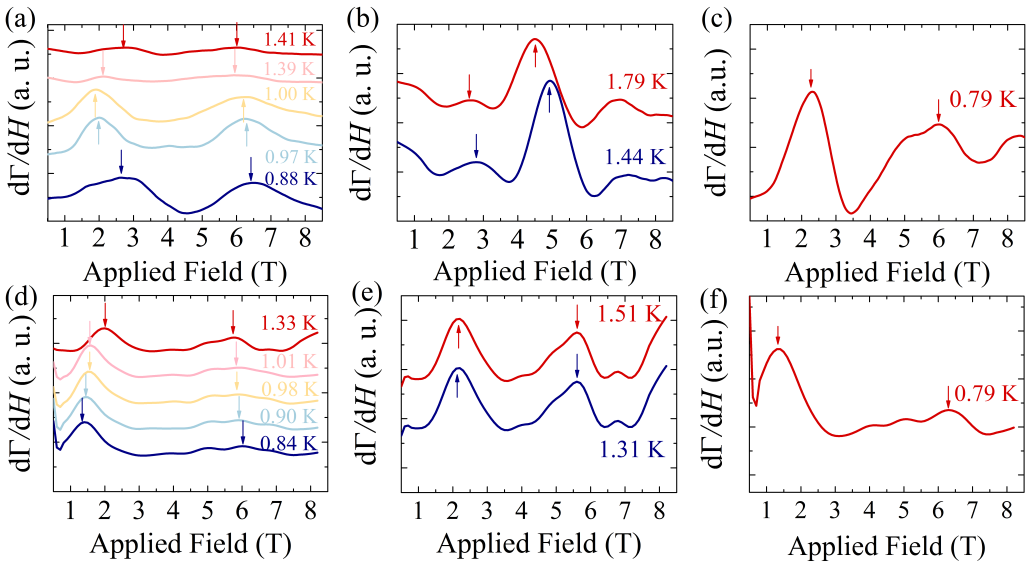

Figure 3.6: Measured values of dΓ/dH, plotted here in arbitrary units (a.u.), for MCE measurements performed with the LP magnet. Using the field profile labelling scheme defined in Fig. 2.3(b), MCE data shown here are measured with profiles: **(a)** A; **(b)** B; and **(c)** C, respectively. Phase transitions, indicated by peaks in dΓ/dH (arrows), are checked for consistency against maxima in dΓ/dH [panels **(d)**−**(f)**] that are found by differentiating the isentropes derived from the heat capacity for constant entropy contours beginning at initial temperatures similar to the MCE experiments. Each curve is labelled by the sample temperature at $H = 0$.

is swept, both the SP and LP MCE measurements are insensitive to the full magnitude of the MCE that is implied from the results of pulsed-field magnetometry and quasistatic heat capacity experiments. This limits the discussion of the MCE data to the features of $T_{\rm Cer}(H)$ for $H \approx H_{\rm c1,2}$ where the changes in Γ are greatest. The apparent increase in sensitivity of the LP measurements to the MCE in the sample (relative to the SP experiments) most likely results from a decrease in the amount of self heating generated by the Cernox™ in these comparatively slow H sweeps. If a future study was performed to improve the thermal coupling of the Cernox™ to a polymeric sample in a MCE measurement, the results of the MCE experiments performed on for Cu(pyz)(gly)ClO_4 suggest that the LP magnet at NHMFL would be an advantageous tool in this investigation. However, the form of the isentropes of Cu(pyz)(gly)ClO_4, and hence the full extent of the MCE, are derived from the results of quasistatic heat capacity experiments. It is therefore concluded that heat capacity measurements are likely to be an efficient means to investigate both the isothermal and adiabatic physics of quantum spin systems for which the full $H - T$ phase diagram is accessible with quasistatic applied magnetic fields.

3.4 Discussion

3.4.1 Section overview

To summarise the results of the last section, the magnetometry measurements of $Cu(pyz)(gly)ClO_4$ performed in pulsed magnetic fields are determined to be adiabatic, whereby a rapid change in H induces a strong and continuous MCE. The first part of this section introduces a heat capacity model that considers the thermal depopulation of bands of triplon states as a function of the sample temperature and this model is used in a discussion of the general form of the isentropes of $Cu(pyz)(gly)ClO_4$. The last two parts of this section discuss the T and H dependence of the experimental heat capacity that, respectively, provide evidence for a two-dimensional universal behaviour and zero-point fluctuations in this material.

3.4.2 A thermodynamic argument to explain the MCE

(a) Heat capacity and entropy for an ensemble of independent spin-dimers: For spin-1/2 dimers exhibiting an antiferromagnetic interdimer spin exchange interaction J, the energy ϵ of the four field dependent dimer spin-states are $\epsilon = 0, J$ and $J \pm \tilde{H}$; where $\tilde{H} = g\mu_B\mu_0 H$. Defining $\beta = (k_B T)^{-1}$, the partition function $\mathcal{Z}$ of an ensemble of dimers is given by the expression

$$\mathcal{Z} = 1 + e^{-\beta J}(1 + 2\cosh\beta\tilde{H}). \tag{3.2}$$

The internal energy, $U = -\partial \ln\mathcal{Z}/\partial\beta$, is then

$$U = e^{-\beta J}\left(\frac{J + 2J\cosh\beta\tilde{H} - 2\tilde{H}\sinh\beta\tilde{H}}{1 + 2\cosh\beta\tilde{H}}\right), \tag{3.3}$$

and an analytical expression for the heat capacity in constant H is derived using $C_{\rm mag} = (\mathrm{d}U/\mathrm{d}T)_H$. This yields the equation

$$\frac{C_{\rm mag}}{k_B\beta^2} = e^{-\beta J}\left(\frac{f(J,\tilde{H})}{1 + 2\cosh\beta\tilde{H}}\right) - e^{-2\beta J}\left(\frac{f(J,\tilde{H})}{1 + 2\cosh\beta\tilde{H}}\right)^2, \tag{3.4}$$

where $f(J,\tilde{H})$ is a function of J and $\tilde{H}$ given by

$$f(J,\tilde{H}) = J^2(1 + 2\cosh\beta\tilde{H}) - 4\tilde{H}J\sinh\beta\tilde{H} + 2\tilde{H}^2\cosh\beta\tilde{H}. \tag{3.5}$$

The heat capacity for an ensemble of independent dimers is determined by plotting Eqs. 3.4 and 3.5 at fixed $\tilde{H}$ [Fig. 3.7(a)]. In zero-field (dark blue line), $C_{\rm mag}$ displays a broad maximum at $T = 0.35J/k_B$, which initially evolves in applied fields $\tilde{H} > 0$ such that the amplitude and temperature of this peak are reduced (pale blue, grey and yellow traces). For $0.8 \leq \tilde{H}/J \leq 1$, two distinct peaks are apparent

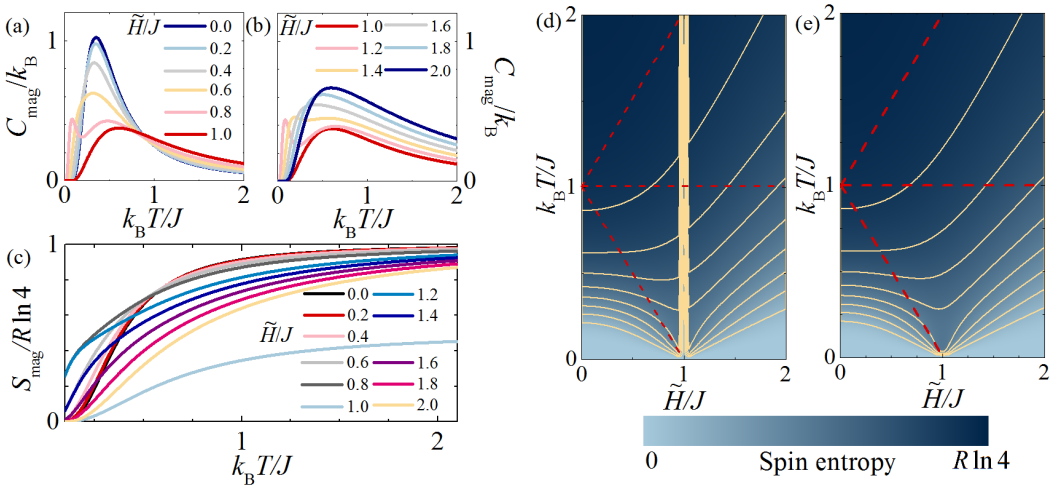

Figure 3.7: The simulated heat capacity per dimer (in units of k_B) for an ensemble of independent dimers with: **(a)** $\tilde{H}/J \leq 1$; and **(b)** $\tilde{H}/J \geq 1$. **(c)** S_{mag} (in units of $R\ln 4$ per dimer) vs. T for an ensemble of independent dimers with $0 \leq \tilde{H}/J \leq 2$. **(d)** Constant entropy contours (solid lines) in the $\tilde{H} - T$ plane for an ensemble of ideal independent dimers. The colourmap depicts the spin-entropy per dimer, while the red dashed lines show the field evolution of the $S = 1$ dimer energy levels. **(e)** The isentropes from panel (d) once the data at $\tilde{H}/J$ is excluded from the calculation.

in $C_{mag}(T)$: (i) a low T maximum (pink curve) that moves to progressively lower temperatures as $\tilde{H}/J \to 1$; and (ii) a broader maximum with a peak temperature that evolves steadily to higher T with increasing $\tilde{H}$. Feature (i) most likely results from the thermal depopulation of the lowest lying $S^z = +1$ dimer energy level to the $S = 0$ ground-state since this peak is no longer present in the heat capacity simulation performed at $\tilde{H} = J$ (red line) where these spin-states are degenerate, while feature (ii) arises from the thermal depopulation of higher triplon energy levels to the singlet ground-state as the separation of these energy levels is enhanced by the applied field.

For $\tilde{H} > J$ the $S^z = +1$ state crosses the $S = 0$ ground state and an energy gap between the lowest lying dimer spin-states re-opens once more, which gives rise to a small low-T anomaly in $C_{mag}(T)$ [Fig. 3.7(b), (pink line)]. This peak proceeds to move to higher T with increasing $\tilde{H}$, catching up to and then superimposing with the broader Schottky anomaly once $\tilde{H} > 1.5J$ (grey curve). For a further increase in $\tilde{H}$ the heat capacity continues to exhibit a single broad maximum, which exhibits a peak amplitude and occurs a temperature that both increase monotonically as the applied field is strengthened (pale blue and dark blue lines).

The spin-entropy in this model is investigated by integrating the simulated

C_{mag}/T curves via Eq. 1.12. For $\tilde{H} \neq J$ [Fig. 3.7(c)], the entropy change on cooling the system from the paramagnetic limit ($T > J/k_{\mathrm{B}}$) to zero-temperature is $R\ln 4$. In the specific case of $\tilde{H} = J$ the $S = 0$ and $S^z = +1$ dimer spin-states are degenerate. The total ΔS_{mag} released on cooling is therefore only $R\ln 4 - R\ln 2 = \frac{1}{2}R\ln 4$ (pale-blue curve). The simulated spin-entropy is plotted across the $\tilde{H} - T$ plane in Fig. 3.7(d) and, as the total spin-entropy per dimer at $\tilde{H} = J$ is only half of the full entropy that is accessible when $\tilde{H} \neq J$, this produces a delta-function type anomaly in the form of the isentropes (yellow lines). This sharp increase in the isentropes is an artefact of the idealized simulations and is unlikely to be observed in real materials, where small perturbations to the spin Hamiltonian will likely prevent a perfectly degenerate ground-state from forming. Constant entropy contours, which are likely to be more suitable for the analysis of experimental data, are considered by considering the spin-entropy across the applied fields ranges $\tilde{H} \leq 0.9J$ and $\tilde{H} \geq 1.1J$ separately and by interpolating S_{mag} over the intermediate region where $\tilde{H} \approx J$. The isentropes in this model [Fig. 3.7(e), solid lines] firstly indicate that a continuous MCE occurs for all $H > 0$; and secondly imply that the temperature of an ensemble of independent spin dimers is expected to initially cool towards a single minimum at $\tilde{H} = J$ for adiabatic applied magnetic field sweeps performed on samples with initial temperatures below $T_0 \approx 0.5J/k_{\mathrm{B}}$.

(b) Heat capacity and entropy for an ensemble of dimers with a two-dimensional triplon dispersion relation: For $Cu(pyz)(gly)ClO_4$, the measured separation of the two field-induced QCPs indicates $|J'|/J = 0.28$ (see above). A J'/J ratio greater than zero leads to a triplon dispersion relation in two-spatial dimensions (Eq. 3.1) and this predicted finite bandwidth of the excited dimer spin-states is accounted for the heat capacity simulation by applying the transformation $J \rightarrow J + 2J' \cos k_x \cos k_y$ to Eq. 3.3. In this model, the average internal energy $\langle U \rangle$ of an ensemble of exchange-coupled spin-dimers is estimated from

$$\langle U \rangle = \frac{\sum_{k_x} \sum_{k_y} U(k_x, k_y)\, \Delta k_x\, \Delta k_y}{\sum_{k_x} \sum_{k_y} \Delta k_x\, \Delta k_y}, \tag{3.6}$$

where each sum runs over 101 evenly spaced discrete values of k_x or k_y in the inclusive range $[-\pi, \pi]$ in order to sample the full band of excited states [Fig. 3.8(a)]. The heat capacity for an ensemble of exchange-coupled dimers with $J' = 0.28J$ is determined in MATLAB by numerically differentiating $C_{\mathrm{mag}} = \mathrm{d}\langle U \rangle / \mathrm{d}T$ at a fixed value of $\tilde{H}$.

The simulated $C_{\mathrm{mag}}(T)$ curves are compared to the measured heat capacity

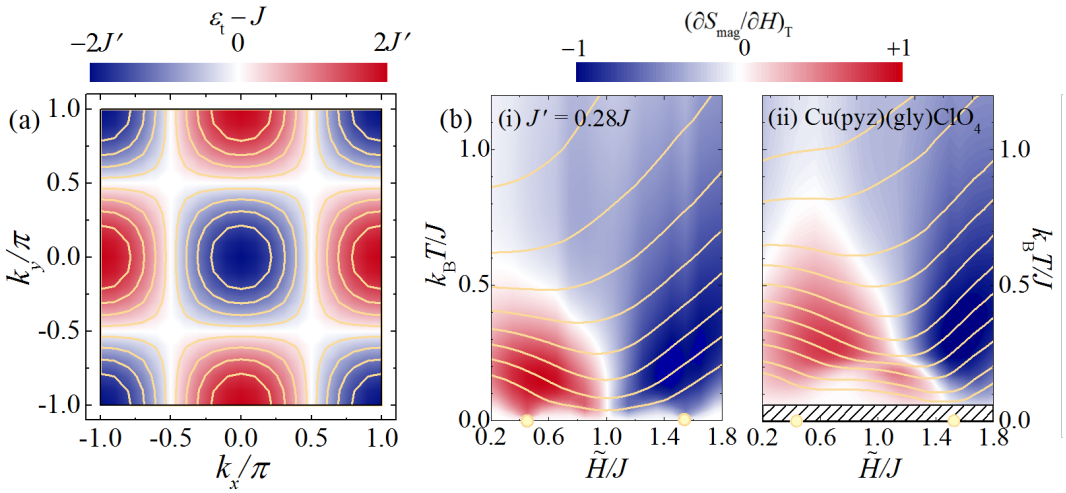

Figure 3.8: **(a)** The triplon dispersion relation $\epsilon_t(\mathbf{k}) - J$ in the $k_x - k_y$ plane (Eq. 3.1). The solid yellow lines are constant energy contours. **(b)** Isentropes in the $\tilde{H} - T$ plane (yellow lines) derived from: (i) the simulated heat capacity for a system of dimers with a triplon dispersion in two dimensions where $J' = 0.28J$; and (ii) the measured heat capacity Cu(pyz)(gly)ClO_4. In panels (i) and (ii), the colourmap depicts $(\partial S_{\rm mag}/\partial H)_T$ (in arbitrary units) and the yellow dots indicate the two QCPs. Data in panel (i) are interpolated over the critical region $\tilde{H} \approx J$, as in Fig. 3.7(e), while the hatched region in panel (ii) marks a zone where there is no heat capacity data available.

in Fig. 3.4(e). While the sharp peaks in the experimental data, which indicate the thermal cross over to the BEC phase, cannot be reproduced by the thermodynamic model, the smoothly-varying broad maxima exhibited by the simulated heat capacity traces share many features with the experimental data and are attributed to a series of Schottky anomalies resulting from the field induced splitting of bands of dimer spin-states. With $\tilde{H} \ll J$ [Fig. 3.4(e) red line] a maximum is evident in the simulated heat capacity at $T \approx 0.4J/k_B$. This is associated with the thermal depopulation of the triplon energy levels to a single ground state. The amplitude and temperature of this peak is diminished in increasing $\tilde{H}$ (pink), which is indicative of a reduction in the energy gap between the lowest lying triplon state and the singlet ground state as the applied magnetic field is strengthened. For $\tilde{H} \approx J$ (yellow) a low T shoulder in the calculated heat capacity develops. This feature, which is distinct from a broader maximum that is observed at higher temperatures at the same $\tilde{H}$, is credited to the thermal depopulation that occurs within the two lowest lying dimer spin-states. The higher temperature feature, on the other hand, most likely arises from changes in the thermal accessibility of higher energy triplon states. Once $\tilde{H}$ reaches, and then exceeds, $1.5J$ (pale and dark blue curves), the peak temperature

of the broad maximum tends towards a linear dependence of the applied field $\tilde{H}$. This behaviour occurs for $H > H_{c2}$ where the zero-field splitting of the dimer spin-states becomes decreasingly relevant compared to the Zeeman energy in the spin Hamiltonian, such that the magnetic heat capacity of the dimer system is similar to that of a paramagnetic ensemble of moments in an applied magnetic field.

The simulated $C_{mag}(T)$ traces at constant $\tilde{H}$ are integrated via Eq. 1.12 to model the spin-entropy in the $\tilde{H} - T$ plane [Fig. 3.8(b), panel (i)] and, as with the analysis in part (a), these curves exclude simulations performed at $\tilde{H} = J$. Regions of large $|(\partial S_{mag}/\partial \tilde{H})_T|$ extend out from each QCP (yellow dots) as is the case for the real spin system [panel (ii)]. These are the areas of the $\tilde{H} - T$ plane where a strong MCE is predicted and observed to occur. The simulated and measured isentropes together indicate that if the initial temperature $T_0 \approx J/k_B$ then no cooling effect is expected once H is swept adiabatically, but once T_0 is reduced below $\approx 0.5J/k_B$ prior to an adiabatic H sweep then cooling is immediately induced once $\tilde{H} > 0$ and not just in the vicinity of $H \approx H_{c1,2}$. A further similarity of the simulated and experimental isentropes of $Cu(pyz)(gly)ClO_4$ is that they together determine that a sample cools in an adiabatic experiment as H_{c2} is approached from the high-field side in decreasing $\tilde{H}$, a field regime that is often inaccessible for the measurement of inorganic BEC systems owing to the large energy scale of H_{c2} (e.g. Ref [52]).

The thermodynamic simulation does not, however, reproduce the two minima in isentropes of $Cu(pyz)(gly)ClO_4$, which are indicative of the effects spin correlations exhibited by the coordination compound that can, for instance, result in field induced symmetry breaking at H_{c1} [52]. One difference between the model and experimental data is that the initial negative gradient of the isentropes persists to higher T_0 values in panel (ii) than is predicted from simulation in panel (i). This suggests there are contributions to the measured heat capacity that cannot be accounted for by the semi-classical thermodynamic model, which might include the effects of spin-correlations or zero-point fluctuations (see below).

(c) Heat capacity for an ensemble of dimers with a three-dimensional triplon dispersion relation: Given the geometry of the likely interlayer spin-exchange pathways J'', which acts to couple spin-dimers in adjacent $[Cu(pyz)(gly)]^+$ sheets [Fig. 3.1(b), green lines], a three-dimensional triplon dispersion relation is considered in the heat capacity simulation by utilizing the transformation $J \rightarrow J + 2J' \cos k_x \cos k_y + 2J'' \cos(k_y/2) \cos(k_x/4 - k_z/4)$. In this model, the two critical fields (in units of energy) occur at $\tilde{H}_{c1,2} = J \mp 2(J' + J'')$. The three parameters J, J' and J'' cannot be determined uniquely from a measurement of the two QCPs.

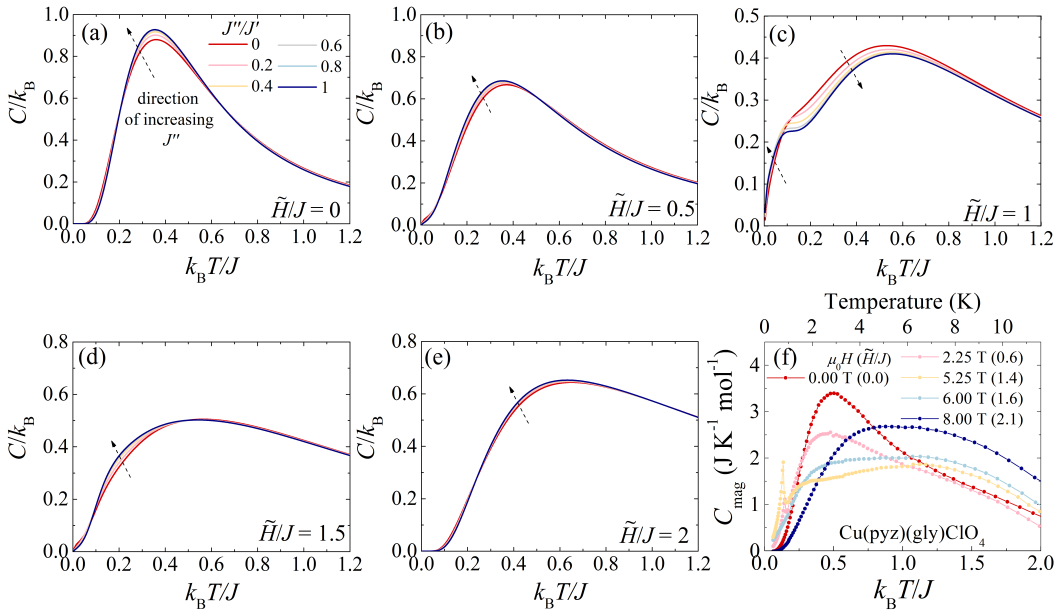

Figure 3.9: The simulated heat capacity for a network of exchange-coupled spin-dimers with a triplon dispersion in three-spatial dimensions for constant values of the applied magnetic field $\tilde{H}/J \leq$ equal to: **(a)** 0; **(b)** 0.5; **(c)** 1; **(d)** 1.5; and **(e)** 2. **(f)** The published [74] experimentally determined heat capacity of $Cu(pyz)(gly)ClO_4$, reproduced from Fig. 3.4(b).

Instead, this simulation first considers a material with $J' = 0.28J$ and $J'' = 0$, and then models the effects on the heat capacity when the ratio J''/J' is raised from 0 to 1, while the critical fields of the system remain fixed.

Each Cartesian component of the triplon wave vector $\mathbf{k} = (k_x, k_y, k_z)$ is considered at 31 evenly spaced values in the inclusive ranges $[-\pi, \pi]$ and the heat capacity is calculated from a modified version of Eq. 3.6 that sums over the three component wave vectors. For $\tilde{H} = 0$ [Fig. 3.9(a)] each simulated $C_{\text{mag}}(T)$ trace exhibits a broad maximum, where the effect of increasing J''/J' in the simulation is to push the temperature of this peak to smaller values of $k_{\text{B}}T/J$. Once $\tilde{H}$ reaches $0.5J$ [Fig. 3.9(b)], the energy gap from the spin-singlet to the first excited state is reduced and, consequently, the broad feature in the heat capacity is suppressed in amplitude and thermal energy. The effect of increasing J''/J' at this value of the applied field is qualitatively the same as the zero-field simulation.

At $\tilde{H} = J$ [Fig. 3.9(c)], the heat capacity of an ideal two-dimensional spin-dimer network ($J' = 0$, red curve) is predicted to display a broad maximum at high temperatures with a small shoulder at lower T. Introducing $J'' > 0$ acts to enhance the temperature of the broad maximum, which essentially distinguishes the

low T shoulder as an independent peak once $J'' \approx J'$ (blue curve). For calculations performed with $\tilde{H} \geq 1.5J$ [Fig. 3.9, panels (d) and (e)] the dependence of the simulated heat capacity on the ratio J''/J' is analogous to that observed in the calculations of $C_{\rm mag}(T)$ obtained for $\tilde{H} \leq 0.5$, whereby an increase in the relative strength of the interlayer coupling acts to slightly reduce the peak temperature of a single broad Schottky anomaly in the simulated heat capacity.

For heat capacity measurements of Cu(pyz)(gly)ClO_4 performed in applied fields in the range $1.4 \leq \tilde{H}/J \leq 1.6$ [e.g. Fig. 3.9(f), yellow points], the $C_{\rm mag}(T)$ curves exhibit a small shoulder that develops at temperature below the large Schottky anomaly. However, this feature is not so prominent so as to be resolvable as an identifiable separate peak. By comparison with the results of the $C_{\rm mag}(T)$ simulations at similar magnitudes of the applied fields, the occurrence of a small shoulder in the data is consistent with a relatively small value for the ratio J''/J' in Cu(pyz)(gly)ClO_4.

3.4.3 Two-dimensional universal behaviour

Plotting the magnetic heat capacity of Cu(pyz)(gly)ClO_4 on a logarithmic scale [Figs. 3.10(a) and (b)], a power law dependence of $C_{\rm mag} \propto T^n$ is observed when H is approximately equal to $H_{\rm c1}$ and $H_{\rm c2}$ (yellow points in each figure). A universal critical exponent n is expected for the heat capacity measurements of BEC systems performed at $H = H_{\rm c1,2}$, where $n = d/2$ and d is the spatial-dimensionality of the spin-exchange network [52,95]. For reliable exponents to be extracted from $C_{\rm mag}(T)$, the data must be modelled in a temperature range for which the upper bound is less than 40% of the maximum temperature of the BEC phase [146]; and the lower bound exceeds the energy scale of uniaxial symmetry breaking perturbations in the spin Hamiltonian [52]. As no symmetry breaking terms are evident in the thermodynamic properties of Cu(pyz)(gly)ClO_4 for experimental investigations above 400 mK, linear fits are made to the $\log C_{\rm mag}$ vs. $\log T$ data of Cu(pyz)(gly)ClO_4 for $0.4 \leq T \leq 0.56$ K to reveal $n = 2.13(2)$ and $0.99(2)$ at $H_{\rm c1}$ and $H_{\rm c2}$, respectively.

The exponent of $n = 0.99(2)$ close to $H_{\rm c2}$ is consistent with $d = 2$, which is indicative of two-dimensional universal behaviour within this quantum spin network. This value for the exponent agrees with the analysis of the structure of this compound (above) that concluded that there is likely to be a large spatial-delocalization of spin-density within individual $[Cu(pyz)(gly)]^+$ layers of the material. However, it is important to stress that the bulk thermodynamic data presented in this chapter would not be consistent with interlayer interactions that are precisely zero. Spin-networks comprised of isolated layers of exchange-coupled antiferromagnetic

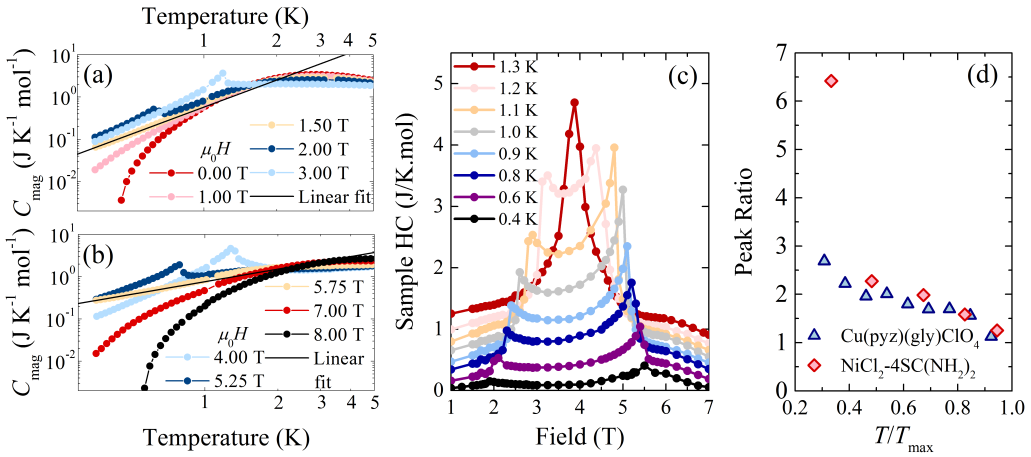

Figure 3.10: Logarithmic plot of the published [74] heat capacity as a function of temperature (points) for quasistatic applied magnetic fields: **(a)** $\mu_0 H \leq 3$ T; and **(b)** $\mu_0 H \geq 4$ T. Solid lines are a linear fit to the data for applied fields close to each QCP. The lattice contribution to the measurement has been subtracted. **(c)** The heat capacity vs. applied magnetic field $\mu_0 H$ exhibits maxima at $H = H_{c1,2}$. The peak amplitude at the low-field QCP is reduced relative that observed at high-field QCP at the same temperature. The T along each isotherm is stable to within ≈ 30 mK. **(d)** The ratio of the high-field to low-field peaks in the measured heat capacity as a function of the sample temperature (normalized to the maximum temperature of the BEC phase T_{max}) as derived from panel (c) for Cu(pyz)(gly)ClO_4 ($T_{max} = 1.3$ K) (triangles) and from the published [52,94] heat capacity of the related BEC material $NiCl_2$-4SC$(NH_2)_2$ ($T_{max} = 1.2$ K [94]) (diamonds).

spin-dimers with uniaxial (or circular) symmetry are anticipated to adopt a low-temperature Berezinskii-Kosterlitz-Thouless (BKT) phase [17, 18, 145] and crossing a BKT phase boundary is not predicted to induce observable signatures in thermodynamic quantities including heat capacity and differential susceptibility. For Cu(pyz)(gly)ClO_4, measured peaks in both $C_{mag}(T)$ and dM/dH mark the boundary to a distinct magnetic phase that forms within a dome in the $H-T$ plane, which necessarily indicates that the interlayer spin-exchange interactions must be finite in this compound. Nevertheless, the $n = 0.99(2)$ heat capacity exponent at H_{c2} corroborates the approximate two-dimensional character of the material because it is well below the $n = 1.5$ expected for three-dimensional (3D) systems, where theoretical predictions derived from an analytical finite-scaling analysis of a 3D quantum critical systems suggest that this power law ought to be obeyed [148].

The separate heat capacity exponent of $n \approx 2$ measured at H_{c1} requires further interpretation within the two-dimensional model, and the thermodynamic properties of related spin-gap materials offers one possible explanation. For in-

stance, the measured magnetic Grüneisen parameter Γ of the spin-ladder compound $(C_4H_{12}N)_4CuCl_4$ exhibits a critical (linear) scaling with temperature at H_{c2} for measurements in the range $0.1 < k_B T/J < 0.4$ (where J is the rung coupling constant), while Γ vs. T only tends towards a linear response H_{c1} for sample temperatures below $\approx 0.1 J/k_B$ [147]. Given that an identical scaling of the thermodynamic quantities of exchange-coupled dimer systems can occur at H_{c1} and H_{c2}, but only when measured over separate T windows, one avenue for future investigations of $Cu(pyz)(gly)ClO_4$ could be to follow $C_{mag}(T)$ at $H_{c1,2}$ down to dilution refrigerator temperatures to determine whether the two exponents are equal at lower T.

An alternative strategy to explain the value of the H_{c1} exponent is to consider the effect that symmetry breaking perturbations in the spin Hamiltonian might have on the expected values of n. One such interaction, that cannot be ruled out from the structure alone [74], is a Dzyaloshinskii-Moriya (DM) interaction. While there is no evidence for a DM interaction from the magnetometry measurements, if their energy scale of a DM term is indeed greater than 400 mK then this would induce a cross over from a BEC phase (i.e. an XY spin model) to an Ising universality class at sufficiently low temperatures. For Ising systems, the critical exponent in heat capacity is expected to be $n = d$, in contrast to $n = d/2$ for an XY model. The measured exponent of $n = 2.13(2)$ at H_{c1}, if it were indeed interpreted in the Ising model, would be consistent with a two-dimensional spin network. However this conclusion would be difficult to reconcile with the result for $n \approx 1$ at H_{c2} and so this model is not appealing as a means to unambiguously explain the discrepancy in the measured exponents. An independent argument, which might account for the difference in n at $H_{c1,2}$, is that zero-point fluctuations are a significant perturbation to the quantum spin system close to H_{c1}, the QCP at the boundary between the BEC and quantum disordered phase, but are less important at H_{c2} for heat capacity measurements at the same temperature.

3.4.4 Evidence for zero-point fluctuations

In an extension of the published C_p measurements of $Cu(pyz)(gly)ClO_4$, additional experiments are performed in this work to determine the applied magnetic field dependence of the heat capacity for quasistatic $\mu_0 H \leq 7$ T. Isothermal cuts through the results of heat capacity measurements performed with constant H [Fig. 3.10 (b)] exhibit maxima that clearly mark each of the two critical fields. However, for a particular isotherm, the amplitude of the heat capacity anomaly at H_{c1} is smaller relative to the size of the peak at H_{c2}. The asymmetry in ratios of the peak heights for $Cu(pyz)(gly)ClO_4$ [Fig. 3.10(d), triangles], which is also evident in the differ-

ential susceptibility measurements [Figs. 3.2(a)−(c)], becomes more pronounced as the sample temperature is reduced. This behaviour is analogous to the results of measurements and QMC simulations of the heat capacity of the related $S = 1$ BEC polymeric material, $NiCl_2$-4SC$(NH_2)_2$ [94] [Fig. 3.10(d), diamonds]. In this Ni^{2+} system, the small amplitude of the H_{C1} heat capacity anomaly is explained by the proximity of this feature to the low-field quantum disordered region, where zero-point fluctuations (ZPFs) are predicted to renormalize the effective mass of bosonic excitations of the system. This in turn reduces the heat capacity of the material relative to measurements collected at the same temperature for $H \approx H_{C2}$, which are performed close to the spin-polarized phase where the magnetization is a conserved quantity [94].

Isothermal powder μ^+SR experiments of Cu(pyz)(gly)ClO_4, which are performed at 20 and 325 mK, indicate that there is almost no discernible change in the root-mean-squared gaussian distribution of the internal magnetic flux at interstitial lattice sites for measurements performed in a range of applied magnetic fields inclusive of $H = H_{C1}$ (see Ref. [74] and the supporting information therein). This implies that, for sample temperatures of the order $\approx$ 100 mK, the thermal fluctuations of the spin quanta are already sufficiently suppressed to the extent that a further decrease in the sample temperature by an order of magnitude has little impact on the time-averaged orientations of the Cu^{2+} moments. This suggests that the asymmetry observed in the H dependence of the heat capacity at 400 mK is attributable (in part) to quantum fluctuations of the spin moments for $H \approx H_{C1}$. The ZPFs fluctuations of the system close to H_{C1} act to increase S_{mag} and therefore the decrease the ability of the Cu^{2+} moments to reorganize in order to absorb a small amount of thermal energy in a heat capacity experiment. Meanwhile, it is likely the suppression of quantum fluctuations in the spin-polarized phase is responsible for the relatively large heat capacity anomaly at $H \approx H_{C2}$.

3.5 Conclusions

The exchange-coupled spin-dimer network Cu(pyz)(gly)ClO_4 exhibits a strong and continuous MCE in rapidly changing applied magnetic fields. An analysis of the isentropes of the material, derived from the published [74] heat capacity measurements, suggests that the initial sample temperature is reduced by as much as 37% during an adiabatic H sweep. Accounting for a MCE removes the need to invoke separate magnetic phases to explain the results of pulsed-field magnetometry experiments, which are concluded to be sensitive to the same magnetic phase as the

published [74] magnetometry, heat capacity and μ^+SR measurements performed in quasistatic H.

The results of MCE experiments performed to directly monitor the sample temperature in rapidly changing H are consistent with the nature of the MCE implied by the isentropes of the system. Limiting the pulsed-field sweep rate $\mu_0|\mathrm{d}H/\mathrm{d}t|$ to approximately 100 Ts^{-1} by using the LP magnet at NHMFL, Los Alamos, is found to increase the coupling of the Cernox™ thermometer to the sample T relative to the SP measurements. However, both the SP and LP MCE measurements fell short of unambiguously following the sample T as a function of H. For future investigations of the MCE in spin-gapped systems that have BEC phase diagrams spanning an $H-T$ range that is fully accessible with quasistatic applied magnetic fields, then the work in this project suggests that it is likely that heat capacity measurements will provide an efficient technique for the determination the isentropes of the system and hence the full extent of the MCE.

A thermodynamic model of the heat capacity predicts that a MCE occurs in Cu(pyz)(gly)ClO_4, and therefore related spin-gapped materials, for all $H > 0$. Two further results from this model are: (i) the temperature of a broad Schottky anomaly peak in the zero-field heat capacity occurs at approximately $T = 0.35J/k_\mathrm{B}$; and (ii) a MCE acts to cool a spin-dimer material immediately once $H > 0$ for experiments performed at initial temperatures less than $\approx 0.5J/k_\mathrm{B}$. In summary, while conductive materials are known to exhibit changes in the sample temperature in rapidly changing H owing to the effects of eddy current heating (see, for instance, Ref. [113]), the experimental and theoretical results of this work suggest that the evolution of the sample T is also likely to be of general importance for the measurements of electrically-insulating materials in pulsed magnetic fields.

The published [74] results of a μ^+SR study of Cu(pyz)(gly)ClO_4 imply that this system is close to the $T = 0$ limit for experiments performed at temperatures in the ≈ 100 mK range. The measured asymmetry in the H dependence of the heat capacity along isotherms with $T \approx 400$ mK therefore suggests that ZPFs manipulate the spin-entropy for $H \approx H_{\mathrm{C}1}$. Different critical exponents are found from the T dependence of the published [74] heat capacity when $H \approx H_{\mathrm{C}1,2}$. The linear evolution of $C_\mathrm{mag}(T)$ at $H \approx H_{\mathrm{C}2}$ is indicative of two-dimensional universal behaviour within this quantum spin system. This result is consistent with an analysis of the published structure of Cu(pyz)(gly)ClO_4, which implies that spin-density is likely to be delocalized most effectively within individual $[\mathrm{Cu(pyz)(gly)}]^+$ sheets.

Chapter 4

Bond disorder and single-ion physics of a spin $S = 1$ kagome lattice

Single-crystal x-ray diffraction measurements of $[H_2F]_2[NiF_2(3\text{-Fpy})_4]_3[SbF_6]_2$ (3-Fpy = 3-fluoropyridine) at 100 K indicate that the Ni^{2+} ions of this polymeric compound reside on the vertices of a two-dimensional kagome lattice, wherein the spin $S = 1$ ions are linked via Ni-F$\cdots$H-F-H$\cdots$F-Ni hydrogen bonded bridges. However, a positional disorder of the H_2F^+ moieties within the kagome planes suppresses the Ni-Ni spin-exchange interactions and powder muon spin-relaxation measurements provide no evidence for long-range magnetic order at temperatures above 19 mK. Polycrystalline electron spin-resonance (ESR), magnetometry and heat capacity experiments each give rise to features that are largely accounted for by the single-ion physics of independent $S = 1$ ions, which exhibit a uniaxial and rhombohedral anisotropy of $D/k_B = 8.3(4)$ K and $E/k_B = 1.2(3)$ K respectively. Some of the results of this chapter, and the publication [75] relating to this work, may guide future investigations that aim to extract estimates of D from the thermodynamic measurements of related compounds when limited to powdered samples.

4.1 Introduction

Long-range magnetic order is an emergent property of spin systems that is contingent upon there being a delicate balance of several microscopic and macroscopic factors.

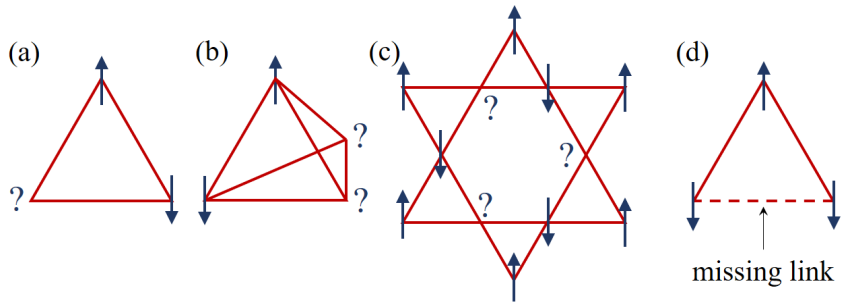

Figure 4.1: Antiferromagnetic spin-exchange interactions (red lines) between spins (blue arrows) arranged on: **(a)** triangular; **(b)** tetrahedral; or **(c)** kagome lattices, results a geometric frustration of the magnetic interactions and multiple degenerate ground states. For a recent overview of the expected spin configurations of frustrated lattices see, for instance, Ref. [159]. **(d)** A structural disorder of these systems often leads to missing linkages between moments (e.g. the dashed line), which relieves the frustration of the spin system.

For instance, the results of quantum Monte-Carlo (QMC) simulations [68] and series expansions [149] performed to investigate the magnetic properties of linear-chain and square-lattice spin $S = 1$ antiferromagnets, respectively, suggest that the precise nature of the ground spin-state in these systems depends upon: (i) the sign of the uniaxial single-ion anisotropy D; and (ii) the relative strength of D compared to the Heisenberg exchange interactions of the spin networks. A current trend of condensed matter research aims to investigate two further structural properties of solid-state spin systems that may also manipulate the magnetic degrees of freedom of a material. These are, in turn, a positional disorder of the underlying lattice; and a geometric frustration of the spin-exchange interactions in the material [150–154].

Taken independently, structural disorder and geometric frustration generally act to suppress the onset of long-range magnetic order in condensed matter systems. Crystalline materials with an inherent and random structural disorder tend to lack the periodicity of superexchange pathways that are typically necessary to support a magnetically ordered ground state. Geometric frustration on the other hand occurs in magnetic materials when there are multiple antiferromagnetic spin-exchange interactions that cannot be simultaneously satisfied, and systems of this type are predicted to exhibit a low-temperature spin liquid state [155–159]; that is, a highly correlated magnetic state in which fluctuations of the spin quanta persist even as $T \rightarrow 0$ [157]. Triangular, kagome or tetrahedral networks [Fig. 4.1, panels (a)−(c)] are just three paradigmatic examples of frustrated magnetic systems that may result in a multitude of degenerate ground spin-states. Here, each system

incorporates antiferromagnetic Heisenberg spin-exchange interactions (red lines) between spin moments (blue arrows) and the Coulomb energy of a particular bond is minimized if the neighbouring moments are collinear and antiparallel. However, due to the geometrical constraints of these lattices there is no net energy gain for a spin to be orientated up or a down at each of the sites labelled with a question mark. When disorder is introduced to frustrated antiferromagnets, broken or missing superexchange pathways [e.g. Fig. 4.1(d), dashed line] typically act to relieve geometric frustration, giving rise to thermodynamically stable magnetic ground-states. The results of mean-field theory calculations performed on an Ising kagome lattice suggest that, in this case and therefore related systems, a small amount of structural disorder in frustrated lattices may also give rise to a low temperature spin-glass state [160], whereby the orientations of moments become "frozen" into random directions and the spin dynamics of the system are considerably slowed (e.g. Refs. [29, 161]).

The scope of this chapter is to examine the interdependence of the structural and magnetic properties of $[H_2F]_2[NiF_2(3\text{-Fpy})_4]_3[SbF_6]_2$ (3-Fpy = 3-fluoropyridine). A refinement of the structure of this compound from the results of single-crystal x-ray diffraction measurements at 100 K (see below) demonstrates that the Ni^{2+} ions are organized into a perfectly two-dimensional kagome lattice, wherein charge-assisted Ni-F$\cdots$H-F-H$\cdots$F-Ni bonds are found to link coplanar spin-centres together, and this material was originally synthesized to explore the physics of an $S = 1$ kagome system. However, there is a structural disorder of the positions of the H_2F^+ moieties within the kagome layers. The experimental and theoretical investigations of the magnetic properties of $[H_2F]_2[NiF_2(3\text{-Fpy})_4]_3[SbF_6]_2$ above 19 mK presented in this chapter imply that this positional disorder acts to suppress, rather than enhance, the onset of bulk magnetic order or spin-glass behaviour in this kagome spin-system.

$[H_2F]_2[NiF_2(3\text{-Fpy})_4]_3[SbF_6]_2$ is the product of an ongoing effort to incorporate poly-HF moieties (e.g. HF_2^-, $H_2F_3^-$ and $H_3F_4^-$) into quantum spin systems and it falls into the larger class of coordination polymers that employ charge-assisted hydrogen-bonds (e.g. F$\cdots$H-F, F$\cdots$O-H and O$\cdots$O-H) to form structurally stable polymeric magnets. Two examples of coordination compounds that utilize hydrogen fluoride derivates to maintain a rigid lattice are the mononuclear species [Cu(di-2-pyridyl-methanediol)$_2$]-$(H_2F_3)_2$ [162]; and the quasi-two-dimensional Heisenberg $S = 1/2$ square lattice AFM $[Cu(HF_2)(pyz)_2]SbF_6$ (see Chapter 5 or Refs. [59, 76]).

In the specific cases of polymeric complexes containing transition metal ions with unpaired electrons in d orbitals that delocalize spin-density towards a hydrogen

bond, these charge-assisted linkages oftentimes directly facilitate superexchange interactions. $CuF_2(H_2O)_2(pyz)$ is one such system that, at ambient pressure, contains Cu-pyz-Cu chains, which are linked to four others via Cu-F$\cdots$H-O-Cu bridges [164]. The Jahn-Teller axis of each $CuN_2O_2F_2$ octahedra is orientated along the pyz chain direction and spin-density is therefore delocalized along the hydrogen bonded pathways that mediate a spin-exchange interaction $J/k_{\mathrm{B}} \approx 12$ K [45, 70, 164]. There are several Ni-F$\cdots$H$\cdots$F-Ni chain compounds, including $[Ni(HF_2)(pyz)_2]SbF_6$ [47], $[Ni(HF_2)(pyz)_2]PF_6$ [47] and $[Ni(HF_2)(3\text{-}Clpy)_4]BF_4$ [66], which also exhibit antiferromagnetic interactions along the hydrogen bonded bridges. The respective intrachain spin-exchange interactions (J/k_{B}) of these three compounds are 13.3 K (see Chapter 5 and the related work, Ref. [77]), 6.8 K [47] and 4.9 K [66]. These finite interactions result from a delocalization of spin-density along the chain directions owing to an unpaired electron in each Ni^{2+} d_{z^2} orbital, whilst the range of J values is dictated (in part) by a difference in the stretching and bending of the constituent HF_2^- ions within the chains of each material [47, 66].

In the present work, the results of powder muon spin-relaxation experiments of $[H_2F]_2[NiF_2(3\text{-}Fpy)_4]_3[SbF_6]_2$ indicate that this system lacks long-range magnetic order for sample temperatures above 19 mK. The observations of powder ESR measurements for $T \geq 3.3$ K, in addition to polycrystalline magnetometry and heat capacity experiments performed at $T \geq 0.4$ K, corroborate the weak nature of the spin-exchange interactions in this compound and the results of these investigations are largely accounted for with the single-ion spin Hamiltonian

$$\hat{\mathcal{H}} = D(\hat{S}^z)^2 + E[(\hat{S}^x)^2 - (\hat{S}^y)^2] + \mu_0\mu_{\mathrm{B}}\mathbf{H}^{\mathrm{T}}\boldsymbol{g}\mathbf{S}. \tag{4.1}$$

Here, $\mathbf{S} = (\hat{S}^x, \hat{S}^y, \hat{S}^z)^{\mathrm{T}}$ is a column vector of dimensionless $S = 1$ operators [23]; D and E are the uniaxial and rhombohedral single-ion anisotropy terms respectively, which lift the degeneracy of the free-ion spin-states [165]; $\boldsymbol{g} = \mathrm{diag}(g_{xy}, g_{xy}, g_z)$ is a tensor of anisotropic g-factors; and $\mathbf{H}$ is an applied magnetic field. As the experimental investigations of the magnetic properties of $[H_2F]_2[NiF_2(3\text{-}Fpy)_4]_3[SbF_6]_2$ are limited to polycrystalline samples, in the analysis and discussion of the experimental results of this chapter (below) attention is paid to some of the general results of this work that may be applicable in future experimental investigations that aim to determine the strength of the single-ion anisotropy of powdered $S = 1$ materials.

4.2 Experimental Details

4.2.1 Sample preparation

$[H_2F]_2[NiF_2(3\text{-}Fpy)_4]_3[SbF_6]_2$ samples are prepared by J. L. Manson, P. M. Spurgeon and J. A. Villa at Eastern Washington University (USA). The synthesis procedure and the related infrared spectroscopic measurements are detailed in Ref. [75].

4.2.2 X-ray diffraction

X-ray diffraction measurements are by performed and analysed by C. Campana and B. Noll at Bruker AXS Inc., Madison (USA). A $355 \times 237 \times 146$ μm single-crystal sample is mounted in the $\lambda = 0.71073$ Å monochromatic beam of a Bruker™ APEX II diffractometer. For experiments performed at 100 K, a total of 300 065 Bragg reflections are generated, which are used to identify the material's unit cell and space group with the Bruker™ APEX II and SAINT [166] software packages. The intensity of 4281 symmetry equivalent Bragg reflections are integrated and the positions of the Ni, N, C, F and Sb atoms in the unit cell are refined within the $R\bar{3}$ space group against the intensities of the scattering peaks using the SHELXT-2914 [167] and SHELXL-2014/7 [168] analysis software. The absorption effects of the sample are corrected for using the multiscan method in the SADABS package [169].

4.2.3 Muon spin-relaxation

Zero-field powder muon spin-relaxation spectra of $[H_2F]_2[NiF_2(3\text{-}Fpy)_4]_3[SbF_6]_2$ are recorded for sample temperatures in the range $0.019 \leq T \leq 10$ K at the Swiss Muon Source (SμS). This work was performed and analysed by T. Lancaster, F. Xiao, and R. C. Williams at Durham University (UK); C. Baines at SμS (Switzerland); F. L. Pratt at the ISIS Pulsed Muon Facility RAL (UK); and S. J. Blundell at the University of Oxford (UK). The measurements employed both the Low Temperature Facility (LTF) and General Purpose Surface-Muon (GPS) spectrometers to access the full temperature range. In each experiment, the polymeric sample is secured inside an Ag foil envelope, which has a thickness 12.5 μm, and the sample is mounted on an Ag plate or Ag fork for the LTF or GPS measurements respectively.

4.2.4 Electron spin-resonance

Transmission ESR spectra are recorded and analysed by J. Liu (University of Oxford, UK) using the homodyne high-frequency spectrometer at NHMFL, Tallahassee

(USA). Microwaves with frequencies in the range $203.2 \leq \nu \leq 633.6$ GHz are incident upon a powdered sample that is loosely restrained in a PTFE sample holder with KBr. Measurements are performed for quasistatic applied fields $\mu_0 H \leq 14$ T, while the sample T is controlled in the range $3.3 \leq T \leq 100$ K with a ^{4}He cryostat.

4.2.5 Pulsed-field and quasistatic magnetometry

(a) Compensation coil extraction magnetometry: Pulsed-field measurements of the differential susceptibility $\mathrm{d}M/\mathrm{d}H$ are recorded by S. Ghannadzadeh and F. Foronda with the capacitor driven short-pulse magnet at the Nicholas Kurti Magnetic Field Laboratory (NKMFL) at the University of Oxford (UK). Measurements are performed at temperatures from 0.53 to 4.55 K using an magnetic field pulses with an amplitude of $\mu_0 H = 10$ T and a rise-time to peak-field of ≈ 5 ms. The analysis and simulations of these data are performed as part of this project.

(b) Dc SQUID magnetometry: In this work, the magnetic moment M of a polycrystalline sample is followed as a function of temperature with a Quantum Design™ (QD) MPMS. These measurements are performed at the University of Warwick (UK). The experiments utilize a quasistatic applied magnetic field $\mu_0 H = 0.1$ T and consider sample temperatures in the range $1.8 \leq T \leq 300$ K. The iQuantum™ Helium-3 insert is used to obtain measurements of M for sample temperatures between 0.45 and 2 K. The two separate measurements of M are repeatable to approximately 3% for $T \approx 2$ K. The linear molar susceptibility is estimated from $\chi = M/(nH)$ where n is the number of moles of the sample.

(c) Ac SQUID magnetometry: Ac susceptibility measurements are performed by C. V. Topping at the University of Oxford (UK). These experiments follow the time dependence of the magnetic moment M in response to an ac applied field with an amplitude $\mu_0 H_{\mathrm{ac}} = 0.1$ mT and sinusoidal frequencies $\nu_{\mathrm{ac}} \leq 1500$ Hz, and they are conducted in quasistatic $\mu_0 H = 0.1$ T for temperatures $2 \leq T \leq 10$ K.

4.2.6 Heat capacity

In this work, heat capacity $C_p(T)$ measurements are performed with a 1.82(5) mg sample using the ^{3}He inset to a QD Physical Property Measurement System at the University of Warwick (UK). The heat capacity is extracted from experiments performed in quasistatic $\mu_0 |H| \leq 9$ T for $0.4 \leq T \leq 20$ K.

4.2.7 Simulations

(a) Powder $M(H)$ and $C_p(T)$ calculations: In this work, simulations of the powder magnetization $M(H)$ are performed in MATLAB by considering an ensemble of $S = 1$ ions described by the spin Hamiltonian in Eq. 4.1 and by utilizing the methodology described in Section 2.7. The values of $D/k_B = 8.3$ K, $E/k_B = 1.2$ K, $g_z = 2.17$ and $g_{xy} = 2.20$ are used in the calculation, which are derived from results of ESR measurements (see below). The magnetization calculations are performed at fixed sample temperatures in the range $0.5 \leq T \leq 2.5$ K and for applied magnetic fields $\mu_0 H \leq 10$ T. Analogous simulations of the powder heat capacity $C_p(T)$ are performed with $0 \leq T \leq 10$ K at fixed magnetic fields $\mu_0 H \leq 9$ T. The H and T axes of the $M(H)$ and $C_p(T)$ simulations are considered in $\mu_0 H = 0.1$ T and $\Delta T = 0.1$ K steps, respectively. The discreteness of these calculations is one source of error in the positions of features observed in these thermodynamic simulations.

(b) Density-functional theory: The density-functional theory (DFT) calculations referenced in this chapter are organized by T. Lancaster, and performed and analysed by S. J. Clark and I. O. Thomas at Durham University (UK). These simulations employ the CASTEP package [170] with Perdew-Burke-Ernzerhof potentials [171, 172] to obtain accurate [173] estimates of the spin-exchange energies within the kagome planes.

4.3 Results and Discussions

4.3.1 The arrangement of Ni^{2+} ions

The crystal structure of $[H_2F]_2[NiF_2(3\text{-}Fpy)_4]_3[SbF_6]_2$ (Table 4.1) is refined against the positions and intensity of Bragg reflections observed at 100 K from the results of single-crystal x-ray diffraction measurements. Each Ni^{2+} ion of this polymeric compound is positioned on a global inversion centre (point group = $\bar{1}$) and is coordinated to four equatorial 3-Fpy molecules along with two axial F^- ions. Using the atomic labelling scheme of Fig. 4.2(a), the 3-Fpy and F^- ligands are found to complete NiN_4F_2 pseudo-octahedral coordination environments for which the three unique bond lengths are Ni-F = 2.000 Å, Ni-N1 = 2.101 Å and Ni-N2 = 2.146 Å, while the N1-Ni-Ni2, N1-Ni-F and N2-Ni-F internal bond angles are measured to be 91.0°, 91.2° and 88.5° respectively.

Coplanar Ni^{2+} spin centres are arranged into two-dimensional kagome lattices spanning the crystallographic **ab**-plane [Fig. 4.2(b)] wherein each of the intra-

Table 4.1: Refinement details for the single-crystal x-ray diffraction measurements of $[H_2F]_2[NiF_2(3\text{-}Fpy)_4]_3[SbF_6]_2$. The trigonal space group $R\bar{3}$ utilizes the hexagonal (H) choice of axes; and $R_{\rm int} = \sum |F^2_{\rm obs} - F^2_{\rm calc}| / \sum F^2_{\rm obs}$, where $F_{\rm obs}/F_{\rm calc}$ are the observed/calculated structure factors and the sum runs over all measurements.

Parameter (units)	Fitted value (error)
Chemical formula	$C_{60}H_{52}F_{32}N_{12}Ni_3Sb_2$
Formula mass (g mol^{-1})	1968.68
Temperature (K)	100(2)
Space group	$R\bar{3}$, H axes
a, b (Å)	14.3617(5)
c (Å)	30.905(1)
γ (°)	120
Unit cell volume (Å^3)	5520.4(4)
Chemical formulae per unit cell	3
$R_{\rm int}$	0.0733

plane nearest-neighbour Ni-Ni distances are 7.181 Å. However, there is a structural disorder of the H_2F^+ moieties that form the central part of the Ni-F$\cdots$H-F-H$\cdots$F-Ni bridges within these planes. Each of the Ni^{2+} triangles of the kagome lattice are symmetry equivalent and Fig. 4.2(c) depicts all of the possible positions for the H_2F^+ cations within one of these triangular plaquettes. There are two levels of disorder: (i) the central F atoms of the cations adopts one of two equally likely positions that each have the point group 3 (upper and lower panels); and (ii) the whole HF_2^+ complex rotates such that the separate H sites are occupied with a probability of one third (indicated with the fractionally filled spheres).

The positional disorder of the poly-HF moieties results in two distinct F$\cdots$H hydrogen bond lengths [Fig. 4.2(c) (red and blue dots)] and there are therefore two possibilities for the distances between spin-centres along the nonlinear Ni-F$\cdots$H-F-H$\cdots$F-Ni pathways, which are 8.71 Å or 8.81 Å respectively. The longest distance between the F atoms within the F$\cdots$H-F-H$\cdots$F complexes is 2.403 Å. This fluorine to fluorine distance is typical of poly-HF moieties and within the sum of the van der Waals radii for two F atoms ($\approx$ 2.9 Å). In the present work, an overall charge neutrality of the crystalline compound is provided by layers of SbF_6^- counterions. These anions ions are organized into a weakly corrugated hexagonal lattice [Fig. 4.2(d)], which acts to keep individual $[H_2F]_2[NiF_2(3\text{-}Fpy)_4]_3^{2+}$ sheets separated by a perpendicular distance of 10.30 Å along the **c**-axis, and each $[SbF_6]_2^{2-}$ sheet is displaced along the $[\mathbf{1\bar{1}0}]$ direction with respect to the nearest anion layer in the crystal [Fig. 4.2(e)].

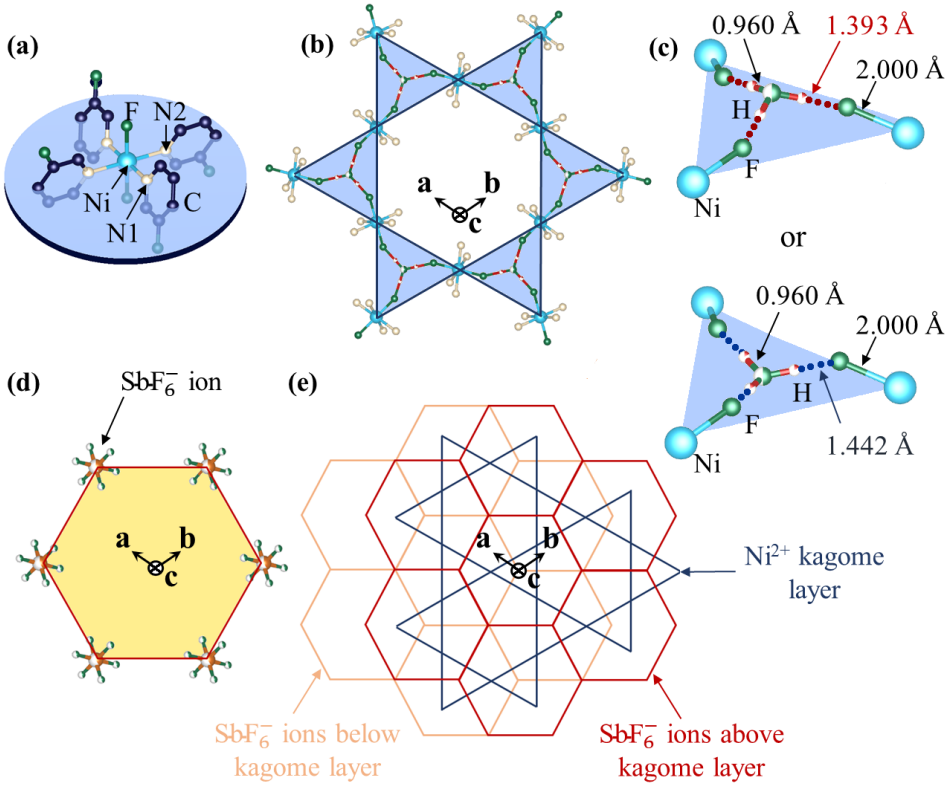

Figure 4.2: **(a)** At 100 K $[H_2F]_2[NiF_2(3\text{-Fpy})_4]_3[SbF_6]_2$ consists of Ni^{2+} spin centres ligated to four equatorial 3-Fpy molecules and two axial F^- ions. **(b)** Coplanar Ni^{2+} ions are positioned on the vertices of a two-dimensional kagome lattice (blue lines). **(c)** The central fluorine of each H_2F^+ moiety occupies one of two sites (upper or lower panel) and, in each case, the whole cation rotates to adopt one of three equally likely orientations. Blue shading here is the kagome plane. **(d)** The SbF_6^- counterions are organized into weakly corrugated hexagonal $[SbF_6]_2^{2-}$ sheets. **(e)** There is an $[SbF_6]_2^{2-}$ sheet positioned above (red lines) and below (pink lines) each kagome plane (blue lines). The fractional filling of spheres in panels (b)−(d) denotes a partial occupation of a lattice site.

4.3.2 Muon spin-relaxation

For powder muon spin-relaxation measurements of $[H_2F]_2[NiF_2(3\text{-Fpy})_4]_3[SbF_6]_2$ performed in zero field, the observed asymmetry $A(t)$ spectra [Fig. 4.3(a) points] are approximately independent of the sample temperature T for data collected in range $0.019 \leq T \leq 10$ K. Each $A(t)$ trace displays weak oscillatory features that are superimposed on a background that decays with time, which implies that the measured asymmetry curves may fitted to the expression

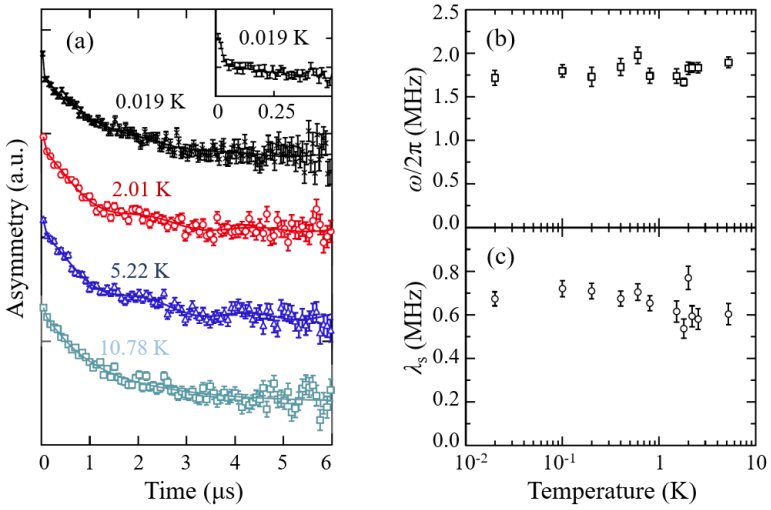

Figure 4.3: **(a)** Powder muon spin-relaxation asymmetry spectra as a function of time for $[H_2F]_2[NiF_2(3\text{-}Fpy)_4]_3[SbF_6]_2$ (points), fitted to Eq. 4.2 (solid lines). Data are plotted in arbitrary units (a.u.). Separate measurements at constant T are offset for clarity. *Inset:* Asymmetry spectra at 0.019 K for times $t \leq 0.5$ μs. Panels **(b)** and **(c)** show the temperature dependence of the fitted values of $\omega/2\pi$ and the slow relaxation rate λ_s, respectively. Both parameters lack any sharp features as a function of T that might indicate a transition to a magnetically ordered state. The average value of $\omega/2\pi = 1.74$ MHz, which indicates that a portion of the implanted muons that come to rest in the sample form F$-\mu^+$ with a bond separation of 1.09 Å.

$$A(t) = A_f\, e^{-\lambda_f t} + A_s e^{-\lambda_s t} + A_{F\mu} D_z(\omega, t) e^{-\lambda_{F\mu} t} + A_{bkgd}. \tag{4.2}$$

The first term in Eq. 4.2 accounts for the amplitude A and decay rate λ of a fast (f) exponential relaxation of the implanted muon's spin polarization. This rapid reduction in $A(t)$ likely owes its origin to μ^+ particles that occupy paramagnetic sites within the crystalline sample (e.g. Ref [174]). The second term in Eq. 4.2 models a relatively slow (s) exponential decay of the μ^+ polarization, which arises from an electromagnetic interaction between an individual μ^+ spin and the fluctuating electronic moments in the material. The parameter λ_s is proportional to the width of the local field distribution $(B - \langle B \rangle)^2$ at each interstitial μ^+ site and is therefore sensitive to changes in the magnetic properties in the material [175]. The third term accounts for the weak oscillatory contribution to the measurement. Oscillatory features are common in the muon spin-relaxation measurements of fluorine compounds and indicate the formation of an entangled state between a μ^+ particle and a ^{19}F nucleus, where the angular frequency ω of this term depends on the ^{19}F$-\mu^+$ separation [176]. The final term in Eq. 4.2 is a non-relaxing background to the measurements that results from muons that come to rest within the Ag sample

holder or cryostat tail (see for instance Ref. [65] and the supporting information therein). The fitted values of $\omega/2\pi$ [Fig. 4.3(b)] and λ_s [Fig. 4.3(c)] show no discernible sharp features at low T, which strongly indicates that there is no long-range magnetic order in $[H_2F]_2[NiF_2(3\text{-}Fpy)_4]_3[SbF_6]_2$ for $T \geq 19$ mK.

4.3.3 Electron spin-resonance

For 435.2 GHz powder ESR measurements of $[H_2F]_2[NiF_2(3\text{-}Fpy)_4]_3[SbF_6]_2$, the differential transmission intensity $\mathrm{d}I/\mathrm{d}H$ [Fig. 4.4(a), lines] exhibits a derivative shape (α) on sweeping the applied magnetic field through $\mu_0 H = 6.3$ T. This resonance is found to occur at the same value of H for spectra collected at sample temperatures in the range $3.3 \leq T \leq 100$ K. For measurements performed at $T \leq 10$ K, two further kinks in $\mathrm{d}I/\mathrm{d}H$ are evident at $\mu_0 H \approx 10$ T and 12 T, which are labelled β (red arrow) and γ (pale-blue arrow) respectively. Each of the α, β and γ resonances become more pronounced on cooling and this, along with the weak temperature dependence of the position of these features, suggests that each absorption derives from a single-ion transition whereby a Ni^{2+} ion the ground spin-state absorbs a photon to become excited to a higher energy level [49].

The ν dependence of the ESR spectra at 3.5 K [Fig. 4.4(b)] demonstrates that: (i) the α transition becomes sharper with increasing ν; (ii) both the α and γ transitions evolve to higher $\mu_0 H$ with increasing ν; and (iii) the β transition is relatively weak in most spectra. The $H - \nu$ dependence of the single-ion resonances [Fig. 4.4(c), points] are described by a powder average model (solid lines), which considers $[H_2F]_2[NiF_2(3\text{-}Fpy)_4]_3[SbF_6]_2$ as an ensemble of $S = 1$ ions governed by the spin Hamiltonian of Eq. 4.1 and the single-ion parameters $D/k_B = 8.3$ K, $E/k_B = 1.2$ K, $g_z = 2.17$ and $g_{xy} = 2.20$ yield simulated powder ESR spectra [e.g. Fig. 4.4(d), red line] that largely reproduce the approximate positions and relative intensities of absorptions observed in the measured spectra (blue line).

The easy-plane nature of the spin moments is well constrained by the data. If simulations are performed with negative D, then the β and γ transitions are predicted to occur at higher applied magnetic fields than are observed in measurements of the real system. Furthermore, the separation of the β and γ resonance into two distinct modes necessarily requires $E \neq 0$, which is in keeping with the low symmetry of the pseudo-octahedral Ni^{2+} coordination environments in the measured crystal structure (see above). An estimate of the size of the error on the parameters D and E is determined by modelling the data in Fig. 4.4(c) by the functional forms the α, β, and γ resonances, which are derived from exact diagonalization Eq. 4.1. In summary, the ESR data are consistent with values of $D/k_B = 8.3(4)$ K

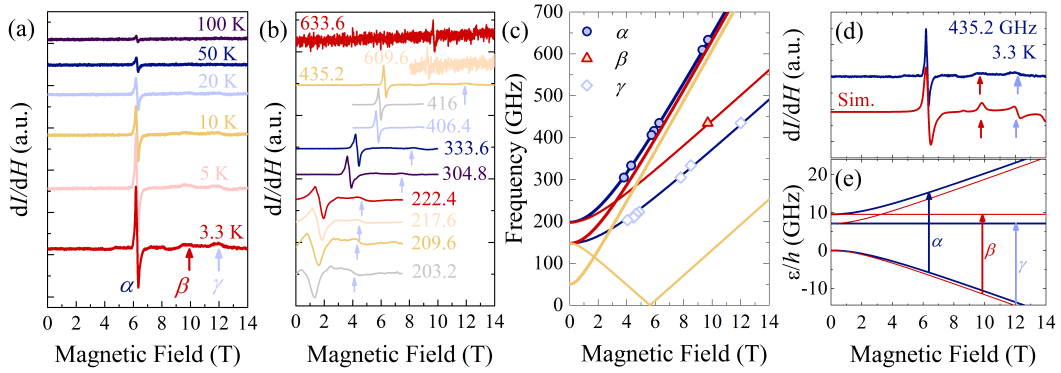

Figure 4.4: **(a)** The applied magnetic field $\mu_0 H$ dependence of the powder differential transmission ESR intensity $\mathrm{d}I/\mathrm{d}H$ of $[H_2F]_2[NiF_2(3\text{-}Fpy)_4]_3[SbF_6]_2$ for $\nu = 435.2$ GHz, plotted in arbitrary units (a.u.). The α, β (red arrow) and γ (blue arrow) absorptions become stronger with decreasing T. **(b)** $\mathrm{d}I/\mathrm{d}H$ vs. $\mu_0 H$ at 3.5 K for constant microwave frequencies in the range $203.2 \leq \nu \leq 633.6$ GHz (and 3.3 K for $\nu = 435.2$ GHz). **(c)** The evolution of the α, β and γ transitions in the $\mu_0 H - \nu$ plane at 3.3 K. Lines model the $H - \nu$ dependence expected for $S = 1$ ions that obey the Hamiltonian in Eq. 4.1 (see text). **(d)** Measured powder ESR spectrum at $T = 3.5$ K and $\nu = 435.2$ GHz (blue line) compared against the powder model (red line). **(e)** The spin-eigenstate energy ϵ vs. $\mu_0 H$ for Ni^{2+} ions in H parallel to the x (blue lines) and y (red lines) axes. Arrows label the α, β and γ transitions. Data in panels (a), (b) and (d) are offset for clarity.

and $E/k_B = 1.2(3)$ K. It is likely that the value of E has the larger percentage error since this quantity scales with the separation of β and γ modes, but the position of the β resonance is difficult to extract from most of the ESR spectra owing to its weak nature.

The strength of the uniaxial anisotropy derived from the results of powder ESR is also within 40% of an estimate of $|D|/k_B = 11.8$ K, which is extracted from an empirical model [179] that parameterizes D in terms of the ratio of the axial and equatorial bond lengths of the Ni^{2+} octahedra. The empirical model does, however, predict an Ising character for the spins, which is inconsistent with the results of this section and (as will be seen below) is furthermore incompatible with the measured and simulated thermodynamic properties of $[H_2F]_2[NiF_2(3\text{-}Fpy)_4]_3[SbF_6]_2$.

In the present study, the β and γ absorptions are attributed to ESR transitions that occur for H parallel to the x and y axes respectively [Fig. 4.4(e)]. Both of these transitions are observed at values of H for which the Zeeman energy exceeds the zero-field splitting of the Ni^{2+} spin-states. Defining m_s as the component of the Ni^{2+} projected along the applied H direction, the β and γ resonances are found to correspond to single-ion spin-transitions with $|\Delta m_s| = 1$. The α absorption, on the

other hand, is credited to a "half-field"' transition, which occurs for H parallel to x and involves a Ni^{2+} ion transitioning from the ground spin-state to the highest energy level (dark blue arrow). Half-field transitions are commonly observed in the ESR spectra of Ni^{2+} compounds for which the spins reside in pseudo-octahedral coordination environments and the measurements are performed with $\nu \approx D/h$ [177] and resonances of this type are permitted when the Zeeman energy is comparable to the zero-field splitting in which case m_s is not a good quantum number [178].

The result that ESR resonances observed at $T > 3$ K may be accounted for within a model of weakly interacting Ni^{2+} ions is consistent with the results of muon spin-relaxation experiments, which show no evidence for long-range magnetic at these temperatures, and it is furthermore in keeping the results of a density-functional theory (DFT) investigation of $[H_2F]_2[NiF_2(3\text{-Fpy})_4]_3[SbF_6]_2$ [75]. In summary, the results of the DFT calculations imply that: (i) while the positional disorder of the fluorine atoms within each H_2F^+ cation has little impact on the magnetic properties of the system, the disorder of the H atoms is predicted to result in a low spin density at the centre of the N-F$\cdots$F-H-F$\cdots$F-Ni bridges such that the strength of the intraplane Ni-Ni spin-exchange interactions are expected to be less than $|J|/k_B \approx 1$ K; and (ii) that this estimate of J is approximately an order of magnitude lower than the strength of the spin-exchange interactions predicted from a separate DFT model that considers an idealized analogue compound in which each of the NiF$\cdots$H-F-H$\cdots$F-Ni linkages are intact. It is therefore likely that the positional disorder of the poly-HF moieties in the real compound is responsible for the suppression of long-range magnetic order in this system and this allows for the results of powder ESR measurements to be largely accounted for with a model consisting of independent $S = 1$ ions.

4.3.4 Pulsed-field magnetometry

For pulsed-field magnetometry measurements of $[H_2F]_2[NiF_2(3\text{-Fpy})_4]_3[SbF_6]_2$ performed at sample temperatures in excess of ≈ 1.4 K, the differential susceptibility $\mathrm{d}M/\mathrm{d}H$ [Fig. 4.5(a)] decreases smoothly in an increasing applied magnetic field as individual spin moments cant towards the direction of H. However, a bump in $\mathrm{d}M/\mathrm{d}H$ develops for applied magnetic fields $\mu_0 H$ in the approximate range $5-6$ T for measurements repeated at $T < 1.4$ K. This feature becomes more pronounced as T decreases further, and the position of this small peak is approximately temperature independent.

By considering an ensemble of $S = 1$ ions described by the Hamiltonian in Eq. 4.1, and by assuming the values of $D/k_B = 8.3$ K, $E/k_B = 1.2$ K, $g_z = 2.17$,

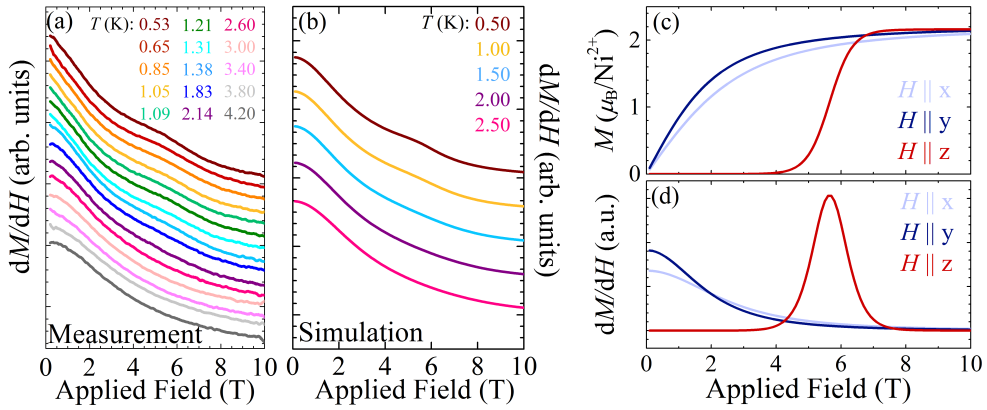

Figure 4.5: **(a)** The measured differential susceptibility $\mathrm{d}M/\mathrm{d}H$ for a polycrystalline sample of $[H_2F]_2[NiF_2(3\text{-}Fpy)_4]_3[SbF_6]_2$. Experiments are recorded at fixed T in the applied magnetic field $\mu_0 H$ of a capacitor-driven short-pulse magnet at NKMFL, University of Oxford (UK). Lines plotted here are measured data that is interpolated from 0.2 to 10 T in 2000 steps and smoothed with the Savitzky-Golay method over a 51 point window. **(b)** Simulation of the powder differential susceptibility using the spin-Hamiltonian in Eq. 4.1 with single-ion anisotropy $D/k_\mathrm{B} = 8.3$ K and $E/k_\mathrm{B} = 1.2$ K, $g_z = 2.17$, $g_{xy} = 2.20$. Data in panels (a) and (b) are plotted in arbitrary units (a.u.) and offset for clarity. The respective panels **(c)** and **(d)** display single-crystal simulations of M and $\mathrm{d}M/\mathrm{d}H$ for Ni^{2+} $S = 1$ ions. These representative calculations use the same D and E values from panel (b) and consider H parallel to the x (light blue), y (dark blue), and z (red) axes.

and $g_{xy} = 2.20$ that are derived from ESR measurements (above), the methodology established in Section 2.7 is employed to simulate the powder differential susceptibility of $[H_2F]_2[NiF_2(3\text{-}Fpy)_4]_3[SbF_6]_2$. The calculated $\mathrm{d}M/\mathrm{d}H$ traces [Fig. 4.5(b)] predict that a small peak develops in the differential susceptibility for $\mu_0 H \approx 5{-}6$ T, a result that is in keeping with the magnetic properties of the real compound. The bump in the simulated $\mathrm{d}M/\mathrm{d}H$ curves is only resolvable once the sample temperature is below ≈ 1.5 K, which corresponds to applied magnetic field sweeps performed at sample temperatures less than $T \approx 0.18 D/k_\mathrm{B}$.

The small peak in the measured and simulated powder $\mathrm{d}M/\mathrm{d}H$ traces is largely accounted for by considering the evolution of the spin-states of independent $S = 1$ ions in an applied magnetic field. For H along z, the three exact eigenvalues of Eq. 4.1 are $\epsilon_z = 0$ and $D \pm [E^2 + (g_z \mu_\mathrm{B} \mu_0 H)^2]^{1/2}$. These expressions, along with the representative energy level diagram in Fig. 2.13(b), together imply that there is a cross-over from a nonmagnetic to a magnetic ground spin-state as H is increased

through a critical applied magnetic field H_{C} that satisfies the condition

$$g_z \mu_{\mathrm{B}} \mu_0 H_{\mathrm{C}} = \sqrt{D^2 - E^2}. \tag{4.3}$$

Thus, when the sample temperature is $T < D/k_{\mathrm{B}}$, sweeping H through H_{C} is expected to induce a large step in the z-component of the magnetization M_z [Fig. 4.5(c), red line] and this, in turn, results in a large peak in $\mathrm{d}M_z/\mathrm{d}H$ [Fig. 4.5(d)]. When H is instead applied within the easy-plane of a Ni^{2+} ion, the ground spin-state does not intersect any other energy levels for $H > 0$ [e.g. Fig. 2.13(b)] and therefore the x and y components of M [Fig. 4.5(c)] and $\mathrm{d}M/\mathrm{d}H$ [Fig. 4.5(d)] evolve smoothly as a function of increasing H. In the magnetometry measurements of powdered $S = 1$ materials, there is a larger probability for H to be perpendicular to, rather than parallel to, the local z axis of each spin-centre (e.g. Eq. 2.24) and the small bump in the polycrystalline measurements and simulations of $\mathrm{d}M/\mathrm{dH}$ at $H \approx H_{\mathrm{C}}$ is therefore relatively weak compared to the peak in the simulations of $\mathrm{d}M_z/\mathrm{d}H$.

One general remark, which is pertinent to the future investigations of easy-plane $S = 1$ materials, is that an estimate of D may be made applying Eq. 4.3 to an approximation of H_{C} extracted from the observation of a small bump in a powder measurement of $\mathrm{d}M/\mathrm{d}H$. This approach is applicable in cases when $E \ll D$, providing an estimate of the g may also be obtained (e.g. from susceptibility measurements, see below, or ESR). The results of the simulations of this section suggest the small peak in $\mathrm{d}M/\mathrm{d}H$ is resolvable for powder magnetometry experiments performed at sample temperatures below $T \approx 0.18D/k_{\mathrm{B}}$ in applied magnetic fields that are sufficient to reach H_{C}. These two experimental conditions set approximate lower and upper bounds on the values of D that may be extracted from powder $\mathrm{d}M/\mathrm{d}H$ measurements. The capacitor-driven pulsed-field systems at NHMFL, Los Alamos (USA), provide access to ^{3}He temperatures ($T \geq 0.4$ K) and applied magnetic fields ($\mu_0 H \leq 65$ T) such that, in principle, $\mathrm{d}M/\mathrm{d}H$ measurements performed with this pulsed-field system are sensitive to values of D in the approximate range $2.2 \leq D/k_{\mathrm{B}} \leq 87.1$ K, where the upper bound assumes $g_z \approx 2$.

4.3.5 Heat capacity

Zero-field heat capacity $C_p(T)$ measurements [Fig. 4.6(a), points] reveal a broad maximum at $T \approx 2.5$ K that is superimposed on a sloping background. The lattice contribution to the measurement C_{latt} is estimated by fitting the measured heat capacity for $T \geq 10$ K to Eq. 1.10 using one Debye (D) and one Einstein (E) mode (red line). The phonon model is interpolated to the temperature of each $C_p(T)$ measurement and the magnetic heat capacity is approximated with the expression

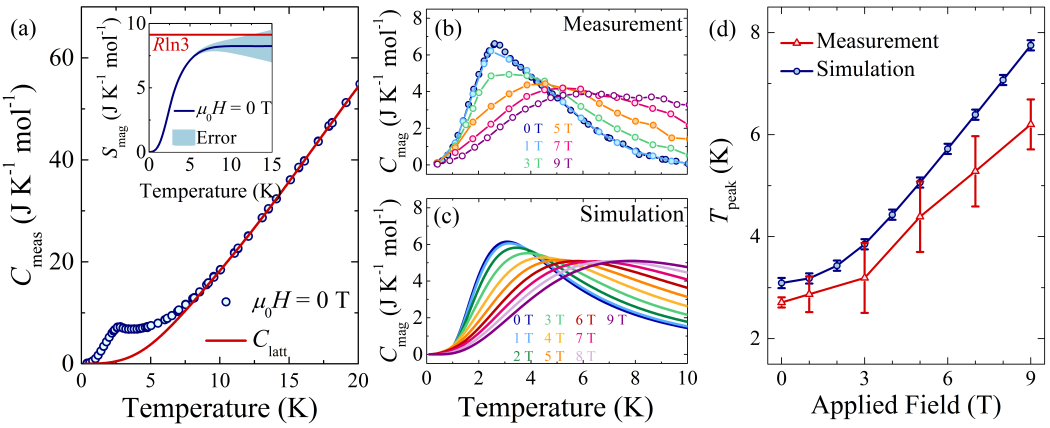

Figure 4.6: **(a)** Zero-field heat capacity of $[H_2F]_2[NiF_2(3\text{-}Fpy)_4]_3[SbF_6]_2$ (points) measured from a polycrystalline sample. Data for $T \geq 10$ K are fitted to Eq. 1.10 with one Debye and one Einstein mode (solid line). The fitted amplitude A and characteristic temperature θ of each mode are: $A_{\rm D} = 44(3)$ JK^{-1}mol^{-1}, $\theta_{\rm D} = 48(2)$ K; and $A_{\rm E} = 94(1)$ JK^{-1}mol^{-1}, $\theta_{\rm E} = 91(3)$ K. *Inset:* Estimate of the spin-entropy $S_{\rm mag}$ vs. temperature in zero-field (blue line) compared to Rln3 (red line). **(b)** Magnetic heat capacity $C_{\rm mag}$ for experiments performed in quasistatic $\mu_0 H \leq 9$ T. These T dependent data are averaged over repeat measurements. **(c)** Simulated $C_{\rm mag}(T)$ using the spin Hamiltonian in Eq. 4.1 with $D/k_{\rm B} = 8.3$ K, $E/k_{\rm B} = 1.2$ K, $g_z = 2.17$, and $g_{xy} = 2.20$. **(d)** Applied magnetic field dependence of the temperature of the Schottky anomaly peak $T_{\rm peak}$, as derived from the measured (triangles) and simulated (circles) $C_{\rm mag}(T)$ data.

$C_{\rm mag} = C_p - C_{\rm latt}$. The zero-field $C_{\rm mag}/T$ curve is integrated via Eq. 1.12 for $T \leq 15$ K to estimate the temperature dependence of the spin-entropy $S_{\rm mag}$, where $C_{\rm mag}$ is assumed to be zero at $T = 0$. The change in $S_{\rm mag}$ on cooling the sample from 15 K [Fig. 4.6(a), inset] is consistent with a value of Rln3 per ion. This indicates that the broad peak in the zero-field heat capacity is a Schottky anomaly that results from each Ni^{2+} ion becoming restricted from three thermally accessible spin-states at high temperatures to a single ground-state at $T \ll D/k_{\rm B}$.

The estimate of $C_{\rm latt}$ is subtracted from heat capacity measurements repeated in quasistatic applied magnetic fields $\mu_0 H \leq 9$ T [Fig. 4.6(b)]. The Schottky anomaly of the $C_{\rm mag}(T)$ traces has a peak temperature that moves monotonically to higher T with increasing H. The amplitude of the maximum in the magnetic heat capacity is initially suppressed with increasing applied fields up to $\mu_0 H \approx 5$ T where after the peak amplitude remains approximately constant with a further increase in the strength of the applied magnetic field.

Simulations [Fig. 4.6(c)] of the powder heat capacity utilize the method outlined in Section 2.7. These calculations consider an ensemble of $S = 1$ Ni^{2+} ions

governed by Eq. 4.1 and use the D, E, g_z and g_{xy} values determined from ESR (above). The calculated $C_{\rm mag}(T)$ traces share many of the broad features of the experimentally determined curves, where the amplitude and temperature dependence [Fig. 4.6(d)] of the measured Schottky anomaly peaks for $\mu_0 H \leq 9$ T are reasonably well approximated by the single-ion simulation. Three factors that might contribute to the slight discrepancy between the positions of the simulated and measured Schottky anomalies are: (i) the discreteness of the data, which indicated by the error bars in panel (d); (ii) the possibility of weak Ni-Ni spin-exchange interactions predicted from the results of DFT simulations [75]; and (iii) the precise nature of the lattice model used to extract $C_{\rm mag}$ from the experimental heat capacity measurements. Points (i)−(iii) might be relevant in future work conducted to examine the heat capacity of $S = 1$ systems with a strong single-ion anisotropy.

4.3.6 Quasistatic magnetometry

The results of ac susceptibility measurements of $[H_2F]_2[NiF_2(3\text{-}Fpy)_4]_3[SbF_6]_2$ for $T \geq 2$ K [Fig. 4.7, panels (a) and (b)] indicate that the time dependent magnetic moment evolves in-phase with an applied sinusoidal modulation field for ac frequencies $\nu_{\rm ac} \leq 1500$ Hz. The lack of an out-of-phase component of the ac susceptibility implies that there is no evidence for spin-glass behaviour (see, for instance, Refs. [29, 161]) in this structural disordered kagome system for $T \geq 2$ K, which is in keeping with the expected weak nature of the spin-exchange interactions of this material at these temperatures. Two further observations from the ac susceptibility data corroborate the easy-plane nature of the Ni^{2+} uniaxial anisotropy. Firstly, Ising-like single-ion and single-molecule magnets are expected to exhibit a slow relaxation of the magnetization (and hence a finite out-of-phase component of the ac susceptibility) as it is these systems for which the zero-field splitting acts as a thermal energy barrier to the reversal of the magnetization for temperatures $T < |D|/k_{\rm B}$ [180–182]; and secondly the ac susceptibility measurements performed on other polymeric single-molecule magnets containing easy-plane Ni^{2+} ions (e.g. Ref. [183]) also exhibit no evidence for an out-of-phase component of the ac susceptibility.

The linear susceptibility $\chi_{\rm mol}$ of $[H_2F]_2[NiF_2(3\text{-}Fpy)_4]_3[SbF_6]_2$ is extracted from quasistatic magnetometry measurements performed on a polycrystalline sample. The magnitude of $\chi_{\rm mol}(T)$ [Fig. 4.7(c), points] is slowly varying for temperatures in the range $0.4 \leq T \leq 2$ K, while the linear susceptibility decreases continuously for $T > 2$ K. For an ensemble of $S = 1$ ions in an applied magnetic field H_i ($i = x$, y, or z), the eigenvalues of Eq. 4.1 are inserted into a partition function and, using the methodology of Ref. [79], the Cartesian components of the linear susceptibility

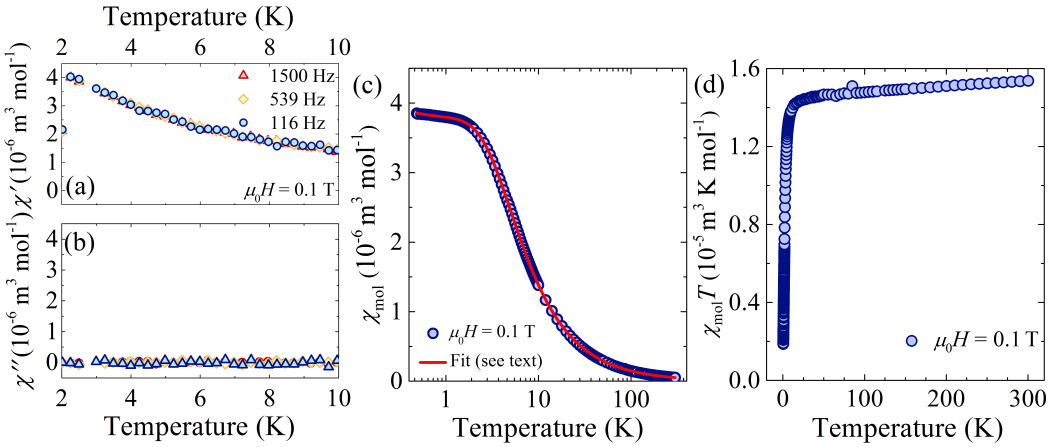

Figure 4.7: **(a)** In-phase, and **(b)** out-of-phase ac susceptibility measurements of $[H_2F]_2[NiF_2(3\text{-}Fpy)_4]_3[SbF_6]_2$. For $T > 2$ K, and ac modulation frequencies $\nu_{ac} \leq 1500$ Hz, the magnetic moment exhibits no slow-relaxation for the experiments performed in quasistatic $\mu_0 H = 0.1$ T. The small value of χ' at 2 K is frequency independent, does not correlate with a rise in χ'' and is not repeatable in the dc measurements [panel (c)]. It is therefore considered as an experimental artefact. **(c)** Zero-field cooled measurement of the linear susceptibility χ_{mol} (points) with $\mu_0 H = 0.1$ T. Data for $T > 1.8$ K are extracted from SQUID magnetometry measurements, whilst data for $0.4 \leq T \leq 1.9$ K are recorded with the iQuantum^{TM} Helium-3 insert and scaled to the results of the high-T experiments with a small multiplicative factor. The data are fitted to Eq. 4.7 across the full T range (solid line, see text). **(d)** $\chi_{mol}T$ vs. T displays an approximately linear dependence for $T \gg D/k_B$, indicating a temperature independent paramagnetic contribution to χ_{mol}.

are determined to take the form

$$\chi_x = \frac{2\mu_0 N_A \mu_B^2 g_{xy}^2}{D+E} \frac{1 - e^{-\beta(D+E)}}{1 + 2e^{-\beta D}\cosh \beta E}, \tag{4.4}$$

$$\chi_y = \frac{2\mu_0 N_A \mu_B^2 g_{xy}^2}{D-E} \frac{1 - e^{-\beta(D-E)}}{1 + 2e^{-\beta D}\cosh \beta E}, \tag{4.5}$$

and

$$\chi_z = \frac{2\mu_0 N_A \mu_B^2 g_z^2}{E} \frac{e^{-\beta D}\sinh \beta E}{1 + 2e^{-\beta D}\cosh \beta E}. \tag{4.6}$$

In the analysis of the measured χ_{mol} data (below), the powder average molar susceptibility of $[H_2F]_2[NiF_2(3\text{-}Fpy)_4]_3[SbF_6]_2$ is approximated by the expression

$$\chi_{mol} = \frac{1}{3}\rho(\chi_x + \chi_y + \chi_z) + (1-\rho)\chi_{para} + \chi_0. \tag{4.7}$$

Here, χ_{para} is an $S = 1$ paramagnetic impurity, which assumes $g = 2$ and accounts

for a fraction $(1-\rho)$ of the sample, while χ_0 accounts for a temperature independent paramagnetic contribution to the measurement (which is necessary to account for the positive gradient of χT vs. T [Fig. 4.7(d)] at the highest temperatures measured and may result from van Vleck paramagnetism e.g. Ref. [184]).

Assuming the g-factor to be isotropic ($g_{xy,z} \approx g$), the experimental $\chi_{\rm mol}(T)$ data are modelled with Eq. 4.7 for temperatures in the range $0.4 \leq T \leq 300$ K [Fig. 4.7(c), solid line]. The resultant fitted parameters are $D/k_{\rm B} = 8.05(1)$ K, $E/k_{\rm B} = 1.73(3)$ K, $g = 2.15(1)$, $\rho = 0.9958(1)$ [i.e. there is a 0.42(1)% paramagnetic impurity phase], and $\chi_0 = 3.2(6) \times 10^{-9}$ m^3 mol^{-1}. The single-ion parameters are in broad agreement with the conclusions of the high-precision ESR measurements (above), and the model also provides a good approximation for the observed temperature dependence of the linear susceptibility. The fitted value of $\rho > 0$ is necessary to account for a slight inflection of $\chi_{\rm mol}(T)$ that is recorded at the lowest temperatures measured, whilst the small value of χ_0 derives from the positive gradient of $\chi_{\rm mol}T$ at temperatures $T \gg D/k_{\rm B}$ [Fig. 4.7(d)]. The magnitude of χ_0 is comparable to the size of the temperature independent paramagnetic response that is observed in the results of magnetometry measurements performed on other coordination complexes designed around octahedrally coordinated Ni^{2+} ions [185].

Single-crystal magnetometry measurements of materials with a single-ion anisotropy are predicted to exhibit an inverse susceptibility that follows a linear dependence on increasing temperature for $T \gg D/k_{\rm B}$, where a linear fit to these data is expected to yield an intercept with the $T = 0$ axis that is sensitive to both the sign and size of D [186]. The single-ion model of this section is used to determine whether a similar result may also be derived from the inverse susceptibility measurements of powdered samples. Given the expressions in Eqs. 4.4−4.6, the inverse molar susceptibility $\chi_{\rm mol}^{-1} = 3/(\chi_x + \chi_y + \chi_z)$ is examined in the high temperature limit by performing a series expansion for $T \gg D/k_{\rm B}$ to give

$$\chi_{\rm mol}^{-1} = C\left[T + \frac{D}{k_{\rm B}}\left(\frac{g_{xy}^2 + g_z^2}{2g_{xy}^2 + g_z^2} - \frac{2}{3}\right)\right]. \tag{4.8}$$

where $C^{-1} = \frac{1}{3k_{\rm B}}\mu_0 N_{\rm A}\mu_{\rm B}^2(\frac{2}{3}g_{xy}^2 + \frac{1}{3}g_z^2)S(S+1)$. Eq. 4.8 implies that in the high temperature limit: (i) that the gradient of $\chi_{\rm mol}^{-1}(T)$ is analogous to the case of measurements performed on paramagnetic ensembles of $S = 1$ ions; (ii) the $T = 0$ intercept is zero for all values of D if the g-factor is isotropic ($g_z = g_{xy}$); (iii) the $T = 0$ intercept is independent of E given the assumption that $g_x = g_y = g_{xy}$; and (iv) for the inverse susceptibility measurements of powdered Ni^{2+} materials, the second term in the square brackets is less than 1% of $D/k_{\rm B}$ for typical g-factor

anisotropies of $|g_z - g_{xy}|/g_z \approx 0.01$. Since $|D|/k_B \approx 10$ K for typical Ni^{2+} materials, the intercept to a linear fit of $\chi^{-1}_{mol}(T)$ with the $T = 0$ axis is therefore likely to be negligible and difficult to reliably extract for measurements of powdered samples.

4.4 Conclusions

A refinement of 100 K structure of $[H_2F]_2[NiF_2(3\text{-Fpy})_4]_3[SbF_6]_2$ indicates that the Ni^{2+} ions of this polymeric compound are arranged into two-dimensional kagome sheets. However, there are two levels of positional disorder within the intraplane charge-assisted Ni-F$\cdots$H-F-H$\cdots$F-Ni linkages: (i) the central fluorine atoms of the intermediary HF_2^+ moieties adopts one of two lattice sites; and (ii) in each of these cases the cation rotates to adopt one of three equally likely orientations. The results of DFT calculations predict that property (ii) acts to significantly weaken the spin-exchange interactions between coplanar Ni^{2+} ions relative to the case for which there is no structural disorder is present and this is corroborated by the results of powder muon spin-relaxation measurements, which imply that there is no long range magnetic order in this compound for sample temperatures greater that 19 mK. Despite the absence of strong magnetic interactions in $[H_2F]_2[NiF_2(3\text{-Fpy})_4]_3[SbF_6]_2$, the intriguing structure of this compound and the strong effect that bond-disorder has on the bulk magnetic properties of this system suggests that future realizations of polymeric magnets consisting of charge-assisted hydrogen bonds will continue to play a role in the ongoing research into the interdependence of structural disorder, geometric frustration and long-range magnetic order in solid-state systems.

Powder ESR measurements of $[H_2F]_2[NiF_2(3\text{-Fpy})_4]_3[SbF_6]_2$ at temperatures $T \geq 3.3$ K, along with the results of polycrystalline pulsed-field magnetometry and heat capacity experiments performed at $T \geq 0.4$ K, exhibit features that are largely accounted for by modelling this Ni^{2+} system as an ensemble of independent ions with a uniaxial and rhombic single-ion anisotropy (Eq. 4.1), where $D/k_B = 8.3(4)$ K and $E/k_B = 1.2(3)$ K. Quasistatic measurements of the linear susceptibility (for $T \geq 0.45$ K), which are also performed on a polycrystalline sample, are furthermore consistent with the suggested magnitudes of D and E. The application of an empirical model [179], which aims to determine D from the ratio of the equatorial and axial bond lengths within the Ni^{2+} octahedra, provides an estimate of the uniaxial anisotropy that is within 40% of the measured value but it is predicted to have the opposite sign. The results of this chapter therefore indicate that there is no substitute for experimental estimates of single-ion parameters.

Along with ESR measurements, pulsed-field magnetometry techniques are

likely to be a useful tool in future work conducted to estimate the strength of the uniaxial easy-plane single-ion anisotropy of powdered $S = 1$ materials. In particular, differential susceptibility measurements of powdered $S = 1$ systems with $E \ll D$, which are performed with the capacitor-driven pulsed-field magnet at NHMFL (Los Alamos), are predicted to be sensitive to a small bump in $\mathrm{d}M/\mathrm{d}H$ vs. H for systems with values of D in approximate range $2.2 \leq D/k_{\mathrm{B}} \leq 87.1$ K. The linear dependence of the inverse susceptibility of a powdered $S = 1$ system at temperatures $T \gg D/k_{\mathrm{B}}$ is, however, predicted to be largely insensitive to the sign and strength of D for Ni^{2+} materials with g-factors that are close to being isotropic.

Chapter 5

Quantum magnetism in three isotructural polymeric systems

A neutron powder diffraction (NPD) study of $[M(HF_2)(pyz)_2]SbF_6$ (where pyz = pyrazine; $M = Cu^{2+}$, Ni^{2+} or Co^{2+}) reveals that each system is tetragonal and that the exchange interactions mediated by both the pyz (J_{pyz}) and HF_2^- (J_{FHF}) ligands are antiferromagnetic. The Heisenberg spin $S = 1/2$ Cu^{2+} system exhibits an ordered moment $\mu = 0.6(1)\mu_B$ that is reduced from its paramagnetic (PM) value by quantum fluctuations, while the Ni^{2+} ($S = 1$) and Co^{2+} ($S = 3/2$) congeners have μ values of $2.03(7)\mu_B$ and $3.02(6)\mu_B$ that are consistent with their respective PM moments. For the Ni^{2+} complex the size of the single-ion anisotropy D and the quantity $(2J_{FHF} + 4J_{pyz})$ are estimated from a semi-classical model and the results of powder magnetization $M(H)$ measurements, though inelastic neutron scattering is necessary to uniquely determine $D/k_B = 13.3(3)$ K, $J_{FHF}/k_B = 10.4(3)$ K and $J_{pyz}/k_B = 1.4(2)$ K. These parameters combine with a published [68] quantum Monte-Carlo study to show that this $S = 1$ system lies close to a zero-temperature critical point that separates magnetic order from two quantum disordered phases. The results of NPD, powder electron spin-resonance and bulk thermodynamic measurements of the Co^{2+} material suggest: (i) this system adopts an Ising-like magnetically ordered ground state below 7.1(1) K; and (ii) its magnetic properties may be modelled with an effective spin-1/2 Hamiltonian for which $\tilde{g}_z = 5.5(7)$, $\tilde{g}_{xy} = 3.6(4)$, and the average Co-Co spin-exchange is $\tilde{J}/k_B \approx 7(1)$ K. Some of the methods of this chapter, and the related publications [59, 77], may act as a guide for future work that aims to characterize similar powdered materials.

5.1 Introduction

Kosterlitz and Thouless' studies of the uniaxial two-dimensional (XY) spin-vector model [17, 18] along with Haldane's investigations of integer-spin chains [19, 20] are just some of the early theoretical works that helped to establish low-dimensional antiferromagnets (AFMs) as archetypal materials in which to explore the macroscopic effects of quantum magnetism. These systems are anticipated to exhibit a number of properties that cannot be explained semi-classically including quantum fluctuations (QFs), i.e. spin excitations that are thought to persist even as the temperature T goes to zero [15]; and quantum critical points (QCPs), which are externally driven phase transitions that are predicted to occur at $T = 0$ K [15, 16]. Given the association of QFs and QCPs with the emergence of strongly correlated electron phenomena in a wide range of AFMs, such as the development of superconductivity in certain heavy-fermion [187, 188] and hole-doped cuprate compounds [14] or the formation of Bose-Einstein condensates in several spin-gapped systems [52], one modern trend of condensed matter research is to develop synthetic electrically-insulating magnetic materials [15] in order to explore the interdependence of quantum magnetism on some of the fundamental properties of the spin-Hamiltonian including the size of the spin quantum number S, the spatial-dimensionality of the spin-exchange network, and the nature of the single-ion anisotropy.

One strategy for the development of new magnetic materials is to exploit the flexibility of heterocyclic synthons, such as pyrazine (pyz) or pyridine (py), along with charge-assisted H$\cdots$F bonds to afford metal-organic frameworks in a wide range of crystalline architectures. For instance, this approach has lead to the experimental investigations of several polymeric Heisenberg $S = 1/2$ materials including $[Cu_2F(HF)(HF_2)(pyz)_4](SbF_6)_2$ [76] and the square-lattice AFMs $[Cu(HF_2)(pyz)_2]Z$ (e.g. $Z = AsF_6^-$, PF_6^-, ClO_4^- or BF_4^-) [45]; along with multiple $S = 1$ AFMs such as the Ising-like complex $[Ni(HF_2)(pyz)_2]PF_6$ [47] and the Haldane chain $[Ni(HF_2)(3\text{-}Clpy)_4]BF_4$ [66, 67]. This chapter provides an experimental and theoretical investigation of a series of three related coordination complexes of the form $[M(HF_2)(pyz)_2]SbF_6$, where $M = Cu^{2+}$, Ni^{2+} or Co^{2+}. The scope of this work is firstly to consider how some of the bulk thermodynamic and local magnetic properties of these isostructural systems evolve according the choice of M, and secondly to build upon previous studies of the Cu^{2+} [45, 76] and Ni^{2+} [47, 189] congeners.

The results of neutron powder diffraction (NPD) measurements (see below) reveal that all three of the polymeric complexes investigated in this work crystallize in the tetragonal space-group $P4/nmm$. In each material, the individual

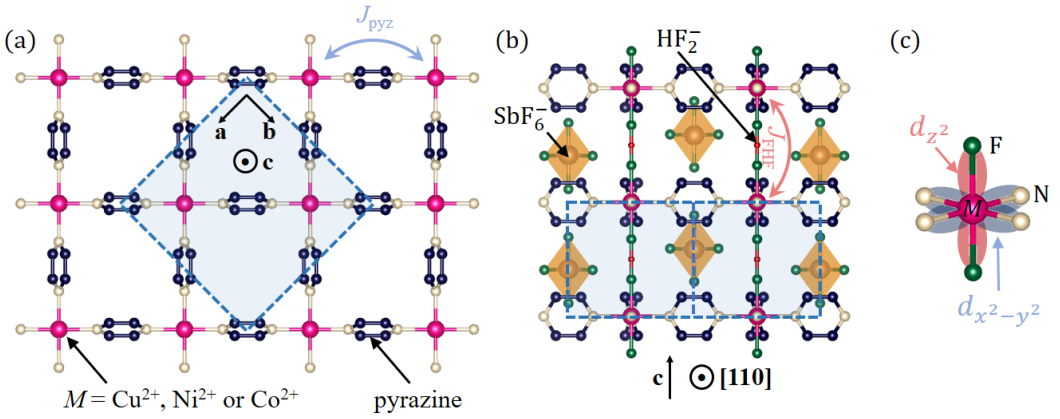

Figure 5.1: **(a)** Crystal structure of $[M(HF_2)(pyz)_2]SbF_6$ ($M = Cu^{2+}$, Ni^{2+} or Co^2) derived from the results of NPD (see below). In each material the spin-centres form square-lattice $[M(pyz)_2]^{2+}$ plaquettes spanning the **ab**-plane. **(b)** Hydrogen-bonded HF_2^- bridges create vertical pillars along **c**, while charge balancing SbF_6^- anions (orange shading) occupy interstitial lattice sites. The blue shading and dashed lines in panels (a) and (b) depicts the chemical unit cell ($P4/nmm$; cell choice 2 [190]). **(c)** The metal ions reside in tetragonally distorted MN_4F_2 octahedra. An unpaired M^{2+} electron in a $d_{x^2-y^2}$ (blue) or d_{z^2} (pink) suborbital leads to a delocalization of spin-density over the equatorial pyz or axial HF_2^- ligands respectively.

spin-centres are arranged into square-lattice $[M(pyz)_2]^{2+}$ plaquettes [Fig. 5.1(a)], wherein the pyz molecules mediate an intraplane spin-exchange interaction J_{pyz} (blue arrow), while separate layers of this type are linked via linear bifluoride (HF_2^-) ions [Fig. 5.1(b)] that give rise to an interlayer exchange J_{FHF} (pink arrow). Non-coordinated hexafluoroantimonate (SbF_6^-) counterions, meanwhile, act to provide an overall charge neutrality and occupy interstitial lattice sites. The structural unit cell (dashed lines) contains two coplanar metal ions, each of which resides within a tetragonally distorted MN_4F_2 octahedra [Fig. 5.1(c)] and the uniaxial crystalline electric field (CEF) around each moment results in a single-ion anisotropy D of the individual Ni^{2+} ($S = 1$) and Co^{2+} ($S = 3/2$) moments (e.g. Ref [36]).

The results [76] of x-ray diffraction measurements of $[Cu(HF_2)(pyz)_2]SbF_6$ at $T \geq 90$ K indicate that each CuN_4F_2 octahedra exhibits an axial (Jahn-Teller) elongation, which acts to constrain the spatial distribution of the unpaired electron in the Cu^{2+} $d_{x^2-y^2}$ orbital (and hence a large proportion of the spin-density) to lie within individual $[Cu(pyz)_2]^{2+}$ layers. This leads to $J_{pyz} \gg J_{FHF}$ such that the system approximates to a quasi-two-dimensional (Q2D) $S = 1/2$ square-lattice AFM [45, 76]. While strong QFs are expected to prevent ideal quadratic (two-dimensional square-lattice) Hesienberg $S = 1/2$ systems from developing magnetic

long-range order (LRO) for $T > 0$ [13], both muon spin-rotation (μ^+SR) and heat capacity C_p measurements of $[Cu(HF_2)(pyz)_2]SbF_6$ imply that this system adopts LRO below a critical temperature $T_C = 4.3$ K [76]. Non-Heisenberg intraplane exchange interactions are one perturbation to the Heisenberg $S = 1/2$ square-lattice model that are predicted to lead to a finite T_C in real compounds [35, 46, 64], and a single-crystal magnetometry study is used in this work to examine the nature of J_{pyz} in $[Cu(HF_2)(pyz)_2]SbF_6$. Quantum-Monte-Carlo (QMC) simulations of Heisenberg $S = 1/2$ square-lattice AFMs suggest that finite interlayer interactions may also give rise to LRO at $T > 0$ [53] and, in this model, the measured $k_B T_C/J_{pyz} = 0.32$ ratio for $[Cu(HF_2)(pyz)_2]SbF_6$ implies that $|J_{FHF}|/J_{pyz} \approx 9 \times 10^{-3}$ [45]. However, little is known about the sign of J_{FHF} and one of aims of this chapter is determine this from the results of NPD measurements.

An additional interest in Q2D Heisenberg $S = 1/2$ AFMs derives from the results of linear spin-wave theory calculations [13,98] and renormalization group analysis of the non-linear sigma model [97], which together imply that each square-lattice plane extracted from these systems lies within the renormalized classical regime at $T = 0$; that is, the material adopts antiferromagnetic LRO at zero-temperature but the size of the ordered moment is anticipated to be reduced by a factor of approximately 0.6 from its paramagnetic value due to QFs [13, 98]. The magnitude of the ordered Cu^{2+} moment in $[Cu(HF_2)(pyz)_2]SbF_6$ is determined from the results of NPD at 1.5 K in this chapter to further examine the extent to which this AFM maps onto the predictions for the Heisenberg $S = 1/2$ model.

Contrastingly, $[Ni(HF_2)(pyz)_2]SbF_6$ is a quasi-one-dimensional (Q1D) $S = 1$ AFM that adopts LRO at temperatures below $T_C = 12.2$ K [47]. The published [47] results of ligand field-theory (LFT) calculations imply that the individual $S = 1$ moments exhibit an intrinsic easy-plane single-ion anisotropy $D/k_B \approx 11.2$ K, while density-functional theory (DFT) simulations [47] suggest that the two unpaired electrons in each of the Ni^{2+} $d_{x^2-y^2}$ and d_{z^2} suborbitals gives rise to a delocalization of spin-density over both the pyz and HF_2^- ligand types resulting in a spatial-exchange anisotropy of the order $J_{FHF}/J_{pyz} \approx 5$. One estimate of $J_{FHF}/k_B \approx 11.3$ K is obtained by fitting the measured powder linear susceptibility to a Heisenberg $S = 1$ spin-chain model [191], however extracting precise experimental estimates of the magnetochemical parameters D, J_{FHF} and J_{FHF} has thus far proven difficult for this compound owing to the limitation of powdered samples.

Part of this chapter is dedicated to characterizing the sign and size of the single-ion anisotropy and spin-exchange interactions of $[Ni(HF_2)(pyz)_2]SbF_6$. The methods used to extract D from thermodynamic measurements of the weakly-

coupled polymeric Ni^{2+} complex in Chapter 4 are not likely to be applicable to this work owing to the comparable sizes of J_{FHF} and D in $[Ni(HF_2)(pyz)_2]SbF_6$. Furthermore, the ratio $J_{\text{FHF}}/D \approx 1$ for compound of the present study makes fitting the linear powder susceptibility to a one-dimensional easy-plane $S = 1$ AFM model [192] an unreliable means to extract independent estimates of D and J_{FHF} since these parameters become coupled during the fitting procedure [77]. In this chapter, the sign of D, J_{FHF} and J_{pyz} are first uniquely determined from NPD experiments and, while a semi-classical model interpretation of the results of pulsed-field powder magnetization $M(H)$ measurements is used to estimate D and the average quantity $(2J_{\text{FHF}} + 4J_{\text{pyz}})$, an inelastic neutron scattering (INS) study of a powdered sample is found to be necessary in order to unambiguously determine unique values for the three magnetochemical parameters.

The results [68] of QMC simulations for Q1D $S = 1$ AFMs predict that isolated chains of spins with $D > 0$ exhibit a Haldane ground-state that yields to a quantum paramagnet (QP) phase once the ratio of the single-ion anisotropy to the intrachain spin-exchange exceeds ≈ 0.97 (e.g. Fig. 1.11). The overall effect of introducing finite interchain spin-exchange interactions in these systems, meanwhile, is to stabilize antiferromagnetic LRO. The expectation that $D/J_{\text{FHF}} \approx 1$ and $J_{\text{pyz}}/J_{\text{FHF}} < 1$ for $[Ni(HF_2)(pyz)_2]SbF_6$ is intriguing as these ratios imply that this particular AFM is an example of a real system that lies in close proximity to the QCP that separates LRO from the two distinct quantum disordered phases and one further aim of this chapter is to use the results of NPD measurements to determine a precise magnetic ground state for $[Ni(HF_2)(pyz)_2]SbF_6$ and, along with the refined estimates of D/J_{FHF} and $J_{\text{pyz}}/J_{\text{FHF}}$, to position this material on the theoretical phase diagram for Q1D $S = 1$ AFMs.

Prior to this project, the magnetic properties of $[Co(HF_2)(pyz)_2]SbF_6$ were unpublished. In general, complexes comprised of octahedrally coordinated Co^{2+} ions are anticipated to exhibit a strong spin-orbit coupling interaction [34] and, consequently, the magnetic properties of these materials are oftentimes accounted for with an effective spin-1/2 Hamiltonian for $T < 30$ K [193]. This can be seen, for instance, in the polymeric materials $[Co(pyO)_6]X_2$ (pyO = pyridine-N-oxide; $X = ClO_4^-$, BF_4^-, NO_3^- or I^-) [194–196] and $Co(pyz)_2X_2$ ($X = Cl^-$ or Br^-) [193] for which the CEF and spin-orbit interactions combine to give rise to a bistable Kramers doublet ground spin-state within each Co^{2+} ion. In this work, the results of a NPD and powder C_p experiments of $[Co(HF_2)(pyz)_2]SbF_6$ combine to show that this AFM adopts LRO for $T \leq 7.1(1)$ K wherein the high-spin ($S = 3/2$) Co^{2+} ions have an Ising character. Finally, an effective spin-half model is employed to

model the results of powder electron spin-resonance (ESR) and $M(H)$ measurements in order to estimate the anisotropic g-tensor components and the strength of the average spin-exchange interactions along the pyz and HF_2^- ligands.

5.2 Experimental Details

5.2.1 Neutron scattering

(a) Wish diffractometer measurements: Time-of-flight NPD data are obtained from finely-ground partially-deuterated samples of $[M(HF_2)(\text{pyz-}d_4)_2]SbF_6$ (M = Cu^{2+}, Ni^{2+} or Co^{2+}) using the Wish diffractometer at the ISIS Neutron and Muon Source, part of the Rutherford Appleton Laboratory (RAL), UK [136]. Here [and in part (b)], pyz ($C_4H_4N_2$) is replaced with pyz-d_4 ($C_4D_4N_2$) to reduce the overall incoherent scattering cross section of the materials and thereby increase the overall signal-to-background ratio of Bragg reflections observed in an experiment. The measurements of the Cu^{2+} and Co^{2+} congeners are conducted by L. Chapon and P. Manuel (both ISIS, RAL, UK), while the measurements of the Ni^{2+} compound are performed by P. Manuel (ISIS, RAL, UK) and R. D. Johnson (University of Oxford, UK). The experiments use ≈ 1 g of the Cu^{2+} and Co^{2+} materials and 1.8 g of the Ni^{2+} compound, which are loaded into separate V cans in an inert He environment. NPD patterns are collected at 1.5 and 5 K for $[Cu(HF_2)(\text{pyz-}d_4)_2]SbF_6$, 4 and 10 K for $[Co(HF_2)(\text{pyz-}d_4)_2]SbF_6$, and at eleven individual setpoints in the range $1.5 \leq T \leq 20$ K for $[Ni(HF_2)(\text{pyz-}d_4)_2]SbF_6$; i.e., above and below the respective T_C values. The low-T Rietveld refinement of the chemical and magnetic structures of each compound is performed by R. D. Johnson (Oxford, UK) and implemented in FULLPROF [197]. The full interpretation of the results of these NPD studies forms part of this work.

(b) DCS measurements: Time-of-flight inelastic neutron scattering measurements are carried out on a powdered sample of $[Ni(HF_2)(\text{pyz-}d_4)_2]SbF_6$ using the Disc Chopper Spectrometer (DCS) at the National Institute of Standards and Technology (NIST), Gaitersburg, USA. These experiments form part of this project and are performed in collaboration with J. L. Manson (Eastern Washington University, USA), C. M. Brown (NIST, Gaitersburg, USA), and M. B. Stone (Oak Ridge National Laboratory, USA). The measurements use 1.8 g of powdered material, which is loaded into a cylindrical Al can in a ^{4}He atmosphere. The sample holder is sealed with In wire and foil, masked with Cd, and lowered into a He-cryostat. With a 3.7 Å monochromatic neutron beam incident on the sample, histograms of

the scattered neutron intensity are recorded at 1.6, 10 and 20 K as a function of the energy and momentum transferred to the sample. The data reduction is performed in MSLICE, part of the DATA ANALYSIS AND VISUALIZATION ENVIRONMENT package [198]. A background count rate of 27 counts per detector per hour is subtracted from histograms plotted (below) at constant T, while this correction factor is not applied to data presented as a difference between two measurements. The spin-wave analysis in Section 3.2 is performed by M. B. Stone (Oak Ridge, USA) using the numerical powder average spin-wave simulation package SPINW [199] in MATLAB [140].

5.2.2 Quasistatic and pulsed-field magnetometry

(a) SQUID Magnetometry: A 17.9 mg single-crystal sample of the Cu^{2+} complex is secured inside a gelatin capsule with cotton wool and a Quantum Design™ (QD) Magnetic Property Measurement System (MPMS) is used to follow the magnetic moment M as a function of: (i) a quasistatic applied magnetic field $\mu_0 H \leq 7$ T at 2 K, and (ii) temperatures $T \geq 1.8$ K with $\mu_0 H = 0.05$ or 0.1 T. The linear molar susceptibility χ_{mol} is derived from the results of experiment (ii) via the relation $\chi_{\text{mol}} = M/(nH)$ where n is number of moles of the sample. Both measurements (i) and (ii) consider various orientations of H with respect to the plane of the single-crystal sample (see Section 5.3.1). Experiments at the University of Warwick (UK) are also performed to monitor $\chi_{\text{mol}}(T)$ for three separate samples of the Ni^{2+} congener (one fully-hydrogenated and two partially-deuterated) using $\mu_0 H = 0.1$ T.

(b) VSM Magnetometry: An Oxford Instruments™ vibrating sample magnetometer (VSM) is used in this project to monitor the magnetic moment M of a powdered $[Co(HF_2)(pyz)_2]SbF_6$ sample. The material is pressed into a pellet, attached to a polyether ether ketone rod with vacuum grease and further secured with polytetrafluoroethene tape, before M is followed for $\mu_0 H \leq 12$ T at quasistatic temperatures in the range $1.4 \leq T \leq 8$ K. A separate experiment of this work is performed by A. J. Steele in collaboration with S. J. Blundell (both University of Oxford, UK) to follow the temperature dependence of the M for $4 \leq T \leq 305$ K with $\mu_0 = 0.1$ T. The analysis of the results of both VSM experiments forms part of the work preformed in this chapter.

(c) Pulsed-field magnetometry: Compensated coil extraction magnetometer measurements are performed on polycrystalline samples of $[Ni(HF_2)(pyz)_2]SbF_6$ and $[Co(HF_2)(pyz)_2]SbF_6$ using the capacitor-driven short pulse magnet at the Na-

tional High Magnetic Field Laboratory (NHMFL), Los Alamos, USA. J. Singleton (NHMFL) performed the measurements on both compounds, while S. Chikara, H. Lu and V. Zapf collaborated on the magnetometry investigation of the Ni^{2+} material. The results of a published [76] pulsed-field powder magnetometry investigation of $[Cu(HF_2)(pyz)_2]SbF_6$ are also reanalyzed in this work. For this system, an $M(H)$ trace obtained at 0.5 K is interpolated to an interval of $\mu_0\Delta H = 0.05$ T, smoothed with a 10 point adjacent averaging window, differentiated with respect to H, and then smoothed once more (as above) to examine the H dependence of the differential susceptibility of $\mathrm{d}M/\mathrm{d}H$. An error of ± 0.5 T is attributed to the $\mu_0 H$ positions of features derived from the $\mathrm{d}M/\mathrm{d}H$ curve owing to the data processing method applied here.

5.2.3 Heat capacity

Zero-field heat capacity C_p measurements of $[Ni(HF_2)(pyz)_2]SbF_6$ for $T \leq 300$ K are collected in this work using a QD Physical Property Measurement System and a 1.91(5) mg powdered sample, which is pressed into a pellet. Experiments are repeated in quasistatic $\mu_0 H \leq 9$ T to examine C_p at temperatures close to T_C. Additional C_p measurements of $[Co(HF_2)(pyz)_2]SbF_2$ are recorded by P. J. Baker (ISIS, RAL, UK). These experiments, which are analyzed as part of this work, utilize a 4.4(1) mg polycrystalline sample and monitor C_p in zero-field for $2 \leq T \leq 200$ K, while C_p is monitored at low temperatures (close to T_C) in quasistatic $\mu_0 H \leq 12$ T.

5.2.4 Electron spin-resonance

High-frequency powder ESR measurements of $[Co(HF_2)(pyz)_2]SbF_6$ are collected and analysed by J. Liu, D. Kaminski and A. Ardavan (University of Oxford, UK) using the homodyne transmission spectrometer at NHMFL, Tallahassee (USA) [200]. A phase-locked oscillator along with a series of frequency ν multiplies and amplifiers provides a quasicontinuous ν coverage for $222.4 \leq \nu \leq 609.6$ GHz. A finely ground is sample placed in a Teflon™ container and the differential microwave transmission intensity is recorded as a function of $\mu_0 H \leq 14$ T with a cold bolometer detector. Quasistatic sample temperatures $T \geq 5$ K are maintained with a ^{4}He flow cryostat.

5.2.5 Sample preparation

The fully-hydrogenated and partially-deuterated samples are prepared by J. L. Manson, S. G. Schwalbe, P. M. Spurgeon, H. E. Tran, P. K. Peterson, J. F. Corbey, and

J. A. Villa at Eastern Washington University (USA). Full details of the synthesis procedures may be found in Refs. [47, 59, 76].

5.2.6 Simulations

The powder-average magnetization of $[Ni(HF_2)(pyz)_2]SbF_6$ is calculated in MATLAB using the semi-classical Monte-Carlo methodology detailed in Section 2.7. The simulation uses the published g-factor [47], and the values of $D/k_B = 13.3$ K, $J_{FHF}/k_B = 10.3$ K and $J_{pyz}/k_B = 1.43$ K derived from the results of INS measurements performed on a powdered sample (see below, Ref. [77]).

5.3 Results and discussion

5.3.1 $[Cu(HF_2)(pyz)_2]SbF_6$

(a) Neutron powder diffraction: The results of time-of-flight NPD measurements of $[Cu(HF_2)(pyz\text{-}d_4)_2]SbF_6$ at 1.5 K [Fig. 5.2(a)] reveal a series of Bragg peaks that occur via the coherent diffraction of neutrons from the sample. The reflections originating from nuclear scattering are removed from these data by subtracting a representative paramagnetic NPD pattern obtained at 5 K and the difference plot [Fig. 5.2(a), inset] exhibits two small maxima. These peaks are attributed to neutrons that scatter from planes of antiferromagnetically ordered Cu^{2+} moments, firstly since the scattering intensity is noted to be weaker at smaller plane spacings d, which is consistent with the expected nature of the magnetic form factor (e.g. Ref. [133]); and secondly because the two features are centred on d values that do not correspond to those measured for the nuclear Bragg reflections.

The chemical unit cell of $[Cu(HF_2)(pyz\text{-}d_4)_2]SbF_6$ at 1.5 K is determined by starting from a Rietveld refinement of the high-T published [76] crystal structure of the fully hydrogenated congener $[Cu(HF_2)(pyz)_2]SbF_6$ [59]. During this analysis each pyz H atom is replaced with deuterium, the isotropic thermal parameters for H atoms are constrained to a constant while those for the independent F atoms are coupled to each other. $[Cu(HF_2)(pyz\text{-}d_4)_2]SbF_6$ is found to be isostructural to the fully hydrogenated complex and the lattice parameters of the deuterated sample (Table 5.1) are furthermore measured to be smaller but within $\approx 0.8\%$ of those measured [76] for $[Cu(HF_2)(pyz)_2]SbF_6$ at 90 K. Collectively, these observations indicate that the magnetic properties of the two polymeric complexes are likely to be comparable. The point group at each Cu^{2+} lattice site is $\bar{4}m2$; i.e., the two axial fluorine atoms of the CuN_4F_2 octahedra are equidistant from the spin centre,

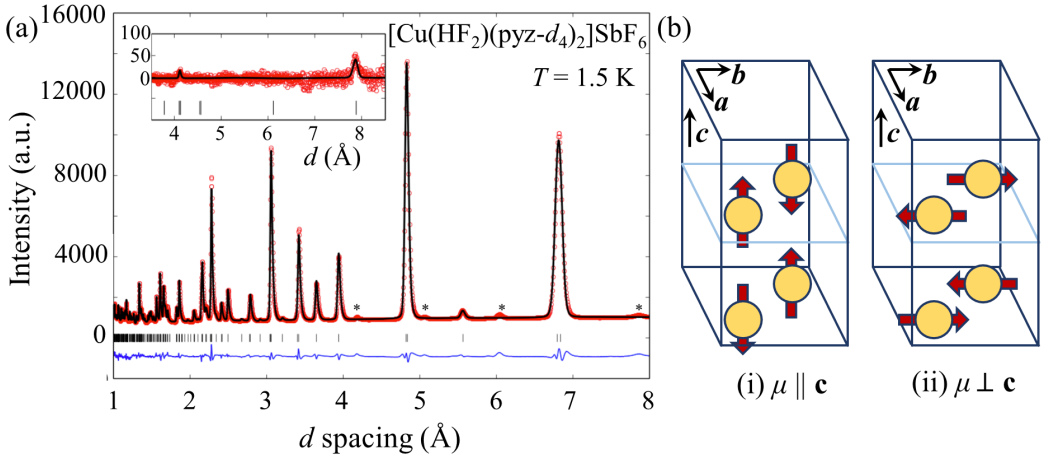

Figure 5.2: **(a)** Time-of-flight NPD pattern for $[Cu(HF_2)(pyz\text{-}d_4)_2]SbF_6$ at 1.5 K (points), collected with detector Bank 2 of the Wish diffractometer. The reflected neutron intensity is plotted in arbitrary units (a.u.) as a function of the plane spacing d of scatterers (nuclei/moments) in the crystal. The solid line is the result of a Rietveld refinement of the nuclear scattering, the ticks are nuclear reflections indexed in the $P4/nmm$ space group, and the blue line is the difference between the model and measured data. The asterisks indicate peaks derived from a small, as yet unidentified, impurity phase. *Inset:* Difference plot of the scattering intensity between measurements recorded at 1.5 K and 5 K (plotted on the same intensity scale as the main panel). The solid line is the refined magnetic scattering model and the ticks mark reflections indexed with the propagation vector $\mathbf{k} = (0, 0, 1/2)$ (r.l.u.). **(b)** At 1.5 K the ordered Cu^{2+} moments μ (red arrows) may be: (i) parallel (||); or (ii) perpendicular ($\perp$) to the **c**-axis. The Ni^{2+} and Co^{2+} congeners adopt the spin states depicted in panels (ii) and (i) respectively (see below).

the four equatorial Cu-N bond lengths are all equal, and each of the N-Cu-F bond angles are 90°. The ratio of the Cu-F to Cu-N bond lengths is measured to be 1.08 at 1.5 K, which confirms that the Jahn-Teller axis of this Q2D square-lattice AFM is perpendicular to the $[Cu(pyz)_2]^{2+}$ sheets for $T < T_C$.

The magnetic Bragg reflections of $[Cu(HF_2)(pyz\text{-}d_4)_2]SbF_6$ observed at 1.5 K are indexed by the commensurate propagation vector $\mathbf{k} = (0, 0, 1/2)$, written here in reciprocal lattice units (r.l.u.). This implies that magnetic supercell is twice the height of chemical cell, which in turn supports the conclusion that the HF_2^- ligands give rise to an antiferromagnetic spin-exchange interaction. Symmetry analysis of the 1.5 K structure and **k**-vector suggests that there are four possible ground-spin states for this system. The Cu^{2+} moments must be collinear and antiparallel with respect to their nearest neighbours along the bifluoride bridges, but J_{pyz} may be ferromagnetic or antiferromagnetic and in each case the spins may be parallel or

Table 5.1: Refinement details for the NPD measurements of $[M(HF_2)(pyz\text{-}d_4)_2]SbF_6$ (M = Cu^{2+}, Ni^{2+} or Co^{2+}), where T is the temperature of the experiment; a, b and c are the lattice vectors; V is the unit cell volume; Z is the number of chemical formulae per structural unit cell; **k** is the magnetic propagation vector in reciprocal lattice units (r.l.u.); and μ is the ordered moment in Bohr magnetons. The Wish diffractometer detector Banks 2 and 9 have the same $|\langle 2\theta \rangle| = 58.330°$ average in-plane scattering angles, while Bank 5 is positioned at $\langle 2\theta \rangle = 152.827°$. The goodness-of fit parameter $R_{\text{Bragg}} = \sum |I_{\text{obs}} - I_{\text{calc}}| / \sum |I_{\text{obs}}|$, where I_{obs} and I_{calc} are the observed and calculated intensities, respectively, and the sums run over all measurements; while R_{mag} is analogously defined but is only applied to the magnetic scattering.

Parameter (units)	Fitted values (errors)		
M	Cu^{2+}	Ni^{2+}	Co^{2+}
Chemical formula	$CuC_8HD_8N_4SbF_8$	$NiC_8HD_8N_4SbF_8$	$CoC_8HD_8N_4SbF_8$
T (K)	1.5	1.5	4
Space group	$P4/nmm$	$P4/nmm$	$P4/nmm$
a, b (Å)	9.6749(1)	9.8933(1)	10.0225(8)
c (Å)	6.7981(3)	6.4318(2)	6.4287(5)
V (Å^3)	636.33(3)	629.53(2)	645.76(9)
Z	2	2	2
k (r.l.u.)	(0, 0, 1/2)	(0, 0, 1/2)	(0, 0, 1/2)
μ (μ_B)	0.6(1)	2.03(7)	3.02(6)
Detector	Bank 2	Banks 2 & 9	Banks 2/5
R_{Bragg}	0.0256	0.0362	0.0402/0.0764
R_{mag}	0.1700	0.0589	0.050/0.134

perpendicular to the **c**-axis. The positions of the magnetic Bragg reflections of $[Cu(HF_2)(pyz\text{-}d_4)_2]SbF_6$ (and, in fact, the results of magnetometry experiments, see below or Ref. [45,76]), are incompatible with a model in which J_{pyz} is ferromagnetic. This leaves two potential antiferromagnetic ground states [Fig. 5.2(b), panels (i) and (ii)]. In general, the structure factors of models (i) and (ii) give rise to simulated NPD patterns for which the magnetic Bragg peaks occur at the same d-spacings but with different relative intensities. However, this property cannot be used to assign a unique ground-state to $[Cu(HF_2)(pyz\text{-}d_4)_2]SbF_6$ owing to the weak amplitude of the observed reflections in Fig. 5.2(a) (inset). Using models (i) and (ii) in turn, the chemical structure and the size of the ordered Cu^{2+} moment μ_{Cu} are simultaneously refined against the absolute intensities of the 1.5 K NPD data. For each model, μ_{Cu} is consistent with a value of $0.6(1)\mu_B$ per ion, which is much smaller than the paramagnetic value $g\mu_B S = 1.07(1)\mu_B$ that is implied from the size of powder-average g-factor extracted from ESR [45] and magnetometry measurements [76].

The results of a previous [76] μ^+SR investigation of $[Cu(HF_2)(pyz)_2]SbF_6$ highlight the significance of the small value of μ_{Cu} measured at 1.5 K. For experiments performed on magnetically ordered systems μ^+SR follows the spin-polarization of a population of muons implanted into a sample, which undergoes a coherent precession at a frequency ν that is proportional to the local internal magnetic flux generated by the ordered moments in the crystal (see, for instance, Ref. [99]). For zero-field μ^+SR experiments performed on a polycrystalline sample of $[Cu(HF_2)(pyz)_2]SbF_6$ at constant $T < T_C$, individual measurements of ν are fitted to a temperature dependence of the form $[1 - (T/T_C)^\alpha]^\beta$, where $\alpha = 2.8(1)$ and $\beta = 0.34(1)$ [76]. This expression implies that ν has reached $\approx 98\%$ of its $T = 0$ limiting value at 1.5 K and, consequently, the measurement of $\mu_{Cu} = 0.6(1)\mu_B$ at 1.5 K is also likely to be close to it zero-temperature value. It is therefore concluded that the ordered Cu^{2+} moment is reduced by quantum (as oppose to thermal) fluctuations that persist in the magnetically ordered phase.

The reduced ordered moment of $[Cu(HF_2)(pyz\text{-}d_4)_2]SbF_6$ is comparable with the results of single-crystal neutron diffraction measurements performed on the related Q2D $S = 1/2$ polymeric AFMs $CuF_2(H_2O)_2(pyz)$ and $Cu(pyz)_2(ClO_4)_2$, for which the respective μ_{Cu} values are $0.60(3)\mu_B$ [201] and $0.47(5)\mu_B$ [101]. In the present study, the measured value of μ_{Cu} is furthermore in good agreement with the results of linear spin-wave perturbation theory calculations for ideal square-lattice Heisenberg $S = 1/2$ AFMs, which predict that ordered moment is reduced by a factor 0.61 with respect to the paramagnetic moment [13]. In this model, spin-flip type excitations at $T = 0$ are anticipated to propagate across the square-lattice planes and interact with the ground-state so as to generate further excitations, and it is by summing over the creation, propagation and annihilation of all possible fluctuations of this type that leads to the overall reduction in the time-averaged moment size.

(b) Quasistatic and pulsed-field magnetometry: Linear susceptibility χ_{mol} measurements are performed on a single-crystal sample of $[Cu(HF_2)(pyz)_2]SbF_6$ with a quasistatic magnetic field $\mu_0 H = 0.1$ T [Fig. 5.3(a)] that is applied parallel (circles) or perpendicular (triangles) to the z-axis, defined here as the direction perpendicular to the plane of the sample. For $T > J_{pyz}/k_B$ the predominant thermal excitations of $[Cu(HF_2)(pyz)_2]SbF_6$ are expected to be quasi-independent spin-flips and this gives rise to the measured Curie-Weiss behaviour at these temperatures. Each $\chi_{mol}(T)$ trace furthermore exhibits a broad maximum at $T = 12(2)$ K and a local minimum at a temperature that is consistent with the published T_C value [45,76]. The broad maximum in χ_{mol} occurs at $T \approx J_{pyz}/k_B$ and is attributed to the forma-

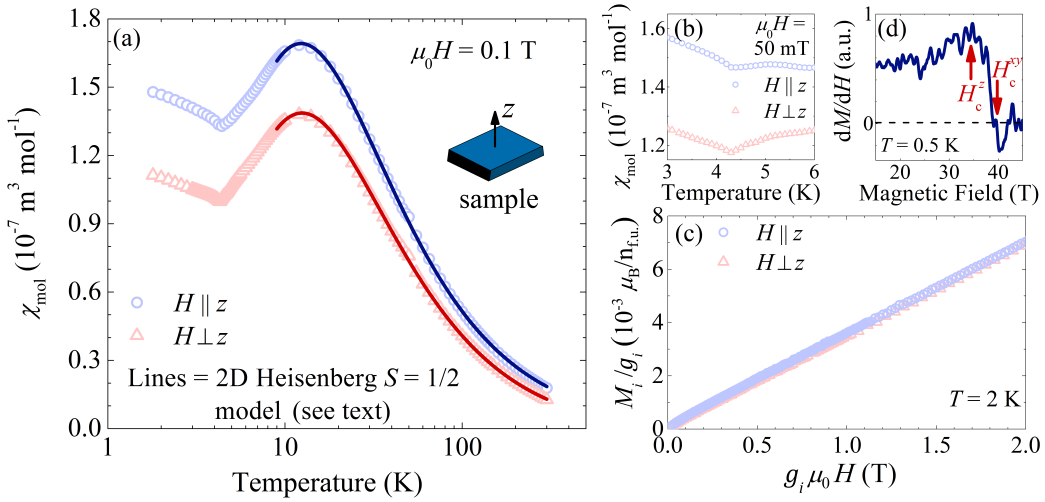

Figure 5.3: Linear susceptibility $\chi_{\rm mol}$ of $[Cu(HF_2)(pyz)_2]SbF_6$ for a magnetic field **(a)** $\mu_0 H = 0.1$ T; and **(b)** $\mu_0 H = 0.05$ T, which is applied parallel (||) or perpendicular ($\perp$) the z-axis [see panel (a) inset]. The data for $T \geq 8$ K are fitted to a Heisenberg S =1/2 square-lattice (2D) AFM model (solid lines, see text). **(c)** In this work, the single-crystal magnetization (normalized to the g-factor) M/g_i scales linearly with $g_i \mu_0 H$ ($i = xy$ or z). **(d)** The differential susceptibility dM/dH vs. H at 0.5 K, derived from the published [76] results of a pulsed-field powder magnetometry study, exhibits an anisotropic saturation field (arrows, see text).

tion of antiferromagnetic clusters within individual Cu-pyz layers, wherein the orientations of neighbouring Cu^{2+} moments are instantaneously colinear and antiparallel. As T is reduced further the size of these clusters (i.e. the intraplane spin-correlation length ξ) increases and, given that the ordered moment $\mu_{\rm Cu} = 0.6\mu_{\rm B}$ [see part (a)], renormalization group analysis of the nonlinear sigma model (Eq. 1.22) [97] predicts that ξ is ≈ 10 times the square-lattice constant at $T = T_{\rm C}$.

A model spin-Hamiltonian for $[Cu(HF_2)(pyz)_2]SbF_6$ takes the form

$$\hat{\mathcal{H}} = \sum_{\langle i,j \rangle} J_{ij} \left[\hat{S}_i^x \hat{S}_j^x + \hat{S}_i^y \hat{S}_j^y + (1 - \Delta_{ij}) \hat{S}_i^z \hat{S}_j^z \right] + \mu_0 \mu_{\rm B} \sum_i \mathbf{H}^{\rm T} \boldsymbol{g} \mathbf{S}_i. \qquad (5.1)$$

Here $\mathbf{S}_i = (\hat{S}_i^x, \hat{S}_i^y, \hat{S}_i^z)^{\rm T}$ is a column vector of $S = 1/2$ operators; the indices label each spin; the sum runs over unique pairs of neighbouring spins; $J_{ij} = J_{\rm pyz/FHF}$ for moments linked via pyz/HF_2, while finite $\Delta_{ij} = \Delta_{\rm pyz/FHF}$ values allows for non-Heisenberg intraplane/interplane exchange interactions; $\mathbf{H}$ is an applied magnetic field; and finally $\boldsymbol{g} = {\rm diag}(g_{xy}, g_{xy}, g_z)$ is the anisotropic g-tensor.

For $T \geq 8$ K the measured $\chi_{\rm mol}$ curves of Fig. 5.3(a) are fitted to a square-lattice Heisenberg $S = 1/2$ model [61, 202] that utilizes the spin-Hamiltonian of

Eq. 5.1 with J_{FHF} and $\Delta_{\mathrm{pyz/FHF}}$ fixed to zero. Additionally, a small constant diamagnetic contribution to the linear susceptibility measurement is included in the fitting function ($\chi_0 = -3.2 \times 10^{-9}$ m^3 mol^{-1}), which accounts for a small T independent contribution to the measurement from the sample holder and the molecular components of the sample (e.g. Ref [78]). The fitted curves [Fig. 5.3(a), solid lines] provide a good representation of the measured data, where the separate amplitudes of the two χ_{mol} measurements are accounted for with $g_z = 2.28(3)$ and $g_{xy} = 2.06(2)$. The quantity $\left[\frac{1}{3}(g_z^2 + 2g_{xy}^2)\right]^{1/2} = 2.14(3)$ is consistent with previous ESR and magnetometry measurements of powder average g-factor [45, 76], while the anisotropic g-tensor also points to a finite spin-orbit coupling interaction in this material. In the present study, the fitted intraplane spin-exchange constants of the two χ_{mol} traces suggest $J_{\mathrm{pyz}}/k_{\mathrm{B}} = 13.3(1)$ K, which is in agreement with the published value of 13.3 K [45, 76]. When the in-plane H is rotated by approximately 45° about z with respect to the direction of the applied field for the measurements shown in panel (a), the fitted values of g_{xy} and J_{pyz} are found to be unchanged within the reported errors after accounting for a small difference in the T independent contribution to these measurements.

Pyz molecules have been observed to facilitate anisotropic intraplane spin-exchange interactions in several tetragonal and monoclinic Q2D $S = 1/2$ polymeric systems based upon on $[\mathrm{Cu(pyz)_2}]^{2+}$ plaquettes [35, 46]. This interaction, which is a consequence of spin-orbit coupling, results in typical values of $\Delta_{\mathrm{pyz}} < 7 \times 10^{-3}$ [35, 46] and provides a net energy gain for the Cu^{2+} moments to be orientated within the pyz layers at $T \leq T_{\mathrm{C}}$. In this model, χ_{mol} is expected to decrease on cooling for $T \leq T_{\mathrm{C}}$ when H is applied within the $[\mathrm{Cu(pyz)_2}]^{2+}$ sheets, while a local minimum in the linear susceptibility at $T \approx T_{\mathrm{C}}$ arises if H is applied perpendicular to this direction [35]. For $[\mathrm{Cu(HF_2)(pyz)_2}]\mathrm{SbF_6}$, $\chi_{\mathrm{mol}}(T)$ exhibits a minimum at $T \approx T_{\mathrm{C}}$ when the applied field $\mu_0 H = 0.1$ T is aligned parallel or perpendicular to the plane of the sample. Linear susceptibility measurements are repeated with $\mu_0 H = 50$ mT [Fig. 5.3(b)] and, while these experiments are likely to have a larger y-axis error compared to the results of panel (a) owing to the small absolute moment of the antiferromagnetic sample for $T \approx T_{\mathrm{C}}$, a local minimum in $\chi_{\mathrm{mol}}(T)$ is clearly reproducible for both orientations H. The $\chi_{\mathrm{mol}}(T)$ traces of panels (a) and (b) both imply that the Cu^{2+} moments are orientated perpendicular to H at $T < T_{\mathrm{C}}$, which most likely occurs such that each spin may cant slightly towards H so as to lower the total Zeeman energy of the sample. For this to be the case the last term in Eq. 5.1, which cannot exceed the energy scale of $g_z \mu_0 \mu_{\mathrm{B}} H S$ per spin, must be greater than the expectation value of $J_{\mathrm{pyz}} \Delta_{\mathrm{pyz}} \langle S^2 \rangle \approx J_{\mathrm{pyz}} \Delta_{\mathrm{pyz}} S(S+1)$ when $\mu_0 H > 50$ mT.

Thus, the linear susceptibility measurements of $[Cu(HF_2)(pyz)_2]SbF_6$ in this work are consistent with an upper bound of $\Delta_{pyz} \approx 3 \times 10^{-3}$.

Single-crystal magnetization M measurements of $[Cu(HF_2)(pyz)_2]SbF_6$ performed at $T = 2$ K with H parallel and perpendicular to z [Fig. 5.3(d)] reveal that M/g_i vs. $g_i\mu_0 H$ ($i = xy$ or z) follows a linear dependence across the measured applied magnetic field range. Given that a change in slope of $M(H)$ has previously been used as an indicator of non-Heisenberg intraplane spin-exchange interactions in related Q2D $S = 1/2$ AFMs [35, 46], the measured magnetization of $[Cu(HF_2)(pyz)_2]SbF_6$ implies that a Heisenberg spin model is appropriate for this high-symmetry tetragonal compound at $T \geq 2$ K. In the absence of direct evidence for non-Heisenberg spin-exchange interactions in $[Cu(HF_2)(pyz)_2]SbF_6$, the finite T_C value for this material is likely to be largely driven by non-zero interplane spin-exchange interactions. The results of QMC simulations for Q2D Heisenberg $S = 1/2$ AFMs relate the finite magnetic ordering temperature to the ratio of the interplane to intraplane spin-exchange interactions (Eq. 1.19) [53] and, given the measured values of $k_B T_C/J_{pyz} = 0.32$ and $J_{pyz}/k_B = 13.3$ K for $[Cu(HF_2)(pyz)_2]SbF_6$ [45, 76], this suggests that $J_{FHF}/k_B \approx 0.12$ K for this material where the sign of this term is deduced from the results of NPD (above).

Finally, the anisotropic g-factor of $[Cu(HF_2)(pyz)_2]SbF_6$ measured in this work is used to interpret the results of a previously published [76] pulsed-field powder magnetization study. At 0.5 K the magnetization is found to exhibit a slightly broadened approach towards saturation, which leads to a separation between the point at which the differential susceptibility dM/dH begins to decrease and when dM/dH reaches zero [Fig. 5.3(d)]. The results of QMC simulations for Q2D Heisenberg $S = 1/2$ AFMs [45] suggest that the saturation field of these materials scales with g^{-1} (Eq. 1.23) and, in cases where there is a g-factor anisotropy, this will lead to a difference in the saturation fields H_c^{xy} and H_c^z obtained when a magnetic field is applied perpendicular or parallel to the z-axis. If the two critical fields in dM/dH for $[Cu(HF_2)(pyz)_2]SbF_6$ at 34.9(5) T and 38.9(5) T are attributed to $\mu_0 H_c^z$ and $\mu_0 H_c^{xy}$ respectively [Fig. 5.3(d), arrows], the measured ratio of $H_c^{xy}/H_c^z = 1.11(3)$ is found to be in agreement with single-crystal measurement of the quantity $g_z/g_{xy} = 1.11(3)$. Thus, while a square-lattice Heisenberg model remains a good approximation to the spin Hamiltonian of this complex one effect of the spin-orbit coupling interaction is to give rise to a g-factor anisotropy (e.g. Ref [203]) that accounts for the measured range of saturation fields, while additional perturbations to the spin Hamiltonian such as non-Heisenberg intraplane spin-exchange interactions are likely to be small for $T > 2$ K and $\mu_0 H > 50$ mT compared to the finite interplane spin-exchange.

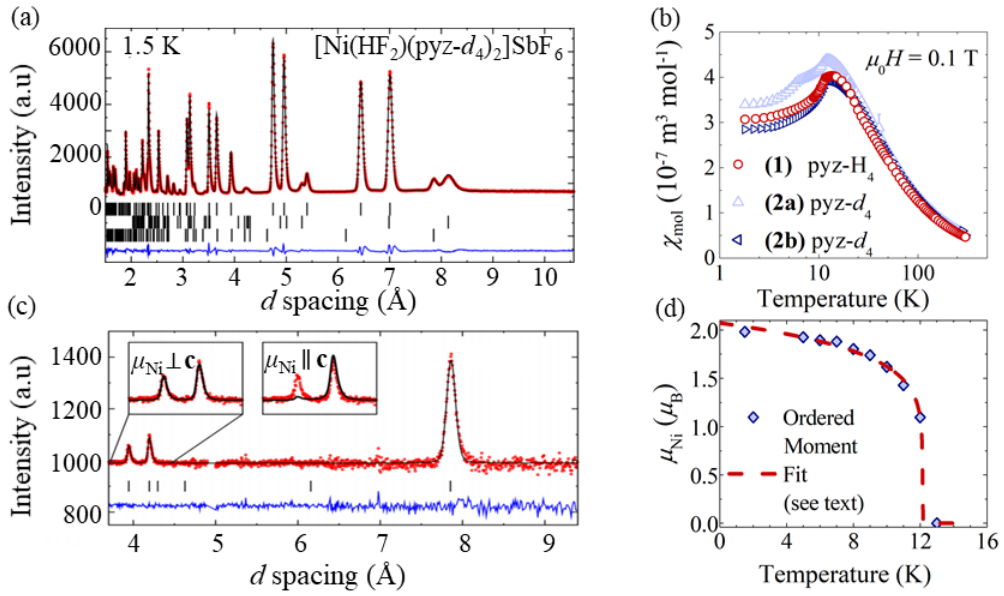

Figure 5.4: **(a)** Time-of-flight NPD pattern of $[Ni(HF_2)(pyz\text{-}d_4)_2]SbF_6$ at 1.5 K (points) measured with Bank 2 of the Wish diffractometer. The black line is the result of a Rietveld refinement of the data; first row of ticks are the nuclear Bragg peaks ($P4/nmm$); the second row corresponds to a 1.6% impurity of $[Ni(pyz)_2(H_2O)_2]FSbF_6$ ($Ibam$); and the third row are the magnetic reflections of $[Ni(HF_2)(pyz\text{-}d_4)_2]SbF_6$ indexed with $\mathbf{k} = (0, 0, 1/2)$ (r.l.u.). Blue line here [and in panel (c)] is the difference between the model and measured data. **(b)** χ_{mol} vs. T for $[Ni(HF_2)(pyz)_2]SbF_6$ (1); and $[Ni(HF_2)(pyz\text{-}d_4)_2]SbF_6$ (2a, 2b). Sample (2a) is measured with Wish, while sample (2b) is measured with DCS [see part (d)]. **(c)** The difference between the results of Wish NPD measurements at 1.5 and 20 K. The ticks mark the indexed magnetic Bragg peaks. *Inset:* Measured magnetic scattering (points) compared to two models (lines) in which the Ni^{2+} spins aligned $\perp$ or $\parallel$ to the **c**-axis. **(d)** Ordered Ni^{2+} moment μ_{Ni} vs. T fitted to a power law (see text).

5.3.2 $[Ni(HF_2)(pyz)_2]SbF_6$

(a) Neutron powder diffraction and linear susceptibility: The structure of $[Ni(HF_2)(pyz\text{-}d_4)_2]SbF_6$ (Table 5.1) is determined from the results of time-of-flight NPD measurements performed at 1.5 K [Fig. 5.4(a), points] and a by starting from a Rietveld refinement of the 15 K chemical structure of the fully hydrogenated sample, which has been previously determined from an independent microcrystal x-ray diffraction study [77]. The hydrogenated and deuterated congeners are found to be isostructural ($P4/nmm$) and this result, together with observation that the pyz and pyz-d_4 materials exhibit similar $\chi_{mol}(T)$ traces [Fig. 5.4(b), red and dark-blue points], implies the two compounds are likely to have similar magnetic properties.

Plotting the difference between the NPD patterns of $[Ni(HF_2)(pyz\text{-}d_4)_2]SbF_6$ obtained at 1.5 K and 20 K [Fig. 5.4(c)] reveals three maxima at d-spacings of 3.94 Å, 4.19 Å, and 7.85 Å. These reflections, which are only present in the data set collected at temperatures below $T_C = 12.2$ K, do not correspond to the positions of nuclear Bragg peaks and are therefore attributed to neutrons that diffract from planes of antiferromagnetically ordered Ni^{2+} moments [77]. The magnetic Bragg reflections are indexed with a commensurate propagation vector $\mathbf{k} = (0, 0, 1/2)$ (r.l.u.) and a magnetic supercell that has twice the height of the chemical unit cell implies that the Ni^{2+} moments are antiferromagnetically coupled along the HF_2^- bridges in the magnetically ordered phase.

A symmetry analysis of the chemical structure and **k**-vector implemented in ISODISTORT indicates that there are four potential magnetic ground states [77]. The Ni^{2+} moments must be colinear and antiparallel with respect to a neighbouring spin displaced along the **c**-axis, but pairs of coplanar moments linked via pyz may be either antiferromagnetically or ferromagnetically coupled and in each case the spins can adopt alignments that are parallel or perpendicular to the $[Ni(pyz)_2]^{2+}$ sheets. The measured d-spacings of the magnetic Bragg reflections of $[Ni(HF_2)(pyz\text{-}d_4)_2]SbF_6$ are inconsistent with the calculated structure factor of either model in which J_{pyz} is ferromagnetic. The two remaining antiferromagnetic ground-states are tested by comparing the relative intensity of magnetic Bragg peaks predicted by each model against the measured data [Fig. 5.4(b), inset]. The amplitudes of the measured magnetic reflections are only reproducible in an XY-antiferromagnetic (XY-AFM) model for which the ordered Ni^{2+} moments are projected along an arbitrary direction within the $[Ni(pyz)_2]^{2+}$ plane [e.g. Fig. 5.2(b), panel (ii)]. The measured NPD data are, however, insensitive to the precise orientation of the spins within these planes.

The structure and the size of the ordered Ni^{2+} moment μ_{Ni} are simultaneously refined against the results of NPD measurements performed for $1.5 \leq T \leq 12$ K [Fig. 5.4(d), points]. The T dependence of μ_{Ni} is modelled by an expression of the form $\mu_{Ni} \propto [1 - (T/T_C)]^{\beta}$ (dashed line), where the fitted values of T_C and β are 12.13(7) K and 0.141(1), respectively. Typically, quantum spin systems only obey a critical behaviour for $(1 - T/T_C) < 0.02$ [204] and the sparse density of measurements in this particular T range suggests that caution should be applied when interpreting β within a particular model. The ordered moment of $[Ni(HF_2)(pyz\text{-}d_4)_2]SbF_6$ at 1.5 K is found to be $\mu_{Ni} = 2.03(7)\mu_B$, which is consistent with the size of the paramagnetic moment $g\mu_B S \approx 2.08\mu_B$ deduced from the published powder-average g-factor [47]. While Q1D $S = 1$ AFMs may, in general, exhibit strong

QFs that can prevent the formation of a magnetic LRO altogether [68], the results of magnetization and INS measurements performed on a powdered sample of $[Ni(HF_2)(pyz)_2]SbF_6$ suggest that it is the precise ratios of D/J_{FHF} and J_{FHF}/J_{pyz} that act to stabilize magnetic LRO from the effects of QFs in this particular compound [see part (d)].

In summary, the results of NPD in this section suggest that a model spin Hamiltonian for $[Ni(HF_2)(pyz)_2]SbF_6$ may be written as

$$\hat{\mathcal{H}} = J_{pyz} \sum_{\langle i,j \rangle} \mathbf{S}_i \cdot \mathbf{S}_j + J_{FHF} \sum_{\langle i,j' \rangle} \mathbf{S}_i \cdot \mathbf{S}_{j'} + \sum_i \left[D(\hat{S}_i^z)^2 + g\mu_0\mu_B \mathbf{H} \cdot \mathbf{S}_i \right], \qquad (5.2)$$

where $\mathbf{S}$ is a column vector of $S = 1$ operators; the first and second sums run over unique pairs of spins within each layer and in adjacent layers respectively; while J_{pyz}, J_{FHF} and D are all positive. Eq. 5.2 is used in a discussion of the results of heat capacity, magnetometry and INS measurements performed on a powdered sample below.

(b) Heat capacity: The results of zero-field heat capacity C_p experiments performed on a powdered sample of $[Ni(HF_2)(pyz)_2]SbF_6$ exhibit a sharp maximum in C_p/T at 12.2(1) K, which is superimposed on a sloping background [Fig. 5.5(a) (points)]. The lattice contribution C_{latt} to the total sample heat capacity is determined by fitting the measured C_p/T curve to Eq. 1.10 for $32 \leq T \leq 300$ K (solid line). This analysis utilizes one Debye and two independent Einstein modes and the fitted phonon spectra is compared against those for the isostructural Cu^{2+} and Co^{2+} complexes in Table 5.2. Whilst the lattice heat capacity of the three isostructural compounds are all accounted for with the same number of phonon terms, the fitted amplitude and energy scale of the respective Debye and Einstein modes for each congener are reasonably distinct and an INS investigation is planned to further investigate the differences between the phonon spectra of these systems.

In the present study, the zero-field magnetic heat capacity of the Ni^{2+} congener ($C_{mag} = C_p - C_{latt}$) is integrated via Eq. 1.12 for $T \leq 30$ K, where C_{mag} is assumed to be zero at $T = 0$ K. The estimated change in spin-entropy S_{mag} that results from cooling the material from the paramagnetic phase is consistent with a value of $R\ln 3$ per ion [Fig. 5.5(a), inset]; i.e. the full value expected for a $S = 1$ system that adopts magnetic LRO. One further observation is that S_{mag} is already significantly lower than its high-T value at T_C. This might be attributable to a reduction in the spin-degrees of freedom that results from the build up of antiferromagnetic spin-correlations along the HF_2^- chains at $T > T_C$ in this Q1D $S = 1$ AFM, or through a thermal depopulation of spin-states that are separated in energy

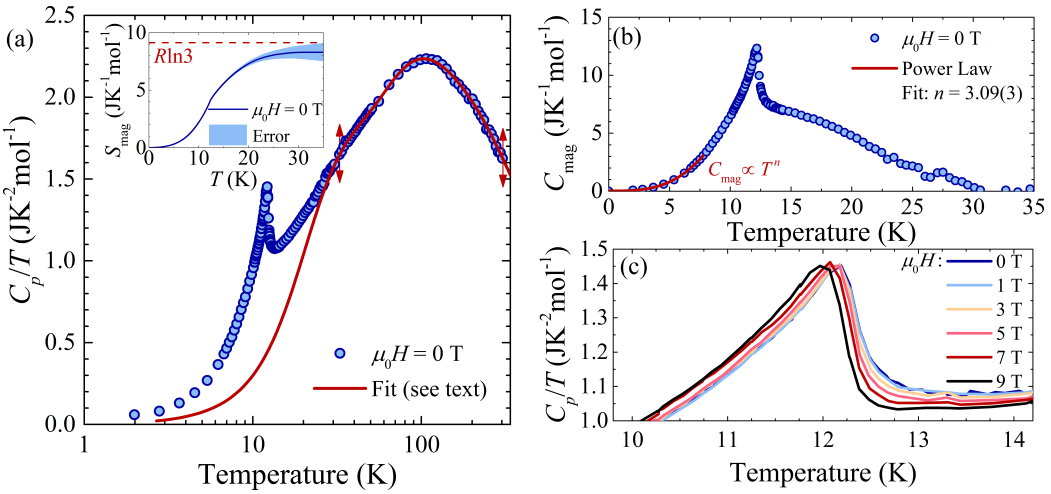

Figure 5.5: **(a)** Zero-field powder heat capacity C_p of $[Ni(HF_2)(pyz)_2]SbF_6$ plotted as C_p/T (points) and fitted for $T \geq 32$ K to a phonon model (Eq. 1.10, solid line). *Inset:* The change in spin-entropy S_{mag} on cooling from 30 K is consistent with a value of Rln3 per Ni^{2+} ion. **(b)** The zero-field magnetic heat capacity C_{mag} (points) exhibits a sharp maximum at 12.2 K. The data for $T \leq 8$ K are fitted to a power law T^d (solid line), which yields a fitted exponent $d = 3.09(3)$. **(c)** For C_p/T measurements repeated with $\mu_0 H \leq 9$ T, T_C is slightly reduced with increasing H.

owing to D.

In cases when antiferromagnetic spin-wave excitations are the dominant contribution to C_{mag} for $T < T_C$, the magnetic heat capacity is predicted to scale as T^d where d is the spatial dimensionality of the spin-exchange network [205]. The zero-field $C_{mag}(T)$ curve for $[Ni(HF_2)(pyz)_2]SbF_6$ [Fig. 5.5(b), points] is fitted to a power-law for $T \leq 8$ K (line) yielding a good representation of the measured T dependence with the exponent $d = 3.09(3)$. This result is in agreement with a previous estimate of d that was extracted from a low-T measurement of C_p [47], but the analysis in this chapter specifically excludes a Debye phonon contribution to the total heat that also obeys a T^3 dependence low temperatures. For comparison, a similar analysis of the magnetic heat capacity of the Q2D Cu^{2+} congener outputs $d = 2.17(1)$ [76]. Together, these fitted exponents imply that the J_{FHF}/J_{mag} ratio is likely to be much closer to one in the Ni^{2+} system and this necessitates the inclusion of both of the pyz and HF_2^- spin-exchange constants in the analysis of the results of magnetometry and INS measurements performed on a powdered sample (below).

Finally, the magnetic ordering temperature $[Ni(HF_2)(pyz)_2]SbF_6$ is found to be suppressed by approximately 1.6% under the application of quasistatic applied magnetic fields $\mu_0 H$ up to 9 T [Fig. 5.5(c)]. The overall reduction of T_C with increas-

Table 5.2: The fitted Debye (D) and Einstein ($E_{1,2}$) modes of $[M(HF_2)(pyz)_2]SbF_6$ derived from powder C_p measurements. Here, A_i and θ_i (i = D, $E_{1,2}$) are the respective amplitude and temperature of each mode. Fitted errors are given in brackets. Data for the Cu^{2+} complex are from Ref. [76]. The phonon models are fitted to C_p measurements up to $T = 200$ K for the Cu^{2+} and Co^{2+} compounds, and $T = 300$ K for the Ni^{2+} material.

M	A_D ($JK^{-1}mol^{-1}$)	θ_D (K)	A_{E_1} ($JK^{-1}mol^{-1}$)	θ_{E_1} (K)	A_{E_1} ($JK^{-1}mol^{-1}$)	θ_{E_1} (K)
Ni^{2+}	123(3)	148(3)	271(6)	345(7)	240(6)	860(30)
Co^{2+}	87(1)	82(1)	191(3)	188(3)	301(4)	498(8)
Cu^{2+}	76(1)	94(8)	134(4)	208(4)	191(4)	500(3)

ing H is in keeping with the antiferromagnetic nature of the magnetic ground-state implied by the results of NPD (above), while the weak nature of this applied magnetic field dependence is furthermore consistent with the relatively large saturation field of this compound (see below, or Ref. [47]).

(c) Pulsed-field magnetometry and semi-classical Monte-Carlo simulation of the powder-average magnetization: For pulsed-field powder magnetometry measurements of $[Ni(HF_2)(pyz)_2]SbF_6$ performed at temperatures $T \leq 11.4$ K [Fig. 5.6(a)], the magnetization M is found to exhibit smooth and broad approach towards saturation. This leads to two critical fields in the differential susceptibility, where dM/dH rises to a small peak at $\mu_0 H_{C1}$ before reaching zero at $\mu_0 H_{C2}$ [Fig. 5.6(b), arrows]. The magnitude of H_{C1} is observed to decrease as T is raised [Fig. 5.6(b), inset] and is no longer present once the initial experimental temperature exceeds T_C (e.g. black curve at 15 K).

The evolution of $\mu_0 H_{C1}$ and $\mu_0 H_{C2}$ with T are combined with the results of C_p and NPD experiments (above) to construct a powder-average phase diagram for $[Ni(HF_2)(pyz)_2]SbF_6$ in the $H-T$ plane [Fig. 5.6(c)]. In zero-field and at $T > D/k_B$ the Ni^{2+} moments are expected to be paramagnetic (PM), while the system adopts a zero-field magnetically ordered XY-AFM ground-state once $T \leq T_C$. In an applied field $H > 0$, the value of T_C is initially reduced before the powdered sample is pulled through an anisotropic saturation field to reach a spin-polarized (SP) phase. The form of the phase boundary to H_{C1} is fitted to an expression of the form

$$T_C(H) = T_0 \left[1 - \left(\frac{H}{H_{C1}}\right)^{\alpha_1}\right]^{\beta_1}, \tag{5.3}$$

which yields values of $\alpha_1 = 4.6(4)$, $\beta_1 = 0.56(4)$, and $\mu_0 H_{C1} = 32.0(3)$ T. The

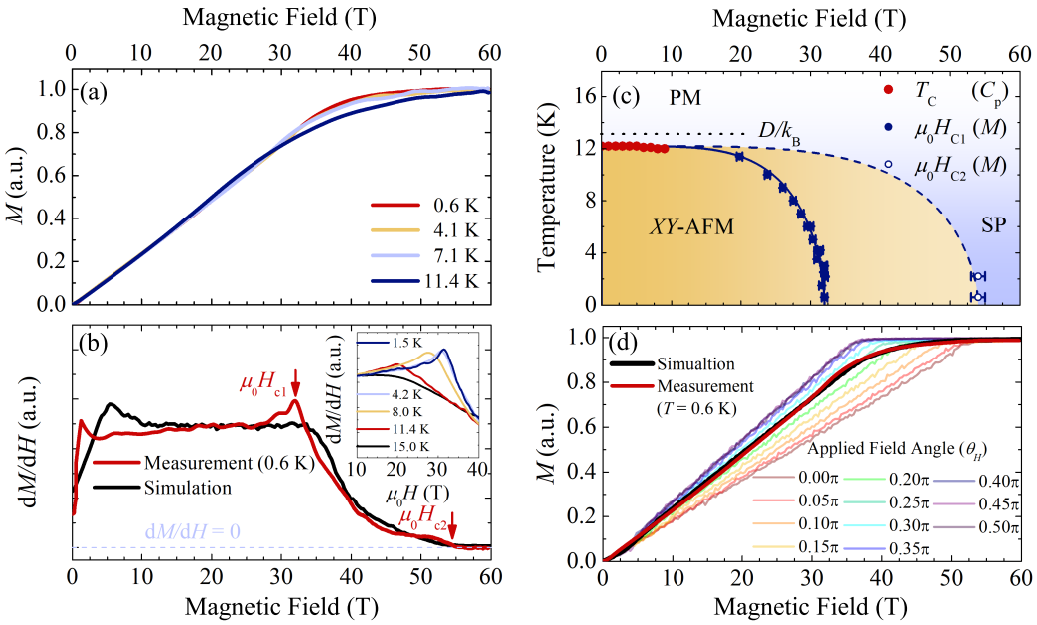

Figure 5.6: **(a)** Powder magnetization M of $[Ni(HF_2)(pyz)_2]SbF_6$ [in arbitrary units (a.u.)] measured in pulsed magnetic fields H. **(b)** At 0.6 K, dM/dH has two critical fields. A small peak occurs at $\mu_0 H_{C1}$ and $dM/dH \to 0$ at $\mu_0 H_{C2}$. The solid-black line is derived from the results of the Monte-Carlo simulation in panel (d). *Inset*: $\mu_0 H_{C1}$ tends to decrease as the temperature T is increases. **(c)** $\mu_0 H - T$ powder-average phase diagram for $[Ni(HF_2)(pyz)_2]SbF_6$, depicting the paramagnetic (PM), spin-polarized (SP), and XY-AFM phases. The T_c and $\mu_0 H_{C1,2}$ values derive from $C_p(T)$ and $M(H)$ measurements respectively. The solid line is a fit to Eq. 5.3 (see text), the dashed pale-blue line is a guide to the eye, and the value of D/k_B is shown for reference. **(d)** Monte-Carlo simulation of the powder average magnetization (black line) derived from Eq. 2.30 and eleven separate calculations of $M(H)$ performed with H at a fixed angle θ_H with respect to the z-axis (faded lines). The 0.6 K $M(H)$ curve from panel (a) is scaled to the simulated data for comparison.

phase-boundary close to H_{C2}, meanwhile, is more difficult to follow in the powder $M(H)$ measurements since dM/dH is much smaller in the vicinity of this critical field. Nevertheless, an estimate of $\mu_0 H_{C2} = 54(1)$ T is extracted from the lowest-temperature differential susceptibility measurements at 0.6 K [Fig. 5.6(b)].

A semi-classical mean-field model is adopted to quantitatively account for the two critical fields of $[Ni(HF_2)(pyz)_2]SbF_6$. Treating each Ni^{2+} spin as a classical vector with length $S = 1$, Eq. 5.2 implies that the average energy per ion ϵ^0 of the zero-field XY-AFM ground state is $\epsilon^0 = -\frac{1}{2} z \langle J \rangle$. Here, J_{FHF} and J_{pyz} are combined into an average spin-exchange interaction $\langle J \rangle$ that couples each moment to z nearest neighbours (i.e., $z\langle J \rangle \equiv 2J_{FHF} + 4J_{pyz}$), while the factor of one-half avoids the double

counting of bonds when summing this quantity over all moments in the system. For a magnetic field H^z applied perpendicular to the $[Ni(pyz)_2]^{2+}$ sheets, each Ni^{2+} moment cants towards H by an angle θ while the projection of the spins into the easy-plane remains antiferromagnetically coupled. In a semi-classical vector model, the average energy per spin ϵ^z of this canted phase is estimated to be

$$\epsilon^z = \frac{1}{2}z\langle J\rangle S^2 \sin^2\theta - \frac{1}{2}z\langle J\rangle S^2\cos^2\theta + DS^2\sin^2\theta - g\mu_B\mu_0 H^z \sin\theta. \quad (5.4)$$

By differentiating ϵ_z with respect to $\sin\theta$, Eq. 5.4 is found to be minimized when $\sin\theta = g\mu_B\mu_0 H^z/[2(D+z\langle J\rangle)]$. A spin-polarized (SP) phase is reached once $\theta = \pi/2$, which occurs at the critical field $H^z = H_{C2}$ given by the expression

$$\mu_0 H_{C2} = \frac{2(D + z\langle J\rangle)}{g\mu_B}. \quad (5.5)$$

If an external magnetic field is instead applied parallel to the $[Ni(pyz)_2]^{2+}$ layers ($H = H^{xy}$), the moments slowly rotate within the easy-plane towards the direction of the applied magnetic field. The average energy per spin for $H^{xy} > 0$ is similar to Eq. 5.4, but as the third term is now zero. By analogy with the calculation above, a SP phase is reached once H^{xy} reaches a value H_{C1} that satisfies the relation

$$\mu_0 H_{C1} = \frac{2z\langle J\rangle}{g\mu_B}. \quad (5.6)$$

Thus, the separation of H_{C1} and H_{C2} largely owes its origin to the single-ion anisotropy D. Measurements of dM/dH performed on powdered $S = 1$ materials are expected to be sensitive to both critical fields; the differential susceptibility decreases at H_{C1} once the portion of the sample with H along the local z-axis reaches the SP phase, while dM/dH only reaches zero at H_{C2} when all of the individual spin moments are aligned with the direction of H.

The experimental measurements of $H_{C1,2}$ for $[Ni(HF_2)(pyz)_2]SbF_6$ (above) combine with Eq. 5.5, Eq. 5.6 and the powder-average g-factor ($g = 2.08$) [47] to estimate $D/k_B = 15(1)$ K and $z\langle J\rangle/k_B = 22.4(2)$ K. In order to deconstruct the measured $z\langle J\rangle$ value into its constituent parts, the strength of spin-exchange interaction along the pyz molecules is estimated by appealing to separate measurements of J_{pyz} derived from other polymeric compounds based upon $[Ni(pyz)_2]^{2+}$ plaquettes (Table. 5.3). The average J_{pyz}/k_B value of compounds (a)−(f) in the table is 0.9(1) K. Given firstly that the nearest-neighbour intraplane Ni-Ni distance of 7.03 Å for $[Ni(HF_2)(pyz)_2]SbF_6$ at 300 K [47] is comparable to those found in compounds (a)−(f) (column 2); and secondly that J_{pyz} does not correlate with other structural factors such as the tilt angle of the pyz molecule from the plane of the Ni^{2+} square-plaquettes [47], a value $J_{pyz}/k_B = 0.9(1)$ K is likely to be a reason-

Table 5.3: Selected magnetostructural parameters for some $S = 1$ Ni^{2+} polymeric magnets containing $[Ni(pyz)_2]^{2+}$ sheets. Here, the spin-centres reside in NiN_4X_2 octahedra, where the Pauling electronegativity of the axially coordinated species X increases down the table; d_{pyz} is the intraplane Ni-Ni distance derived from the results of x-ray diffraction experiments performed at 100 K for compound (a) and room-temperature for systems (b)−(f); $J_{pyz/\perp}$ are the intraplane/interplane Heisenberg spin-exchange constants respectively; D is the uniaxial single-ion anisotropy; and T_C is the antiferromagnetic ordering temperature. Magnetic properties are obtained from powders using pulsed-field magnetization (†); fitting the linear susceptibility to a Heisenberg $S = 1$ model [206], which assumes $D = 0$ (‡); heat capacity (∗); and ESR experiments (⋄).

Compound	d_{pyz} (Å)	J_{pyz}/k_B (K)	$J_\perp/k_B$ (K)	D/k_B (K)	T_C (K)	Ref.
(a) $NiI_2(pyz)_2$	7.06	$<1.19^\dagger$	$>1.19^\dagger$	$0.0^\diamond$	2.5^*	[48]
(b) $NiBr_2(pyz)_2$	7.06	$1.00^\dagger$	$0.26^\dagger$	$0.0^\diamond$	1.8^*	[48]
(c) $Ni(NCS)_2(pyz)_2$	7.12	$0.82^\dagger$	$0.47^\dagger$	$0.0^\diamond$	1.8^*	[48]
(d) $Ni(NCO)_2(pyz)_2$	7.07	$0.63^\ddagger$	–	$0.0^\ddagger$	–	[207]
(e) $NiCl_2(pyz)_2$	7.04	$0.49^\dagger$	$<0.05^\dagger$	$8.0^\diamond$	–	[48]
(f) $[Ni(H_2O)_2(pyz)_2](BF_4)_2$	6.98	$1.05^\dagger$	–	$5.5^\dagger$	3.0^*	[208]

able approximation for the magnitude of Ni-pyz-Ni spin-exchange interaction in the present study. Using this value in conjunction with the estimate of $z\langle J\rangle$ above implies that $J_{FHF}/k_B = 9.4(5)$ K for $[Ni(HF_2)(pyz)_2]SbF_6$.

The magnitudes of the spin-exchange constants across the pyz and HF_2^- linkages derived above are in approximate agreement with the results of recent periodic density field-theory calculations (DFT) performed on $[Ni(HF_2)(pyz)_2]SbF_6$, which imply that $J_{pyz}/k_B = 1.8$ K and $J_{FHF}/k_B = 9.2$ K [77]. These DFT simulations additionally suggest that pyz molecules mediate a spin-exchange interaction owing to a spatial overlap of the Ni^{2+} $d_{x^2-y^2}$ suborbital with the molecular σ-orbitals of the heterolytic ligands. In this case the Ni-pyz-Ni superexchange pathway follows the bonds around the pyz ring, which amounts to a distance of ≈ 8.3 Å at 1.5 K, and since this is longer than the ≈ 6.4 Å separation of the Ni^{2+} spin-centres along the HF_2^- bridges this is likely to be one reason why $J_{FHF} > J_{pyz}$ in this compound.

The powder-average magnetization of $[Ni(HF_2)(pyz)_2]SbF_6$ is simulated in this work using the semi-classical Monte-Carlo routine outlined Section 2.7, and by furthermore appealing to the results of INS measurements (detailed below), which are used to extract estimates of $D/k_B = 13.3$ K, $J_{FHF}/k_B = 10.4$ K and $J_{pyz}/k_B = 1.4$ K. By taking these parameters as given, the comparison of the simulated and measured $M(H)$ traces in this section acts as a consistency check on the interpreta-

tion of the experimental magnetometry data. The calculated powder-average $M(H)$ curve [Fig. 5.6(d), black line] recaptures the broad approach towards saturation exhibited by the real system at 0.6 K (red line). The anisotropic saturation field of the sample is more clearly seen by plotting individual single-crystal simulations of $M(H)$ performed with the applied magnetic field at a fixed angle θ_H with respect to the magnetic hard axis (coloured lines). The position of the field-induced transition to a SP phase is observed to increase monotonically from H_{c1} to H_{c2} as the applied magnetic field rotates from within the magnetic easy-plane towards the z-axis, which is in keeping with the prediction of the mean-field semi-classical calculation above. By differentiating the simulated powder-average magnetization with respect to H, the resultant $\mathrm{d}M/\mathrm{d}H$ curve [Fig. 5.6(b), black line] is seen to decrease at H_{c1} and tends to zero at H_{c2} in approximate agreement with the form of the measured differential susceptibility.

One difference between the simulated and measured $M(H)$ curves is that the magnetization of the real compound displays a slight concavity as H approaches each critical field, such that $\mathrm{d}M/\mathrm{d}H$ [Fig. 5.6(b), red line] is observed to rise to a small peak H_{c1} and a small hump before H_{c2}. These small features, which are not reproduced by the semi-classical calculation, might be evidence for the presence of QFs in this Q1D $S = 1$ AFM. A second difference between the measured and simulated $\mathrm{d}M/\mathrm{d}H$ traces is a small peak that occurs at $\mu_0 H \approx 2$ T and 5 T in the respective data sets. The peak in the 0.6 K measured differential susceptibility might indicate the presence of a small XY symmetry perturbation to Eq. 5.2 that leads to a preferred orientation of the spin-moments at very low temperatures, or it could result from the break up of antiferromagnetic domains as H increases. Zero-field cooled and field-cooled quasistatic magnetization measurements at ^{3}He temperatures might be one way to differentiate between these possible explanations in a future experiment. In this work, the small peak in the simulated $\mathrm{d}M/\mathrm{d}H$ curve is an artefact of the calculation. The Monte Carlo routine used to derive this $\mathrm{d}M/\mathrm{d}H$ trace tests a fixed number of spin-configurations at each value of H and, since the uniaxial zero-field Hamiltonian (Eq. 5.2) gives rise to multiple spin-states with similar energies for small H, this leads to the slight underestimation of the magnetization (and hence a small kink) at low fields when averaging over multiple $M(H)$ curves estimated in this way.

In future work, if powder $\mathrm{d}M/\mathrm{d}H$ measurements are to be used to estimate the easy-plane single-ion anisotropy and spin-exchange interactions of related $S = 1$ quantum spin-systems, H must firstly be sufficient to reach $\mu_0 H_{c2}$ (Eq. 5.5). For $M(H)$ measurements performed with the 65 T capacitor-driven short-pulse magnet

at NHMFL (Los Alamos), this implies the quantity $(D + z\langle J\rangle)/k_{\rm B}$ of the material ought to be less than 43.6 K (assuming $g = 2$). Furthermore, an estimate of $\langle J\rangle$ can only be obtained from the results of magnetization measurements for compounds in which z is known. This might be the case if: (i) the structure implies that the system consists of close-to-ideal chains ($z = 2$) or planes ($z = 4$) of spins; (ii) the dimensionality of the spin-exchange network can be estimated from theoretical (e.g. DFT) calculations; or (iii) if the power-law dependence of the low-T magnetic heat capacity suggests a particular spatial-dimensionality for the exchange interactions. In principle if $H_{\rm C2}$ falls within an experimentally accessible H range then $H_{\rm C1}$ will too. However, Eq. 5.3 indicates that $H_{\rm C1}$ only reaches 90% of its $T = 0$ limiting value for measurements of $[{\rm Ni}({\rm HF}_2)({\rm pyz})_2]{\rm SbF}_6$ performed at $T < 0.6T_{\rm C}$ and, given that experimental temperatures as low as ≈ 500 mK are accessible at NHMFL (Los Alamos), this implies that $H_{\rm C1}$ is only likely to measurable within a 10% accuracy for similar systems to $[{\rm Ni}({\rm HF}_2)({\rm pyz})_2]{\rm SbF}_6$ if the $T_{\rm C}$ values of the compounds in the future work exceed ≈ 800 mK.

(d) Inelastic neutron scattering: INS measurements are performed on a powdered sample of $[{\rm Ni}({\rm HF}_2)({\rm pyz}\text{-}d_4)_2]{\rm SbF}_6$ using the time-of-flight instrument DCS at NIST (USA). Each experiment utilizes a 3.7 Å monochromatic neutron beam to obtain histograms of the scattered neutron intensity as a function of the energy $\hbar\omega$ and momentum $|\mathbf{Q}|$ transferred to the sample. The INS measurements of this section are performed on a separate powdered sample to the NPD investigation in part (a). While the linear susceptibility of these two partially-deuterated samples individually exhibit a broad peak in $\chi_{\rm mol}$ at the same approximate T [Fig. 5.4(b), light and dark blue points], which is furthermore in agreement with the results of $\chi_{\rm mol}(T)$ measurements of the fully hydrogenated material (red points), the $\chi_{\rm mol}(T)$ trace for the pyz-d_4 sample of the present study (light-blue points) suggests this material has a larger impurity phase with respect to the sample investigated with Wish. Nevertheless, the neutron scattering investigations of this section and part (a) are shown below to be sensitive to the same XY-AFM ordered phase of $[{\rm Ni}({\rm HF}_2)({\rm pyz}\text{-}d_4)_2]{\rm SbF}_6$ and the main aim of this study is to refine the estimates of D, $J_{\rm FHF}$ and $J_{\rm pyz}$ that are independently estimated from the results of the magnetometry investigation (above).

For DCS experiments conducted at 20 K ($T > T_{\rm C}$) [Fig. 5.7(a)] the inelastic neutron scattering data are dominated by phonon excitations that give ries to a relatively smooth scattered neutron intensity across the $\hbar\omega - |\mathbf{Q}|$ plane. At 1.6 K [Fig. 5.7(b)], however, an additional band of scattering at $\hbar\omega \approx 3.4$ meV emerges.

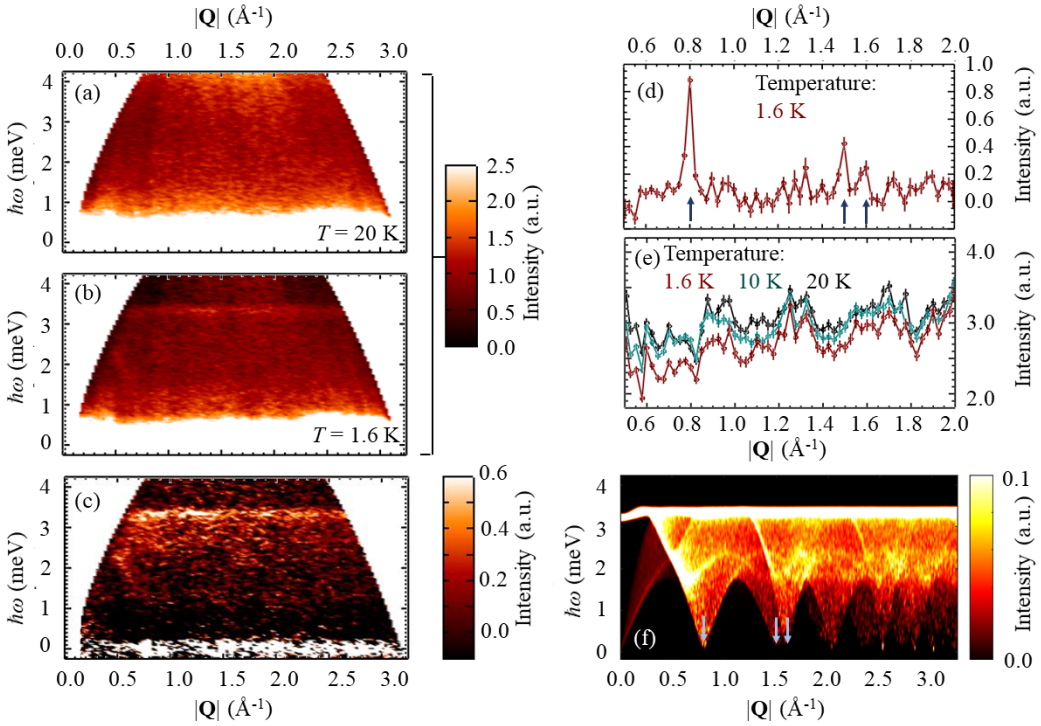

Figure 5.7: Scattered neutron intensity I in the $\hbar\omega - |\mathbf{Q}|$ plane for DCS measurements of $[Ni(HF_2)(pyz\text{-}d_4)_2]SbF_6$ at **(a)** 20 K; and **(b)** 1.6 K. **(c)** A difference plot of panels (a) and (b) reveals the magnetic contribution to the measurement, which includes a bright band of scattering at $\hbar\omega \approx 3.4$ meV. **(d)** Integrating data in panel (c) over energy transfers in range $[-1, 4]$ meV reveals three magnetic Bragg peaks (see text). **(e)** I vs. $|\mathbf{Q}|$ (integrated from [0.25, 1] meV) at 1.6, 10 and 20 K tends to increase with T. **(f)** Simulated INS data performed with the SPINW package in MATLAB (see text). Intensity scales of panels (a)−(e) are in the same units; panels (a)−(c) are smoothed once with a 3×3 bin Gaussian kernel; while the arrows in panels (d) and (f) mark the positions of magnetic Bragg peaks from Fig. 5.4(c).

This relatively bright region of scattering, which is more clearly seen by subtracting the 20 K measurements from the low temperature data [Fig. 5.7(c)], has an intensity that falls off with increasing $|\mathbf{Q}|$ as is required for neutron diffraction that is modulated by a magnetic form factor (e.g. Ref. [133]). Secondly, the difference plot also suggests that there is another relatively intense region of scattering for $|\mathbf{Q}| \approx 0.5$ Å^{-1} and $\hbar\omega \geq 2$ meV. Integrating the data in panel (c) over $\hbar\omega$ values in the range $[-1, 4]$ meV [Fig. 5.7(d)] reveals three magnetic Bragg peaks at momentum transfers of $|\mathbf{Q}| \approx 0.8$, 1.5 and 1.6 Å^{-1}. The intensity of these maxima is reduced at larger values of $|\mathbf{Q}|$ by the magnetic form factor and, furthermore, they correspond to respective d-spacings ($2\pi/|\mathbf{Q}|$) of 7.9, 4.2 and 3.9 Å, which are

in agreement with the positions of the magnetic Bragg reflections derived from the high resolution NPD experiments [blue arrows in panel (d)]. This implies that the strongest features of the inelastic neutron spectra at 1.6 K, which are not present at 20 K, are attributable to spin-wave excitations of $[Ni(HF_2)(pyz\text{-}d_4)_2]SbF_6$.

For energy-transfers $\hbar\omega \leq 1$ meV, there is a slight over subtraction of the paramagnetic background leading to the darkest region of the colourmap in panel (c). Integrating the scattered neutron intensity over the range $0.25 \leq \hbar\omega \leq 1$ meV for three separate measurements performed at 1.6, 10 and 20 K [Fig. 5.7(d)] demonstrates firstly that the overall strength of the neutron diffraction tends to increase with T, and secondly that the integrated intensity is not diminished at large $|\mathbf{Q}|$ by a magnetic form factor. These two observations together imply that acoustic phonons dominate the INS measurements at small positive energy transfers and this portion of the data is therefore not included in the analysis of the spin-wave spectrum below.

Estimates of J_{pyz}, J_{FHF} and D for $[Ni(HF_2)(pyz)_2]SbF_6$ are obtained by modelling the 1.6 K measured spin-wave spectrum for $2 \leq \hbar\omega \leq 4$ meV with the numerical powder-average spin-wave calculation package SPINW in MATLAB [77]. The analysis proceeds as follows: (i) the zero-field XY-AFM magnetic ground-state derived from the Wish diffractometer NPD measurements (above) is used as an initial input for the calculation; (ii) for a given set of (D, J_{FHF}, J_{pyz}) parameters, a powder-average spin-wave spectrum is calculated across the $\hbar\omega - |\mathbf{Q}|$ plane; (iii) the simulated spectrum is scaled to the measured data with an additive constant and an overall scale factor to obtain a reduced χ^2 value by subtracting the experimental and simulated scattering-intensity [210, 211]; and (iv) a global minimum in χ^2 is obtained with the parameters $D/k_B = 13.3(1)$ K, $J_{FHF}/k_B = 10.4(3)$ K and $J_{pyz}/k_B = 1.4(2)$ K [77]. These values are in good agreement with the semi-classical interpretation of the results of pulsed-field powder magnetometry (above), and this independent estimate of J_{pyz} is in approximate agreement the typical energy scale of the Ni-pyz-Ni spin-exchange interaction in related polymeric complexes (Table 5.3).

In this work, the fitted D, J_{FHF} and J_{pyz} values from this section are combined with the lattice parameters derived from results of part (a) to calculate the spin-wave spectrum of $[Ni(HF_2)(pyz\text{-}d_4)_2]SbF_6$ in SPINW [Fig. 5.7(f)]. The powder-average simulated spectrum reproduces some of the key features of measured magnetic INS data at 1.6 K including: (i) a bright region of scattering observed at $|\mathbf{Q}| \approx 0.5$ Å and $\hbar\omega \approx 2$ meV; and (ii) an intense band at $\hbar\omega = 3.4$ meV, which is noted to occur at a value of $\hbar\omega \approx D + 2J_{FHF} + 4J_{pyz}$. The simulation reveals that feature (i) forms part of one of the spin-wave branches that emerges from each of the magnetic Bragg peak along the elastic scattering line [light-blue arrows in panel (f)].

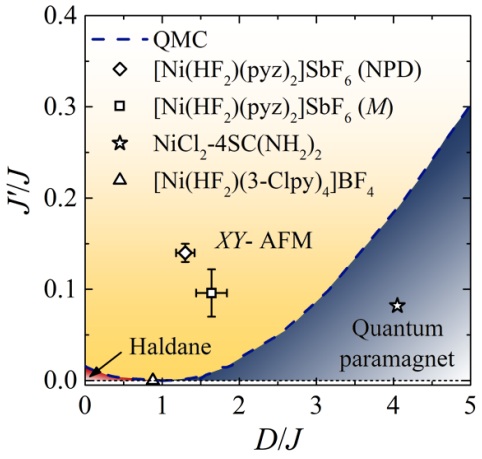

Figure 5.8: The results of a published [68] QMC study of Q1D $S = 1$ AFMs predicts that the zero-temperature phase boundaries (dashed lines) between the Haldane, XY-AFM and quantum paramagnetic ground-states meet at a QCP when $D/J \approx 0.97$ and $J' = 0$. Here, J (J') is the intrachain (interchain) spin-exchange interaction. $[Ni(HF_2)(pyz)_2]SbF_6$ is positioned on this theoretical phase diagram using the results of INS (this section) and magnetization M experiments [part (c)] performed on a powdered sample. The positions of the Haldane compound $[Ni(HF_2)(3\text{-}Clpy)_4]BF_4$ [66] and the quantum paramagnet $NiCl_2\text{-}(4SC)(NH_2)_2$ [92] are also depicted.

Observation (ii), meanwhile, is relevant to future investigations that to aim to measure the inelastic neutron spectra of related $S = 1$ complexes with DCS at NIST (USA). Given that the maximum energy that may be transferred to a sample by a 3.7 Å monochromatic neutron beam is approximately 6.0 meV this implies that, in future work, the quantity $(D + z\langle J\rangle)/k_B$ likely needs to be lower than ≈ 69.6 K for a significant portion of the spin-excitation spectrum to be measurable. Thus, while a semi-classical interpretation of the results of powder pulsed-field magnetometry measurements ought to provide an accessible way to obtain estimates of the single-ion anisotropy and average spin-exchange interactions of XY-like $S = 1$ AFMs, INS measurements with DCS might be necessary for the characterization of powdered samples in which the saturation field H_{C2} exceeds the applied-field capabilities of pulsed-field systems.

The published [68] results of QMC calculations performed on Q1D $S = 1$ AFMs with $D > 0$ (where the intrachain and interchain exchange interactions are redefined as J and J' respectively) suggest that it is the combined ratios of D/J and J'/J that dictate whether the system adopts a zero temperature Haldane, quantum

paramagnet, or XY-AFM phase (Fig. 5.8). The measurements of D/J and J'/J for $[Ni(HF_2)(pyz)_2]SbF_6$, which are derived from the results of magnetometry and INS performed on powders both suggest that this system falls within the XY-AFM region of the phase diagram and this prediction is consistent with measurement of the magnetic unit cell from part (a). $[Ni(HF_2)(pyz)_2]SbF_6$ is also concluded to be a rare example of a real material that is positioned within the XY-AFM phase and in close proximity to the QCP where three magnetic ground states of Q1D $S = 1$ AFMs are predicted to meet, and one avenue for future work could be to follow this compound across this phase-diagram as it is perturbed by control parameters such as isotopic substitution, mechanical pressure p or uniaxial stress. In particular, p might provide a means to tune the J'/J ratio of $[Ni(HF_2)(pyz)_2]SbF_6$. This is inferred from the results of infrared absorption spectroscopy measurements [189], which imply that there are changes to the molecular vibrational modes of the HF_2^- ligands at $p \approx 1$ GPa, while both of the pyz and bifluoride ligands become perturbed once $p \approx 3$ GPa.

5.3.3 $[Co(HF_2)(pyz)_2]SbF_6$

(a) Neutron powder diffraction: The results of time-of-flight NPD measurements of $[Co(HF_2)(pyz\text{-}d_4)_2]SbF_6$ are examined with two fixed angle detectors of the instrument Wish: Bank 2, a detector array with an average in-plane scattering angle $\langle 2\theta \rangle = 58.330°$ that has a large flux at long d spacings and is therefore suited to the investigation of magnetic Bragg reflections; and Bank 5, which is positioned at $\langle 2\theta \rangle = 152.827°$ and provides a high structural resolution. The chemical structure of $[Co(HF_2)(pyz\text{-}d_4)_2]SbF_6$ is determined from the measured positions and intensities of the nuclear Bragg reflections observed at 4 K in Banks 2 and 5 of the diffractometer Wish via a Rietveld refinement of the published [76] structure of the fully-hydrogenated Cu^{2+} congener (where the Cu^{2+} and pyz H atoms are replaced with Co^{2+} and D, respectively). The result of this analysis (Table 5.1) reveals: (i) all three of the Cu^{2+}, Ni^{2+} and Co^{2+} compounds studied in this chapter are isostructural at He temperatures; (ii) the M-pyz-M distance increases across the Cu^{2+}, Ni^{2+} and Co^{2+} series; and (iii) the corresponding interlayer separation decreases. One specific property of the Co^{2+} system is that spin-centres are found to occupy axially compressed CoN_4F_2 octahedra, where the ratio of the Co-F to Co-N bond lengths at 4 K is 0.97.

Subtracting the results of NPD measurements of $[Co(HF_2)(pyz\text{-}d_4)_2]SbF_6$ recorded at 4 and 10 K for [that is, above and below $T_C = 7.1(1)$ K (see below)], four prominent magnetic Bragg reflections are observed (Fig. 5.9, inset). These

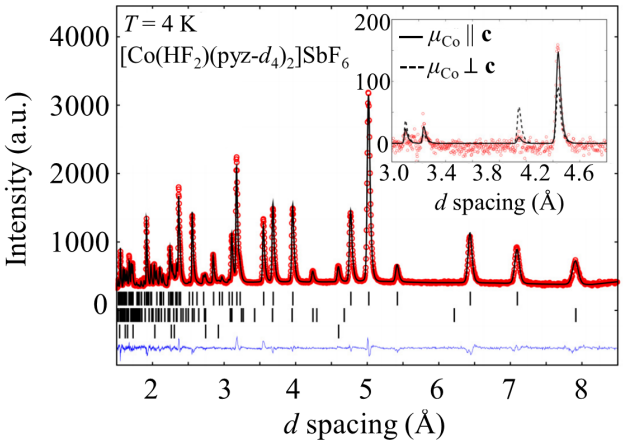

Figure 5.9: NPD pattern for $[Co(HF_2)(pyz\text{-}d_4)_2]SbF_6$ recorded with Bank 2 of the Wish diffractometer (points). The black line and the first row of ticks is the result of a Rietveld refinement of the chemical unit cell. The second row of ticks mark the positions of nuclear Bragg peaks of a 12.4(7)% impurity phase of $NaHF_2$ ($R\bar{3}m$). The third row of ticks are magnetic Bragg reflections for $[Co(HF_2)(pyz\text{-}d_4)_2]SbF_6$ indexed with $\mathbf{k} = (0, 0, 1/2)$ (r.l.u.). *Inset:* Subtraction of NPD data at 4 and 10 K. Two antiferromagnetic models are tested in which the Co^{2+} spins are parallel ($||$) or perpendicular ($\perp$) to the **c**-axis. The unique ground-state is determined to be Ising-like [e.g. Fig. 5.2(b), panel (i)].

maxima do not correspond to the d-spacings of nuclear Bragg peaks, indicating that the ground spin-state of this complex has an antiferromagnetic character. The magnetic peaks are indexed with the commensurate propagation vector $\mathbf{k} = (0, 0, 1/2)$ (r.l.u.); i.e. J_{FHF} is antiferromagnetic. By analogy with the analysis of the Cu^{2+} and Ni^{2+} systems (above), there are four symmetry-allowed magnetic supercells for the Co^{2+} complex. The observed d-spacings of the peaks in Fig. 5.9 (inset) are only consistent with spin-states in which J_{pyz} is also antiferromagnetic and, furthermore, the measured relative intensities of the magnetic Bragg reflections at 4 K are only reproduced by an Ising model in which each Co^{2+} moment is collinear with the crystallographic **c**-axis [e.g. Fig. 5.2(b), panel (i)].

The magnitude of the ordered moment μ_{Co} for $[Co(HF_2(pyz\text{-}d_4)_2]SbF_4$ is refined within the Ising model (along with the chemical structure) against the results of 4 K NPD measurements collected in detector Banks 2 and 5 of the Wish diffractometer. A fitted value of $\mu_{\mathrm{Co}} = 3.02(6)\mu_{\mathrm{B}}$ is obtained, which consistent with each Co^{2+} moment adopting a $S = 3/2$ configuration. For octahedrally coordinated high-spin Co^{2+} ions the expected effect of the CEF is to split the free-ion spin-states into three terms [165, 212], while an axial compression of the coordination sphere

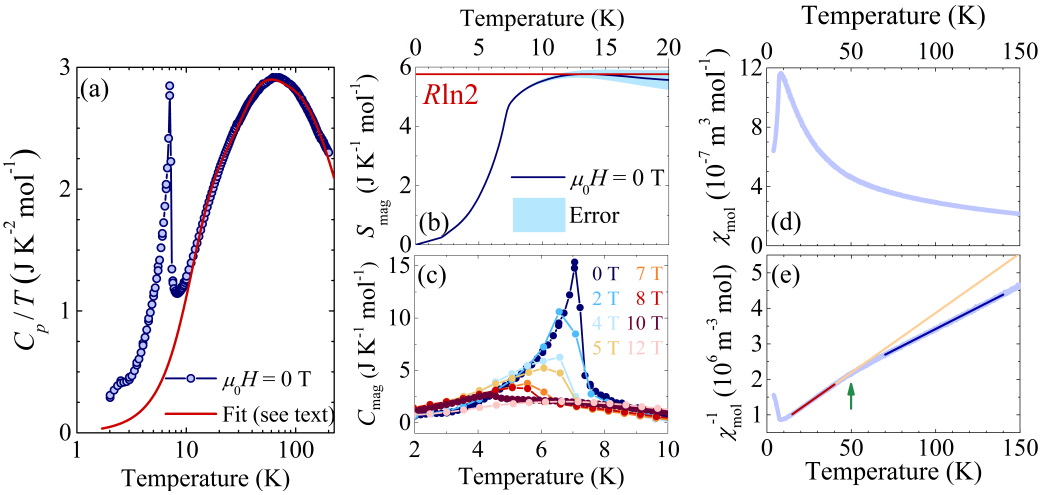

Figure 5.10: **(a)** Zero-field powder heat capacity C_p for $[Co(HF_2)(pyz)_2]SbF_6$ (points) fitted to Eq. 1.10 for $T \geq 11$ K (solid line). There is a weak, as yet unexplained, peak in the zero field $C_p(T)$ curve at $T \approx 2$ K, which might be related to a small impurity phase detected from the results of ESR experiments (below). **(b)** The change in spin entropy $S_{\rm mag}$ on cooling through $T_{\rm C}$ in zero-field is consistent with a value of $R\ln 2$ per ion. **(c)** The H dependence of $C_{\rm mag}$ reveals $T_{\rm C}$ is reduced for $\mu_0 H \leq 12$ T. **(d)** The powder-average linear susceptibility $\chi_{\rm mol}$ exhibits a broad maximum at ≈ 8 K. **(e)** A linear fit to $\chi^{-1}_{\rm mol}(T)$ is performed for $15 \leq T \leq 40$ K (red line) and the measured data departs an extrapolation of this linear fit (yellow line) once T exceeds ≈ 50 K (arrow). The solid blue line represents a linear fit for $70 \leq T \leq 140$ K (see text).

is predicted to result in an orbital singlet ground-state [34, 212]. In this case, the CEF leads to a term in the $S = 3/2$ Hamiltonian of the form $\hat{\mathcal{H}}_{\rm CEF} = D(\hat{S}^z)^2$ (e.g. Ref [36]), which gives rise to a bistable Kramers-doublet ground-state.

(b) Heat capacity: Heat capacity C_p measurements of $[Co(HF_2)(pyz)_2]SbF_6$ performed on a powdered sample in zero-field display a sharp peak at $T_{\rm C} = 7.1(1)$ K in addition to a slowly-varying background owing to the phonon contribution to the measurement [Fig. 5.10(a)]. The lattice component $C_{\rm latt}$ of the total heat capacity is modelled by fitting C_p/T to Eq. 1.10 for $T \geq 11$ K using one Debye and two independent Einstein modes (Table 5.2). The resultant phonon model [Fig. 5.10(a), solid line] is subtracted from the C_p data to estimate $C_{\rm mag}$ and, by assuming that $C_{\rm mag} = 0$ at $T = 0$ K, the magnetic heat capacity is integrated via Eq. 1.12 for $T \leq 20$ K to determine that the change in spin-entropy $\Delta S_{\rm mag}$ associated with the phase transition at $T_{\rm C}$ is approximately $R\ln 2$ per ion [Fig. 5.10(b)]. This suggests that each moment has only two spin degrees of freedom for $T \leq 20$ K; that is, only

the lowest-energy Kramers doublet spin-state is likely to be thermally occupied at these temperatures. The calculation of ΔS_{mag} furthermore implies that the fitted phonon model has absorbed a broad Schottky anomaly that is anticipated to occur in the measurement of the real $S = 3/2$ system owing to the thermal depopulation of non-degenerate spin-states within each Co^{2+} ion. However, the amplitude of this anomaly is only expected[1] to be ≈ 3.7 $JK^{-1}mol^{-1}$, which is one to two orders of magnitude smaller than (and within the sum of the fitted errors of) the amplitudes of the phonon modes for $[Co(HF_2)(pyz)_2]SbF_6$ (Table 5.2).

When $C_{\mathrm{mag}}(T)$ is extracted from heat capacity experiments repeated in quasistatic $\mu_0 H \leq 12$ T [Fig. 5.10(c)], the magnetic ordering temperature T_c of the Co^{2+} complex is found to decrease as the strength of an applied magnetic field is raised. This behaviour is in accord with the results of NPD measurements (above), which unambiguously determine the antiferromagnetic nature of the magnetically ordered phase. The width of peak in C_{mag} at $T = T_{\mathrm{C}}$ is broadened with increasing H and, as a result, the magnetic ordering temperature becomes difficult to distinguish from the sloping background for experiments conducted in quasistatic $\mu_0 H > 11$ T.

There are four observations derived from the results of parts (a) and (b) that collectively suggest that $J_{\mathrm{FHF}}/J_{\mathrm{pyz}}$ is likely to be larger for $[Co(HF_2)(pyz)_2]SbF_6$ with respect to the value of this ratio in the Cu^{2+} congener: (i) high-spin Co^{2+} ions contain an unpaired electron in the d_{z^2} orbital, which allows spin-density to become delocalized over the HF_2^- ligands; (ii) the investigation of the Ni^{2+} complex (above) shows that HF_2^- is an effective mediator of spin-exchange in cases when this ligand couples directly to magnetic d-orbitals; (iii) the results of NPD for the Co^{2+} complex imply that separation of ions along the HF_2^- bridges at 4 K is approximately 5% shorter compared to the equivalent distance in Cu^{2+} congener at 1.5 K; and (iv) $[Co(HF_2)(pyz)_2]SbF_6$ has a critical temperature T_{C} that is an order of magnitude greater than the related system $CoCl_2(pyz)_2$, which is a tetragonal ($I4/nmm$) AFM based upon non-coordinated (i.e. weakly coupled) $[Co(pyz)_2]^{2+}$ plaquettes [213], which only adopts magnetic LRO for $T \leq 0.855(5)$ K [193].

The overall form of $C_{\mathrm{mag}}(T)$ for $[Co(HF_2)(pyz)_2]SbF_6$ can be used to make some further assertions about the $J_{\mathrm{FHF}}/J_{\mathrm{pyz}}$ ratio for this system. The results of QMC simulations [103] of the heat capacity for Ising spins on a cubic lattice predict that a sharp peak occurs in C_{mag} at $T = T_{\mathrm{c}}$ [e.g. Fig. 1.10(c))]. For ideal quadratic Ising systems, meanwhile, correlated-effective-field theory simulations [105] and Onsager's analytical calculations [106] suggest that a similarly distinct feature is ex-

[1] See for instance the heat capacity of a two-level system in Ref. [79], which has the same T dependence as the Schottky anomaly resulting from the thermal depopulation between two sets of bistable Kramers doublets.

pected to occur in the heat capacity at the transition to a magnetically ordered state. However, the correlated-effective-field theory simulations anticipate that a sharp peak at $T = T_{\mathrm{C}}$ gives way to a small broad maximum in the magnetic heat capacity at $T > T_{\mathrm{C}}$ in instances when a material is a close-to-ideal realization of an Ising spin chain. The sharp and distinct peak in C_{mag} at $T = T_{\mathrm{C}}$ $[\mathrm{Co(HF_2)(pyz)_2}]\mathrm{SbF_6}$ is therefore consistent with a spin-Hamiltonian in which $J_{\mathrm{FHF}} \approx J_{\mathrm{pyz}}$ or $J_{\mathrm{FHF}} \ll J_{\mathrm{pyz}}$. Thus, while observations (i)−(iv) above suggest $J_{\mathrm{FHF}}/J_{\mathrm{pyz}}$ may be larger in this compound compared to the Cu^{2+} complex, the results of heat capacity measurements suggest that it cannot be so large so as to move the system towards the Q1D limit and it is therefore concluded that J_{FHF} and J_{pyz} are likely to have comparable energy scales in $[\mathrm{Co(HF_2)(pyz)_2}]\mathrm{SbF_6}$.

(c) Linear susceptibility: For experiments performed in quasistatic $\mu_0 H = 0.1$ T, the linear powder susceptibility χ_{mol} of $[\mathrm{Co(HF_2)(pyz)_2}]\mathrm{SbF_6}$ [Fig. 5.10(d)] exhibits a peak at a temperature $T \approx 8$ K. For $T > 10$ K, i.e. when the sample is in the paramagnetic phase, the inverse susceptibility begins to evolve linearly with increasing temperature [Fig. 5.10(e)] and Curie-Weiss (linear) fit to these data for $15 \leq T \leq 40$ K (red line) suggests that the powder-average effective moment of the sample is $\mu_{\mathrm{eff}} = 4.35\mu_{\mathrm{B}}$ per ion. However there is a departure from this model once the sample temperature exceeds ≈ 50 K (green arrow) where there is noted to be an approximately 28% reduction in the gradient of χ_{mol}^{-1} giving rise to a separate region of Curie-Weiss behaviour (dark blue line) for which $\mu_{\mathrm{eff}} = 5.13\mu_{\mathrm{B}}$. The high temperature effective moment falls within the typical range for octahedrally coordinated Co^{2+} compounds, which often take values in the range $4.7\mu_{\mathrm{B}}$ to $5.2\mu_{\mathrm{B}}$ [214]. The smaller effective moment of $[\mathrm{Co(HF_2)(pyz)_2}]\mathrm{SbF_6}$ below 50 K, meanwhile, is in approximate agreement with the results of ESR measurements (below) that suggest that the individual spin moments are predominantly projected along the local z-axis at these temperatures, which leads to an overall reduction in the powder-average μ_{eff} value. In this interpretation of the linear susceptibility data, 50 K represents the thermal energy at which the paramagnetic spins tend to adopt an easy-axis character and this temperature therefore acts as an order of magnitude estimate for the energy scale of the single-ion anisotropy of this complex.

In summary, the results of parts (a)−(c) suggest that $[\mathrm{Co(HF_2)(pyz)_2}]\mathrm{SbF_6}$ behaves as two-level spin system at low-temperatures compared to the zero-field splitting. In more general terms, the two lowest-energy eigenstates of octahedrally coordinated high-spin Co^{2+} materials map onto an effective spin-half ($\sigma = 1/2$) Hamiltonian $\hat{\mathcal{H}}_{\mathrm{eff}}$ in an applied magnetic field wherein the single-ion anisotropy is

reparametrized as a non-Heisenberg spin-exchange interaction (e.g. Refs. [39, 40, 193]) and an anisotropic g-tensor $\tilde{\boldsymbol{g}}$ =diag $(\tilde{g}_{xy}, \tilde{g}_{xy}, \tilde{g}_z)$ (e.g. Refs. [39, 193]). Both of these terms also act to absorb the full size of the Co^{2+} moments and, in this model, $\hat{\mathcal{H}}_{\text{eff}}$ is given by an expression of the form

$$\hat{\mathcal{H}}_{\text{eff}} = \tilde{J} \sum_{\langle i,j \rangle} \left[\hat{\sigma}_i^z \hat{\sigma}_j^z + a \left(\hat{\sigma}_i^x \hat{\sigma}_j^x + \hat{\sigma}_i^y \hat{\sigma}_j^y \right) \right] + \mu_0 \mu_{\text{B}} \sum_i \mathbf{H}^{\text{T}} \, \tilde{\boldsymbol{g}} \, \boldsymbol{\sigma}_i, \tag{5.7}$$

where $\boldsymbol{\sigma} = (\hat{\sigma}_x, \hat{\sigma}_y, \hat{\sigma}_z)^{\text{T}}$ is a column vector of spin-1/2 operators; the first sum runs over unique pairs of neighbouring spins, while the second sum runs over each spin; $\tilde{J}$ is the average spin-exchange constant to z nearest neighbours; the parameter $a < 1$ accounts for the larger projection of the easy-axis moments on to the z-axis; and $\mathbf{H}$ is the applied magnetic field. Eq. 5.7 is used in an analysis of the results of powder ESR and magnetization measurements of $[Co(HF_2)(pyz)_2]SbF_6$ below.

(d) Electron spin-resonance: For constant frequency (ν = 416 GHz) powder ESR measurements of $[Co(HF_2)(pyz)_2]SbF_6$ performed at temperatures in the range $20 \leq T \leq 30$ K [Fig. 5.11(a)], the differential transmission intensity $\mathrm{d}I/\mathrm{d}H$ exhibts a small peak at $\mu_0 H \approx 5$ T and a larger derivative shape centred on 8 T (arrows). The weak H dependence of these peaks, in addition to the observation that they become stronger as T is reduced, together imply that these absorptions derive from single-ion resonances within the lowest-energy Kramers doublet of each Co^{2+} ion. The low-field resonance has the smaller amplitude of the two features and is therefore attributed to excitations induced in the portion of the sample for which H is parallel to the z-axis and, with this assumption, the powder ESR measurements at 20 K [Fig. 5.11(b), blue line] are modelled with a paramagnetic effective-spin half Hamiltonian using the values $\tilde{g}_z = 5.5(7)$ and $\tilde{g}_{xy} = 3.6(4)$ (red line). The errors here derive from the finite widths of the measured single-ion ESR resonances that, in turn, leads to an error in determining the precise fields of these features. The powder-average value $\tilde{g} = \left[\frac{1}{3}(\tilde{g}_z^2 + 2\tilde{g}_{xy}^2)\right]^{1/2} = 4.3(5)$ derived from this result implies that the effective moment in the $\sigma = 1/2$ model is $\mu_{\text{eff}} = \tilde{g}[\sigma(\sigma+1)]^{1/2}\mu_{\text{B}} = 3.7(5)\mu_{\text{B}}$, which is in approximate agreement with the value derived from the analysis of the powder-average inverse linear-susceptibility for $15 \leq T \leq 40$ K in part (c).

At 20 K, the size of the paramagnetic Co^{2+} moment projected onto the local z-axis $\tilde{g}_z \mu_{\text{B}} \sigma = 2.8(4)\mu_{\text{B}}$ is furthermore consistent with the magnitude of the ordered moment $\mu_{\text{Co}} = 3.02(6)\mu_{\text{B}}$ derived from the results of NPD in part (a). The Co^{2+} system therefore does not exhibit a renormalized moment $T \leq T_{\text{C}}$, in contrast to the Cu^{2+} congener. There are three key differences between the Cu^{2+} and Co^{2+} materials of this chapter that may account for this observation: (i) $S = 1/2$ for

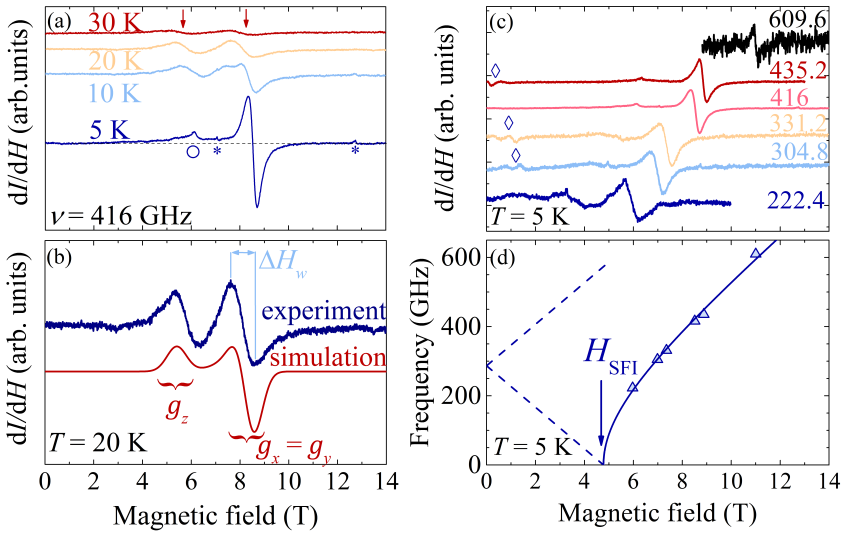

Figure 5.11: **(a)** For constant ν powder ESR measurements of $[Co(HF_2)(pyz)_2]SbF_6$ at $T > T_C$, the differential transmission intensity dI/dH vs. $\mu_0 H$ (lines) exhibits two single-ion resonances (red arrows), while a strong antiferromagnetic resonance centred on $\mu_0 H \approx 8.5$ T develops for $T < T_C$. The circle in the 5 K ESR spectrum marks a spin-flop resonance (see text), the dashed line is a guide to the eye and the asterisks mark peaks attributed to a paramagnetic impurity. **(b)** At 20 K, the observed form of the single-ion resonances (blue line) is broadly reproduced with an effective spin-half model wherein $\tilde{g}_z = 5.5(7)$, $\tilde{g}_{xy} = 3.6(4)$ and the isotropic line width (i.e. full width at half maximum) is 800 mT. **(c)** For measurements of dI/dH vs. $\mu_0 H$ at 5 K, the strong antiferromagnetic resonance mode (derivate shape) moves to higher H with increasing ν. A series of weaker absorptions (diamonds) at lower values of H evolve linearly with ν and are consistent with $\tilde{g}_z \approx 6.3$. **(d)** The ν dependence of the antiferromagnetic resonance mode (triangles) is approximately accounted for with a theoretical Ising model (solid line) (Eq. 5.8, see text). Data in panels (a)−(c) are plotted in arbitrary units and are offset for clarity.

Cu^{2+}, whilst $S = 3/2$ for Co^{2+}; (ii) the J_{FHF}/J_{pyz} ratio is likely to be closer to one for the Co^{2+} complex; and (iii) the Co^{2+} moments have an Ising character as opposed to the Heisenberg Cu^{2+} spins. Point (i) by itself is not sufficient to explain the lack of a reduced moment in the Co^{2+} system as the results of linear spin-wave theory calculations for Heisenberg square-lattice AFMs, for instance, predict $S = 3/2$ systems to exhibit a $T = 0$ ordered moment that is reduced from its paramagnetic value by 87% [98]. Instead, it is points (ii) and (iii) that combine to stabilize μ_{Co} from the effects of QFs in $[Co(HF_2)(pyz)_2]SbF_6$. Ideal square-lattice Ising systems are expected to order at a finite temperature with the full ordered moment [217] and, furthermore, spin-waves are not observed in the experimental investigation of real Q2D Co^{2+} compounds [218] thus removing the mechanism by which the reduced

moment was observed in the Cu^{2+} system. While one-dimensional Ising systems are expected to order with the full moment at $T = 0$ unless perturbed, for instance, by a small transverse magnetic field [16] the experimental investigation of real Co^{2+} materials that approximately map onto the Q1D Ising model have been shown to exhibit a reduced ordered moment in the ordered phase [219, 220]. The observation of the full moment at $T \leq T_C$ for $[Co(HF_2)(pyz)_2]SbF_6$, suggests that while J_{FHF}/J_{pyz} is expected to be larger for this system with respect to the Cu^{2+} complex, this ratio is unlikely to be so large so as to give rise to Q1D behaviour; that is, the results of this section are consistent with the discussion of the heat capacity (above).

In the present ESR study, the results of measurements conducted at 5 K with $\nu = 416$ GHz [Fig. 5.11(a), dark-blue trace] exhibit a strong antiferromagnetic resonance mode centred on $\mu_0 H \approx 8.5$ T. The width of this mode ΔH_w is approximately two orders of magnitude greater than the AFM resonance of the $S = 1/2$ system $[Cu(HF_2)(pyz)_2]SbF_6$. Heisenberg systems are expected to exhibit narrow ESR resonances [49] and, thus, the ESR measurements of the Co^{2+} complex are indicative of non-Heisenberg type spin-exchange interactions in this material [215]. In an isothermal ν-dependent ESR study at 5 K [Fig. 5.11(c)], the AFM resonance mode of $[Co(HF_2)(pyz)_2]SbF_6$ is observed to move to increasingly higher H as ν is raised. This frequency dependence [Fig. 5.11(d), points] is fitted to an expression [216] for ideal Ising spins of the form

$$\nu = \frac{\tilde{g}\mu_0\mu_B}{h}\left(H^2 - H_{SFI}^2\right)^{1/2}, \tag{5.8}$$

where $\tilde{g}$ is the powder-average $\sigma = 1/2$ g-factor and H_{SFI} estimates the value of a field induced spin-flop (SF) transition that is expect to occur in easy-axis AFMs for an applied magnetic field along the z direction. Specifically, H_{SFI} is a lower bound of the spin-flop field that is realized in the case of purely Ising spins, while the spin-flop field of the real compound is $H_{SF} > H_{SFI}$. Fitting Eq. 5.8 to the measured data [Fig. 5.11(d), solid line] yields $\mu_0 H_{SFI} = 4.9$ T (arrow) and $\tilde{g} = 4.21$. The fitted powder-average g-factor is consistent with the value of $\tilde{g}$ derived from the analysis of the single-ion ESR resonances at 20 K (above).

One final note is that there is a small broad feature in the 5 K transmission ESR spectrum [marked with a circle in panel (a)] that occurs for applied magnetic fields in the approximate range $5 \leq \mu_0 H \leq 6$ T; i.e. in the approximate vicinity of H_{SFI}. A frequency-independent ESR resonance mode is predicted to occur at the true spin-flop transition $H = H_{SF}$ once $T < T_C$ [216] and this might be the cause of this particular feature, although it was not observed over a wide ν range as this feature quickly becomes masked by the AFM mode for $\nu \leq 331.2$ GHz.

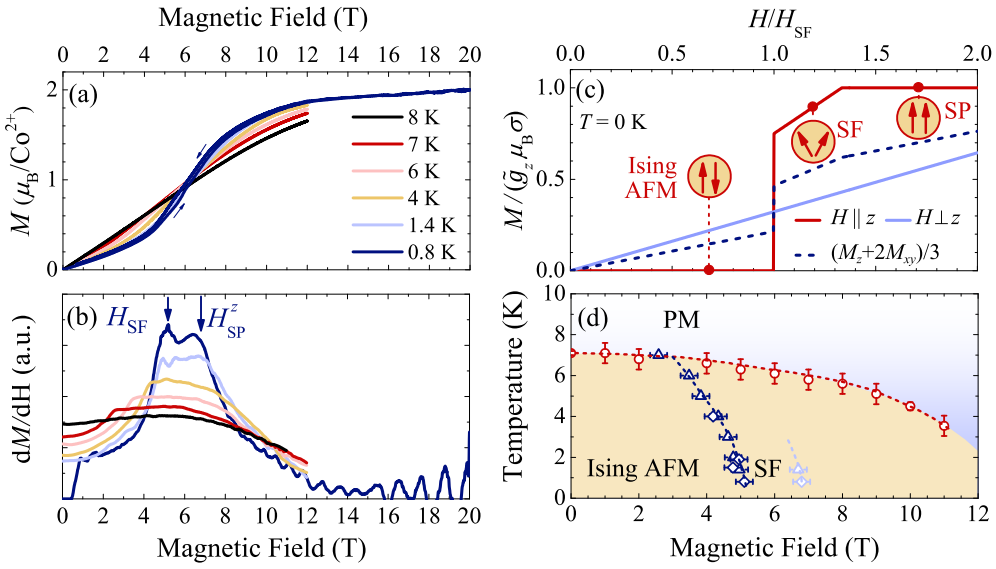

Figure 5.12: Applied magnetic field $\mu_0 H$ dependence of: **(a)** the magnetization M; and **(b)** the differential susceptibility $\mathrm{d}M/\mathrm{d}H$, for a powdered sample of $[Co(HF_2)(pyz)_2]SbF_6$. Data are extracted from VSM ($T \geq 1.4$ K) and pulsed-field magnetometry ($T = 0.8$ K). Here, a.u. = arbitrary units; arrows in (a) show the direction of H; while arrows in (b) mark the positions of the critical fields (see text). **(c)** Schematic $M(H)$ curves for an easy-axis $\sigma = 1/2$ AFM at $T = 0$. For $H \parallel z$ (red line) there is a transition to a spin-flop (SF) and spin-polarized (SP) phase at H_{SF} and H^z_{SP} respectively. The lines drawn here assume $H_{\mathrm{SF}}/H^z_{\mathrm{SP}} = 0.75$ and $\tilde{g}_{xy}/\tilde{g}_z = 0.65$ (as measured for $[Co(HF_2)(pyz)_2]SbF_6$). **(d)** Powder-average phase diagram for $[Co(HF_2)(pyz)_2]SbF_6$. Here, the critical temperature and fields are derived from the results of heat capacity (circles), VSM (triangles) and pulsed-field magnetometry (diamonds) measurements. The dashed lines are a guide to the eye.

(e) Quasistatic and pulsed-field powder magnetometry: The powder magnetization M of $[Co(HF_2)(pyz)_2]SbF_6$ is studied with VSM measurements at temperatures in the range $1.4 \leq T \leq 8$ K and compensated coil extraction magnetometry experiments performed at 0.8 K with $\mu_0 H \leq 20$ T [Fig. 5.12(a)]. When the pulsed-field magnetization trace is (approximately) normalized to the 1.8 K VSM measurement (blue curve), M is found to reach a value of $\approx 2\mu_{\mathrm{B}}$ per ion at $\mu_0 H = 20$ T. This is significantly below the value of $3.02\mu_{\mathrm{B}}$ expected in the spin-polarized phase, which suggests that the single-ion anisotropy of this complex is strong compared to the powder-average Zeeman energy $\tilde{g}\mu_{\mathrm{B}}\mu_0 H\sigma/k_{\mathrm{B}} \approx 29$ K of the effective spin-half moments at $\mu_0 H = 20$ T.

For isothermal magnetometry measurements performed at $T < T_{\mathrm{C}}$ a large

kink develops in $M(H)$ at $\mu_0 H \approx 5$ T, which corresponds to a rapid increase in $\mathrm{d}M/\mathrm{d}H$ [Fig. 5.12(b)]. The differential susceptibility then approximately plateaus until $\mu_0 H$ reaches ≈ 7 T where after $\mathrm{d}M/\mathrm{d}H$ begins to decrease with increasing H. For $\mu_0 H < 5\ T$, the initial gradient of $\mathrm{d}M/\mathrm{d}H$ tends to increase with sample temperatures up to 8 K. This observation is in keeping with the measured peak in the linear suscetpbility at 8 K [see part (c)] and is therefore likely to be a reflection of the $k_{\mathrm{B}}T/\tilde{J}$ ratio of a particular expeiment; i.e. at low temperatures compared to $\tilde{J}$ then pairs of neighbouring Co^{2+} moments become preferentially antiferromagneticically coupled, which makes the invidvidual spin orientations less susceptible to a small applied magnetic field. One final observation is that the oscillations for $\mu_0 H > 8\ T$ in the pulsed-field measurements are an artefact of the experimental procedure. The measurement signal in compensated coil extraction magnetometry is proportional to $\mathrm{d}M/\mathrm{d}H$ [45] and, while this makes this technique very sensitive to kinks and inflections in the magnetization curves, this quantity becomes increasing diminished and susceptible to noise once a greater proportion of the powdered sample becomes spin-polarized.

A quantitative interpretation of the kinks in $\mathrm{d}M/\mathrm{d}H$ at $\mu_0 H \approx 5$ and 7 T proceeds with a semi-classical model that considers the Co^{2+} moments as vectors governed by the spin-Hamiltonian of Eq. 5.7. Given the results of NPD measurements (above), which imply that the zero-field magnetic ground-state consists of colinear and antiferromagnetically coupled moments, Eq. 5.7 dictates that the average energy per spin is $\epsilon^0 = -\frac{1}{2} z\tilde{J}\sigma^2$, where the factor of one-half avoids the double counting of bonds when averaging this quantity over the entire spin-ensemble. For a magnetic field H^z applied parallel to the z-axis, the Ising ground state competes with a spin-canted phase in which the spins are antiferromagnetically coupled in the xy-plane but each moment is rotated by an angle θ towards the direction of H^z. The energy ϵ^z of the canted phase is given by the expression

$$\epsilon^z = \frac{1}{2} z a \tilde{J}\sigma^2 \sin^2\theta - \frac{1}{2} z\tilde{J}\sigma^2 \cos^2\theta - \tilde{g}_z \mu_0 \mu_{\mathrm{B}} H^z \sigma \sin\theta, \tag{5.9}$$

which is minimized when $\sin\theta = \tilde{g}_z \mu_0 \mu_{\mathrm{B}} H^z / [z(1+a)\tilde{J}\sigma]$. Once H^z is sufficient for ϵ^z to become lower in energy than ϵ^0, the spins rotate from the Ising ground-state to the canted phase in a spin-flop (SF) transition [Fig. 5.12(c), red-line]. This occurs at $H = H_{\mathrm{SF}}$, which satisfies the relation

$$\mu_0 H_{\mathrm{SF}} = \frac{z\tilde{J}(1-a^2)^{1/2}\sigma}{\tilde{g}_z \mu_{\mathrm{B}}}. \tag{5.10}$$

As H increases the Co^{2+} moments continue to rotate until a spin-polarized phase (SP) is reached when $\theta = \pi/2$. The equilibrium value of $\sin\theta$ (above) suggests this

will occur once $H^z = H^z_{\rm SP}$, which is given by

$$\mu_0 H^z_{\rm SP} = \frac{z\tilde{J}(1+a)\sigma}{\tilde{g}_z \mu_{\rm B}}. \tag{5.11}$$

When H is instead applied perpendicular to the easy-axis [Fig 5.12(c), pale-blue line] the spins rotate to align with the applied magnetic field with no discontinuities in $M(H)$ for $H < H^z_{\rm SP}$. The first two kinks in the powder-average magnetization are therefore concurrent with field-induced phase transitions from the portion of the sample with H along the z-axis.

The observed sharp rise and subsequent decrease in the 0.8 K powder $\mathrm{d}M/\mathrm{d}H$ measurements of $[\mathrm{Co(HF_2)(pyz)_2}]\mathrm{SbF_6}$ [Fig. 5.12(b)] at 5.1(1) T and 6.8(2) T (arrows) are attributed to $\mu_0 H_{\rm SF}$ and $\mu_0 H^z_{\rm SP}$ respectively. With the result from ESR that $\tilde{g}_z = 5.5(7)$, these critical fields combine with Eqs. 5.10 and 5.11 to yield values of $z\tilde{J}/k_{\rm B} = 39(9)$ K and $a = 0.28(6)$. Given the discussions in parts (b) and (d) that $J_{\rm FHF}$ and $J_{\rm pyz}$ are likely to have comparable energy scales in this system, assuming a value of $z = 6$ leads to an estimate of the average nearest-neighbour spin-exchange constant $\tilde{J}/k_{\rm B} = 7(1)$ K. In this model, the measured ratio $k_{\rm B}T_{\rm C}/\tilde{J}$ is found to be 1.1(2), which agrees with a value of 1.1 that is predicted for networks of exchange-coupled ideal Ising spins arranged on the vertices of a cubic lattice [193].

Finally, the results of this section are collated with those from the heat capacity and NPD measurements (above) to form a powder-average $H - T$ phase diagram for $[\mathrm{Co(HF_2)(pyz)_2}]\mathrm{SbF_6}$ [Fig. 5.12(d)]. In zero-field and for temperatures $T > T_{\rm C}$, the $\mathrm{Co^{2+}}$ moments are paramagnetic (PM), but are likely to retain an easy-axis character for temperatures below ≈ 50 K, while for $T \leq T_{\rm C}$ the moments adopt a colinear Ising-like antiferromagnetic ground state. The effect of an applied magnetic field $H > 0$ is firstly to reduce $T_{\rm C}$ and secondly to induce two phase transitions in a powdered sample such that, in the portion of the sample with H parallel to the z-axis, the spins firstly reach a spin-flop (SF) phase before reaching a spin-polarized phase. Future work on this compound might be aimed at examining the field induced phase transition to a fully polarized spin-state or to obtain an accurate estimate for the CEF splitting of the individual $\mathrm{Co^{2+}}$ spin-states.

5.4 Conclusions

A NPD investigation of the polymeric series $[M(\mathrm{HF_2})(\mathrm{pyz}\text{-}d_4)_2]\mathrm{SbF_6}$ ($M = \mathrm{Cu^{2+}}$, $\mathrm{Ni^{2+}}$ or $\mathrm{Co^{2+}}$) reveals that each material is isostructural at He temperatures, crystalizing in the $P4/nmm$ space group. The Q2D $S = 1/2$ $\mathrm{Cu^{2+}}$ congener is measured to exhibit an ordered moment $\mu_{\rm Cu} = 0.6(1)\mu_{\rm B}$ that is determined to be reduced from

its paramagnetic value $g\mu_{\rm B}S = 1.07(1)\mu_{\rm B}$ by quantum fluctuations that persist in the magnetically ordered phase. A single-crystal magnetometry study of this compound furthermore implies that the $S = 1/2$ moments are well approximated by a Heisenberg model for $T \geq 2$ K, which is most likely to be a consequence of the high-symmetry of this tetragonal complex. This implies that related polymeric systems of this type might provide a platform on which to further investigate the magnetic properties of the Heisenberg $S = 1/2$ model in future experimental work. The main effect of a finite spin-orbit coupling interaction in $[Cu(HF_2)(pyz)_2]SbF_6$ is to give rise to an anisotropic g-factor, which accounts for the range of saturation fields observed [76] in pulsed-field powder magnetization measurements. However, the single-crystal magnetometry measurements performed in this work found no direct evidence for non-Heisenberg intraplane spin-exchange interactions in this compound and this result is used to infer that the finite ordering temperature of this Q2D $S = 1/2$ AFM is largely attributable to an antiferromagnetic exchange interaction $J_{\rm FHF}/k_{\rm B} = 0.12$ K along the HF_2^- ligands.

$[Ni(HF_2)(pyz)_2]SbF_6$ exhibits an XY-AFM ground-state for $T \leq 12.2$ K wherein the ordered Ni^{2+} moment $\mu_{\rm Ni} = 2.03(7)\mu_{\rm B}$ is consistent with the full paramagnetic value $g\mu_{\rm B}S \approx 2.08\mu_{\rm B}$ [47]. Estimates of the uniaxial single-ion anisotropy $D/k_{\rm B} = 15(1)$ K and the quantity $(2J_{\rm FHF} + 4J_{\rm pyz})/k_{\rm B} = 22.4(2)$ K are extracted for this compound using a semi-classical interpretation of the results of pulsed-field powder magnetization measurements. However, given the non-negligible size of $J_{\rm pyz}$, INS experiments performed on a powder are necessary to uniquely determine $D/k_{\rm B} = 13.3(3)$ K, $J_{\rm FHF}/k_{\rm B} = 10.4(3)$ K and $J_{\rm pyz}/k_{\rm B} = 1.4(2)$ K. These three magnetochemical parameters are used in a semi-classical Monte-Carlo simulation of the powder-average magnetization, which is found to provide a good approximation to the measured magnetization trace and furthermore suggests that the anisotropic saturation field of this exchange-coupled system compound largely derives from the easy-plane nature of D. Lastly, the results of a published [68] QMC study suggest that it is combination precise combination of the ratios $D/J_{\rm FHF}$ and $J_{\rm pyz}/J_{\rm FHF}$ that act to stabilize magnetic LRO in this Q1D $S = 1$ AFM system with respect to the disordered Haldane and quantum paramagnet phases.

Collectively, the work performed on the Ni^{2+} complex in this chapter outlines a strategy that may be used for the efficient characterization of related XY-like $S = 1$ powdered compounds. Firstly, elastic NPD measurements may be used to obtain the nature of the magnetic ground-state, thereby determining the sign of the single-ion anisotropy and nearest neighbour spin-exchange interactions. For systems with $g \approx 2$, $(D + z\langle J\rangle)/k_{\rm B} < 43.6$ K, and $T_{\rm C} > 800$ mK, then a semi-

classical interpretation of the results of powder-average magnetization measurements performed at ^{3}He temperatures with the 65 T capacitor-driven pulsed-field magnet at NHMFL (Los Alamos) may be used to infer the strengths of the D and the average nearest-neighbour spin-exchange $z\langle J\rangle$. In specific cases when the number of nearest neighbours z may be estimated (e.g. by inference from the structure, via DFT calculations, or by measuring power-law dependence of the low-T magnetic heat capacity), then powder magnetometry measurements alone are likely to be sufficient to characterize the spin Hamiltonian of the system. If the saturation field of a particular $S = 1$ compound exceeds the capabilities of pulsed-field magnets, or if the exchange constants are strong along multiple ligand types (as is the case for $[Ni(HF_2)(pyz)_2]SbF_6$), then INS measurements may be warranted in order to determine unique estimates of D and the individual components of $z\langle J\rangle$.

For $[Co(HF_2)(pyz)_2]SbF_6$, the results of powder heat capacity and NPD investigations demonstrate firstly that this spin system exhibits antiferromagnetic order for $T \leq 7.1(1)$ K; secondly that the Co^{2+} ions adopt the high-spin ($S = 3/2$) configuration; and thirdly that the combined effect of spin-orbit coupling and the CEF produced by the axially compressed CoN_4F_2 octahedra is to give rise to a low-energy Ising-like Kramers doublet within each Co^{2+} ion. A Curie-Weiss analysis of the powder-average inverse linear-susceptibility suggests that an effective spin $\sigma = 1/2$ Hamiltonian is applicable to this compound at temperatures $T < 50$ K and, within this model, the results of powder ESR measurements and magnetometry measurements indicate that the effective g-tensor components are $\tilde{g}_z = 5.5(7)$ and $\tilde{g}_{xy} = 3.4$, while the average spin-exchange interaction $z\tilde{J}/k_B = 39(9)$ K. Given that each $S = 3/2$ Co^{2+} spin-centre contains an unpaired electron in a suborbital with d_{z^2} character, in addition to the observations of the Ni^{2+} congener (above) that charge assisted H$\cdots$F bonds are efficient mediators of magnetic exchange, it is likely that the J_{FHF}/J_{pyz} ratio for $[Co(HF_2)(pyz)_2]SbF_6$ is greater than in the Cu^{2+} system. However, the absence of a broad maximum in the magnetic heat capacity for the Co^{2+} complex, in conjunction with the observation that the ordered Co^{2+} moment [$3.02(6)\mu_B$] accounts for the full paramagnetic value in the $\sigma = 1/2$ model implied by the results of ESR, suggests that the J_{FHF}/J_{pyz} ratio cannot be so large so as to move $[Co(HF_2)(pyz)_2]SbF_6$ towards the Q1D limit. Under the assumption that the exchange interactions along the pyz and HF_2^- molecules are comparable (i.e. $z = 6$), the measured ratio $k_BT_C/\tilde{J} = 1.1(2)$ is found to be consistent with the expectation value of 1.1 that is predicted for cubic Ising systems [193].

Chapter 6

Conclusions

This thesis provides an experimental and theoretical examination of five separate homometallic-organic coordination polymers. These investigations include an exploration of: (i) the adiabatic physics, zero-point fluctuations and possible two-dimensional universal behaviour of $Cu(pyz)(gly)ClO_4$ (pyz = pyrazine; gly = glycinate), an exchange-coupled spin-dimer complex; (ii) the significance of bond-disorder and the nature of the single-ion anisotropy in $[H_2F]_2[NiF_2(3\text{-}Fpy)_4]_3[SbF_6]_2$ (3-Fpy = 3-fluoropyridine), a spin $S = 1$ system for which the Ni^{2+} ions are arranged on the vertices of a two-dimensional kagome lattice; and (iii) the relation between some of the bulk thermodynamic and local magnetic properties of the isostructural series of tetragonal antiferromagnets (AFMs) $[M(HF_2)(pyz)_2]SbF_6$, where M is Cu^{2+} ($S = 1/2$), Ni^{2+} ($S = 1$) or Co^{2+} ($S = 3/2$).

$Cu(pyz)(gly)ClO_4$ is a spin-gapped system that adopts a zero-field quantum disordered ground-state [74]. In an applied magnetic field H the material exhibits a field-induced phase that is bounded by two zero temperature quantum critical points (QCPs) $H_{c1,2}$, between which the magnetic properties map onto the formation of a Bose-Einstein condensate that develops from a nonmagnetic vacuum. This electrically-insulating spin-dimer complex undergoes a strong and continuous magnetocaloric effect (MCE) (i.e. a change in the sample temperature T) under the application of adiabatic H sweeps that, when accounted for, explains an apparent discrepancy between the results of magnetometry measurements recorded in quasistatic and pulsed-magnetic fields. A direct pulsed-field measurement of the MCE implies that the sample T is perturbed by H, although the isentropes of the system (and therefore the full extent of the MCE) are most readily derived from an examination of heat capacity experiments performed in quasistatic H. A general thermodynamic model of the magnetic heat capacity C_{mag} is found to largely

account the observed form of the constant entropy contours in $Cu(pyz)(gly)ClO_4$, and these heat capacity simulations furthermore suggest that the MCE is a general property of spin-dimer systems; that is, if the antiferromagnetic intradimer exchange constant is given by J, then the initial sample temperature T_0 is expected to be immediately reduced by an adiabatic applied field $H > 0$ once $T_0 < 0.5J/k_B$. Thus, the MCE is concluded to be an important consideration for the pulsed-field measurements of electrically-insulating samples and not just for conductive materials, which are known to display effects such as eddy current heating in rapidly changing H (e.g. Ref. [113]).

Isothermal cuts through heat capacity measurements of $Cu(pyz)(gly)ClO_4$ reveal two sharp anomalies at H_{c1} and H_{c2}, where the peak height at the first critical field is substantially reduced relative to the maximum observed at the second critical point at the same sample T. This property is attributed to an extraordinary contribution to the heat capacity measurements from zero-point fluctuations that persist at $T > 400$ mK and, therefore, future work aimed at examining the bulk thermodynamic properties of polymeric Heisenberg $S = 1/2$ AFMs may provide an accessible means to further explore the macroscopic effects of fundamental microscopic spin fluctuations in the laboratory. For measurements recorded in quasistatic $H \approx H_{c2}$, the T dependence of C_{mag} for $Cu(pyz)(gly)ClO_4$ displays a power law exponent that is consistent with two-dimensional universal behaviour of this quantum spin system. This observation is furthermore in keeping with an analysis of published [74] room temperature structure of the compound, which suggests that the spin-density is likely to be largely distributed within individual $[Cu(pyz)(gly)]^+$ layers in this material.

The results of 100 K single-crystal x-ray diffraction measurements performed on the kagome complex $[H_2F]_2[NiF_2(3\text{-}Fpy)_4]_3[SbF_6]_2$, meanwhile, imply that each of the charge-assisted Ni-F$\cdots$H-F-H$\cdots$F-Ni hydrogen-bonded bridges that connect the individual spin-centres within the kagome layers exhibits two-levels of positional disorder: (i) the central F atom of the H_2F^+ moiety adopts one of two possible positions; and (ii) for each F site the whole poly-HF cation rotates to adopt one of three equally-likely orientations. A computational density-functional theory (DFT) study [75] suggests that while property (i) is expected to have little impact on the magnetic properties of the system, the effect of (ii) is to suppress the strength of the intraplane Ni-Ni spin-exchange interactions. The results of polycrystalline muon spin-rotation experiments corroborate the predicted weak nature of the exchange interactions, revealing that there is no long-range magnetic order in this system for $T \geq 0.019$ K. In addition, the observations derived from powder electron spin-

resonance (ESR), heat capacity and magnetometry experiments are all accounted for by considering the uniaxial D and rhombic E single-ion anisotropy of the Ni^{2+} ions alone, where $D/k_B = 8.3(4)$ K and $E/k_B = 1.2(3)$ K respectively. The interesting structure of $[H_2F]_2[NiF_2(3\text{-}Fpy)_4]_3[SbF_6]_2$ and the surprisingly strong effect that the positional disorder of the H_2F^+ moieties has on the bulk magnetic properties of this compound suggests that similar polymeric magnets consisting of charge-assisted hydrogen-bonds are likely to continue to play a key role in the investigation of the interdependence of magnetic order, geometric frustration, and structural disorder in condensed matter systems.

The results of time-of-flight neutron powder diffraction (NPD) and single crystal magnetometry measurements of $[Cu(HF_2)(pyz)_2]SbF_6$ suggest that this quasi-two-dimensional $S = 1/2$ square-lattice AFM is well approximated by a Heisenberg (isotropic) spin model at $T \geq 2$ K. The ordered Cu^{2+} moment $\mu_{Cu} = 0.6(1)\mu_B$ is determined to be reduced from a powder-average paramagnetic (PM) value of $g\mu_B S = 1.07(1)\mu_B$ [45, 76] by quantum fluctuations (QFs) that persist within the magnetically ordered phase. In the absence of direct evidence for anisotropic intraplane spin-exchange interactions mediated by the pyz linkages, this compound is most likely to be driven to magnetic long-range order below a critical temperature $T_C = 4.3$ K as a result of antiferromagnetic interlayer spin-exchange interactions $J_{FHF}/k_B = 0.12$ K facilitated by the HF_2^- ligands. In summary, this work suggests that similar tetragonal polymeric $S = 1/2$ systems might provide a set of compounds in which to further examine the magnetic properties of the Heisenberg square-lattice model in future experimental work.

A NPD investigation of $[Ni(HF_2)(pyz)_2]SbF_6$ and $[Co(HF_2)(pyz)_2]SbF_6$ implies that the ordered Ni^{2+} [$\mu_{Ni} = 2.03(7)\mu_B$] and Co^{2+} [$\mu_{Co} = 3.02(6)\mu_B$] moments of these systems are consistent with their respective PM values. While these systems both have a larger S quantum number with respect to the isostructural Cu^{2+} congener, the suppression of QFs in each of the Ni^{2+} and Co^{2+} compounds is attributed to a combined effects of: (i) the single-ion anisotropy; and (ii) the larger J_{FHF}/J_{pyz} ratio of the interplane to intraplane spin-exchange constants for these materials. Point (ii) further suggests that Ni^{2+} and Co^{2+} complexes are likely to play a significant part in evaluating the role charge-assisted hydrogen bonds can play in facilitating magnetic exchange interactions within crystalline polymeric compounds.

The NPD study of $[Ni(HF_2)(pyz)_2]SbF_6$ additionally indicates that D has an XY-like (easy-plane nature) in this polymeric complex. A semi-classical interpretation of the measured anisotropic saturation field of this compound is employed to provide quantitative estimates of $D/k_B = 15(1)$ K and the average quantity

$z\langle J\rangle/k_{\rm B} \equiv (2J_{\rm FHF} + 4J_{\rm pyz})/k_{\rm B} = 22.4(2)$ K. However, since the results of DFT calculations predict that there is a significant delocalization of spin-density over both the pyz and HF_2^- ligands in this particular system [77], inelastic neutron scattering (INS) measurements of a powdered sample are necessary to uniquely determine $D/k_{\rm B} = 13.3$ K, $J_{\rm FHF}/k_{\rm B} = 10.3$ K and $J_{\rm pyz}/k_{\rm B} = 1.6$ K. The measured $D/J_{\rm FHF}$ and $J_{\rm pyz}/J_{\rm FHF}$ ratios combine with a published [68] quantum Monte-Carlo study of the phase-diagram of quasi-one-dimensional (Q1D) $S = 1$ AFMs to suggest that $[Ni(HF_2)(pyz)_2]SbF_6$ lies close to a QCP that is predicted to separate long-range magnetic order from two topologically distinct quantum disordered phases. Future work might aim to perturb $[Ni(HF_2)(pyz)_2]SbF_6$ (e.g. with pressure or uniaxial stress) in order to explore a greater proportion of this low-temperature theoretical phase diagram in the laboratory.

The results of heat capacity and NPD measurements of the Co^{2+} complex combine to show that this material adopts an Ising-like antiferromagnetic spin-state at temperatures below $T_{\rm C} = 7.1(1)$ K. The ratio $J_{\rm FHF}/J_{\rm pyz}$ is likely to be greater in this high-spin Co^{2+} compound relative to the size of this ratio in the Cu^{2+} congener, although an absence of a broad hump in $C_{\rm mag}$ at $T \geq T_{\rm C}$ for $[Co(HF_2)(pyz)_2]SbF_6$ in addition to the observation that the ordered Co^{2+} moment accounts for the full PM value in the effective spin $\sigma = 1/2$ model that is observed with ESR, the ratio of the spin-exchange constants along the HF_2^- and pyz ligands cannot be so large so as to move the Co^{2+} material towards the Q1D limit. With this deduction, the results of powder magnetization experiments imply that average nearest-neighbour spin-exchange interaction in the effective $\sigma = 1/2$ Hamiltonian is $\tilde{J}/k_{\rm B} = 7(1)$ K and the measured ratio of $k_{\rm B}T_{\rm C}/\tilde{J} = 1.1(2)$ is consistent with the value expected in the case of Ising spins arranged on the corners of a cubic lattice [193].

The thesis also pays attention to some of the general results of Chapters 4 and 5 that may be pertinent to future work that is aimed at the characterization of powdered XY-like $S = 1$ materials. For systems comprised of weakly-coupled ions, pulsed-field magnetometry is determined to be an efficient means to estimate the strength of D. Specifically, a small bump in the differential powder susceptibility is predicted to occur at a critical field $\mu_0 H_{\rm C} = (D^2 - E^2)^{1/2}/(g\mu_{\rm B})$ for temperatures performed below $\approx 0.18D/k_{\rm B}$. Thus, in cases when $D \ll E$ and $g = 2$, this implies that ^{3}He magnetometry measurements performed with the 65 T capacitor-driven short-pulse magnets at the National High Magnetic Field Laboratory (NHMFL), Los Alamos, are likely to be sensitive to single-ion anisotropies in the approximate range $2.2 \leq D/k_{\rm B} \leq 87.1$ K. If, however, the $S = 1$ ions have an average spin-exchange $\langle J\rangle$ to z nearest neighbours, then NPD measurements of the magnetic ground-state are

a reliable way to extract the sign of individual terms in the spin Hamiltonian. Following this, pulsed field magnetometry at NHMFL (Los Alamos) ought to be useful as a means to estimate the sizes of D and $z\langle J\rangle$ providing $(D + z\langle J\rangle)/k_{\mathrm{B}} < 43.6$ K, $g = 2$, and $T_{\mathrm{C}} > 800$ mK. An INS investigation is likely to be most appropriate in instances when: (i) z cannot be estimated from the structure, via DFT calculations, or through measurements of the low-temperature power-law dependence of $C_{\mathrm{mag}}(\mathrm{T})$; (ii) there are comparable spin-exchange interactions over multiple ligand types; or (iii) the energy scale of $2(D + z\langle J\rangle)/(g\mu_{\mathrm{B}})$ exceeds the maximum $\mu_0 H$ that can be achieved with experimental systems.

Perhaps, above all else, this thesis shows that polymeric magnets provide an accessible means to experimentally investigate a wide range of emergent magnetic phenomena even when the compounds themselves are comprised from a relatively small number of molecular building blocks. Given firstly that there has been a sustained theoretical and experimental interest in the tunable nature of condensed matter magnetism, which goes back as far as Pierre Curie's early examination of the temperature dependent properties of ferromagnets in the 19^{th} century [1]; and secondly that metal-organic frameworks offer physicists, chemists and materials scientists an unprecedented degree of control over some of the microscopic characteristics of solid-state systems including the size of the spin quantum number, the dimensionality of the spin-exchange network, and the nature of the single-ion anisotropy (e.g. Refs. [4, 22–24]), it seems beyond doubt that coordination polymers will continue to play an integral role in condensed matter research by facilitating many more laboratory-based investigations of quantum magnetism in the future.

Bibliography

[1] (a) P. Curie, *Propriétés magnétiques des corps à diverses températures*, Docteur ès Sciences Physiques, University of Paris (1895); (b) For a review of P. Curie's early work in electromagnetism see: R. F. Mould, Curr. Oncol. **14**, 74 (2007).

[2] (a) P. Zeeman, Versl. Kon. Ak. Wet. **5**, 181 (1896); (b) P. Zeeman, Phil. Mag. **43**, 226 (1897) (English translation).

[3] P. Weiss, J. Phys. **6**, 661 (1907).

[4] C. P. Landee and M. M. Turnball, Eur. J. Inorg. Chem., 2266 (2013).

[5] A. Sommerfeld, Verlagd. KB Akad. d. Wiss (1915).

[6] A. Sommerfeld, Naturwissenschaften, **8**, 61 (1920).

[7] W. Gerlach and O. Stern, Z. Phys. **9**, 349 (1922).

[8] For a review see: A. Komech, *Electron Spin and Pauli Equation*, In: *Quantum Mechanics: Genesis and Achievements* (Sprinder, Dordrecht, 2013) pp 151-164.

[9] W. Heisenberg, Z. Phys. **49**, 619 (1928).

[10] P. W. Anderson, Phys. Rev. **115**, 2 (1959).

[11] L. Néel, Ann. Phys. (Paris) **17**, 5 (1932).

[12] C. G. Shull and J. Samuel Smart, Phys. Rev. **76**, 1256 (1949).

[13] E. Manousakis, Rev. Mod. Phys. **63**, 1 (1991).

[14] C. W. Chu, Nat. Phys. **5**, 787 (2009).

[15] S. Sachdev and B. Keimer, Phys. Today **64**, 29 (2011).

[16] S. Sachdev, *Quantum Phase Transitions*, 2^{nd} Ed. (Cambridge University Press, Cambridge, 2011).

[17] J. M. Kosterlitz and D. J. Thouless, J. Phys. C: Solid State Physics. **5**, 124 (1972).

[18] J. M. Kosterlitz and D. J. Thouless, J. Phys. C: Solid State Physics. **6**, 1181 (1973).

[19] F. D. Haldane, Phys. Lett. A, **93**, 464 (1983).

[20] F. D. Haldane, Phys. Rev. Lett **50**, 1153 (1983).

[21] The Nobel Prize in Physics 2016 Advanced Information, Nobelprize.org., Nobel Media AB 2014, http://www.nobelprize.org/nobel_prizes/physics/laureates/2016/advanced.html.

[22] S. J. Blundell, Contemp. Phys. **48**, 275 (2007).

[23] O. Khan, *Molecular Magnetism* (Wiley-VCH, Belrin, 1993).

[24] T. R. Cook, Y.-R. Zheng, and P. J. Stang, Chem. Rev. **113**, 734 (2013).

[25] N. Thejo Kalyani and S. J. Dhoble, Renew. Sustain. Energy Rev. **16**, 2696 (2012).

[26] G. Saito and Y. Yoshida, Chem. Rec. **11**, 124 (2011).

[27] A. Y. Ganin, Y. Takabayashi, Y. Z. Khimyak, S. Margadonna, A. Tamai, M. J. Rosseinsky, and K. Prassides, Nat. Mater. **7**, 367 (2008).

[28] J. Duan, W. Jin, and S. Kitagawa, Coord. Chem. Rev. **332**, 48 (2017).

[29] S. J. Blundell, *Magnetism in Condensed Matter* (Oxford University Press, Oxford, 2001).

[30] C. J. Foot, *Atomic Physics* (Oxford University Press, Oxford, 2005).

[31] J. Binney and D. Skinner, *The Physics of Quantum Mechanics* (Oxford University Press, Oxford, 2014) pp. 167-218.

[32] K. Konishi and G. Paffuti, *Quantum Mechanics A New Introduction* (Oxford University Press, Oxford, 2009) p. 97.

[33] W. Pauli, Z. Phys **26**, 178 (1924).

[34] J. Titiš and R. Boča, Inorg. Chem. **50**, 11838 (2011).

[35] F. Xiao, F. M. Woodward, C. P. Landee, M. M. Turnball, C. Mielke, N. Harrison, T. Lancaster, S. J. Blundell, P. J. Baker, P. Babkevich, and F. L. Pratt, Phys. Rev. B **79**, 134412 (2009).

[36] U. Walter, J. Phys. Chem. Solids. **45**, 401 (1984).

[37] R. Boča, Coord. Chem. Rev. **248**, 757 (2004).

[38] (a) J. R. Schrieffer and P. A. Wolff, Phys. Rev. **149**, 491 (1966); (b) For a recent review see: S. Bravyi, D. P. DiVincenzo, and D. Loss, Ann. Physics **326**, 2793 (2011).

[39] O. Breunig, M. Garst, E. Sela, B. Buldmann, P. Becker, L. Bohatý, R. Müller, and T. Lorenz, Phys. Rev. Lett. **111**, 187202 (2013).

[40] S. K. Niesen, O. Breunig, S. Salm, M. Seher, M. Valldor, P. Warzanowski, and T. Lorenz, Phys. Rev. B **90**, 104419 (2014).

[41] K. Momma and F. Izumi, J. Appl. Crystallogr. **44**, 1272 (2011).

[42] H. W. Richardson, J. R. Wasson, and W. E. Hatfield, Inorg. Chem. **16**, 484 (1977).

[43] F. Mohri, K. Yoshizawa, T. Yambe, T. Ishida, and T. Nogami, Mol. Eng. **8**, 357 (1999).

[44] L. H. R. Dos Santos, A. Lanza, A. M. Barton, J. Brambleby, W. J. A. Blackmore, P. A. Goddard, F. Xiao, R. C. Williams, T. Lancaster, F. L. Pratt, S. J. Blundell, J. Singleton, J. L. Manson, and P. Macchi, J. Am. Chem. Soc **138**, 2280 (2016).

[45] P. A. Goddard, J. Singleton, P. Sengupta, R. D. McDonald, T. Lancaster, S. J. Blundell, F. L. Pratt, S. Cox, N. Harrison, J. L. Manson, H. I. Southerland, and J. A. Schlueter, New. J. Phys. **10**, 083025 (2008).

[46] P. A. Goddard, J. Singleton, I. Franke and J. S. Möller, T Lancaster, A. J. Steele, C. V. Topping, S. J. Blundell, F. L. Pratt, C. Baines, J. Bendix, R. D. McDonald, J. Brambleby, M. R. Lees, S. H. Lapidus, P. W. Stephens, B. W. Twamley, M. M. Conner, K. Funk, J. F. Corbey, H. E. Tran, J. A. Schlueter. and J. L. Manson, Phys. Rev. B **93**, 094430 (2016).

[47] J. L. Manson, S. H. Lapidus, P. W. Stephens, P. K. Peterson, K. E. Carreiro, H. I. Southerland, T. Lancaster, S. J. Blundell, A. J. Steele, P. A. Goddard,

F. L. Pratt, J. Singleton, Y. Kohama, R. D. McDonald, R. E. Del Sesto, N. A. Smith, J. Bendix, S. A. Zvyagin, J. Kang, C. Lee, M-H. Whangbo, V. S. Zapf, and A. Plonczak, Inorg. Chem. **50**, 5990 (2011).

[48] J. Liu, P. A. Goddard, J. Singleton, J. Brambleby, F. Foronda, J. S. Möller, Y. Kohama, S. Ghannadzadeh, A. Ardavan, S. J. Blundell, T. Lancaster, F. Xiao, R. C. Williams, F. L. Pratt, P. J. Baker, K. Wierschem, S. H. Lapidus, K. H. Stone, P. W. Stephens, J. Bendix, T. J. Woods, K. E. Carreiro, H. E. Tran, C. J. Villa, and J. L. Manson, Inorg. Chem. **55**, 3515 (2016).

[49] A. Bencini and D. Gatteschi, *EPR of exchange coupled systems* (Dover Publications, Mineola, 2012).

[50] K. Yosida, *Theory of Magnetism* (Springer-Verlag, Berlin, 1996).

[51] E. A. Abbot, *Flatland: A Romance in Many Dimensions*, (Penguin Books Ltd., New York, 1998) p 7.

[52] V. Zapf, M. Jaime and C. D. Batista, Rev. Mod. Phys. **86**, 563 (2014).

[53] C. Yasuda, S. Todo, K. Hukushima, F. Alet, M. Keller, M. Troyer, and H. Takayama, Phys. Rev. Lett. **94**, 217201 (2005).

[54] A. Santoro, A. D. Mighell, and C. W. Reimann, Acta. Cryst. B **26**, 979 (1970).

[55] (a) J. L. Manson, J. G. Lecher, J. Gu, U. Geiser, J. A. Schlueter, R. Henning, X. Wang, A. J. Schultz, H.-J. Koo, M.-H. Whangbo, Dalt. Trans. **0**, 2905 (2003); (b) Note the factor of 2 difference between the definition of J in this reference and this thesis.

[56] P. R. Hammar, M. B. Stone, D. H. Reich, C. Broholm, P. J. Gibson, M. M. Turnball, C. P. Landee, and M. Oshikawa, Phys. Rev. B. **59**, 1008 (1999).

[57] T. Lancaster, S. J. Blundell, M. L. Brooks, and P. J. Baker, F. L. Pratt, J. L. Manson, C. P. Landee, and C. Baines, Phys. Rev. B **73**, 020410(R) (2006).

[58] T. Lancaster, S. J. Blundell, M. L. Brooks, P. J. Baker, F. L. Pratt, J. L. Manson, and C. Baines, Phys. Rev. B **73**, 172403 (2006).

[59] J. Brambleby, P. A. Goddard, R. D. Johnson, J. Liu, D. Kaminski, A. Ardavan, A. J. Steele, S. J. Blundell, T. Lancaster, P. Manuel, P. J. Baker, J. Singleton, S. G. Schwalbe, P. M. Spurgeon, H. E. Tran, P. K. Peterson, J. F. Corbey, and J. L. Manson, Phys. Rev. B **92**, 134406 (2015).

[60] J. Choi, J. D. Woodward, J. L. Musfeldt, C. P. Landee, M. M. Turnball, Chem. Mater. **15**, 2797 (2003).

[61] F. M. Woodward, P. J. Gibson, G. B. Jameson, C. P. Landee, M. M. Turnball, and R. D. Willett, Inorg. Chem. **46**, 4256 (2007).

[62] J. Darrier, M. S. Haddad, E. N. Duesler, and D. N. Hendrickson, Inorg. Chem. **18**, 2679 (1979).

[63] M. S. Haddad, D. N. Hendrickson, J. P. Cannady, R. S. Drago, and D. S. Bieksza, J. Am. Chem. Soc. **101**, 898 (1979).

[64] A. Cuccoli, T. Roscilde, V. Tognetti, R. Vaia, and P. Verrucchi, Phys. Rev. B **67**, 104414 (2003).

[65] P. A. Goddard, J. L. Manson, J. Singleton, I. Franke, T. Lancaster, A. J. Steele, S. J. Blundell, C. Baines, F. L. Pratt, R. D. McDonald, O. E. Ayala-Valenzuela, J. F. Corbey, H. I. Southerland, P. Sengupta, and J. A. Schlueter, Phys. Rev. Lett. **108**, 077208 (2012).

[66] J. L. Manson, A. G. Bladwin, B. L. Scott, J. Bendix, R. E. Del Sesto, P. A. Goddard, Y. Kohama, H. E. Tran, S. Ghannadzadeh, J. Singleton, T. Lancsater, J. S. Möller, S. J. Blundell, F. L. Pratt, V. S. Zapf, J. Kang, C. Lee, M-H. Whangbo, and C. Baines, Inorg. Chem. **51**, 7520 (2012).

[67] J.-S. Xia, A. Ozarowski, P. M. Spurgeon, A. G. Baldwin, J. L. Manson, and M. W. Meisel, arXiv:1409.5971v1.

[68] K. Wierschem and P. Sengupta, Mod. Phys. Lett. B **28**, 1430017 (2014).

[69] H. J. Buser, D. Schwarzenbach, W. Petter, and A. Ludi, Inorg. Chem. **16**, 2704 (1977).

[70] S. Ghannadzadeh, J. S. Möller, P. A. Goddard, T. Lancaster, F. Xiao, S. J. Blundell, A. Maisuradze, R. Khasanov, J. L. Manson, S. W. Tozer, D. Graf, and J. A. Schlueter, Phys. Rev. B **87**, 241102(R) (2013).

[71] R. Yu, L. Yin, N. S. Sullivan, J. S. Xia, C. Huan, A. Paduan-Filho, N. F. Oliveira Jr, S. Haas, A. Steppke, C. F. Miclea, F. Weikert, R. Movshovich, E.-D. Mun, B. L. Scott, V. S. Zapf, and T. Roscilde, Nature **489**, 379 (2012).

[72] I. A. Zalinznyak, D. C. Dender, C. Broholm, and R. H. Reich, Phys. Rev. B **57**, 5200 (1998).

[73] J. Brambleby, P. A. Goddard, J. Singleton, M. Jaime, T. Lancaster, L. Huang, J. Wosnitza, C. V. Topping, K. E. Carreiro, H. E. Tran, Z. E. Manson, and J. L. Manson, Phys. Rev. B **95**, 024404 (2017).

[74] T. Lancaster, P. A. Goddard, S. J. Blundell, F. R. Foronda, S. Ghannadzadeh, J. S. Möller, P. J. Baker, F. L. Pratt, C. Baines, L. Huang, J. Wosnitza, R. D. McDonald, K. A. Modic, J. Singleton, C. V. Topping, T. A. W. Beale, F. Xiao, J. A. Schlueter, A. M. Barton, R. D. Cabrera, K. E. Carreiro, H. E. Tran, and J. L. Manson, Phys. Rev. Lett. **112**, 207201 (2014).

[75] J. L. Manson, J. Brambleby, P. M. Spurgeon, J. A. Villa, J. Liu, S. Ghannadzadeh, F. Foronda, P. A. Goddard, J. Singleton, T. Lancaster, S. Clarke, I. O. Thomas, F. Xiao, R. C. Williams, F. L. Pratt, S. J. Blundell, C. V. Topping, C. Baines, C. Campana, and B. Noll, Sci. Rep. **8**, 4745 (2018).

[76] J. L. Manson, J. A. Schlueter, K. A. Funk, H. I. Southerland, B. Twamley, T. Lancaster, S. J. Blundell, P. J. Baker, F. L. Pratt, J. Singleton, R. D. McDonald, P. A. Goddard, P. Sengupta, C. D. Batista, L. Ding, C. Lee, M.-H. Whangbo, I. Franke, S. Cox, C. Baines, and D. Trial, J. Am. Chem. Soc. **131**, 6733 (2009).

[77] J. Brambleby, J. L. Manson, P. A. Goddard, M. B. Stone, R. D. Johnson, P. Manuel, J. A. Villa, C. M. Brown, H. Lu, S. Chikara, V. Zapf, S. H. Lapidus, R. Scatena, P. Macchi, Y.-S. Chen, L.-C. Wu, and J. Singleton, Phys. Rev. B **95**, 134435 (2017).

[78] G. A. Bain and J. F. Berry, J. Chem. Edu. **85**, 532 (2008).

[79] S. J. Blundell and K. M. Blundell, *Thermal Physics*, 2$^{\text{nd}}$ Ed. (Oxford University Press, Oxford, 2013).

[80] P. Debye, Ann. Phys. (Leipzig) **81**, 1154 (1926).

[81] W. F. Giauque, *J. Am. Chem. Soc.* **49**, 1864 (1927).

[82] Y. Kohama, C. Marcenat, T. Klein, and M. Jaime, Rev. Sci. Inst. **81**, 104902 (2010).

[83] B. Wolf, A. Honecker, W. Hofstetter, U. Tutsch, and M. Lang, Intl. J. Mod. Phys. B **28**, 1430017 (2014).

[84] O. V. Lounasmaa, *Experimental Principles and Methods Below 1 K* (Academic Press, New York, 1974).

[85] A. M. Tishin and Y. I. Spichkin, *The Magnetocaloric Effect and its Applications* (Institute of Physics Publishing, Bristol, 2003).

[86] K. A. Gschneidner Jr., V. K. Pecharsky, and A. O. Tsokol, Rep. Prog. Phys. **68**, 1479 (2005).

[87] U. Tutsch, B. Wolf, S. Wessel, L. Postulka, Y. Tsui, H. O. Jeschke, I. Opahle, T. Saha-Dasgupta, R. Valentí, A. Brühl, K. Remović-Langer, T. Kretz, H.-W. Lerner, M. Wagner, and M. Lang, Nat. Comm. **5**, 5169 (2014).

[88] D. Strassel, P. Kopietz, and S. Eggert, Phys. Rev. B **91**, 134406 (2015).

[89] B. Bleaney and K. A. Bowers, Proc. R. Soc. A **214**, 451 (1952).

[90] T. Giamarchi, C. Rüegg, and O. Tchernyshyov, Nat. Phys. **4**, 198 (2008).

[91] S. E. Sebastian, N. Harrison, C. D. Batista, L. Balicas, M. Jaime, P. A. Sharma, N. Kawashima, and I. R. Fisher, Nature (London) **441**, 617 (2006).

[92] V. S. Zapf, D. Zocco. B. R. Hansen, M. Jaime, N. Harrison, C. D. Batista, M. Kenzelmann, C. Niedermayer, A. Lacerda, and A. Paduan-Filho, Phys. Rev. Lett. **96**, 077204 (2006).

[93] M. Lang, B. Wolf, A. Honecker, L. Balents, U. Tutsch, P. T. Cong, G. Hofmann, N. Krüger, F. Ritter, W. Assmus, and A. Prokofiev, Phys. Status Solidi B **250**, 457 (2013).

[94] Y. Kohama, A. V. Sologubenko, N. R. Dilley, V. S. Zapf, M. Jaime, J. A. Mydosh, A. Paduan-Filho, K. A. Al-Hassanieh, P. Sengupta, S. Gangadharaiah, A. L. Chernyshev, and C. D. Batista, Phys. Rev. Lett. **106**, 037203 (2011).

[95] F. Weickert, R. Küchler, A. Steppke, L. Pedrero, M. Nicklas, M. Brando, F. Steglich, M. Jaime, V. S. Zapf, A. Paduan-Filho, K. A. Al-Hassenieh, C. D. Batista, and P. Sengupta, Phys. Rev. B **85**, 184408 (2012).

[96] H. Bethe, Z. Phys. **71**, 205 (1931).

[97] S. Chakravarty, B. I. Halperin, and D. R. Nelson, Phys. Rev. Lett. **60**, 1057 (1988).

[98] P. W. Anderson, Phys. Rev. **86**, 694 (1952).

[99] S. J. Blundell, Contemp. Phys. **40**, 175 (1999).

[100] A. Schenck and F. N. Gygax, *Magnetic materials studied by muon spin rotation*, In: K. H. J. Buschow (ed), *Handbook of Magnetic Materials* (Elsevier, Amsterdam, 1995) pp 57-302.

[101] N. Tsyrulin, F. Xiao, A. Schneidewind, P. Link, H. M. Rønnow, J. Gavilano, C. P. Landee, M. M. Turnball, and M. Kenzelmann, Phys. Rev. B **81**, 134409 (2010).

[102] P. Sengupta, A. W. Sandvik, and R. P. Singh, Phys. Rev. B. **68**, 094423 (2003).

[103] X. Feng and H. W. J. Blöte, Phys. Rev. E **81**, 031103 (2010).

[104] H. W. J. Blöte and W. J. Huiskamp, Phys. Lett. A **29**, 304 (1969).

[105] R. Honmura, Phys. Rev. B **30**, 348 (1984).

[106] L. Onsager, Phys. Rev. **65**, 117 (1944).

[107] H. Ikeda, I. Hatta, and M. Tanaka, J. Phys. Soc. Jpn. **40**, 334 (1975).

[108] D. I. Khomskii, *Basic Aspects of the Quatum Theory of Solids Order and Elementary Exciations* (Cambridge Unversity Press, Cambridge, 2010) pp 105-106.

[109] Z. Honda, K. Katsumara, Y. Nishiyama and I. Harada, Phys. Rev. B **63**, 064420 (2001).

[110] D. J. Sellmyer, B. Balamurugan, W. Y. Zhang, B. Das, R. Skomski, P. Kharel, and Y. Liu, *Advances in Rare-Earth-Free Permanent Magnets*, In: F. Marquis (eds) *Proceedings of the 8th Pacific Rim International Congress on Advanced Materials and Processing* (Spinger, Cham, 2013) pp 1689-1696.

[111] (a) H. C. Ørsted, J. Chem. Phys. Phys. **29**, 275 (1820); (b) H. C. Ørsted Ann. Philosophy **16**, 273 (1820); (c) H. C. Ørsted, *Experimenta circa effectum conflictus electrici in acum magneticam*, Copenhagen (1820) (orginal publication, in Latin).

[112] W. J. Duffin, *Electricity and Magnetism*, 4$^{\text{th}}$ Ed. (McGraw-Hill, Maidenhead, 1990) p 172.

[113] F. Herlach, Rep. Prog. Phys. **62**, 859 (1999).

[114] Resistive Magnets, Nationalmaglab.org, National MagLab 2017, *http://www.nationalmaglab.org/user-facilities/dc-field/instruments-dcfield/resistive-magents.*

[115] F. J. Brown, N. W. Kerley, R. B. Know, and K. W. Timms, Physica B, **216**, 203 (1996).

[116] D. Dew-Hughes, Low. Temp. Phys. **27**, 713 (2001).

[117] R. Gupta, *High Temperature Superconductor (HTS) Magnet R&D and Designs*, In: *USPAS Course on Superconducting Accerator Magnets* (Brookhaven National Laboratory, 2003) p 6.

[118] 32 Tesla All-Superconducting Magnet, Nationalmaglab.org, National MagLab 2017, *http://www.nationalmaglab.org/magnet-development/magnet-science-technology/magnet-projects/32-tesla-scm.*

[119] 60 tesla long pulse magnet, Lanl.gov, Los Alamos National Security 2010-11, *http://www.lanl.gov/orgs/mpa/nhmfl/60TLP.shtml.*

[120] M. McElfresh, *Fundamentals of Magnetism and Magnetic Measurements* (Quantum Design, Inc., San Diego, 1994) pp 1-34.

[121] MPMS Application Note 1014-208 A (Quantum Design, Inc., San Diego, 2001) pp 1-12.

[122] *Magnetic Property Mesurement System MPMS MultiVu Application User's Manual*, 3rd Ed. (Quantum Design Inc., San Diego, 2004). pp **3**-1 - **3**-21.

[123] J. F. Annett, *Superconductivity, Superfluids and Condensates* (Oxford University Press, Oxford, 2013) pp 116-120.

[124] *Magnetic Property Measurement System AC Option User's Manual*, 2nd Ed. (Quantum Design, Inc., San Diego, 1999) pp **1**-1 - **2**-1.

[125] D. Martien, *Intorduction to: AC Susceptibility* (Quantum Design, Inc., San Diego) pp 1-2.

[126] *Physical Property Measurement System Vibrating Sample Magnetometry (VSM) Option User's Manual*, 5th Ed. (Quantum Design Inc., San Diego, 2008). pp. **1**-1 - **1**-3.

[127] M. M. Altarawneh, C. H. Mielke, and J. S. Brooks, Rev. Sci. Instrum. **80**, 066104 (2009).

[128] S. Ghannadzadeh, M. Coak, I. Franke, P. A. Goddard, J. Singleton, and J. L. Manson, Rev. Sci. Instrum. **82**, 113902 (2011).

[129] J. C. Lashley, M. F. Hundley, A. Migliori, J. L. Sarrao, P. G. Pagliuso, T. W. Darling, M. Jaime, J. C. Cooley, W. L. Hults, L. Morales, D. J. Thoma, J. L. Smith, J. Boerio-Goates, B. F. Woodfield, G. R. Stewart, R. A. Fisher, and N. E. Phillips, Cryogenics, **43**, 369 (2003).

[130] *Physical Property Measurement System Heat Capacity Option User's Manual*, 11$^{\text{th}}$ Ed. (Quantum Design Inc., San Diego, 2004) pp **1**-1 - **1**-4, **3**-1 - **3**-3, and **4**-3 - **4**-6.

[131] J. S. Hwang, K. J. Lin, and C. Tien, Rev. Sci. Inst. **68**, 94 (1997).

[132] S. H. Simon, *The Oxford Solid State Basics* (Oxford University Press, New York, 2013) pp. 139-160.

[133] I. A. Zaliznyak and S.-H. Lee, In: Y. Zhu (ed), *Modern Techniques for Characterizing Magnetic Materials*, (Springer, Heidelberg, 2005).

[134] J. R. D. Copley and T. J. Udovic, J. Res. Natl. Inst. Stand. Technol. **98**, 71 (1993).

[135] V. F. Sears, Neutron News **3**, 26 (1992).

[136] L. C. Chapon, P. Manuel, P. Radelli, C. Benson, L. Perrott, S. Ansell, N. Rhodes, D. Raspino, D. Duxbery, E. Spill, and J. Norris, Neutron News **22**, 22 (2011).

[137] J. R. D. Copley, Physica B **180-181**, 914 (1992).

[138] J. R. D. Copley and J. C. Cook, Chem. Phys. **292**, 477 (2003).

[139] J. R. D. Copley, *The Disc Chopper Spectrometer at NIST: The Good, The Bad and The Ugly* (17th Meeting of the International Collaboration on Advanced Neutron Sources, Santa Fe, 1992) pp 1-10.

[140] MATLAB v.8.0.0.783; The Math Works, Inc.: Natick, MA, 2012.

[141] R. K. Kaul, R. G. Melko, and A. W. Sandvik, Ann. Rev. Condens. Matter Phys. **4**, 179 (2013).

[142] D. P. Landau and K. Binder, *A Guide to Monte Carlo Simulations in Statistical Physics*, 3$^{\text{rd}}$ Ed. (Cambridge University Press, Cambridge, 2009) pp. 68-137.

[143] Z. Wang, D. L. Quinter-Castro, S. Zherlitsyn, S. Yasin, Y. Skourski, A. T. M. N. Islam, B. Lake, J. Deisenhoefer, and A. Loidl, Phys. Rev. Lett, **116**, 147201 (2016).

[144] Z. Wang, D. L. Quinter-Castro, S. Zherlitsyn, S. Yasin, Y. Skourski, A. T. M. N. Islam, B. Lake, J. Deisenhoefer, and A. Loidl, Phys. Rev. Lett, **117**, 189901(E) (2016).

[145] V. L. Berezinkskii, Sov. Phys. JETP **34**, 610 (1972).

[146] N. Kawashima, J. Phys. Soc. Jpn. **74**, 145 (2005).

[147] H. Ryll, K. Kiefer, Ch. Rüegg, S. Ward, K. W. Krämer, D. Biner, P. Bouillot, E. Coira, T. Giamarchi, and C. Kollath, Phys. Rev. B **89**, 144416 (2014).

[148] M. A. Continentino, J. Magn. Magn. Mater. **310**, 849 (2006).

[149] J. Oitmaa and C. J. Hamer, Phys. Rev. B **77**, 224435 (2008).

[150] J. A. Mydosh, *Spin Glasses: An Experimental Introduction* (Taylor and Francis, New York, 1993).

[151] S. Mukherjee, A. Garg, and R. Gupta, Appl. Phys. Lett. **100**, 112904 (2012).

[152] T. Chakrabarty, A. V. Mahajan, and S. Kundu, J. Phys.: Condens. Matter **26**, 405601 (2014).

[153] T.-H. Wan, J. Singleton, and J. A. Schlueter, Phys. Rev. Lett **113**, 227203 (2014).

[154] N. Woo, D. M. Silvitch, C. Ferri, S. Ghosh, and T. F. Rosenbaum, J. Phys.: Condens. Matter **27**, 296001 (2015).

[155] A. P. Ramirez, Ann. Rev. Mater. Sci. **24**, 453 (1994).

[156] R. Moessner, Can. J. Phys. **79**, 1283 (2001).

[157] L. Balents, Nature **464**, 199 (2010).

[158] M. J. P. Gingras and P. A. McClarty, Rep. Prog. Phys. **77**, 056501 (2014).

[159] T. Imai and Y. Lee, Phys. Today **69**, 30 (2016).

[160] M. Schmidt, F. M. Zimmer, and S. G. Magalhaes, Physica A **438**, 416 (2015).

[161] K. Binder and A. P. Young, Rev. Mod. Phys. **58**, 801 (1986).

[162] J. L. Manson, H. I. Southerland, B. Twamley, R. Rai, and J. L. Musfeldt, Dalt. Trans. **0**, 5665 (2007).

[163] D. Mootz and K. Bartmann, Angew. Chem. Int. Ed. Engl. **27**, 391 (1988).

[164] J. L. Manson, M. M. Conner, J. A. Schlueter, A. C. McConnell, H. I. Southerland, I. Malfant, T. Lancaster, S. J. Blundell, M. L. Brooks, F. L. Pratt, J. Singleton, R. D. McDonald, C. Lee, and M.-H. Whangbo, Chem. Mater. **20**, 7408 (2008).

[165] R. Boča, Coord. Chem. Rev. **248**, 757 (2004).

[166] SAINT v8.38A; Bruker AXS Inc.: Madison WI, 2013.

[167] SHELXT-2914; Bruker AXS Inc.: Madison WI, 2014.

[168] SHELXL-v.2014/7; Bruker AXS Inc.: Madison WI, 2014.

[169] SADABS v.2014/15; Bruker AXS Inc.: Madison WI, 2014.

[170] S. J. Clark, M. D. Segall, C. J. Pickard, P. J. Hasnip, M. J. Probert, K. Refson, and M. C. Payne, Z. Kristall. **220**, 567 (2005).

[171] D. Vanderbilt, Phys. Rev. B **41**, 7892 (1990).

[172] J. P. Perdew, K. Burke, and M. Ernzerhof, Phys. Rev. Lett. **77**, 3865 (1996).

[173] K. Lejaeghere *et al.*, Science **351**, aad3000 (2016).

[174] T. Lancaster, S. J. Blundell, M. L. Brooks, P. J. Baker, F. L. Pratt, J. L. Manson, C. P. Landee, and C. Baines, Phys. Rev. B **73**, 020410R (2006).

[175] R. S. Hayano, Y. J. Uemura, J. Imazato, N. Nishida, T. Yamazaki, and R. Kubo, Phys. Rev. B **20**, 850 (1979).

[176] T. Lancaster, S. J. Blundell, P. J. Baker, M. L. Brooks, W. Hayes, F. L. Pratt, J. L. Manson, M. M. Conner, and J. A. Schlueter, Phys. Rev. Lett. **99**, 267601 (2007).

[177] J. Reedijk and B. Nieuwenhuijse, Rec. Trav. Chim. **91**, 533 (1972).

[178] J. Krzystek, A. Ozarowskim and J. Telser, Coord. Chem. Rev. **250**, 2308 (2006).

[179] J. Titiš and R. Boča, Inorg. Chem. **49**, 3971 (2010).

[180] S. J. Blundell and F. L. Pratt, J. Phys.: Condens. Matter **16**, R771 (2004).

[181] D. Gatteschi and R. Sessoli, Angew. Chem., Int. Ed. **42**, 268 (2003).

[182] G. Christou, D. Gatteschi, D. N. Hendrickson, and R. Sessoli, MRS Bull., **25**, 66 (2000).

[183] S. Biswas, J. Goura, S. Das, C. V. Topping, J. Brambleby, P. A. Goddard and V. Chandrasekhar, Inorg. Chem. **55**, 8422 (2016).

[184] D. Zhang, M. Johnsson, S. Lidin, and R. K. Kremer, Dalt. Trans. **42**, 1394 (2013).

[185] C. P. Landee, D. M. Mudgett, and B. M. Foxman, Inorg. Chem. Acta. **186**, 45 (1991).

[186] B. K. Cho, B. N. Harmon, D. C. Johnston and P. C. Canfield, Phys. Rev. B **53**, 2217 (1996).

[187] P. Gegenwart, Q. Si, and F. Steglich, Nat. Phys. **4**, 186 (2008).

[188] W. Knafo, S. Raymond, P. Lejay, and J. Flouquet, Nat. Phys. **5**, 753 (2009).

[189] K. R. O'Neal, B. S. Holinsworth, Z. Chen, P. K. Peterson, K. E. Carreiro, C. Lee, J. L. Manson, M.-H. Whangbo, S. Li, Z. Liu, and J. L. Musfeldt, Inorg. Chem. **55**, 12172 (2016).

[190] International Tables for Crystallography (2006). Vol. A, part 7, pp. 488-449.

[191] (a) C. Y. Weng, Ph.D. Thesis, Carnegie Institute of Technology (1968); (b) A. Meye, A. Gleizes, J. J. Girerd, M. Verdaguer, and O. Kahn, Inorg. Chem **21**, 1729 (1982).

[192] J. J. Borrás-Almenar, E. Coronado, J. Curley, and R. Georges, Inorg. Chem. **34**, 2699 (1995).

[193] (a) R. L. Carlin, D. W. Carnegie Jr., J. Bartolomé, D. González, and Luis. M. Floría, Phys. Rev. B **32**, 7476 (1985); (b) Note a factor of 2 difference between the definition of the spin-exchange constant in this reference and the spin-Hamitlonian in Eq. 5.7.

[194] H. A. Algra, L. J. de Jongh, W. J. Huiskamp, and R. L. Carlin, Physica B **83**, 71 (1976).

[195] J. Bartolomé, H. A. Algra, L. J. de Jongh, and R. L. Carlin, Physica B **94**, 60 (1978).

[196] A. van der Bilt, K. O. Joung, R. L. Carlin, and L. J. de Jongh, Phys. Rev. B **24**, 445 (1981).

[197] J. Rodríguez-Carvajal, Physica (Amsterdam) **192**, 55 (1993).

[198] R. T. Azuah, L. R. Kneller, Y. Qiu, P. L. W. Tregenna-Piggott, C. M. Brown, J. R. D. Copley, and R. M. Dimeo, J. Res. Natl. Inst. Stan. Technol. **114**, 341 (2009).

[199] S. Toth and B. Lake, J. Phys.: Condens. Matter **27**, 166002 (2015).

[200] A. K. Hassan, L. A. Pardi, J. Krzystek, A. Sienkiewicz, P. Goy, M. Rohrer, and L.-C. Brunel, J. Magn. Reson. **142**, 300 (2000).

[201] C. H. Wang, M. D. Lumsden, R. S. Fishman, G. Ehlers, T. Hong, W. Tian, H. Cao, A. Podlesnyak, C. Dunmars, J. A. Schlueter, J. L. Manson, and A. D. Christianson, Phys. Rev. B **86**, 064439 (2012).

[202] F. M. Woodward, A. S. Albrecht, C. M. Wynn, C. P. Landee, and M. M. Turnball, Phys. Rev. B **65**, 144412 (2002).

[203] D. Craik, *Magnetism Principles and Applications* (Wiley, Chichester, 1995) pp. 184-188.

[204] R. F. Wielinga, In: C. J. Gorter (ed), *Progress in Low Temperature Physics* Vol. VI; (North Holland, Amsterdam, 1970) p. 333.

[205] L. J. de Jongh and A. R. Miedema, Adv. Phys, **23**, 1 (1974).

[206] M. E. Lines, J. Phys. Chem. Solids **31**, 101 (1970).

[207] Q.-L. Wang, F. Qi, G. Yang, D.-Z. Liao, G.-M. Yang, and H.-X. Ren, Z. Anorg. Allg. Chem. **636**, 634 (2010).

[208] W. J. A. Blackmore, J. Brambleby *et al.*, in preparation (2018).

[209] R. A. J. Driessen, F. B. Hulsbergen, W. J. Vermin, and J. Reedijk, Inorg. Chem. **21**, 3594 (1982).

[210] M. B. Stone, G. Ehlers, and G. Granroth, Phys. Rev. B **88**, 104413 (2013).

[211] M. B. Stone, M. D. Lumsden, Y.Qiu, E. C. Samulon, C. D. Batista, and I. R. Fisher, Phys. Rev. B **77**, 134406 (2008).

[212] F. Lloret, M. Julve, J. Cano, R. Ruiz-García, and E. Pardo, Inorg. Chim. Acta. **361**, 3432 (2008).

[213] P. W. Carreck, M. Goldstein, E. Mary McPartlin, and W. D. Unsworth, J. Chem. Soc. D **0**, 1634 (1971).

[214] R. L. Carlin, *Magnetochemistry* (Spinger-Verlag, Berlin, 1986) p. 65.

[215] T. G. Castner, Jr. and M. S. Seehra, Phys. Rev. B **4**, 38 (1971).

[216] K. Katsumata, J. Phys.: Condens. Matter **12**, R589 (2000).

[217] C. N. Yang, Phys. Rev. **85**, 808 (1952).

[218] D. Vaknin, J. L. Zarestky, L. L. Miller, J.-P. Rivera, and H. Schmid, Phys. Rev. B **65**, 224414 (2002).

[219] A. K. Bera, B. Lake, W.-D. Stein, and S. Zander, Phys. Rev. B **89**, 094402 (2014).

[220] Y. Kawasaki, J. L. Gavilano, L. Keller, J. Schefer, N. B. Christensen, A. Amato, T. Ohno, Y. Kishimoto, Z. He, Y. Ueda, and M. Itoh, Phys. Rev. B **83**, 064421 (2011).